Hydro-sedimentary dynamics of the Rance estuary : processes, evolution and management

Rajae Rtimi

THÈSE PRÉSENTÉE

POUR OBTENIR LE GRADE DE

DOCTEUR DE

L'UNIVÉRSITÉ DE BORDEAUX

ÉCOLE DOCTORALE DES SCIENCES ET ENVIRONNEMENTS

SPÉCIALITÉ : PHYSIQUE DE L'ENVIRONNEMENT

Par **Rajae RTIMI**

DYNAMIQUE HYDROSÉDIMENTAIRE DE L'ESTUAIRE DE LA RANCE: FONCTIONNEMENT, ÉVOLUTION ET GESTION

Sous la direction de: **Aldo SOTTOLICHIO** et **Pablo TASSI**

Soutenue le 23 février 2022

Convention CIFRE n° 2018-1653

Préparée au laboratoire EPOC, Université de Bordeaux, Pessac et EDF R&D LNHE, Chatou

Membres du jury :

Mme Isabelle BRENON	Maître de conférence	Univ. de la Rochelle	Rapporteur
M. Sylvain GUILLOU	Professeur	Univ. de Caen	Rapporteur
Mme Claude ESTOURNEL	Dir. de Recherche CNRS	Univ. de Toulouse	Examinatrice
Mme Monica FOSSATI	Assistant Professor	Univ. de la República (Uruguay)	Examinatrice
M. Florent GRASSO	Chargé de Recherche	IFREMER	Examinateur
M. Athanasios ANGELOUDIS	Lecturer	Univ. of Edinburgh (UK)	Invité
M. Bruno CASTELLE	Dir. de Recherche CNRS	Univ. de Bordeaux	Président
M. Aldo SOTTOLICHIO	Professeur	Univ. de Bordeaux	Directeur
M. Pablo TASSI	Ingénieur-Chercheur Expert	EDF R&D / LHSV	Encadrant

Résumé

Dynamique hydro-sédimentaire de l'estuaire de la Rance: fonctionnement, évolution et gestion

L'estuaire de la Rance est une *ria* relativement petite (20km de long) avec un faible débit fluvial. Elle est située sur la côte bretonne dans le nord de la France, avec un marnage qui peut atteindre 13,5m au maximum de vive-eau. En profitant de ces marées, la première usine marémotrice opérationnelle au monde (actuellement la deuxième plus grande) a été construite dans les années 1960 à l'embouchure de l'estuaire. Le bassin de la Rance est également caractérisé par sa complexe morphologie et l'aménagement de sa limite fluviale (l'écluse du Chatelier). Un envasement net a été observé dans la partie amont de l'estuaire depuis les années 1980 par plusieurs études. Cependant, l'impact de l'usine sur l'hydrodynamique, le transport sédimentaire et la morphodynamique n'est toujours pas quantifié. En outre, la connaissance des processus physiques régissant la dynamique hydro-sédimentaire dans ce système complexe reste très limitée. Ce travail de thèse vise à mieux comprendre la dynamique hydro-sédimentaire dans ce système aménagé d'une usine marémotrice à son embouchure et d'une écluse à sa limite fluviale. Pour atteindre cet objectif, une approche complémentaire entre les mesures terrain et la modélisation numérique a été déployée. D'une part, le suivi terrain des variables hydro-sédimentaires a été réalisé pour calibrer et valider les modèles numériques. D'autre part, deux modèles numériques hydro-sédimentaires 2D et 3D ont été développés dans le système de modélisation TELEMAC-MASCARET. Les résultats numériques montrent que l'usine induit (*i*) une diminution importante du marnage et du prisme de marée ainsi que la submersion de plusieurs zones intertidales ; (*ii*) une limitation des niveaux hauts à l'intérieur du bassin ce qui lui protège contre les inondations marines ; et (*iii*) une diminution générale des courants sauf dans la région proche de l'aménagement. De plus, la morphologie de l'estuaire amplifie les courants de jusant dans le rétrécissement au Port-Saint-Hubert. Par ailleurs, le fonctionnement de l'usine repousse l'interface eau douce-eau salée d'environ 5km vers l'amont, cette position est également sensible à la variation saisonnière du débit fluvial. Le modèle hydro-sédimentaire 3D montre qu'à l'échelle d'un cycle de marée (*i*) les pics de matières en suspension sont constatés pendant la phase de remplissage de l'estuaire ; et (*ii*) les sédiments pourraient être remis en suspension localement pendant la phase de turbinage (étape de production d'électricité en jusant). A l'échelle d'un cycle de 14 jours, le flux sédimentaire résiduel est constamment orienté vers l'amont de l'estuaire. Par conséquent, les importants taux de sédimentation sont observés dans le chenal principal amont. Ce comportement morphodynamique est également observé sans usine marémotrice, mais avec des taux de sédimentation plus faibles. A l'échelle d'un an, les résultats numériques hydro-sédimentaires 2D ont évalué la nécessité d'un débit fluvial considérant les chasses hydrauliques pour simuler correctement les processus morphodynamiques à long terme. Par ailleurs, les chasses hydrauliques réalisées à l'écluse du Chatelier et l'ouverture des vannes pendant le jusant ont prouvé leur efficacité pour diminuer l'accumulation des sédiments dans la partie amont de l'estuaire. Enfin, les modèles numériques complémentaires 2D et 3D ont démontrés leur pertinence pour aider à définir un plan de gestion durable de l'estuaire.

Mots-clés : Hydrodynamique, transport sédimentaire, morphodynamique, énergie marémotrice, l'estuaire de la Rance, modélisation numérique, mesures terrain.

Abstract

Hydro-sedimentary dynamics of the Rance estuary : processes, evolution and management

The Rance estuary is a relatively small low-discharge steep-sided *ria*, located along the Brittany coast in northern France, with a maximum spring tidal range of 13.5m. Taking advantage of this hyper-tidal regime, the first operational tidal power station (TPS) in the world (and currently the second largest) was built at the estuary mouth and has been in operation since the 1960s. In addition to the TPS, the Rance estuary is characterized by its complex morphology and the configuration of its uppermost limit (Chatelier lock). Net siltation and sediment accumulation were reported in the basin since the 1980s by various studies based on field measurements. However, the impact of the TPS on hydrodynamics, sediment transport and morphodynamic is still unquantified. In addition, the relevance of each physical processes driving hydrodynamics and sediment dynamics in this complex system is still unclear. This PhD thesis aims to better understand hydro-sedimentary dynamics in this highly engineered system by the presence of a tidal power plant on its mouth and a lock on its uppermost limit. To this goal, a complementary approach accounting for both field measurements and numerical modelling was deployed. On the one hand, field surveys of hydro-sedimentary variables were carried out to calibrate and validate the numerical models. On the other hand, 2D and 3D hydro-sedimentary numerical models were developed in the TELEMAC-MASCARET modelling system. Numerical results reveal that the TPS induces (*i*) a major decrease in tidal range and tidal prime along with the increase of submerged intertidal zones; (*ii*) a limitation of high-water level inside the estuary protecting it against marine flooding; and (*iii*) an overall decrease in currents except in the region close to the TPS. Moreover, the morphology of the estuary amplifies ebb currents in the narrowing at Saint-Hubert-Port. Furthermore, the TPS pushes the freshwater-saltwater interface roughly 5km upstream in the estuary. Its position is also sensitive to seasonal river discharge variation. The 3D hydro-sedimentary model shows that at the scale of a tidal cycle (*i*) peak suspended sediment concentrations (SSC) are noticed during the estuary's infilling phase; and (*ii*) sediment could be resuspended locally during the turbining phase (electricity production stage), but would not be transported further than 3km from the uppermost limit. At the scale of a fortnight, residual sediment flux is continuously oriented towards the upper estuary. Consequently, significant sedimentation rates were observed in the main upstream channel. This morphodynamic behavior was also captured by the model under natural tidal forcing (without TPS), but with lower sedimentation rates. At the time-scale of one year, 2D hydro-sedimentary numerical results assess the need to provide an accurate river discharge considering hydraulic flushes to correctly simulate long term morphodynamic processes. Furthermore, hydraulic flushes at the Chatelier lock and the opening of sluice gates during ebb prove their efficiency in decreasing sediment accumulation in the upper estuary. Finally, the complementary 2D and 3D numerical models showed to be invaluable tools to define a sustainable management plan of the Rance estuary.

Key words: Hydrodynamics, sediment transport, morphodynamics, tidal energy, the Rance estuary, numerical modelling, field measurements.

Acknowledgements

I would like to acknowledge the French National Association of Research and Technology (ANRT) and EDF R&D for funding this CIFRE Ph.D. through the project GESED24; EPOC Laboratory and Bordeaux University; the thesis jury members for their deep interest to my work, their precious time to evaluate the dissertation and the oral presentation and their comments and suggestions that helped improve and clarify this manuscript; my supervisors Pablo Tassi and Aldo Sottolichio for appreciating my research strengths and patiently encouraging me to improve in my weaker area, for their precious advice to avoid the wrong directions and for sharing their passion and enthusiasm about estuaries; the members of my thesis committee, Tom Benson, Bruno Castelle, Pierre Le Hir and Erik Toorman for the fruitful and very interesting discussions; Christine Bertier, Matthieu Le Brun, measurement crews of EDF R&D, EDF-DTG and EPOC for their patience and sense of humor during field campaigns; members of EDF-CIH, Rance Energies, Conseil Scientifique of the Rance, Bruno Caline and Bernard Goguel for their feedback; my interns Marine Vandenhove and Luca Parquet who contributed to this work; Nicolas Huybrechts, my co-workers in the EDF-LNHE departement and LHSV for their kind advice, my co-worker Fatna Oukaili for her encouragement during hard times; my family, my friends, my brothers, my husband and my parents for their confidence and constant support through the ups and downs.

Contents

List of figures

List of tables

List of abbreviations

2D / 3D:	Two / Three dimensional.
2DH:	2D Horizontal depth-averaged model.
ADCP:	Acoustic Doppler Current Profiler.
BE:	Bed evolution.
CGEDD:	Conseil Général de l'Environnement et du Développement Durable.
CPU:	Central Processing Unit.
DEM:	Digital Elevation Model.
EDF:	Electricité De France.
EPOC:	Environnements et Paléoenvironnements Océaniques et Continentaux.
ETM:	Estuarine Turbidity Maximum.
LES:	Large Eddy Simulations.
LHSV:	Laboratoire d'Hydraulique de Saint-Venant.
LNHE:	Laboratoire National de l'Hydraulique et Environnement.
NTU:	Nephelometric Turbidity Unit.
R&D:	Research and Development.
RANS:	Reynolds-Averaged Navier-Stokes equations.
RTPS:	Rance Tidal Power Station.
SPM:	Suspended Particle Matter.
SSC:	Suspended Sediment Concentration.
TPS:	Tidal Power Station.

Glossary

Estuarine Turbidity Maximum zone: Corresponds to the zone of highest turbidity resulting from turbulent resuspension of sediment and flocculation of particulate matter in an estuary.

Highest astronomical tide: Highest tide that can be expected to occur under average meteorological conditions and at the spring and autumn equinox

Hydrodynamics: Physics that deals with the motion of fluids and the forces acting on solid bodies immersed in fluids and in motion relative to them.

Hydromorphology: Physical, hydrological and hydrodynamic characteristics of transitional and coastal waters including the underlying processes from which they result

Intertidal zone: Zone alternately covered and uncovered by the tide.

Mixing: Blending of waters of different characteristics (e.g. temperature, turbidity, salinity) by turbulence and diffusion, caused by tides, winds, waves, currents and river runoff

Morphodynamics: Study of the interaction and adjustment of the topography and fluid hydrodynamic processes (estuaries, coasts, rivers, lakes, *etc*).

Ria: A coastal inlet formed by the partial submergence of a river valley.

Sediment transport: Physical process involving the motion of particles subjected to the energy of the water flows, at the origin of the morphological evolution.

Storm surge: Change in water level as a result of meteorological forcing (wind, high or low barometric pressure) additional to the astronomic tide; it may be positive or negative

Stratification: Layering of water column due to density differences resulting from changes in temperature, turbidity or salinity with depth

Tidal power station: Structure converting energy from tides into useful forms of power, mainly electricity. It makes use of the potential energy in the difference in height (or hydraulic head) between high and low tides. When the sea level rises and the tide begins to come in, the temporary increase in tidal power is channeled into a large basin behind the dam, holding a large amount of potential energy. With the receding tide, this energy is then converted into mechanical energy as the water is released through large turbines that create electrical power through the use of generators.

Tidal prism: The volume of water leaving an estuary at ebb tide.

Tidal range: The height difference between high tide and low tide.

Tidal regime: Parameters characterising tides including levels, periods, frequencies, harmonics, phases and spectra

Turbidity: Reduction of transparency of a liquid caused by the presence of suspended particulate matter

CHAPTER 1

INTRODUCTION

1.1 Global scientific context

1.1.1 What is an estuary ?

An estuary has over 40 different definitions according to Perillo [1995]. Cameron and Pritchard [1963] stated that *an estuary is a semi-enclosed coastal body of water which has free connection to the open sea and within which sea water is measurably diluted with freshwater derived from land drainage*. This definition increased in complexity with time, for example with the inclusion of the influence of tides. For instance, Dyer [1997] defined an estuary as *a semi-enclosed coastal body of water which has free connection to the open sea, extending into the river as far as the limit of tidal influence, and within which sea water is measurable diluted with freshwater derived from land drainage*. Later on, Elliott and McLusky [2002] concluded that existing definitions will never be suitable for all needs, and provided thus a worldwide checklist approach to define an estuarine area while still acknowledging the inherent variability of such systems. From a physical point of view and for simplicity sake, an estuary is a delimited area where freshwater from the river interacts with saline water from the sea. According to The Open University [1999], an estuary can usually be divided into three geographical zones: (i) an upper estuary, dominated by freshwater but subject to daily tidal rise and fall, (ii) a middle estuary, where most of the mixing between seawater and river water occurs; and (iii) a lower estuary, dominated by seawater influence and directly connected with the open sea (Figure 1.1). Boundaries of each zone can naturally shift according to tides, seasons and weather.

1.1.2 Estuaries classifications

Each estuary has its unique characteristics such as tidal range, river discharge, geomorphology, etc. Nevertheless, some similarities can be observed between estuaries which allow unified principles to better understand and predict behavior of these complex systems. These similarities lead to classification schemes based on various criteria. For instance, Valle Levinson [2010] proposed estuarine classifications based on water balance, geomorphology, vertical structure of salinity and hydrodynamics. Recently, Geyer and MacCready [2014] provided a new classification approach by mapping various estuaries onto a two-parameter space based on freshwater Froude number and mixing parameter. Each estuary can be represented by a square in this space in order to consider the spring-neap variability. Estuaries can also be classified onto 3 classes simply based on tidal range at their mouth: (i) microtidal estuary with tidal range below $2m$, (ii) mesotidal estuary with tidal range between 2 to $4m$ and (iii) macrotidal estuary with tidal range above $4m$ [Whitfield and Elliott, 2011]. A further category consists of hyper-tidal estuaries that exhibit larger tidal range (i.e., mean tidal range above 6 m). Since maximum tidal currents are roughly proportional to local tidal range [Dyer, 1997], these latter types are expected to develop the strongest tidal currents and are ideal locations for tidal renewable energy projects.

1.1.3 Tidal energy

Tidal energy is a form of hydro-power with potential as one of the future sources of renewable energy. Historically, it started by tide mills that were in operation back in the middle ages (Figure 1.2.a), then with larger tidal power station projects such as the Rance tidal barrage [Charlier, 2007], and very recently strategic cases for tidal lagoon power plants were studied (Figure 1.2.b) [Hendry, 2017]. The principle of generating electricity from tides relies on creating an artificial phase difference by impounding water, and then allowing it to flow through turbines. Tidal

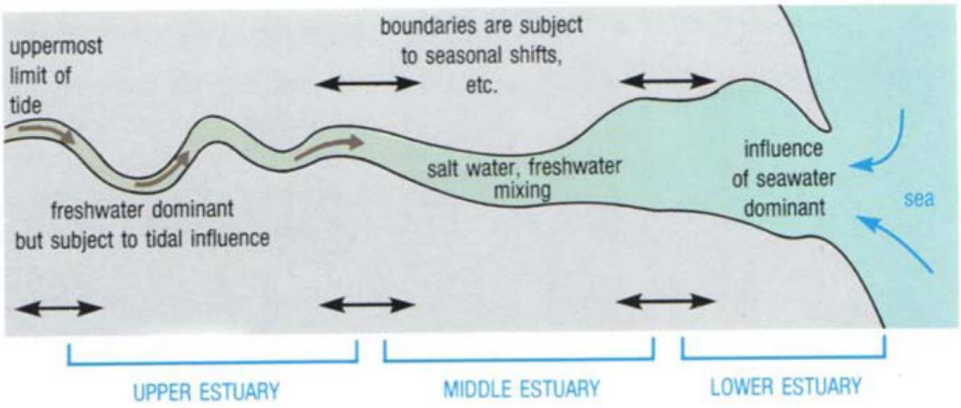

Figure 1.1: Schematic division of an estuary into upper, middle and lower estuary [The Open University, 1999].

power plants can be designed to produce power one-way, i.e. flood generation such as the Sihwa lake station (South Korea) or ebb generation such as the Annapolis Royal Generating Station (Canada). They can also be designed to generate power two-way, i.e. during both flood and ebb such as the Rance tidal power station (France). Neil et al. [2018] reviewed the worldwide tidal range energy resource and stated that 90% of this renewable energy source is distributed among just five countries with Australia in the first rank hosting 30% of the global tidal range resource. The global theoretical tidal range resource is estimated around 25,880TWh per year [Neil et al., 2018]. Since a significant portion of this energy is dissipated around the globe, only 380TWh could be potentially extracted per year, which represents 1.5 to 2% of the worldwide power demand [Énergie marémotrice, 2018]. Although tidal power stations have great potential to provide predictable renewable energy resources, they are engineering structures that considerably intervene in the natural landscape; therefore they could have an impact on hydrodynamics, sediment dynamics, water quality and ecosystems [Angeloudis and Falconer, 2017; Xia et al., 2010; Cornett et al., 2013; Kim et al., 2021; Kirby and Retière, 2009] at the local scale close to the structure but also at the scale of the whole system.

1.1.4 Importance of estuaries

Besides being suitable locations for tidal energy projects, estuarine environments are perfect habitat for diverse aquatic species. Indeed, import of nutrients and minerals from the river inside the estuary, foster primary production of algae and phytoplankton, which in turn nourish many inhabitants. Beyond the influence of tidal power projects, estuaries are subject to large-scale anthropogenic pressure due to the fast industrial evolution and the subsequent growth of trade. Estuarine systems continually evolve and are shaped as a result of the balance between internal processes (e.g., physical, chemical, biological, etc.) and external drivers (primarily climatic and anthropogenic) [Zhou et al., 2017]. For instance, for navigation purposes the depth of estuarine main channels needs to be constantly maintained below a given threshold [Orseau et al., 2021]. This activity may increase siltation processes induced by natural or artificial tidal forcing, which in turn need to be controlled by expensive engineering interventions such as dredging activities. These operations may also induce imbalance in biological systems. Thus, these activities cause various issues on both the economic and ecological levels. Therefore, a better understanding

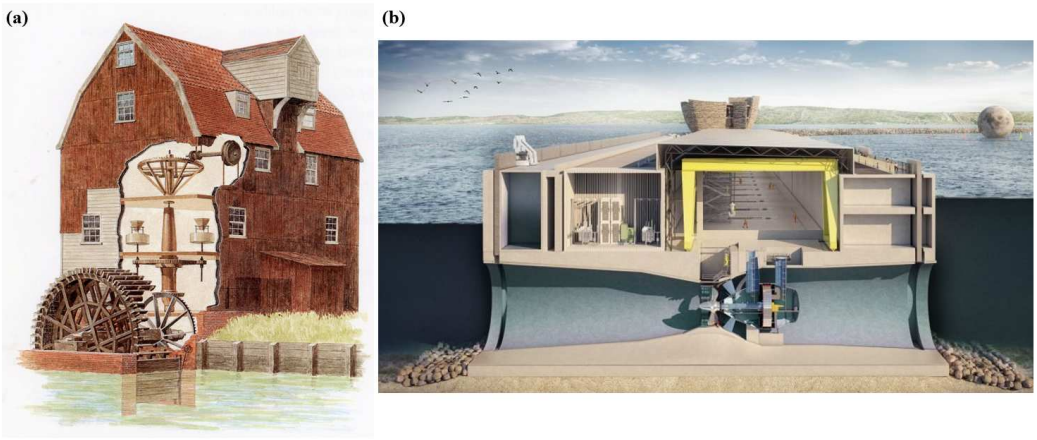

Figure 1.2: Tidal energy between the past and the present. (a) Tidal mild from [Tide Mill, 2018] and (b) tidal lagoon project from [Tidal Lagoon Power, 2020].

of estuarine processes is crucial to reduce negative impacts resulting from Man's uses and to develop a suitable management plan for estuaries subject to anthropogenic perturbations.

1.1.5 Physical processes in estuarine environments

Physical processes in estuarine environments can be classified within 3 general aspects : (i) *hydrodynamics*, (ii) *sediment transport* and (iii) *morphodynamics*.
Hydrodynamic behavior in estuaries is primarily driven by three factors: (i) the tidal wave propagating from the ocean and due to the gravitational forces of the Moon and the Sun combined with the rotation of the Earth; (ii) the estuary's morphology, and (iii) the freshwater discharge [Guillou et al., 2011; Stark et al., 2017b,a; Thurman, 1994; Sumich, 1996]. Hydrodynamics in macrotidal estuaries is mainly governed by tides and tidal currents, which dominate the trends on residual sediment transport; therefore the deposition and erosion fluxes, and consequently morphological evolution [Zhang et al., 2018]. Several studies assessed the importance of tidal asymmetry which induces residual sediment transport in estuaries [Aubrey and Speer, 1985; Speer and Aubrey, 1985; Friedrichs and Aubrey, 1988; Nidzieko and Ralston, 2012; Guo et al., 2018; McLachlan et al., 2020; Mandal et al., 2020]. Tidal asymmetry is quantified from flow velocity and water elevation Friedrichs and Aubrey [1988]; Nidzieko and Ralston [2012]; Bolle et al. [2010]. The former identifies the nature of the asymmetry: *i.e.*, ebb- or flood-dominance in the estuary. The latter compares the respective durations of rising and falling tides. This indicates the predominant direction of residual transport of cohesive sediment displaced by suspension and of non-cohesive sediment transported by bedload and/or suspension. Asymmetry in low and high slack water duration is also relevant to the net transport of the finer sediment fraction in the water column [Dronkers, 2005]. A human intervention such as the presence of a tidal power plant at a seaward boundary modifies the tidal asymmetry, the hydrodynamic regime and significantly alters non-linear tidal interactions [Speer and Aubrey, 1985; Hoitink et al., 2003; Vellinga et al., 2014].
Sediment can be transported by bedload and/or by suspension [Van Rijn, 2006]. The former is related to non-cohesive sediment and allows particles to stay in contact with the bed continuously while their motion is conducted by rolling or sliding over the bed within a thin boundary layer. The latter is relevant to both cohesive and non-cohesive sediment and consists on lifting particles

outside the boundary layer to be suspended in the water column and then transported due to advective and diffusive processes to finally settle to the bed by gravity. In this PhD project, it is assumed that particles in the Rance estuary are transported only by suspension. Consequently, only physical processes relevant to suspended load are described hereafter. Sediment dynamics in the water column and near the bed are governed by various processes (Figure 1.3.a), namely erosion, turbulent mixing, flocculation, settling, deposition and consolidation of the deposit [Mehta, 2014].
Erosion occurs when the frictional velocity; in other words bed shear-stress; surpasses a critical threshold. Alternatively stated, sediment is eroded when lift force from the water motion is stronger than the gravitational force. Once eroded, sediment is transported thanks to advective and diffusive (mixing) processes. A particle in suspension is subject to forces induced by the gravity, mean flow, turbulent mixing inertia and collision with other particles. Consequently, cohesive sediment can collide and associate with others to create a floc. The latter moves through the water column and may combine with other particles or flocs and grow, or it may break up due to high turbulent shear, or it may settle [Mehta and McAnally, 2008; Winterwerp, 2002; Manning et al., 2011]. The degree of flocculation is highly dependent upon both the suspended particle matter (SPM) concentration and turbulent intensity [Van Leussen, 1994; Manning, 2004].
Whether primary particles or aggregated flocs, suspended particles settle and are deposited in the bed under the force of gravity. Once eroded, particles are transported and deposited in a different location from where they have been eroded. This outcomes in a net sediment transport in estuarine environments, inflow or outflow with respect to the land-sea continuum. Sediment particles are eroded from different regions along an estuary, but can be transported to a trapping area called the estuarine turbidity maximum (ETM) (Figure 1.3.b). Burchard et al. [2018] explained that the formation of an ETM is due to estuarine circulation, induced from estuarine salinity gradient and river discharge [Knudsen, 1900; MacCready and Geyer, 2004], generating an up-estuary SPM transport leading to high sediment concentration. As it is the place of sediment high sediment transfer between the bed and the water column and between continental and coastal waters, ETM is an essential feature to analyze sediment dynamics in macrotidal estuaries [Sottolichio et al., 2011; Toublanc et al., 2016; Grasso et al., 2018]. Furthermore, it plays an important role in controlling channels siltation, but also in modulating biological and biogeochemical processes [Kirby and Retière, 2009; Passy et al., 2016].
In case of high rates of cohesive sediment in the water column, fluid mud can form because settling is hindered at very high SSC near the bed (Figure 1.3.a). In case of low deposition rates and the absence of high-concentration benthic layer, the settling sediment may deposit directly to form a bed without forming fluid mud. After sedimentation, deposited mud consolidates, i.e. it experiences the reduction of volume deposition by the removal of pore water [Mehta and McAnally, 2008].
Other processes such as biological or chemical ones interact with sedimentary processes and are important for ecology or water quality and need to be considered in studies of estuarine environments. The present work focuses more on the interaction between the basic processes described above, i.e. hydro-sedimentary dynamics but other processes can be considered in future work.

1.1.6 Understanding physical processes in estuarine environments

Many tools can be deployed to understand estuarine physical processes, ranging from field and laboratory measurements, conceptual models, to real scale numerical models. All these approaches are complementary. Field and laboratory experiments provide reliable, but often

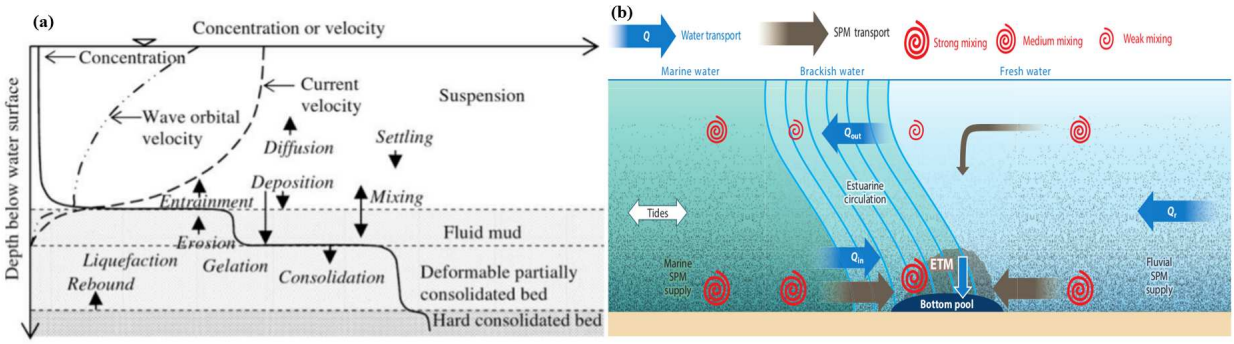

Figure 1.3: (a) Sediment transport processes relative to concentration/velocity profiles (After [Mehta, 2014]). (b) Estuarine Turbidity Maximum (ETM) formation (After [Burchard et al., 2018]).

space-dependent, analyses on physical processes. However, they often include the sum of many processes, which makes it difficult to examine the magnitude and sensitivity to each particular process. Whereas, field and laboratory data are mandatory to calibrate and validate a numerical model. Once calibrated and validated, a numerical model has the advantage to correctly reproduce the physical behavior of a complex system in which specific physical mechanisms can be assessed separately. It has also the ability to first quantify, and second help reducing the anthropogenic impact in heavily engineered environments.

Hydrodynamics

Acoustic Doppler Current Profilers are widely deployed to assess longitudinal, transverse and vertical variability of flow in macrotidal estuaries under natural, or artificial tidal forcing (dams or tidal power stations), e.g. the Gironde estuary [Ross et al., 2017], Geum river [Figueroa et al., 2020], and Sihwa lake [Kim et al., 2021]. Furthermore, two-dimensional (2D) depth-averaged and three-dimensional (3D) models have been used to study hydrodynamics in various estuaries. For instance, in the Río de la Plata hydrodyanmics were investigated from salinity field behaviour and its seasonal variability [Fossati and Piedra-Cueva, 2008], to the impact of a power plant cooling water discharge [Fossati et al., 2011] and 3D estuarine circulation [Fossati and Piedra-Cueva, 2013]. Likewise, both 2D and 3D numerical models have been among the tools used to assess the hydrodynamic impacts of existing or on-development tidal power plant projects [Angeloudis and Falconer, 2017]. With the third highest tidal range in the world (7m in spring tide), the Severn estuary (United Kingdom) would be an optimal location for tidal power projects. A 2D numerical model has been developed by Xia et al. [2010] to estimate the impacts of three renewable-energy projects, *i.e.* the Cardiff–Weston, the Fleming lagoon and the Shoots barrages. For the latter three structures, the basic barrage operation regime adopted was the mode of ebb generation only. They concluded that the Fleming Lagoon project would have little influence on the hydrodynamic processes in the Severn estuary, however the construction of the barrages would be responsible of significant environmental impacts Xia et al. [2010]. Young *et al.* conceived a 2D hydrodynamic model to highlight the impact of the world's first tidal power station, the Sihwa lake tidal power plant (South Korea) Young et al. [2010]. The tidal energy scheme of this plant is a single flood-generation mode. The study established that the limitation of water surface elevation would modify the estuary's ecosystem. However, this type of power generation can create useful building ground Young et al. [2010]. Another optimal location for tidal power plant would be the bay of Fundy, located on the Atlantic coast of North America,

where tidal range can exceed 16 m during spring tides. The 2D and 3D hydrodynamic models of Cornett et al. [2010, 2013] allowed to perform the simulation of a range of hypothetical development scenarios with three different operating modes: ebb generation only, flood generation only and ebb-flood generation. They assessed that the choice of operating mode has considerable influence on local velocities near the bay, particularly near the powerhouse. However, it seemed to have little influence on the magnitude of far-field hydrodynamic impact Cornett et al. [2010, 2013]. Turbulence induced by turbines in the near- and far-fields from tidal structures is also an important factor in estuarine environments hosting power stations. This aspect was addressed by 3D numerical models with sophisticated turbulence approaches, namely various Reynolds Averaged Navier-Stokes (RANS) models [Nguyen et al., 2016] and Large Eddy Simulation (LES) model [Bourgoin et al., 2019]. Although they provided a better understanding of the wake induced by the turbines, these sophisticated models are computationally expensive for large scale applications.

Sediment transport and morphodynamics

Physical processes driving the sediment transport in estuarine environments are various and highly variable from an estuary to another. Nevertheless, some common features can be identified. Estuarine turbidity maximum (ETM) is a main feature in sediment dynamics in macrotidal estuaries. This physical phenomenon can be extensively analyzed based on field measurements and numerical models. Based on automatic monitoring stations recording continuously turbidity, Uncles et al. [1985]; Sottolichio et al. [2011] and Jalón-Rojas et al. [2015] analyzed respectively the ETM dynamics in the Tamar estuary (United Kingdom) and the Gironde estuary (France) at different timescales. In the high-concentrated Ems River (Germany-Netherlands), Winterwerp [2011] characterized fine sediment transport by internal tidal asymmetry using a 1D numerical model. ETM dynamics is also largely studied in the Seine estuary (France) Brenon and Le Hir [1999]; Grasso et al. [2018]. Recently, Grasso et al. [2018] quantified the influence of each forcing among river discharge, tides and waves on the ETM location and mass changes in the Seine estuary (France) based on realistic 3D numerical models accounting for mud and sand transport processes. It concluded that ETM mass and location are primarily driven by tidal range and are modulated by neap-spring periods. In addition, energetic wave conditions substantially influence the ETM mass Grasso et al. [2018]. On a longer timescale (multi-decades), Jalón-Rojas et al. [2021] examined the evolution of ETM zone in the Garonne estuary (France) under climate and anthropogenic pressures. ETM feature is relative to short term alternation between erosion and deposition processes. On longer timescales, a residual erosion/deposition fluxes can be observed on the bed leading to morphodynamic evolution. Accurate morphodynamic trends in numerical models result from the correct simulation of erosion and deposition fluxes. These latter pass through the calibration of various parameters describing sediment behaviour and water/bed particle exchanges expressed in empirical laws. To this goal, single point field measurements surveys can be particularly useful. ALTUS probes in intertidal mudflats give continuous time series of erosion and deposition on the bed [Verney et al., 2006; Deloffre et al., 2005]. In the Loire estuary (France), Kervella et al. [2012] examined single point morphodynamics based on this technique, and the study provided a valuable bed evolution data sets to calibrate and validate a numerical model developed for applied operational applications by the GIP Loire Estuaire [Walther et al., 2012]. Morphodynamic processes are highly dependent on the sediment size classes, transport modes, and sediment states [Wu, 2008]. Santoro et al. [2017] quantified the impact of consolidation and complexities arising from the presence of fine sediment dynamics in the Rio De La Plata and specifically the Montevideo Bay. Similar complexities were also highlighted in the Charente estuary by Toublanc [2013]. Furthermore, mixture of cohesive and

non-cohesive sediment is usually found in estuarine environments and its behavior is different from a single class sediment dynamics. Consequently, their numerical simulation can be very challenging Chavarrias et al. [2018].
In summary, understanding physical processes driving hydrodynamics, sediment transport and morphodynamics in estuaries relies on two complementary approaches: field measurements and numerical modelling. Studies on estuaries under natural tidal forcing (tides) highlights the complexity of such environments, namely by the river discharge, the system's geomorphology and grain-size distribution. This complexity is increased in systems with high anthropogenic structures such as dams and tidal power plants.

1.2 The Rance estuarine system

1.2.1 The Rance estuary as a worldwide example

Located on the Brittany coast of northern France (Figure 1.4), the Rance estuary is a relatively small steep-sided, 20km long *ria* [Evans and Prego, 2003]. Its maximum perigean spring tidal range reaches 13.5m at the mouth (Saint Servan, Figure 1.5.a and 1.5.b). Taking advantage of this hyper-tidal regime, the first ever tidal power station in the world was built at the estuary mouth (Figures 1.5.a and 1.5.c). The plant has been in operation and managed by Electricité de France (EDF) since 1966 and is currently the second largest operational tidal power station in the world [Pelc and Fujita, 2002], behind the Sihwa Lake tidal power plant [Young et al., 2010]. With a peak (mean) output capacity of 240MW (57MW), it supplies 0.12% of the power demand in France, which is equivalent to a medium-size city such as Rennes (*c.* 225,000 in habitants) [EDF, 2020].
The main characteristics of the Rance tidal power plant are as follows (Figure 1.5.c): (i) a 65m lock, with 20,000 vessels per year passing through; (ii) 24 Kaplan bulb turbines appropriate for very low head and high flow rates [Hydrelect, 2012], 323m long and 33m wide, each unit producing 10MW; (iii) a rockfill dyke 165m long; (iv) 6 sluice gates composing 114x15m dam; and (v) a road on which 30,000 (60,000 in summer) vehicles per day travel between the cities of Dinard and Saint Malo. The particularity of the Rance tidal power plant is its ability to produce electricity during both falling and rising tides, operating by one- and two-way generation modes thanks to the capacity of its Kaplan bulb turbines to rotate in both directions [Charlier, 2007; Young et al., 2010]. The Rance River drains a small catchment area, with an average river discharge of $7m^3/s$, low water flow rate of $0.5m^3/s$ and a decennial flood of $80m^3/s$. These magnitudes are small compared to the tidal flux observed upstream of the plant, with about $9{,}000m^3/s$ maximum in neap tide and $18{,}000m^3/s$ in spring tide. Consequently, the Rance is considered a macrotidal estuary with high influence of tides compared to river influence [Whitfield and Elliott, 2011].
The Rance estuary is characterized by the complex configuration of its upstream boundary (Chatelier lock, Figures 1.5.a and 1.5.g). Indeed, this boundary is composed by a lock and 2 sluice gates that maintain a constant water level in the harbour located upstream. This system is deployed to perform occasional hydraulic flushes during flood events. Neither water flow rate nor solid discharge passing through this boundary are measured and the nearest hydrometric station is located 33km upstream. Only dates and duration of hydraulic flushes are saved.
Compared to a typical funnel-shaped estuary, the morphology of this *ria* is complex (Figure 1.5.a), between the Chatelier lock and Mordreuc, the basin maintains the narrowness and sinuosity of the Rance river. Mordreuc plain is a key site of the Rance estuary due to the presence of many intertidal mudflats in this zone (Figure 1.5.f). Downstream of Mordreuc, the estuary widens into large coves till the narrowing of Saint-Hubert-Port (Figure 1.5.e). The latter is characterized by

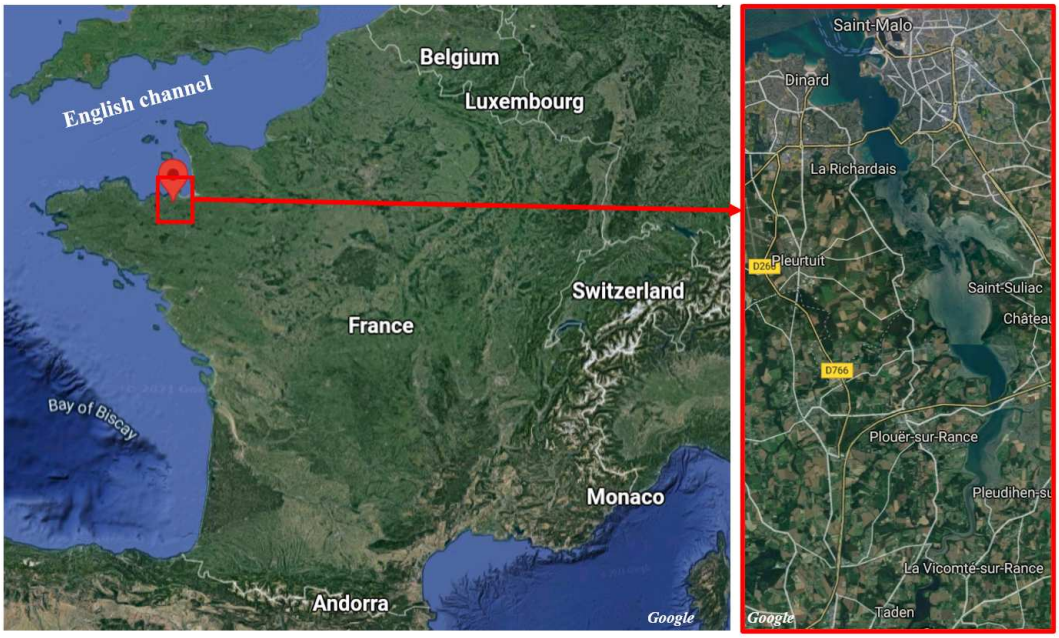

Figure 1.4: Location map with a zoom on the Rance estuary [Google Earth, 2020].

a deeper bed level (Figure 1.5.a) and the presence of a bridge linking the left and right banks of the estuary. Then, from Saint-Hubert-Port onwards, the basin become larger and delimited by coves separated by rocky heads, passing by Saint-Suliac (Figure 1.5.d) representing the middle of the estuary and the limit of deep channels (Figure 1.5.a). Furthermore, the valley between Saint-Servan and Saint-Hubert-Port follows a SSE-NNW direction, while between Saint-Hubert-Port and Chatelier lock it changes to a SW-NE direction.
In a nutshell, the Rance estuary is a particular enclosed water body, characterized by its complex morphology, the presence of a tidal power station at its mouth and a lock at its uppermost limit.

1.2.2 Previous work on the Rance estuary

Net siltation and sediment accumulation were reported in the Rance estuary since the 1980s (about 20 years after the construction of the tidal power plant) by various studies based on field measurements [LCHF, 1982; Bonnot-Courtois and Lafond, 1991; Dubien and Waeraas De Saint Martin, 1994; Jigorel and Ledrappier, 2003; Brossault et al., 2013]. These studies were interesting to assess an overall sedimentary state in the Rance estuary but were insufficient to quantify the impact of the tidal power station on sedimentation behaviour in the basin. In addition, these field data and their location have a high degree of uncertainty and bad accuracy levels which made them hardly useful for numerical model calibration or validation. Furthermore, based on field measurements, estuarine physical processes are evaluated as a whole and could not be separately addressed to quantify their respective roles in sediment dynamics.
Experimental and numerical studies were conducted, mainly focusing on qualitative analysis of sediment dynamics or ecosystem evolution in the estuary, without prior investigation of how hydrodynamics was influenced by the tidal barrier Kirby and Retière [2009]; Bonnot-Courtois et al. [2002]; Guesmia [2001]; Guesmia et al. [2001]; Thiebot [2008]. Despite a well-known effect on estuarine water levels Bonnot-Courtois et al. [2002], little attention has been given to

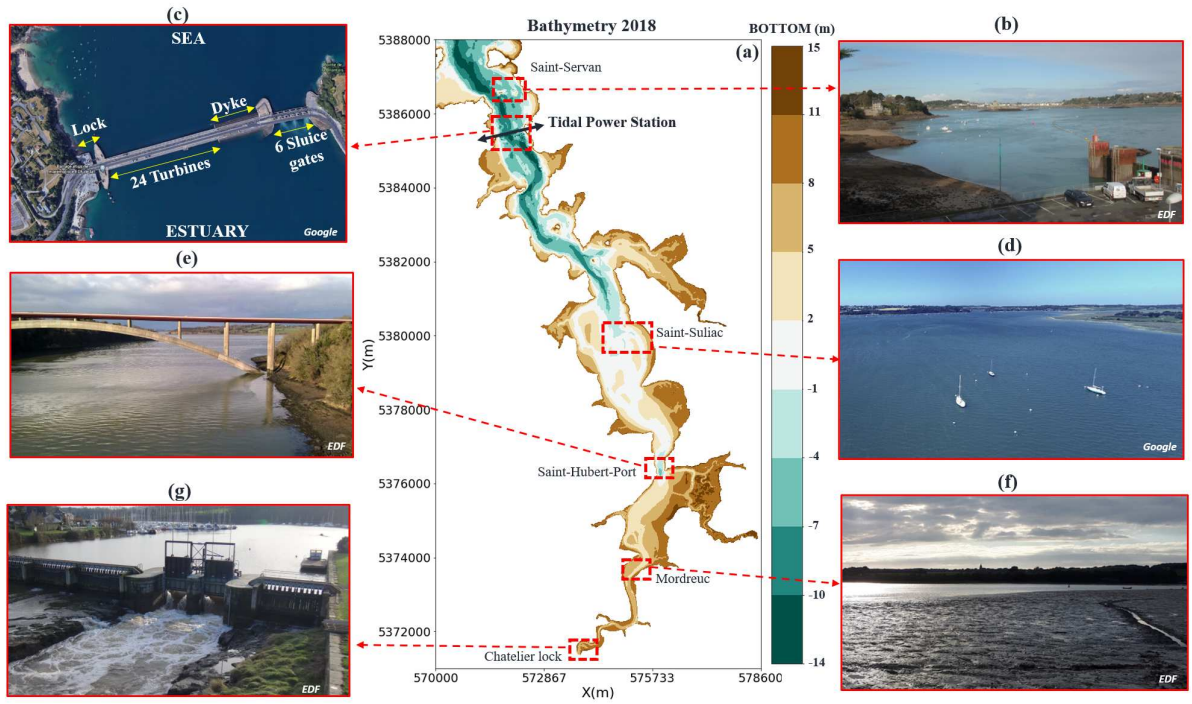

Figure 1.5: (a) The Rance estuary with bathymetry of 2018 with zoom on (b) Saint-Servan, (c) the tidal power station (T.P.S.), (d) Saint-Suliac, (e) Saint-Hubert-Port, (f) Mordreuc and (g) Chatelier lock.

quantifying the effect of the plant on the propagation, and on the vertical and horizontal tidal asymmetry of the tidal wave. The first numerical hydrodynamic model of the Rance estuary was developed in 2001 Guesmia et al. [2001]. It consisted in a two-dimensional horizontal (2DH) model used to separately study the sea-side and estuary-side regions of the dam. The aim was to determine hydrodynamic parameters for morphological simulations [Thiebot, 2008]. Although it provided good results with respect to measurements [Guesmia et al., 2001], the approach did not evaluate the influence of the power plant on flow characteristics and tidal asymmetry, which could have significant implications for sediment dynamics and morphological changes in the estuary. In 2018, 2D and 3D numerical models were developed, to evaluate bacteriological impact in the estuary [Chevé and Le Noc, 2018]. The study area included both the basin and the offshore region. However, the constant mesh resolution of $30m$ over the computational domain was insufficient to capture flow structure close to the plant and between Mordreuc and Chatelier lock (Figure 1.5.a). The main conclusions of this study were based on the 2D model results, without any further hydrodynamic analysis.
Bonnot-Courtois *et al.* reported qualitative influence of the plant on sediment dynamics in the Rance estuary mainly based on measurements performed after the construction of the barrage [Bonnot-Courtois, 1993; Bonnot-Courtois and Le Vot, 1993; Bonnot-Courtois et al., 2002]. Such studies allow to assess the present-day sediment dynamics in an estuarine system, but in the absence of any reference data prior to the barrage, they were unable to quantify the impact of the plant on sedimentary processes. To this goal, Thiebot [2008] developed a two-dimensional (2D) hydro-sedimentary model of the Rance estuary but the simulated bed level changes could not be validated due to lack of bathymetry survey data [Thiebot, 2008]. In addition, only cohesive sediment was considered in this model [Thiebot, 2008]. Therefore, Thiebot's model did not address sediment processes related to the mixture between cohesive and non-cohesive matter. Moreover, the former work considered a continuous solid discharge at the plant while marine sediment enter inside the Rance estuary occasionally during storm periods [LCHF, 1982]. Therefore, it was difficult to quantify the influence of each physical processes on sediment dynamics in this complex system. Similarly, Guillou et al. [2011] developed a numerical model of the Rance estuary's filling accounting only for cohesive sediment. Numerical results were overall consistent with results obtained by Thiebot [2008]. However, the numerical model could not be quantitatively validated due to lack of bed evolution data. Recently, Motte [2017] extracted information from artistic shoreline iconography to observe the evolution of selected geomorphological features in the Rance estuary. Despite the originality of this work, no reliable estimates could be determined from the proposed qualitative approach.
In summary, various studies were carried out in the Rance estuary based on field measurements and numerical models to assess the overall sediment state in the marine basin. However, the impact of the tidal power station on hydrodynamics, sediment transport and morphodynamics is still unquantified. Furthermore, physical processes driving hydrodynamics and sediment dynamics in this complex system were studied as a whole which made it difficult to correctly evaluate their relevance.

1.3 Research questions and main objectives

Sedimentation in the Rance estuary is a complex and controversial subject that has seen strong pressure from local stakeholders. A mission of assessment and evaluation of the sedimentary situation of the Rance estuary was conducted by the General Council of Environment and sustainable Development (CGEDD) on ministerial directive. In the Rance Sediment Management

report [Caude et al., 2017] a sustainable action plan was set out to address this issue. The scientific program is focused on understanding sediment dynamics in this complex estuarine system. This PhD project takes part in this context. The main objective of this work is to better understand hydro-sedimentary dynamics in this highly engineered system by the presence of a tidal power plant on its mouth and a lock on its upstream limit. To this goal, the following research questions were addressed:

- *How relevant are 2D and 3D numerical models at reproducing the main features of hydro-sedimentary dynamics observed in macrotidal estuaries influenced by the presence of a tidal power station?*
- *How hydrodynamics, sediment transport and morphodynamics processes are influenced by the presence of the world's second-largest tidal power station?*
- *Which are the dominant physical mechanisms driving the sediment dynamics in the Rance estuary?*
- *What recommendations can be given to stakeholders for a more efficient estuary management?*

To answer these research questions, both field measurements and numerical modelling complementary approaches were deployed. On one hand, a continuous (annual) field survey of hydro-sedimentary variables, namely water levels, salinity, turbidity and bed evolution was carried out from June 2019 to May 2021. Punctual (13-hours) field campaigns were also performed to complement and validate the continuous monitoring measurements. The main objective of this field survey was to to update hydro-sedimentary data sets in the Rance estuary with a better accuracy level, to be used for the calibration and validation of the numerical model, and also for a better understanding of physical processes observed in the Rance estuary. On the other hand, 2D and 3D numerical models of the Rance estuary were developed in the framework of the TELEMAC-MASCARET modelling system[1], through the modules TELEMAC-2D and TELEMAC-3D (respectively hydrodynamics 2D and 3D) and GAIA (sediment transport and bed evolution). These numerical models were first calibrated and validated in terms of (i) hydrodynamics, namely on water levels and horizontal and vertical flow field structure, (ii) sediment transport based on Suspended Sediment Concentration (SSC) and (iii) morphodynamics, established from bed level evolution on timescales ranging from a neap-spring tidal period up to 3 months. Then, numerical models quantified the influence of the tidal power station on hydrodynamics, sediment transport and morphodynamics in the Rance estuary. Afterwards, numerical models were deployed to assess the dominant physical mechanisms driving sediment dynamics in the Rance estuary though various scenarios. Finally, the examination of different configurations provided recommendations aiming to help the estuary's management.
The research outcomes and issue recommendations from this PhD work can be extrapolated to existing and future projects involving estuarine systems presenting anthropogenic structures such as dams and tidal power plants.

1.4 Outline of the manuscript

The methodology proposed above leads to organize the present thesis manuscript into seven chapters, where some of them are in the format of scientific publications. Because the articles are kept in their entirety to improve readability and guarantee self-standing, the content presented

[1] `www.opentelemac.org`

in the articles can be in part found to be replicated with other parts of the thesis manuscript.
In **Chapter** 2 an overview of punctual and continuous monitoring data measurements performed in the Rance estuary over nearly 2 years (June 2019 - May 2021) is presented. Throughout the development and application of pre- and post-processing tools and data analysis techniques on large datasets, the collected data aimed to (*i*) better describe the sediment dynamics and processes observed in the Rance estuary from field data, and (*ii*) provide a valuable data set of velocity field, bed evolution at mudflats, salinity, turbidity and suspended solid concentration to be used for calibration and validation of numerical models implemented in the thesis's work.
In **Chapter** 3, hydrodynamics and tidal wave patterns were analyzed, based on a calibrated and validated two-dimensional (2D), depth-averaged shallow-water hydrodynamic model of the Rance estuary. Afterwards, the influence of the plant on the propagation and the asymmetry of the tidal wave inside the estuary was quantified.
In **Chapter** 4, the three-dimensional (3D) aspects of the flow field distribution along the horizontal and vertical directions, as well as the impact of the plant on the dynamics of the freshwater-saltwater interface were examined based on a calibrated and validated 3D Reynolds-Averaged Navier-Stokes hydrodynamic model.
Chapter 5 introduces the implementation, calibration and validation of a 3D hydro-morphodynamic model of the Rance estuary, aiming at improve the understanding of the sediment dynamics in response to power generation and also to quantify the impact of the plant on sediment transport and morphodynamics.
In **Chapter** 6, the experience gained in the previous chapters allowed to implement a 2D coupled hydrodynamic and morphodynamic numerical model suitable to perform simulations over longer time scales, by keeping a good ratio between model accuracy versus CPU time. This model was calibrated and validated to simulate the present-day main features of sediment transport and morphodynamics in the Rance estuary over fortnightly time scales to monthly time scales. Furthermore, based on hypothetical scenarios covering variable river discharge, storm-like conditions and alternative operation mode of the plant, complementary sediment dynamics processes were assessed and recommendations were proposed to a more efficient estuary management.
Infine, **Chapter** 7 closes this manuscript by summarizing the answers to the stated research questions and giving recommendations for future research work.

CHAPTER 2

DATA FROM SURVEY CAMPAIGNS AND IN-SITU PROBES

▷ Objectives of this chapter

This chapter provides an overview on field surveys performed to monitoring hydro-sedimentary variables in the Rance estuary, from data acquisition to data analyses. The collected data aimed mainly to provide a valuable data set to be used for calibration and validation of numerical models implemented in the next chapters. In addition, it provided insights on sediment dynamics observed in key locations of the Rance estuary. The work presented in this chapter has been carried out together with Marine Vandenhove and Luca Parquet within two M2 internships [Vandenhove, 2021; Parquet, 2021] co-supervised by Aldo Sottolichio and Pablo Tassi. Further hydro-sedimentary investigations performed with the collected data can be found in Vandenhove [2021] and Parquet [2021].

Highlights

- Velocity field measurements are reliable to be used for hydrodynamic models calibration and validation.
- Salinity, turbidity and bed evolution measurements need to be cautiously selected on short and reliable time windows for morphodynamic models calibration and validation.

2.1 Introduction

This chapter introduces the methodology adopted for the acquisition, pre- and post-processing, and analyses of continuously and punctually measured hydro-sedimentary variables in the Rance estuary, namely currents, salinity, turbidity and bed evolution. Continuous measurements were acquired over a period of two years from June 2019 to May 2021. Punctual measurements were obtained from data acquisition campaign that took place from October 14th to 21st 2020. Field measurements aimed to (*i*) better understand sediment dynamics and processes observed in the Rance estuary; and (*ii*) to provide a valuable data set of velocity field, bed evolution at mudflats, salinity and suspended solid concentration to be used for the parameterization, calibration and validation of numerical models implemented in this thesis's work.

2.2 Data acquisition

Based on bed evolution spanning a period of over 60 years, continuous measurements were conducted in the Rance estuary between June 2019 and May 2021, in order to assess the sediment dynamics in the basin. Maintenance operations have been also carried-out regularly in order to collect data, perform maintenance operations, change devices and gather suspended and bottom sediment samples. This medium-term monitoring of the different hydro-sedimentological variables allowed to cover many hydro-meteorological conditions and management conditions of the tidal power station (TPS) and the Chatelier lock. Moreover, on October 2020 a field campaign was conducted in order to perform velocity measurements and to collect water and sediment samples for probes calibration. The continuous and punctual survey covers the whole estuary from the Chatelier lock to the TPS, with a main focus on the lower estuary (**Figure 2.1**). As this later corresponds to a dynamically active region of the estuary in terms of suspended concentration and bed evolution. The main variables of interest are currents, salinity, turbidity and bed evolution. Materials and methods used in the acquisition of these variables are described hereafter.

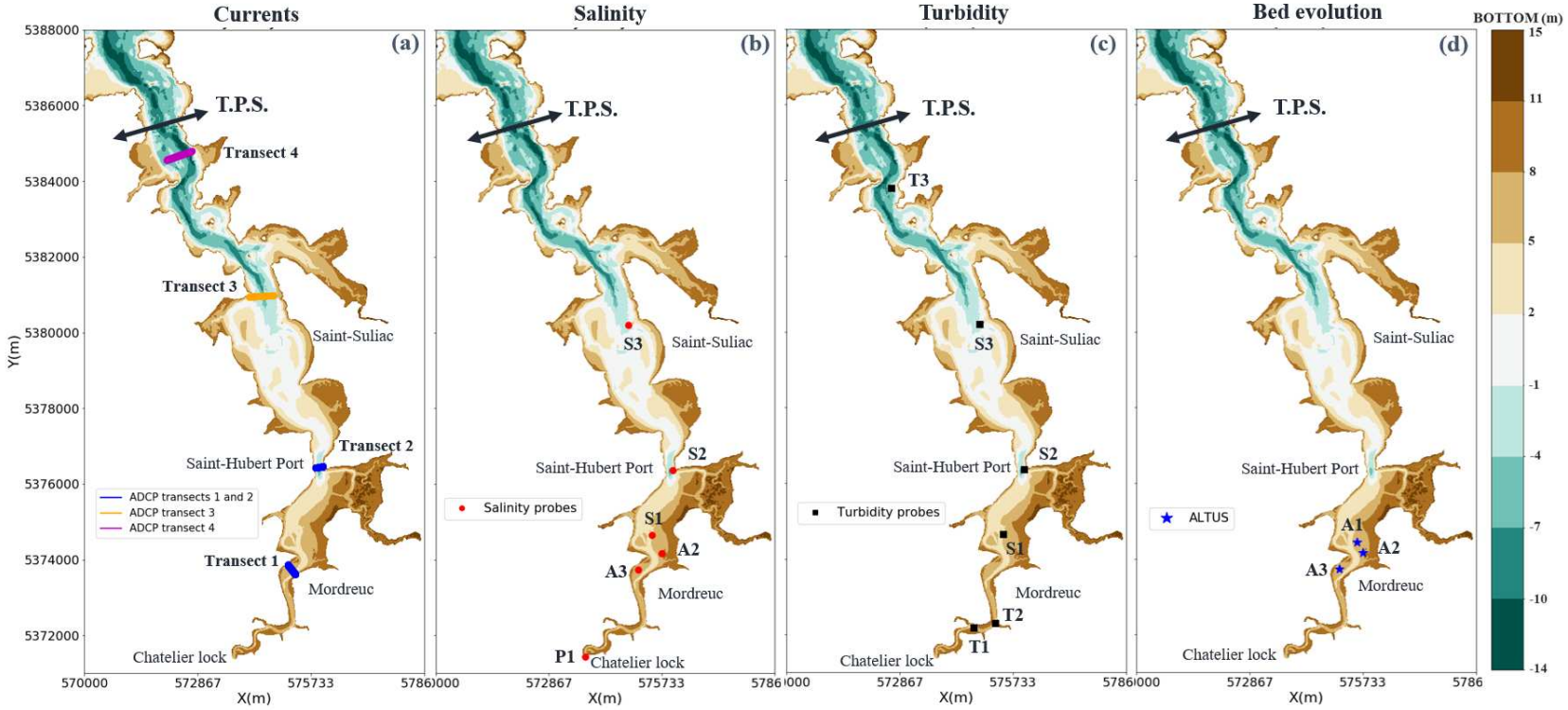

Figure 2.1: Location of punctual and continuous measurements of: (a) currents, (b) salinity, (c) turbidity and (d) bed evolution.

2.2.1 Currents

Surveys of current velocities were conducted at four locations along the estuary, on 14th, 15th and 21st October 2020. At each location, horizontal current velocities were collected through cross-sectional transects with a vessel-towed 1200kHz RDI Workhorse Acoustic Doppler Current Profiler (ADCP) in 0.25m bins (**Figure 2.2**). At locations of transects 1, 2 and 3 (**Figure 2.1**), currents were collected throughout a semidiurnal tidal cycle (12.42 h), with a total of 30 full transects being completed at each location. At transect 4 (**Figure 2.1**), close to the tidal power plant, measurements were limited to a period of 3 hours during the opening of the sluice gates and 10 full transects were completed. For each completed transect, measurements were then averaged over 20 ensembles to reduce noise.

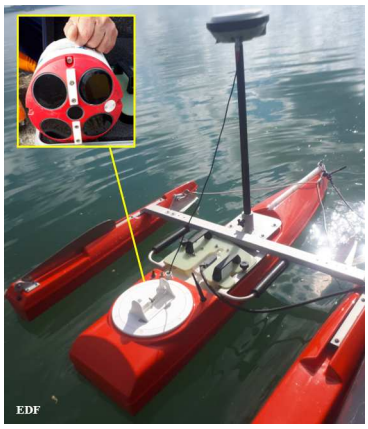

Figure 2.2: Acoustic Doppler Current Profiler (ADCP).

2.2.2 Salinity

Salinity was continuously measured with two probes deployed in the Rance estuary: near-surface salinity with the SAMBAT multi-parameter probe and near-bottom salinity with the STPS mono-parameter probe.
The SAMBAT from NKE is an autonomous multi-parameter probe assembled on a buoy (**Figure 2.3**). It is quipped with a GPS, a remote transmission, a fast wireless configuration thanks to a communication interface (Radio Data Pencil), and uses a brush to protect optical sensors from biofouling [Bertier, 2020b]. This instrument allows the measurement of the main physicochemical water parameters (temperature, depth, conductivity for the calculation of salinity, turbidity, fluorescence (*Chlorophylla*, *Phycocyanin*, *Phycoerythrin*), dissolved oxygen, pH and the detection of hydrocarbons) 1 meter below the water surface over a period of several months.

(a) SAMBAT probe (NKE).

(b) Probe on its buoy with remote transmission antenna.

(c) SAMBAT probe installed near surface.

Figure 2.3: SAMBAT probe. (After [Bertier, 2020b]).

Physical characteristics of the equipment are provided below [Bertier, 2020b]:

- Total height: 1.7m
- Total weight: 20 kg (chain included)
- Support pole + antenna + SAMBAT total weight: 6 kg
- Float with a buoyancy of 20 liters. EVA material (Ethylene-vinyl acetate)
- Central body in High-Density Poly-Ethylene (HDPE)
- Crowfeet chain: two chains DN10 (2.2 kg/m) + chain plates and shackles.

The deployment of the SAMBAT probes is done with the integrated buoy, and the with mooring to a dead weight. Near-surface salinity was measured at 3 locations in the Rance estuary (**Figure 2.1**). S1 corresponds to the edge of right bank facing Plouër; S2 is located under the bridge between Port-St-Hubert and Port-St-Jean; and S3 is found near the tide gauge of Saint-Suliac (4 km, 6 km and 9 km from the Chatelier lock, respectively).

The STPS mono-parameter probe (NKE) (cf. **Figure 2.4**) (length < 30 cm, diameter < 3.5 cm, mass < 500 g) records pressure variation (i.e., depth) and salinity. They can be installed in open water on a buoy or on the bed. The STPS probes were deployed in locations P1, A2 and A3 (cf. **Figure 2.1**).

Figure 2.4: STPS probe (NKE). (After [Bertier, 2020b])

2.2.3 Turbidity

Turbidity is a measure of the degree of transparency that water loses due to the presence of suspended particles. In general, the higher the amount of suspended matter in the water, the higher the turbidity is. Near-surface turbidity was continuously measured with the SAMBAT (NKE) probes, while turbidity at different heights in the water column was recorded with the STBD and WiSensTBD (NKE) probes.

The STBD and WiSensTBD are mono-parameter probes (NKE) (length < 32 cm, diameter < 4 cm, mass < 500 g) [Bertier, 2020b] (cf. **Figure 2.5**). The instruments are equipped with an external automated wiper brush and a sensor emitting a modulated light at 880 nm. The light reflected by the particles is detected by a cell which provides a signal proportional to their concentration in the medium. The instruments record turbidity measurements in a range up to 3000 NTU (accuracy < 2%), depth (up to 6m) and temperature ($-2° < C < 35°$). These instruments were installed at 3 locations in the Rance estuary (cf. **Figure 2.1**) on buoys close to the water surface. Except at S3, where the probe was deployed close to the bottom for most of the recording time (except between June and July 2020 where it was deployed close to the surface). During the maintenance operations, the probes were cleaned, the data were collected and, if necessary, the probes were replaced.

Figure 2.5: STBD and WiSensTBD probes (NKE). After: Bertier [2020b]

The SAMBAT (NKE) multi-parameter probe (cf. **Figure 2.3**) also records turbidity (NTU) at locations S1, S2 and S3 (cf. **Figure 2.1**).

2.2.4 Bed evolution

The ALTUS system *ALTimètre à Ultrasons Submersibles* from NKE was developed in order to accurately measure the bed level variations in muddy dominant environments, mudflats and shallow waters such as bays and estuaries [Jestin et al., 1998]. The ALTUS altimeter (cf. **Figure 2.6**) is an autonomous self-contained device equipped with:

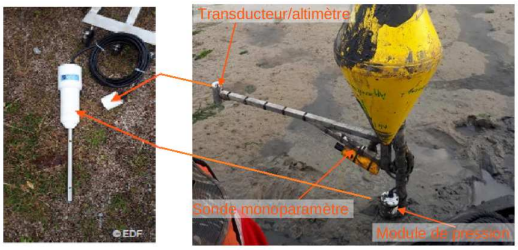

Figure 2.6: Continuous measurement probe: ALTUS altimeter. After: [Bertier, 2020b]

- a 2 *MHz* acoustic transducer positioned about 30 *cm* above the sediment and facing downwards,
- a recording module. The travel time from the emission of the acoustic wave and its reception by the transducer is converted into distance. These speed of sound depends on the temperature and salinity of the environment,
- a pressure sensor buried on the surface of the bed, which allows to determine the water height above it.

The ALTUS system records four distances between the transducer and the seabed through 4 beams (1, 2, 3, 4), a «*Maximum echo* »value to assess the quality of the measurements, and pressure for water height. To determine whether erosion or sediment deposition has occurred, the mudflat's evolution $\mathrm{MFE}_i(t)$ is calculated from **Equation 2.1**.

$$\mathrm{MFE}_i(t) = d_i(t_{ini}) - d_i(t), \tag{2.1}$$

with $\mathrm{MFE}_i(t)$ is mudflat evolution at time $t = t_{init} + \Delta t$, Δt is the time elapsed from the beginning of the measurement, $d_i(t_{ini})$ and $d_i(t)$ are distances between the transducer and the bottom through beam i (with $i = 1, 2, 3, 4$) at the initial time and time t respectively. Thus the initial elevation of the mudflat is fixed for the start of the survey and the mudflat evolution is evaluated with respect to it for the duration of the recording period.
To measure erosion or sedimentation of the mudflats, the ALTUS system was deployed on 3 locations in the Rance estuary : A1, A2 and A3 (cf. **Figure 2.1**).

2.2.5 Other variables

As seen above, temperature and depth are measured by the probes previously described. In addition, another type of probe was also deployed to specifically measure depth and temperature in specific locations of interest, the SP2T (NKE) probe.

The SP2T (NKE) mono-parameter probe (cf. **Figure 2.7**) (length < 17.1 *cm*, diameter < 2.5 *cm*, mass < 100 *g*) was deployed at three different locations assembled on the ALTUS frames (A2 and A3) and in P1 at the Chatelier lock (cf. **Figure 2.1**).

Figure 2.7: SP2T probe (NKE). After [Bertier, 2020b]

2.3 Data preparation

In this section, the different steps of data preparation prior to the analysis are presented.

2.3.1 Currents

ADCP probes generates text files where measurements are stored. These data have been read, pre- and post-processed thanks to algorithms developed in Python.
A text file is created for each of the transects at the four stations studied along the Rance estuary (transect 1, 2, 3 and 4 in **Figure 2.1**). The vertical profiles are represented by matrices where each column corresponds to: (0) the depth of the vertical profile, (1,2) current magnitude $Vel_{mag}(cm/s)$ and direction $Vel_{dir}(°)$, (3,4,5) the East, North and vertical components in cm/s, (6) the velocity error, (7,8,9,10) the four raw signals of backscattered intensities in counts, (11) the « %Good » (quality criterion) and (12) the instantaneous flow.
Currents measurements were filtered by removing all values with a «%Good » below 60 and an absolute value of the velocity error above 10. The latter is estimated by quantifying the difference between two estimated vertical velocity values [Ross et al., 2019].
Along-channel and cross-channel velocities, U and V respectively, were computed from the currents magnitude and direction measured by the ADCP. Currents direction was corrected by the orientation of the channel axis (α) at three transects, equal to 45° for transect 1, $-5°$ for transect 2 and $-2°$ for transect 3. Then, velocity components U and V were computed from Equations 2.2 and 2.3 respectively.

$$U = -Vel_{mag} \times cos[(Vel_{dir} - \alpha) \times \frac{\pi}{180}] \tag{2.2}$$

$$V = -Vel_{mag} \times sin[(Vel_{dir} - \alpha) \times \frac{\pi}{180}] \tag{2.3}$$

Afterwards, mean locations along each transect were selected in order to analyze temporal evolution of depth-averaged velocity components over a complete semidiurnal tidal cycle. For instance, at transect 3 (**Figure 2.8**), three locations were selected to represent the western, central and eastern channel's sides.

2.3.2 Salinity

In this section, the raw and filtered salinity data measured with the `SAMBAT` (NKE) and `STPS` (NKE) probes will be described. `SAMBAT` probes are installed near the surface at locations S1, S2 and S3 (**Figure 2.1**). Probe sensors are installed below the buoy at a distance between $[80 - 90]$ (cm) from the water surface.
Four different `SAMBAT` probes where installed in S1 location. The following is a brief description of technical difficulties observed in each probe:

- First probe (`SAMBAT, Id=37040`): Bad signal recovered in spite of two maintenance operations performed. Development of biofouling affected the measurements, therefore this data is not reliable;
- Second probe (`SAMBAT, Id=37038`): After changing the probe in February 2020, salinity measurements return to consistent values, biofouling has developed on the probe but they were removed during the maintenance operations. During the first lockdown

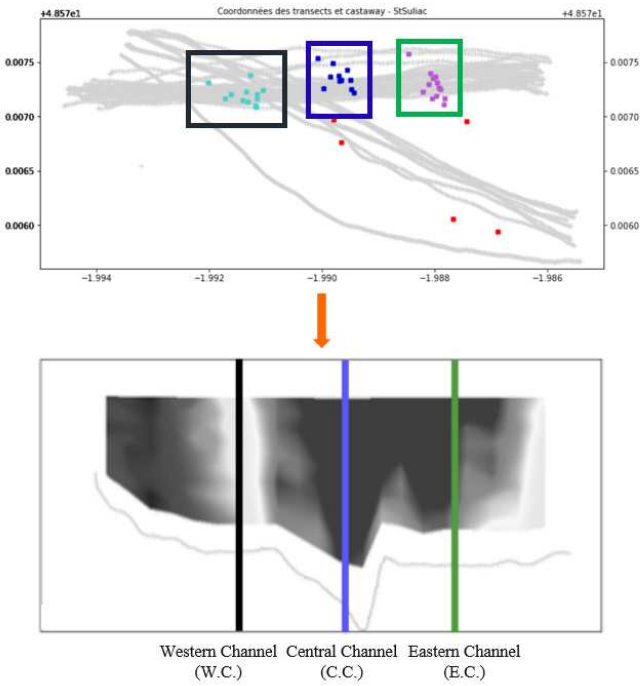

Figure 2.8: (a) Spatial distribution of ADCP measurements along transect 3 (Saint-Suliac) and (b) mean locations generated to represent the western, central and eastern channel's sides of the transect 3. (see **Figure** 2.1 for transect location).

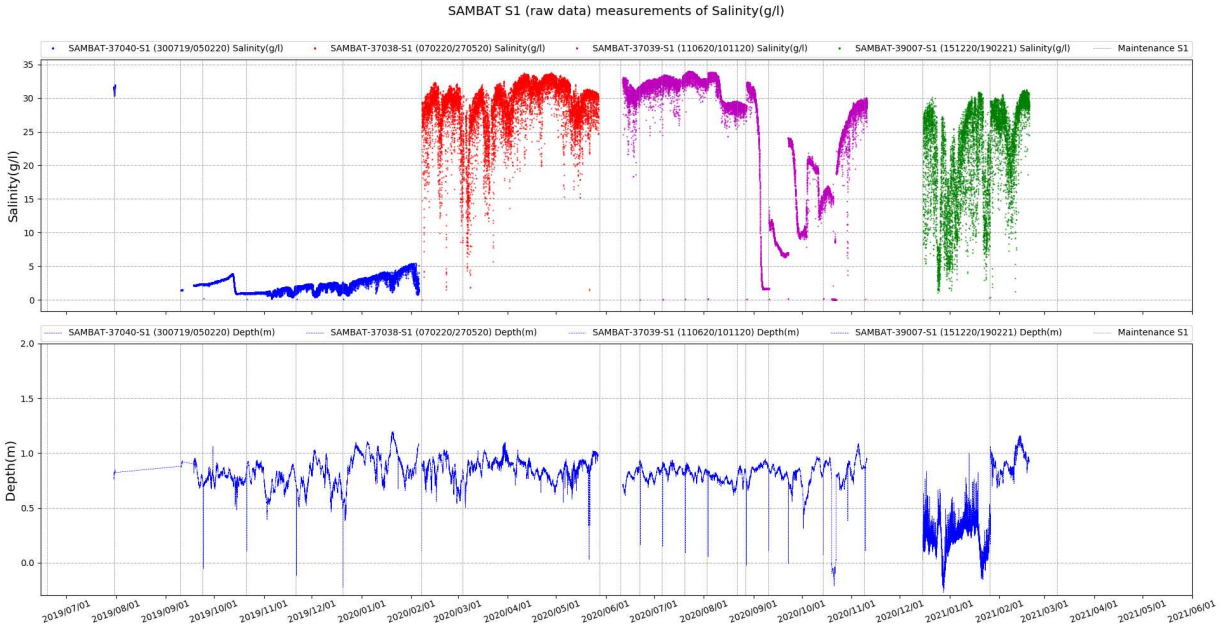

(a) On subplot 1: *Salinity* (g/l) measurements from `SAMBAT` probes at location S1. **(b)** On subplot 2: *Depth* (m) measurements from `SAMBAT` probes at location S1.

Figure 2.9: `SAMBAT` S1 Raw data.

(17/03/2019 - 11/05/2019), maintenance operations were suspended. This probe has drifted approximately $\sim 375m$ south between 6 May and 28 May;

- Third probe (`SAMBAT, Id=37039`): Measurements are consistent during the first 2 months recorded. Then, the probes battery drops affecting the measurements quality;
- Fourth probe (`SAMBAT, Id=39007`): After maintenance operations, maximum values registered are consistent with the expected values. However, the probe was installed without the chain that allows to ballast, ensuring its verticality. The probe tends to lengthen and the sensors are often weakly immersed, this explains the low depths registered. This can be a shortcoming since these probes measure near-surface variables, but they are not permanently immersed into the water body. Data from these probes are of mediocre quality.

The raw salinity data at location S1 are presented in **Figure 2.9**. The unusable data are not due to the displacement of the probes, but rather to the calibration of the sensors, battery failure, the probe not being immersed in water and the development of biofouling. For example, it shows anomalies due to a low water column above the sensor. The probes are mounted above a buoy so the distance to the water surface should remain relatively constant despise the tidal variation. At the S2 location two different probes were installed. Below is a brief description of the technical difficulties encountered with each one:

- First probe (`SAMBAT, Id=37039`): Regular drifting of the probe was observed. During the maintenance operation of 31/07/2019, the probe was installed closer to the bridge pier. However, data was lost due to manipulation errors until up this date. The probe was re-positioned more towards the north, in order to move it away from the bridge pier. During maintenance operation (12/09/2019), many lures and hooks were removed in the anchorage. The probe drifted towards the anchorage area of Port-St-Jean (South 250m) (e.g. 11/11/19). After the maintenance operation, the probe was positioned at the intended position, but it shifted once again (e.g. 25/11/19 - 10/02/20). To prevent these skids, the weight of the ballast was doubled during the intervention in early February 2020. The probe was re-installed on 12/02/2020 slightly further downstream to move it away from the bridge pier and thus from the fishing lines of the amateur fishermen. It remained near its position until 26/03/2020. Since the displacement of 09/04/2020, the probe was trapped on the channel under the bridge. The new position is unstable, the buoy sinks about 1 m during each tide, the anchor line is too short for the new depth in a deeper area of the channel. The probe sinks up to 4 m from March 26 to April 7 at each tide, then up to 13 m from April 8 and emerges only a few minutes during low tide (the probe is no longer near the surface);
- Second probe (`SAMBAT, Id=37038`): The probe installed on 29/05/2020 seems to find consistent values of the expected order of 35 (g/l). The probe drifts in a few tens of meters until the end of the measurement period. During maintenance operations, biofouling development was observed (e.g. 10/06/20). Consequently, the salinity decreases progressively up to 4 (g/l). After the cleaning operations during the summer of 2020, the data recover the previous values before the presence of the biofouling is once again observed. That is why the data between 01/06/2020 and 13/10/2020 are considered of medium quality since they are deteriorated due to the presence of biofouling.

At location S3, three `SAMBAT` probes were installed. The technical difficulties encountered with each probe are the following:

- First probe (SAMBAT, Id=37038): Consistent data at the beginning of the measurements until 01/08/2019. Then, the development of biofouling impacts the measurements by underestimating it. The data from the beginning of August 2019 is not usable;
- Second probe (SAMBAT, Id=39007): The values are consistent after the probe change. The probe has not drifted significantly. The peaks observed in the depth variable are due to the probe remaining underwater (e.g. from 23/02/2020 to 08/03/2020), this is due to the double anchorage. The buoy sinks during important tides. This phenomenon is observed in the first part of the flow, not at full tide. It is therefore likely that this is due to a strong current, dragging the buoy to the point of drowning it when the sluice gate of the Rance TPS are opened. During the field campaign the day 10/06/2020 the probe buoy was changed, after that the measurements are more stable. The data between 10/06/2020 and 14/10/2020 are exploitable and can be considered of good quality;
- Third probe (SAMBAT, Id=37040): The values are consistent after the probe change. The development of biofouling affects the measurements, during the maintenance operations the cleaning of the equipment is performed.

In order to ensure a near-surface measurements, all salinity data relative to depths lower than 35 *cm* are filtered for the three probes S1, S2 and S3. Raw data from SAMBAT probes located at stations S2 and S3 are available in Appendix A.
The STPS probes were deployed in 3 locations : P1, A2 and A3 (**Figure 2.1**).
At station P1, the STPS probe was installed on the pier between the spillway and the Châtelier lock. There are periods in the series where the salinity does not vary with each tidal cycle. This can occur for reasons such as: opening of the spillway discharges fresh water from the Rance River downstream of the Châtelier lock which dilutes the measurement; flushing sediment operations at the Châtelier lock, during maintenance activities of the bottom channel a significant volume of freshwater is discharged to set in motion the bottom sediment and displaced it downstream.
At station A2, STPS probe is installed on the ALTUS probe $\approx 0.3\ m$ above the bottom (cf. **Figure 2.6**). The probe was replaced on date 02/06/2020. From June 14, 2020, the pressure sensor seems to drift, it overestimates the depth of immersion by about $50cm$ (**Figure 2.10**). Another observation is from 06/02/2020, where the STPS pressure sensor sinks about $8cm$ in the mudflat. The difference between the depth measured by the STPS and ALTUS pressure sensors was determined. The ALTUS pressure sensor is closer to the bottom while the STPS sensor is $20cm$ above it (cf. **Figure 2.6**). The difference of the depth measurements of both pressure sensors in June 2020 varies between $[50 - 75](cm)$. The pressure sensor of the ALTUS (which is inserted into the mudflat) has remained in its position (measurements are not altered) while the STPS pressure probe was displaced vertically. The development of biofouling impacted the measurements where the salinity decreases until the maintenance operation (e.g. 27/08/2020) where the values become coherent again. Overall, the time series is complete and of excellent quality.
At location A3, the STPS probe is installed also on the ALTUS frame (cf. **Figure 2.6**). The salinity is measured at the bottom and during low tide the probe is no longer submerged. Due to manipulation errors, data was lost over some periods (e.g. from 19/12/20 to 04/02/2020, see section A.1.1). Starting from 25/09/2019 the salinity sensor underestimates the measurements, despite maintenance operations the values are still atypical. The data of this period are of poor quality. After the maintenance operation of 04/02/2020 the values are again consistent. Moreover, the presence of biofouling causes an underestimation of the measurements (e.g. 22/06/2020 and 06/07/2020). After the maintenance operations the values are correct again. Finally, the series

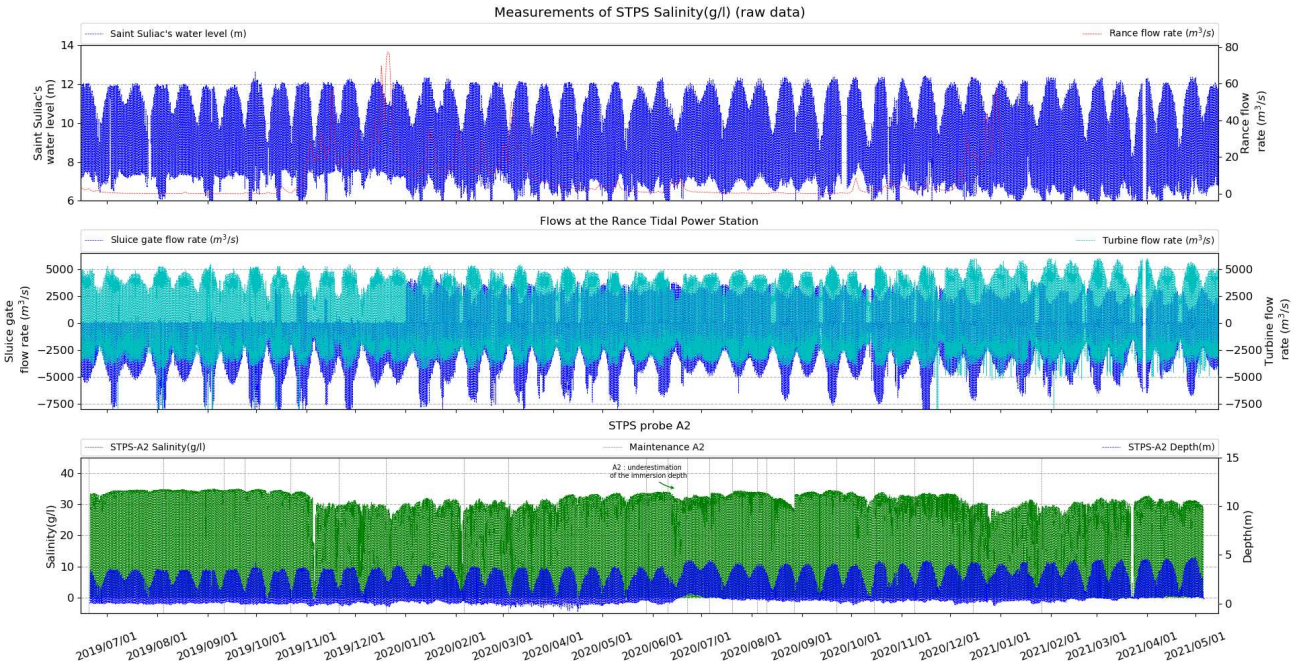

(a) On the primary axis of subplot 1: Water *Depth(m)* at Saint-Suliac. On the secondary axis of subplot 1: *Simulated Rance flow rate* (m^3/s). **(b)** On the primary axis of subplot 2: *Sluice gate flow rate* (m^3/s) *of the Rance TPS*. On the secondary axis of subplot 2: *Turbine flow rate* (m^3/s) *of the Rance TPS*. **(c)** On the primary axis of subplot 3: Salinity (g/l) measurements from STPS probe at location A2. On the secondary axis of subplot 3: *Depth* (m) measurements from STPS probe at location A2.

Figure 2.10: STPS A2 raw data.

presents gaps and periods where the data are inconsistent. However, there are parts where the data are of good quality and can be exploited. For all STPS measurements, errors in the series occur at low tide when the pressure under the water column above the sensor is low, giving negative depths. So, all salinity data related to negative depths were filtered. Raw data from STPS probes located at stations P1 and A3 are available in Appendix A.

2.3.3 Turbidity

Turbidity (expressed in NTU units[1]) was continuously measured with the SAMBAT, STBD and WisenSTBD probes in order to determine the suspended sediment concentration (SSC) at 6 different locations in the Rance estuary (**Figure 2.1**). During the October 2020 measurement campaign, all turbidity probes (SAMBAT, STBD and WisenSTBD) were removed from October 19 to October 22. Samples of water and sediment were collected in order to calibrate the probes in the laboratory. A laboratory calibration [Bertier, 2020a] was performed on the observed SSC(mg/l) and NTU values for each probe in order to establish the NTU-SSC transforming equations.
Due to unforeseen circumstances, some probes could not be calibrated (e.g. STBD (Id=36006), WisenSTBD (Id=4A53, 4A57) and SAMBAT (Id=37040, 39007)). For this reason, this work focuses only on the calibration of STPS and SAMBAT probes. However, for probes of the same brand and batch which have not been calibrated, it is possible to consider the application of calibration curves for probes of the same model.

[1]NTU stands for Nephelometric Turbidity unit, i.e. the unit used to measure the turbidity of a fluid or the presence of suspended particles in water.

2.3.3.1 SAMBAT : Id = 37038

Laboratory values (NTU-SSC) allow to establish transformation curves for the SAMBAT probe (Id=37038). However, the point data that produces an inversion of the bell on the vetical axis is not considered since it provides a decreasing function and SSC in the Rance estuary do not exceed 5000 (mg/l). As shown in the figure below (cf. **Figure 2.11**), seven pairs of values are considered, of which one point is based on the hypothesis that for a null NTU value a null SSC value is associated. These values are used to establish 3 increasing transformation curves *SSC=f(NTU)* (cf. **Equation 2.4**) for each range of NTU values:

$$\begin{cases} y_1 = 0.5967x & \text{for } x \in [0:30](NTU) \\ y_2 = -0.0027x^2 + 2.6709x - 59.817 & \text{for } x \in [30:461](NTU) \\ y_3 = 0.0251x^2 - 20.334x + 4641.4 & \text{for } x \in [461:918](NTU) \end{cases} \tag{2.4}$$

where x is the turbidity in NTU units, y_1, y_2, y_3 are SSC values expressed in (mg/l).
On average, the relative error of the 3 curves is 0.34%. This is to be expected since the curves are set between two points for the linear equation and the polynomials are set with few points.

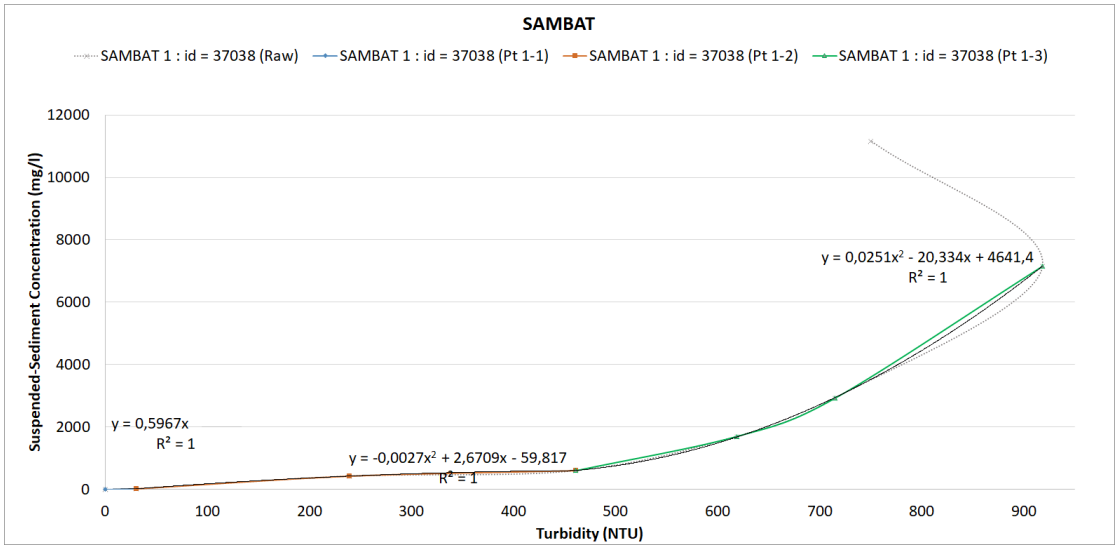

(a) On the primary axis: Three calibration curves for SAMBAT (Id=37038) and Raw relation between NTU-SSC.

Figure 2.11: Probe calibration of (SAMBAT, 37038).

2.3.3.2 SAMBAT : Id = 37039

The number of calibration points needed to establish the relation between NTU and SSC for the SAMBAT probe 37039 is less than for the previous probe. Similar to the last case, the point data for which the inversion of the bell occurs is not considered because in the Rance estuary the SSC does not reach values of 5000 (mg/l). For this probe, there are 5 points, of which one of these values is based on the hypothesis that for a null value of NTU a null value of SSC is associated. The laboratory data are used to establish 3 increasing transformation curves (cf. **Figure 2.12**) for

each range of NTU values (cf. **Equation 2.5**).

$$\begin{cases} y_1 = 1.5x & \text{for } x \in [0:23](NTU) \\ y_2 = 0.0052x^2 + 0.3537x + 23.612 & \text{for } x \in [23:714](NTU) \\ y_3 = 30.827x - 19082 & \text{for } x \in [714:851](NTU) \end{cases} \tag{2.5}$$

Where x is the turbidity in NTU and y_1, y_2, y_3 are SSC values in (mg/l).
Due to the few number of points used to establish the 3 equations, in addition to the fact of defining two linear equations with 2 points and a polynomial of degree 2 defined by 3 points, the average relative error between the SSC(mg/l) values observed and calculated with the 3 curves is of the order of 0.014%.

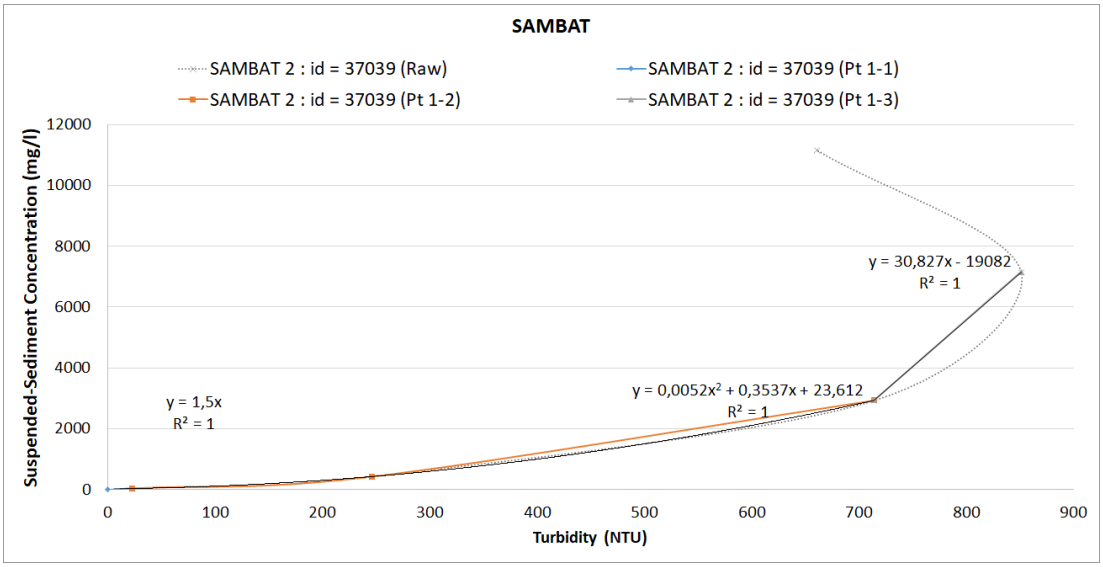

(a) On the primary axis: Three calibration curves for `SAMBAT (Id=37039)` and Raw relation between NTU-SSC.

Figure 2.12: Probe calibration `(SAMBAT, 37039)`.

2.3.3.3 `STBD: Id=37009`

As shown in **Figure 2.13**, the relationship between SSC(mg/l) and turbidity NTU of the `STBD` probe shows a typical bell-shaped backscatters curve in the SSC axis, which means that a given NTU measurement corresponds to two possible SSC values [Fettweis et al., 2019]. The pairs of values of the relation NTU-SSC of the `STBD` probe (`Id=37009`) show typical bell-shaped backscatters curve (cf. **Figure 2.13**). This implies that for a single value of NTU there can be 2 values of SSC(mg/l). Consequently, only the values that define the increasing curve are adopted. The increasing transformation equations (cf. **Equation 2.6**) are established based on six pairs of values, one of these points is based on the hypothesis that a null value of NTU corresponds to a null value of SSC(mg/l) .

$$\begin{cases} y_1 = 0.0015x^2 + 0.8252x & \text{for } x \in [0:323](NTU) \\ y_2 = 0.00219458x^2 - 0.4710114x + 339.8407 & \text{for } x \in [323:1016](NTU) \end{cases} \tag{2.6}$$

Where x is the turbidity in NTU units and y_1, y_2 are SSC values in (mg/l) . The average relative

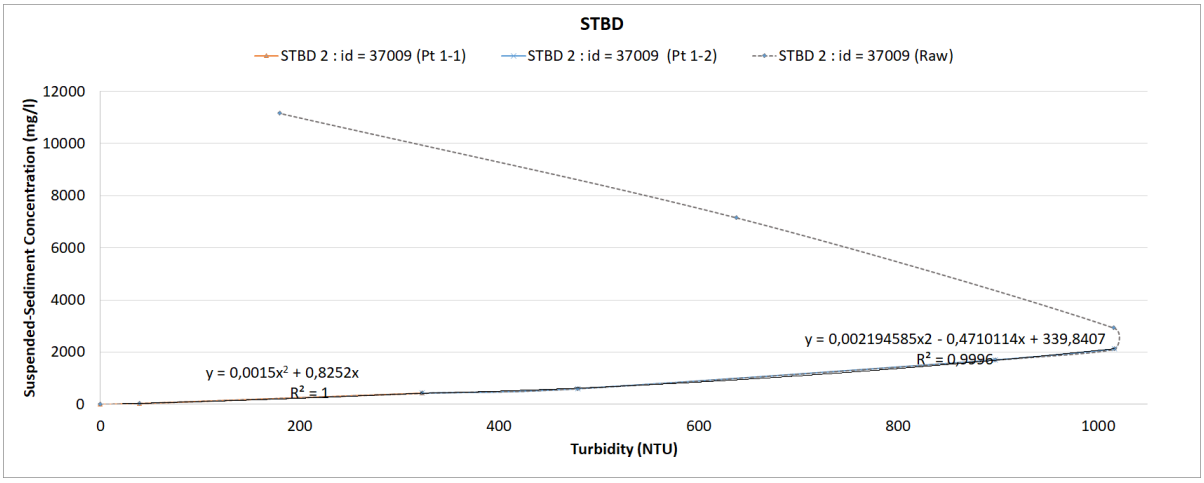

Figure 2.13: Probe calibrated (`STBD`, `Id=37009`).

error between the observed and calculated values with the calibrated equations of the `STBD (Id=37009)` probe is approximately 1%.

2.3.3.4 `STBD : Id = 37011`

Calibration data from the `STBD` probe (`Id=37011`) show typical bell-shaped backscatters curve (cf. **Figure** 2.14). The two increasing curves (cf. **Equation** 2.7) are then defined by three NTU-SSC(mg/l) points.

$$\begin{cases} y_1 = 1.0777x + 33.207 & \text{for } x \in [0:364](NTU) \\ y_2 = 3.1368x - 716.31 & \text{for } x \in [364:1162](NTU) \end{cases} \tag{2.7}$$

where x is the turbidity in NTU units and y_1, y_2 are SSC values in (mg/l) . The average relative

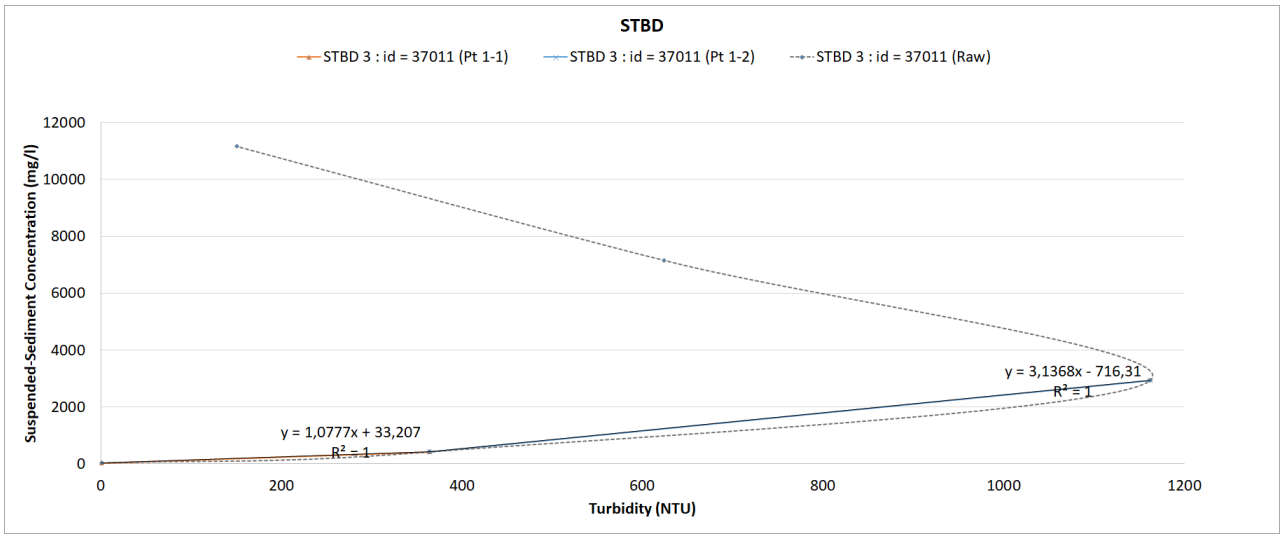

Figure 2.14: Probe calibrated (`STBD`, `Id=37011`).

error between the observed and calculated values with the calibrated equations of the `STBD`

(Id=37011) probe is in the order of 0.002%. This is to be expected since we are considering two linear equations, each of which is defined between two points.
The turbidity measurement probes installed in the estuary consisted of four SAMBAT, four STBD and two WisenSTBD. However, turbidity calibration could only be performed on 2 SAMBAT (Id = 37038 and 37039) and 2 STBD (Id=37009 and 37011). Therefore, the WisenSTBD probes will not be able to be converted from NTU into SSC(mg/l). In addition, the data from the SAMBAT probe (Id= 39007) are false because it was not calibrated before installation.
However, it is proposed to apply the calibration equations of calibrated probes to probes that have not been calibrated but for which turbidity data are available. In order to do this, we assumed that the related probes have the same degree of sensitivity (because the probes belong to the same manufacturer and batch), but this is not necessarily valid and may lead to errors in the SSC(mg/l) conversion. Thus, the equations of the SAMBAT probe (Id=37038) (cf. **Equation 2.4**) will be applied to the SAMBAT probe (Id=37040). While to the STBD probes (Id=36006 and 36004) the equations of the STBD probe (Id=37009) (cf. **Equation 2.6**) are applied. The equations were adopted because they were established with a greater number of calibration data than the other probes. Finally, the equations established have been obtained with few laboratory results. This may be problematic particularly for low NTU values, where insufficient data are available to obtain reliable sensitivity conversions.
As shown in **Figure 2.15**, the raw turbidity series from the STBD probes are simultaneously plotted with the water lever at Saint-Suliac, the simulated Rance Flow rate, sluice gate flow rate and the turbine flow rate from the Rance TPS. Probes are plotted following the positions from upstream to downstream in the estuary. The following is a brief description of the series:

- Probe at location T1: This is the most upstream location in the estuary, the probe is installed on a buoy 80cm below the surface. The measurements are representative of near-surface conditions, but during low tide the probe runs ground. Two STBD probes were installed at this location during the recording period.

  - Probe STBD, Id=36006 (from 19/06/2019 to 15/12/2020): Probe's brushes were quickly misaligned, probably due to being crushed by the buoys while running aground at low tide. This caused the development of a large amount of biofouling around the sensor. This is why the measurements up to 31/07/2019 decrease in an atypical way. After this maintenance operation the values are much more coherent. The presence of biofouling was observed again on 10/09/2019, this time the brush was once again damaged. The probe will have recurrent problems with the brush and the presence of biofouling which impacts the quality of the measurements (e.g. 21/10/2019, 21/11/2019, 19/12/2019, 20/07/2020). Due to connection problems with the probe on 09/11/2020 and 14/12/2020 it was not possible to retrieve the data. For this reason the series ends on date 15/10/2020.
  - Probe STBD, Id=37010 (from 26/01/2021 to 05/05/21): After the probe change the measurements are consistent, during the maintenance operations no significant amount of biofouling was observed.

- Probe at location T2: Corresponding to the second most upstream location in the estuary, a single STBD probe (Id=37039) was deployed. The probe was placed on a buoy 90cm below the surface and therefore measures turbidity near-surface. At low tide the probe is no longer submerged. The data from the beginning of the recording period until 06/08/2019 have been strongly disturbed by the development of biofouling. In fact, when the probe

was installed, the automatic cleaning system with a brush was not activated. The brush was strongly damaged (probably due to being crushed by the buoys during running aground), it was therefore removed but not replacement was installed. On 24/09/2019 the cleaning brush was missing. No replacement part was installed on the probe until the end of the recording period. Therefore during the successive maintenance operations the development of biofouling was observed (e.g. 24/09/2019, 21/10/2019, 21/11/2019, 19/12/2019, 07/07/2019, 20/07/2019, 03/08/2019, 27/08/2019, 09/10/2019). Thereby, the data in this location are likely to be significantly affected.

- Probe at location S3: Location in the middle part of the estuary, the series was recorded with a single `STBD` probe (`Id=37011`) (from 11/02/2020 to 05/05/2021). The probe was installed on the retrieval chain of the `SAMBAT` S3 probe. During most of the recording period the probe was placed at 1 m above the bottom, so it measured bottom turbidity. However, between 10/06/2020 and 06/07/2020 the probe was positioned 90cm from the surface. Hence, the measurements from this short period are representative of near-surface conditions. This is the reason why in this period the depth remains relatively constant (because the probe buoys with the tidal variation) while for the rest of the series the depth is observed to vary with each tidal cycle and with the neap-tide and spring-tide. On 20/07/2020 the probe was displaced 40 m to the east. Then, on 22/09/2020 and 13/10/2020 it was observed that the brush was not working, which explains the atypical measurements. The series has no data between 26/01/2021 and 05/05/2021 due to a connection problem related to the battery that was out of service.

- Probe at location T3: The most downstream location in the estuary, near the Rance TPS. One `STBD` probe, then two `WisenSTBD` probes (different models from the manufacturer NKE) were installed.

  - Probe `STBD Id=36004` (from 19/06/2019 to 24/09/2019): it only recorded turbidity and therefore no depth data are available. The presence of biofouling was observed on the probe (e.g. 10/09/2019). The buoy of the `STBD` probe went missing (10/09/2019). The cause of its disappearance is unknown. Then, on 24/09/2019 it was noted that the probe went missing and was no longer found.

Stations T1 and T2 are located in a zone where probes can emerge at low tide. Therefore, probe measurements at T1 and T2 during high tide are measurements of near-surface suspended sediment concentration but at low tide the measurements are representative of bed concentrations. This can lead to misinterpretation if the distinction between low tide and high tide is not made during data analysis.
To ensure a better quality of SSC (mg/l) measurements, the following filters were applied to data from `STBD` and `SAMBAT` probes: (i) depth below 50cm to filter bed concentrations, and (ii) NTU values outside definition interval of each (NTU-SSC) calibration equation deployed.

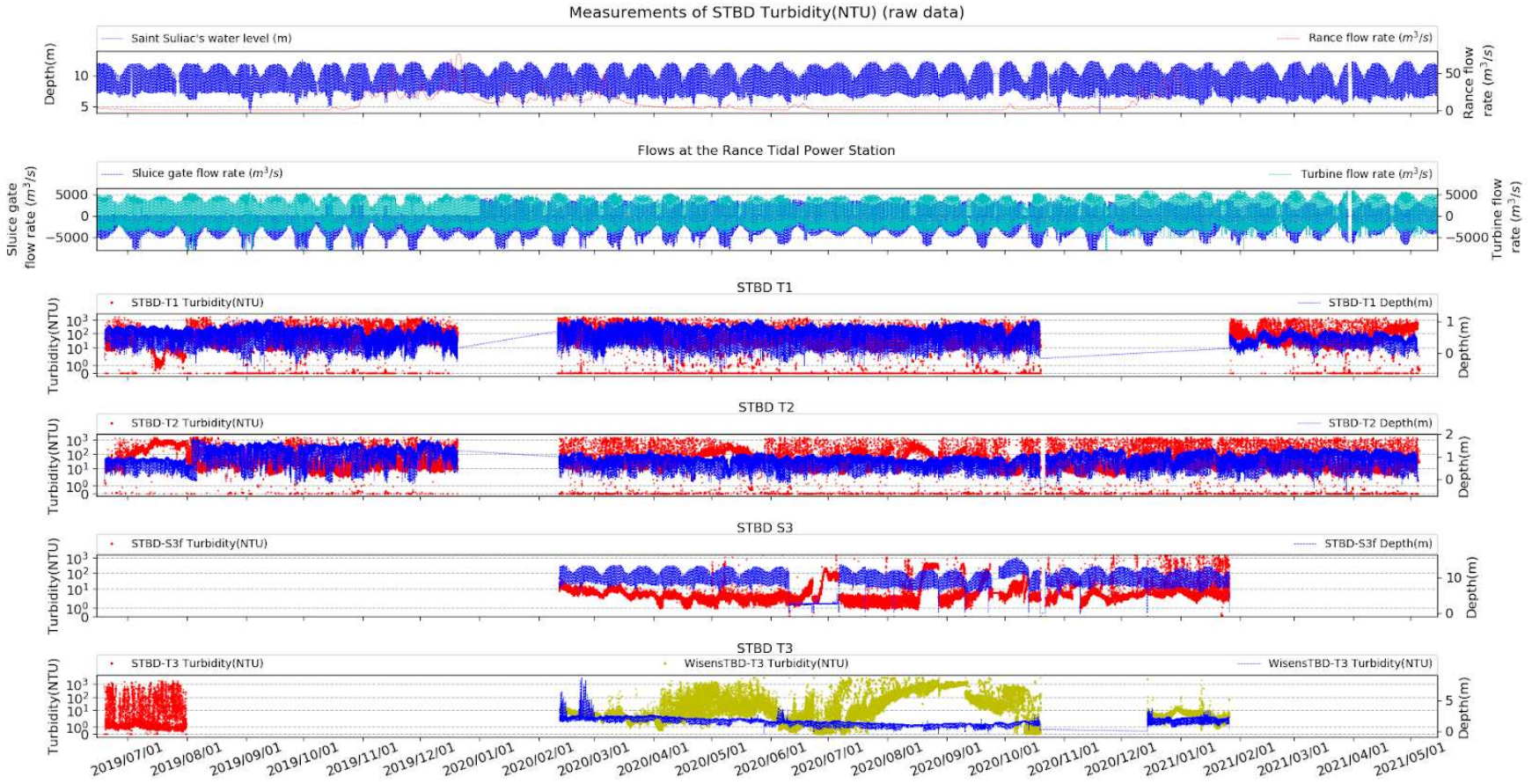

(a) On the primary axis of subplot 1: Water *Depth(m)* at Saint-Suliac. On the secondary axis of subplot 1: *Simulated Rance flow rate* (m^3/s). **(b)** On the primary axis of subplot 2: *Sluice gate flow rate* (m^3/s) *of the Rance TPS*. On the secondary axis of subplot 2: *Turbine flow rate* (m^3/s) *of the Rance TPS*. **(c)** On the primary axis of subplot 3: *Turbidity* (NTU) measurements from STBD probe at location T1. On the secondary axis of subplot 3: *Depth* (m) measurements from STBD probe at location T1. **(d)** On the primary axis of subplot 4: *Turbidity* (NTU) measurements from STBD probe at location T2. On the secondary axis of subplot 4: *Depth* (m) measurements from STBD probe at location T2. **(e)** On the primary axis of subplot 5: *Turbidity* (NTU) measurements from STBD probe at location S3. On the secondary axis of subplot 5: *Depth* (m) measurements from STBD probe at location S3. (f) On the primary axis of subplot 6: *Turbidity* (NTU) measurements from STBD and WisenSTBD probes at location T3. On the secondary axis of subplot 6: *Depth* (m) measurements from WisenSTBD probe at location T3.

Figure 2.15: STBD measurements (raw data) in T1, T2, T3 and S3.

2.3.4 Bed evolution

ALTUS probes were deployed to monitoring the bed evolution at 3 different locations of mudflats found in the uppermost part of the estuary: A1, A2 and A3 (**Figure 2.1**). The quality of each measure is represented by the variable *Echo. Max (%)*. The higher the value of this variable, the more reliable the measure is.
At station A1, the mudflat evolution from raw data at location A1 has periods with no data until March 2020 (**Figure 2.16**). This was due to a programming error in the registration frequency that led to memory saturation. This is a drawback for the first part of the series where it is more difficult to determine whether there is erosion or deposition at this location. Furthermore, 3 months of data (between March and June 2020) was lost due to an error in data manipulation during maintenance operations. The development of biofouling was observed during the field campaigns. Consequently, the measurements of each beam were affected (e.g. 22/06/2019, 10/03/2020, 10/07/2020). The values of *Echo. Max (%)* values are above 60%. Therefore these measurements are considered to be correct. Finally, only the negative distances will be filtered out later. At station A2, continuous bed temporal evolution is mostly complete except for two

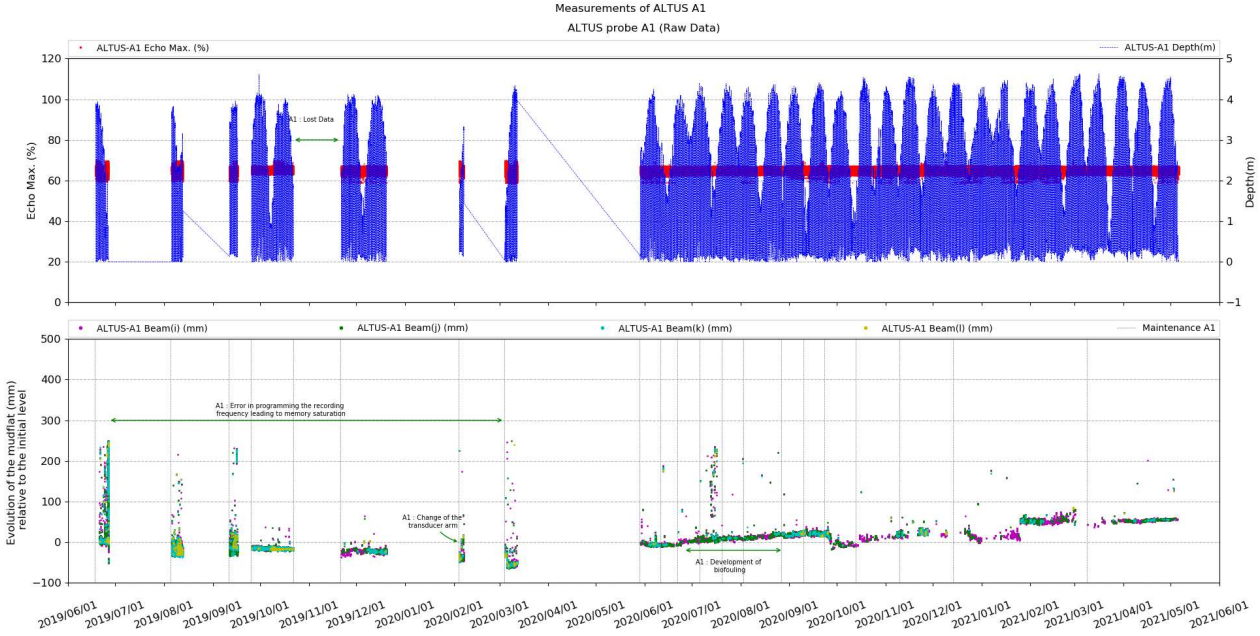

(a) On the primary axis of subplot 1: *Echo. Max (%)* return signal. On secondary axis of subplot 2: *Water Depth(m)*. **(b)** On the primary axis of subplot 2: Mudflat evolution of the 4 beams.

Figure 2.16: ALTUS A1 Raw Data.

periods (between October 2019 and February 2020, see section A.1.2) where data were lost due to difficulties encountered during field campaigns. In consequence, for this location it is challenging to determine whether there was bed erosion or deposition during the first part of the record. Discontinuity in the vertical might be due to vandalism, mast sinking or the equipment's handling during maintenance. Despite the vertical discontinuity, the second half of the series (from June 2020) shows an overall trend towards sediment deposition at location A2. Although the whole series presents a vertical discontinuity, the main significance of the record is the relative evolution in periods presenting a continuity in the vertical. This is useful when studying the evolution of the bottom over short periods of months, which is discussed later

on. The site is frequently visited by shellfish fishermen, this may explain the vertical deviation of measurements observed in July 2019. Overall, the values of *Echo. Max (%)* vary between 0 and 90%, therefore data must be filtered. Biofouling was also observed in station A2 which resulted in the dispersion between measurements of each beam (e.g. 24/09/2019, 20/07/2020, 09/09/2020).
At station A3, Mudflat evolution present periods where data was lost due to data manipulation errors. However, the data from this location is the most complete series with respect to locations A1 and A2. The development of biofouling on the probe is clearly identifiable in the measurements (e.g. 28/07/2019, 15/09/2019, 15/07/2020, see section A.1.2). Consequently, the quality of the measurements is affected. For example, between the end of July and the beginning of August 2019, the *Echo. Max (%)* decreases progressively and thus corresponding measurements are less reliable. Another issue with the probe was the obstruction of the sensor with barnacles at the end of August 2019, which led to no data to be recorded. Overall, the *Echo. Max (%)* varies between 0 and 80 *(%)*. The quality of measurements is moderated.
As observed previously, the raw data present anomalies that need to be filtered in order to avoid wrong interpretations. Thus, the following criteria were applied:

- the negative distances measured between the transducer and the bottom,
- the negative depth measurements,
- the *Echo. Max (%)* lower than 20 %.

Application of these filters reduces noise in the measurements. Then, the distances measured by the 4 beams are corrected with Coppens equation 5.1 given the speed of sound in sea-water as a function of temperature and salinity. These last were measured either by the `STPS` or SP2T probes installed on the `ALTUS` frame.

$$V_s(S,T) = 1449.05 + 45.7\,T - 0.0521\,T^2 + 0.00023\,T^3\left(1.333 - 0.0126\,T + 0,00009\,T^2\right)(S-35), \tag{2.8}$$

where T is the temperature in degrees Celsius °C and S is the salinity in (g/L). The range of validity is 0°C to 35 °C and 0 (g/L) to 45 (g/L) for the temperature and salinity, respectively. Measurements are taken at a near-surface distance.
In order to apply the correction given by **Equation 5.1**, data must be averaged every 10 minutes, the same time step as the temperature and salinity variables. `ALTUS` probes are calibrated with a constant speed of sound in salt water between $[1461 - 1464](m/s)$ depending on the beam. Once the speed of sound in salt water is corrected, it is applied to the measurements for beams (i, j, k, l) according to:

$$D_{cor*} = D_{ori}\left(\frac{V_{s_{(cor*)}}}{V_{s_{(cte)}}}\right), \tag{2.9}$$

where D_{cor*} is the corrected distance with the speed of sound in saltwater; D_{ori} is the distance originally measured; $V_{s_{(cor*)}}$ is the speed of sound in salt water corrected with temperature and salinity; and $V_{s_{(cte)}}$ is the speed of sound in salt water adopted by `ALTUS` probes with constant value.
The difference between corrected and non-corrected data from `ALTUS` probes can reach up to $2cm$ at stations A1-A2 and up to $1.5cm$ at station A3.

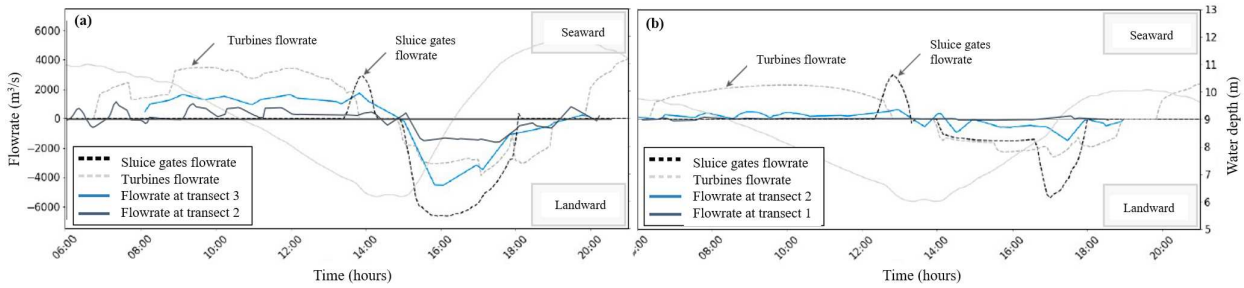

Figure 2.17: Flowrates evolution over a semidiurnal tidal cycle (a) at transects 2 and 3 performed on the 15th October, 2020 and (b) at transects 1 and 2 performed on the 14th October, 2020. (see **Figure 2.1** for transects location).

2.4 Data analyses

The developed tools and pre- and post-processing tasks presented in the previous sections provided a suitable framework to analyze the continuously and punctually measured variables in the Rance estuary. The main currents analyses are presented in Chapter 4 simultaneously with results of numerical simulations. Complementary analyses of flowrates will be presented hereafter. Analyses of salinity, suspended sediment concentration and mudflats bed evolution were carried out over winter periods. Time windows were carefully chosen according to the availability of reliable data at different probes simultaneously. Further, hydro-sedimentary investigations was carried out by Vandenhove [2021] and Parquet [2021].
The goal of these analyses is to identify patterns and correlations with the main hydrodynamics forcing (e.g. the tidal signal), as well as between the different variables measured continuously throughout the period of recording. This information is of paramount importance to (*i*) better understand the sediment dynamics and processes observed in the Rance estuary, and (*ii*) to provide a valuable data set of bed evolution at mudflats, salinity and suspended solid concentration to be used for calibration and validation of numerical models.

2.4.1 Currents

Flowrates variation on the scale of a semidiurnal tidal cycle for the four transects is presented in **Figure 2.17**. It allows to relate variations observed in flowrates along the estuary to those passing through the turbines (gray dotted lines) and sluice gates (black dotted lines). The positive (negative) values indicate that the flow is oriented toward the sea (the estuary). The opening of the sluice gates and the turbines seem to directly influence the instantaneous flow rates at Saint-Suliac (transect 3) and at Saint-Hubert-Port (transect 2), both $5km$ and $11km$ upstream of the plant respectively. Indeed, peaks of ebb currents (14h00) and flood currents (16h00) and their corresponding flowrates correlate with the flow passing through the sluice gates and the turbines. Furthermore, flowrates decrease going further upstream of the tidal power station.

2.4.2 Salinity

During spring-tide (02/12/2020) the river discharge $Q_R = 0\ (m^3/s)$ (cf. **Figure 2.18 (a)**). At high tide, salinity reached 30(g/l) at P1 (cf. **Figure 2.18 (c)**); 31(g/l) at A3 (cf. **Figure 2.18 (d)**); and 30(g/l) at A2 (cf. **Figure 2.18 (e)**). No data are available for this period at S1 (cf. **Figure 2.19**

(c)). Salinity in S2 (cf. **Figure 2.19 (d)**) varies between $[29-32]$ (g/l) while in S3 (cf. **Figure 2.19 (e)**) it remains relatively constant 35 (g/l) with each tidal cycle.
During neap-tide (08/12/2020) $Q_R = 10$ (m^3/s). The mix between saline and fresh water is more noticed at S2 comparing to S3. Salinity at S2 varies between $[20-32]$ (g/l) while at S3 salinity remains relatively constant 35 (g/l). Furthermore, the bottom salinity in the upstream locations presents a higher degree of dilution reaching values of; 21 (g/l) at P1: values of 31 (g/l) at A3; and 30 (g/l) at A2. Data in S1 are of questionable quality, the probe sensors tended to be poorly submerged. As a filter on the depth was applied, the small amount of data does not allow a meaningful analysis. The analysis is done on the raw data in S1 (cf. **Figure 2.19 (c)**).
The simultaneous effect of river discharge $Q_R = 20$ (m^3/s) and the spring-tide (15/12/2020), seems to be responsible of a greater salinity variation between each tidal cycle for both near-surface and near-bottom measurements. At S1 the salinity varies between $[10-30]$ (g/l), at S2 $[15-30]$ (g/l) and at S3 $[28-33]$ (g/l). Near-bottom salinity measurements are closer to the upper limit of the estuary and influenced more by the Rance river. At P1, salinity values are inferior to 20 (g/l), while at A3 and A2 locations, salinity values are approximately equal to 30 (g/l) during high tide.
On neap-tide (24/12/2020), a higher flow rate of $Q_R = 40$ (m^3/s) produces an even greater salinity dilution compared to the first neap-tide. However, the dilution is only observed for a time period of the order of days, the time that the volume of water deplaces downstream. Even though this phenomenon seems to be more pronounced at S1, observed values at this location are unreliable due to probe problems. The salinity at the most upstream points is diluted to a greater extent due to the lower saline water volume entering the system and the high flow rate from the Rance river. At S2, salinity values vary between $[10-20]$ (g/l). At S3, salinity values are in the range $[20-30]$ (g/l).
At P1, salinity and depth are almost null (probes are poorly submerged), while the water level at Saint-Suliac is low during low-tide. So, the flow from the TPS does not fully reach the most upstream points of the estuary. However, in A3 and A2, values of 24 (g/l) are recorded at both points.
When the Rance river discharge increases (i.e. $Q_R = 40$ (m^3/s)), a stronger impact on the mix between saline and fresh water is observed in the upper estuary.
The process that seems to influence the most salinity patterns at upstream locations is the Rance river discharge. The further downstream a point is located from the freshwater input, the longer it will take to impact the salinity mixing. High river discharges $Q_R(m^3/s)$ superimposed to neap-tide periods cause the greatest dilution of salinity during the winter period. In contrast, salinity values at downstream locations are governed by the volume of saline water entering the system through the TPS. This may explain the presence of relatively constant values of salinity throughout a tidal cycle. Nevertheless, for higher discharges $Q_R(m^3/s)$, salinity values at downstream locations varies within a tidal cycle.

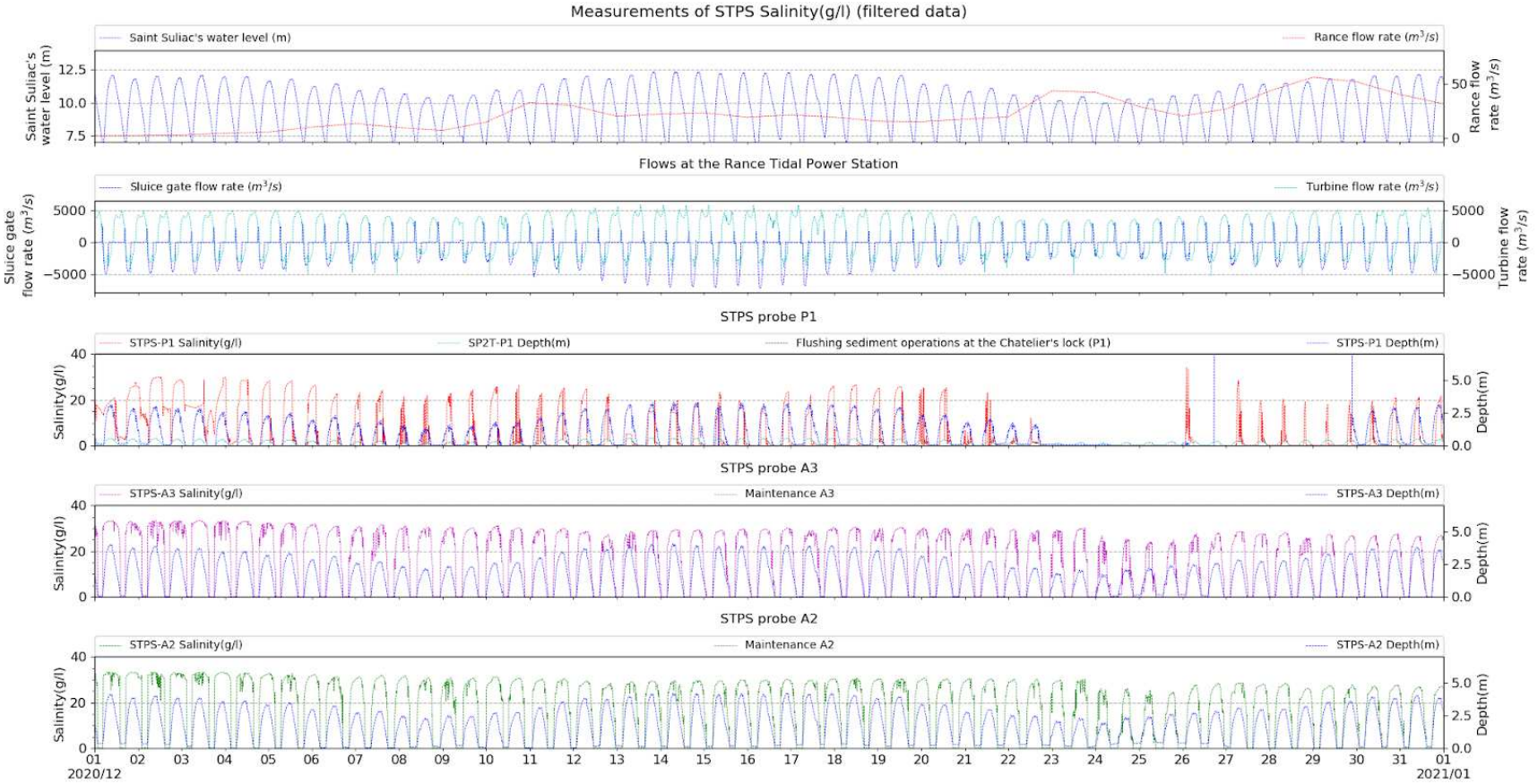

(a) On the primary axis of subplot 1: Water *Depth(m)* at Saint-Suliac. On the secondary axis of subplot 1: *Simulated Rance flow rate* (m^3/s). **(b)** On the primary axis of subplot 2: *Sluice gate flow rate* (m^3/s) *of the Rance TPS*. On the secondary axis of subplot 2: *Turbine flow rate* (m^3/s) *of the Rance TPS*. **(c)** On the primary axis of subplot 3: *Salinity* (g/l) measurements from STPS probe at location P1. On the secondary axis of subplot 3: *Depth* (m) measurements from STPS probe at location P1. **(d)** On the primary axis of subplot 4: *Salinity* (g/l) measurements from STPS probe at location A3. On the secondary axis of subplot 4: *Depth* (m) measurements from STPS probe at location A3. **(e)** On the primary axis of subplot 5: *Salinity* (g/l) measurements from STPS probe at location A2. On the secondary axis of subplot 5: *Depth* (m) measurements from STPS probe at location A2.

Figure 2.18: STPS measurements (filtered data) in P1, A2 and A3: Winter 2021.

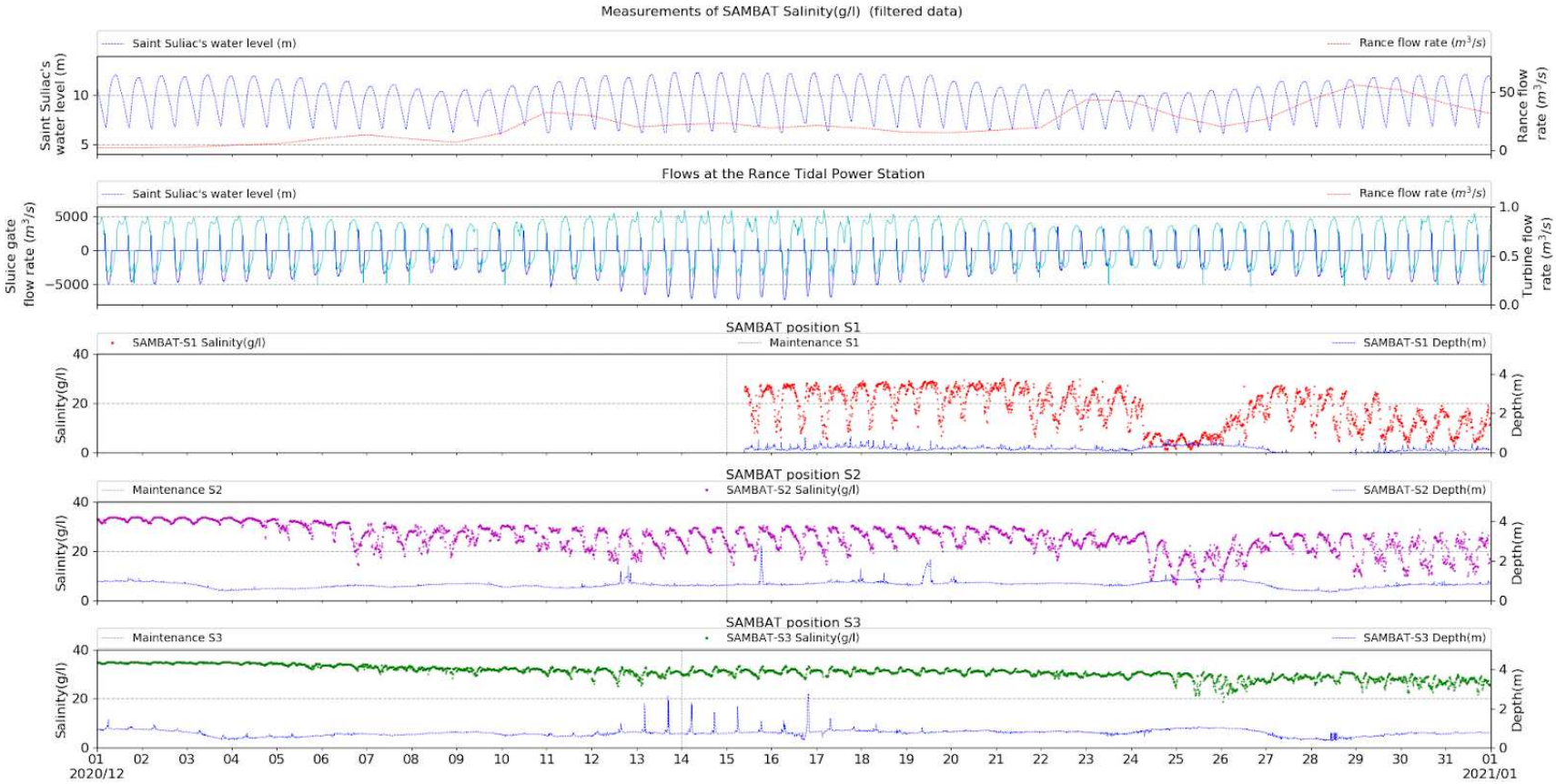

(a) On the primary axis of subplot 1: Water *Depth(m)* at Saint Suliac. On the secondary axis of subplot 1: *Simulated Rance flow rate* (m^3/s). **(b)** On the primary axis of subplot 2: *Sluice gate flow rate* (m^3/s) *of the Rance TPS*. On the secondary axis of subplot 2: *Turbine flow rate* (m^3/s) *of the Rance TPS*. **(c)** On the primary axis of subplot 3: Salinity (g/l) measurements from `SAMBAT` probes at location S1. On the secondary axis of subplot 3: *Depth* (m) measurements from `SAMBAT` probes at location S1. **(d)** On the primary axis of subplot 4: Salinity (g/l) measurements from `SAMBAT` probes at location S2. On the secondary axis of subplot 4: *Depth* (m) measurements from `SAMBAT` probes at location S2. **(e)** On the primary axis of subplot 5: Salinity (g/l) measurements from `SAMBAT` probes at location S3. On the secondary axis of subplot 5: *Depth* (m) measurements from `SAMBAT` probes at location S3.

Figure 2.19: `SAMBAT` (Salinity, filtered data except S1) S1, S2 and S3: Winter 2021.

2.4.3 Turbidity

This winter period had an important flow entering the estuary as shown in the turbine and sluice gates flow rates in **Figure 2.20 (a)**. At the upstream points (T1 and T2), near-surface turbidity was recorded at high tide. Then, at low tide, the records correspond to bottom turbidity, because the probe are no longer submerged. SSC (mg/l) records at T1, T2, $S3_{bottom}$ are shown in **Figure 2.20** (**c**, **d** and **e**, respectively); SSC (mg/l) in S1 and S2 are show in **Figure 2.21 c** and **d**, respectively), no data was recorded at S3 (cf. **Figure 2.21 (e)**). At point T3, near the TPS, no SSC (mg/l) transformation is performed due to lack of laboratory data. The winter period experiences a variation in the flow of the Rance river Q_R (m^3/s) (unlike the summer period), which allows to study its impact on the measurements.
During the first spring-tide (12/02/2020) the Rance flow rate is $Q_R = 10$ (m^3/s). Near-surface SSC at upstream points take the following values within a tidal cycle: between $[30-100]$ (mg/l) in T1; $[10-70]$ (mg/l) in T2 and $[5-500]$ (mg/l) in S1. At the midpoint S2, SSC varies between $[10-100]$ (mg/l), while at the downstream point S3, near-bottom SSC (STBD) varies between $[40-60]$ (mg/l). Turbidity in T3 (WisenSTBD probe) has a similar behavior to S3 under the influence of the tidal signal along this winter period, but no SSC (mg/l) transformation is performed.
For the neap-tide period (18/02/2020) the simulated flow is $Q_R = 20$ (m^3/s). The SSC values varies between $[30-100]$ (mg/l) in T1 and $[8-30]$ (mg/l) in T2 (a decrease compared to the previous spring-tide). Further downstream, near-surface SSC varies between $[0-80]$ (mg/l) at S1 and $[0-20]$ (mg/l) at S2. Therefore, SSC in both positions along a tidal cycle are of lower magnitude in neap-tide than during spring-tide.
Under spring-tide conditions (for date 23/02/2020) and $Q_R = 10$ (m^3/s), the same SSC trend is observed at all locations (T1, T2, S1, S2 and $S3_{bottom}$). Turbidity range increases in spring-tide periods throughout the estuary but with greater intensity at the upstream points.
During the next neap-tide (05/03/2020) the flow rate increases to $Q_R = 40$ (m^3/s). Under these conditions the SSC varies between $[20-60]$ (mg/l)) at T1, $[5-20]$ (mg/l) at T2, and $[0-10]$ (mg/l) both at S1 and S2. $S3_{bottom}$ SSC remains constant with a value of 40 (mg/l). At this location it is not expected such a high value. This might be explained by the calibration data that is not sufficient enough for a reliable transformation. In addition, the measurements were made at the bottom, so they are not representative of the entire water column (with a depth of 12 m at high tide). It is only at the end of the neap-tide period, when the flow of the Rance increases to 50 (mg/l), that an apparent influence on the records is observed. Turbidity increases slightly, especially at the more upstream locations. Near-surface SSC varies between $[40-80]$ (mg/l) at T1; $[20-60]$ (mg/l) at T2; $[20-100]$ (mg/l) at S1; $[8-100]$ (mg/l) at S2. At the downstream point $S3_{bottom}$ the influence of the Rance flow rate is not observed.
In general, near-surface SSC has higher values during spring-tide simultaneously with high river discharge than during neap-tide. Currents generated by the turbines and sluice gates moves the sediments from the bed to the water column, then the suspended matter is accumulated along the whole estuary and transported further upstream by the water motion. This patterns are more evident at the most upstream locations T1, T2 and S1. Nevertheless, transformed SSC values should be taken with caution as they are obtained from few laboratory data, especially the peak values at low tide when the sensor is under saturation for T1, T2 and S1. Upstream points are located where the maximum values of turbidity in the entire estuary are found. However, when the flow discharge of the Rance River presents higher values, e.g. $Q_R \approx 50$ (m^3/s), the sediment is transport in suspension and the SSC can reach a magnitude two times higher than during a normal discharge. This influence is especially noticeable upstream of the estuary.

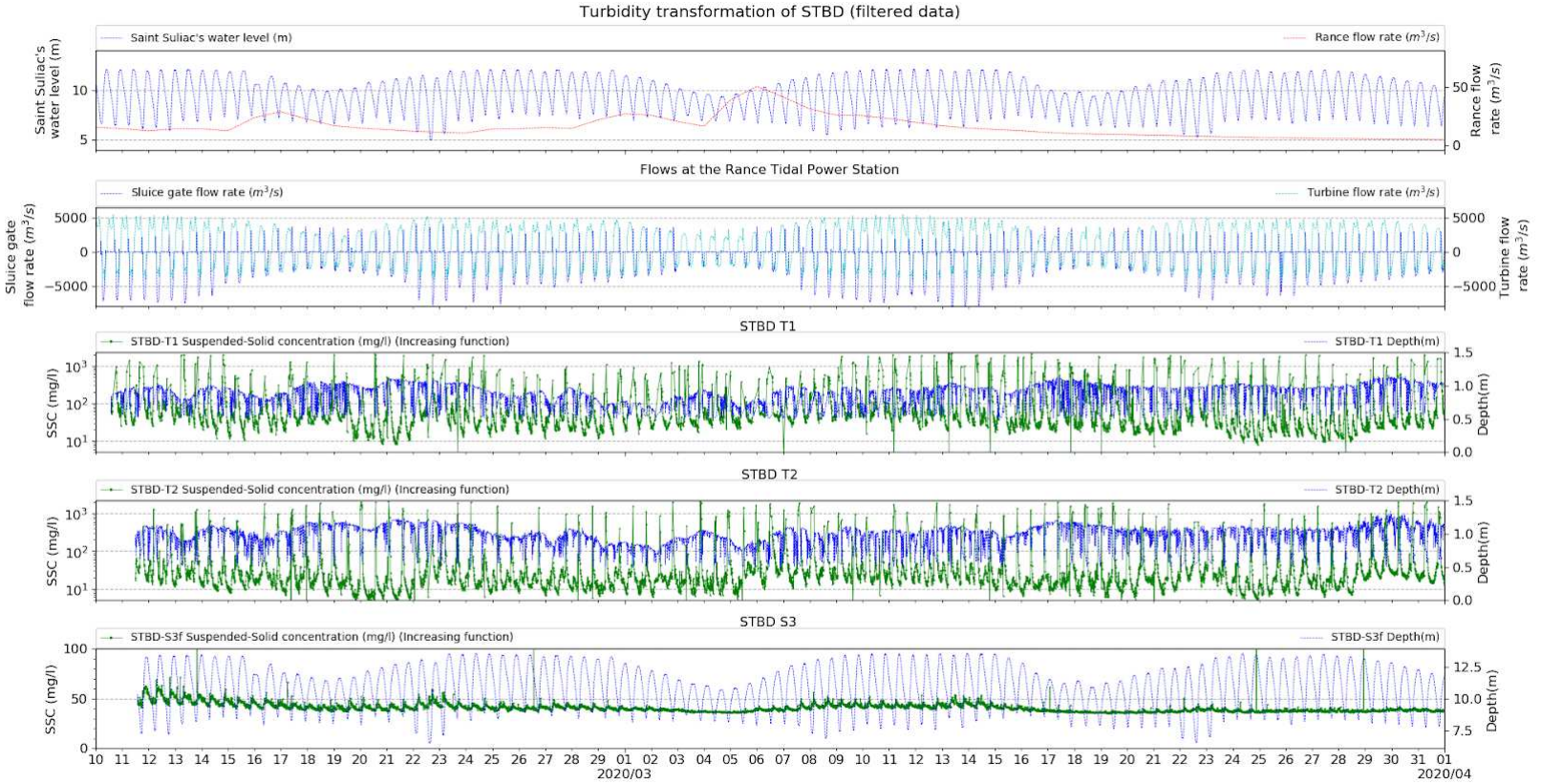

(a) On the primary axis of subplot 1: Water *Depth(m)* at Saint-Suliac. On the secondary axis of subplot 1: *Simulated Rance flow rate* (m^3/s). **(b)** On the primary axis of subplot 2: *Sluice gate flow rate* (m^3/s) *of the Rance TPS*. On the secondary axis of subplot 2: *Turbine flow rate* (m^3/s) *of the Rance TPS*. **(c)** On the primary axis of subplot 3: *SSC* (mg/l) measurements from `STBD` probe at location T1. On the secondary axis of subplot 3: *Depth* (m) measurements from `STBD` probe at location T1. **(d)** On the primary axis of subplot 4: *SSC* (mg/l) measurements from `STBD` probe at location T2. On the secondary axis of subplot 4: *Depth* (m) measurements from `STBD` probe at location T2. **(e)** On the primary axis of subplot 5: *SSC* (mg/l) measurements from `STBD` probe at location S3. On the secondary axis of subplot 5: *Depth* (m) measurements from `STBD` probe at location S3.

Figure 2.20: `STBD` measurements (SSC, filtered data) in T1, T2, T3 and S3: Winter 2020.

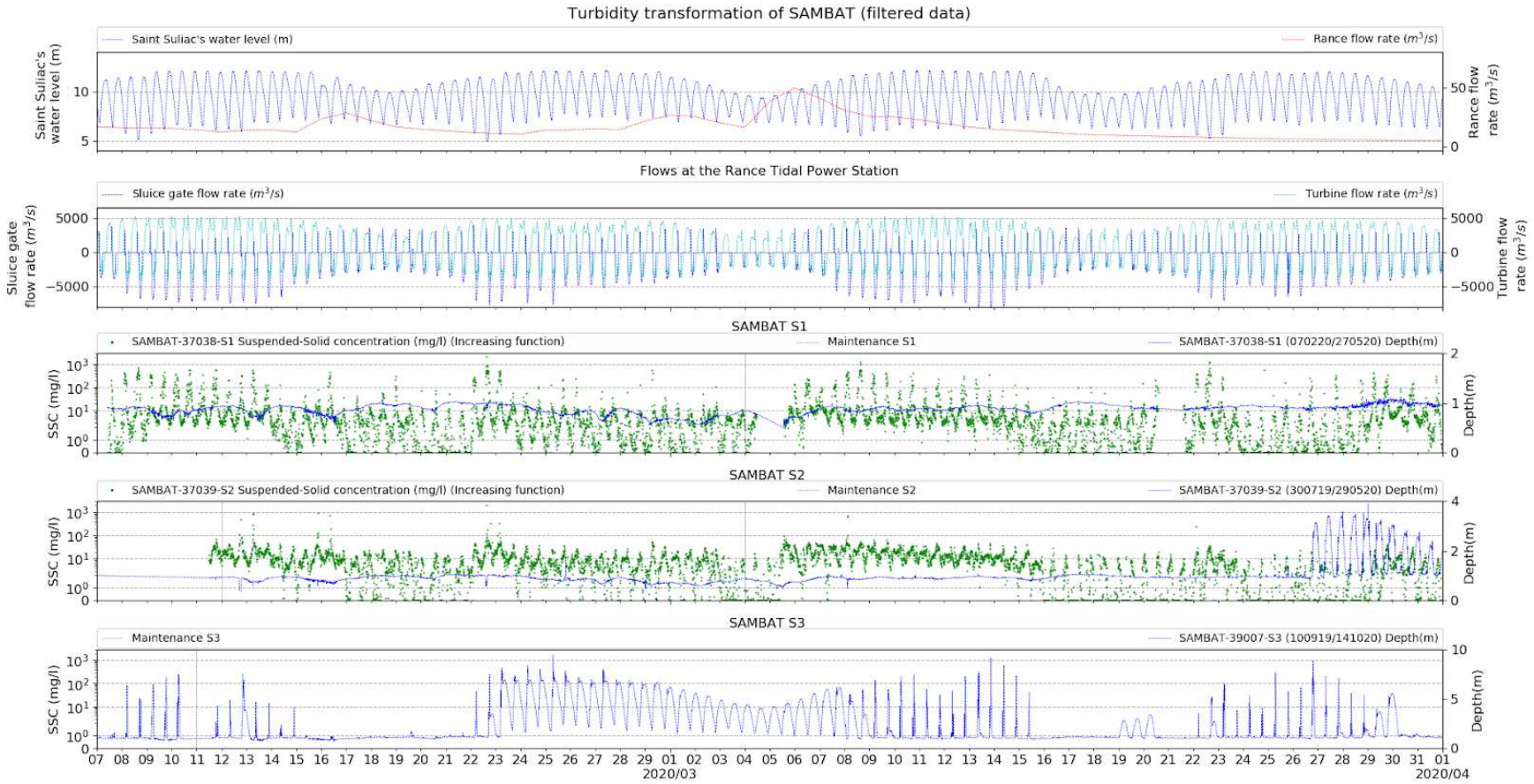

(a) On the primary axis of subplot 1: Water *Depth(m)* at Saint Suliac. On the secondary axis of subplot 1: *Simulated Rance flow rate* (m^3/s). **(b)** On the primary axis of subplot 2: *Sluice gate flow rate* (m^3/s) *of the Rance TPS*. On the secondary axis of subplot 2: *Turbine flow rate* (m^3/s) *of the Rance TPS*. **(c)** On the primary axis of subplot 3: *SSC* (mg/l) measurements from `SAMBAT` probes at location S1. On the secondary axis of subplot 3: *Depth* (m) measurements from `SAMBAT` probes at location S1. **(d)** On the primary axis of subplot 4: *SSC* (mg/l) measurements from `SAMBAT` probes at location S2. On the secondary axis of subplot 4: *Depth* (m) measurements from `SAMBAT` probes at location S2. **(e)** On the primary axis of subplot 5: *SSC* (mg/l) measurements from `SAMBAT` probes at location S3. On the secondary axis of subplot 5: *Depth* (m) measurements from `SAMBAT` probes at location S3.

Figure 2.21: `SAMBAT` (SSC, filtered data) S1, S2 and S3: Winter 2020.

2.4.4 Bed evolution

Bed evolution results at location A3 are shown in **Figure 2.22 (c)**. On 16/02/2020, an important vertical discontinuity is observed in the measurement register. It is not possible to ensure the validity of this measurement. Furthermore, traces of footsteps were observed near the probe in February. Therefore, measurements after the date of occurrence of the vertical discontinuity are considered as reliable.
During the first neap-tide period (18/02/2020), the Rance discharge is estimated to $Q_R = 20\ (m^3/s)$. The mudflat evolution appears to be constant $(db/dt = 0)$. Later, on 24/02/2020, a local erosion is noted, which might be explained by the influence of the Rance river the days prior.
During the spring-tide period (24/02/2020), $Q_R = 10\ (m^3/s)$ and the evolution of the mudflat appears to accelerate $(db/dt > 0)$, but then decreases as the river flow rate increases to $Q_R = 25\ (m^3/s)$.
The second neap-tide period (04/03/2020) exhibits a constant bottom $(db/dt = 0)$. The following days, the river discharge increases until it reaches $Q_R = 50\ (m^3/s)$ on 06/03/2020. Then a change of mudflats evolution is observed $(db/dt < 0)$, this local erosion could have been caused by the influence of the Rance river.
The next spring-tide period (12/03/2020) presents an important evolution of the bottom $(db/dt > 0)$ during several days. Only at the beginning of the neap-tide (18/03/2020) this trend stops and a change of slope $(db/dt = 0)$ is observed, while the bottom remains constant. Then, the last spring-tide period (24/03/2020) sees again an increase in the slope $(db/dt > 0)$ and a positive bed evolution.
At A2 location, less measurements points are available due to the applied filters (cf. **Figure 2.22 (d)**), so it is difficult to notice any general trend. Nevertheless, during neap-tide (04/03/2020) the bottom remains constant $(db/dt = 0)$. Then on 06/03/2020 a vertical discontinuity is also observed, possibly caused by Rance river ($Q_R = 50\ (m^3/s)$). Meanwhile, at location A1, a vertical discontinuity due to maintenance operations is noticed. The next spring-tide (14/03/2020) presents a positive evolution of the bottom $(db/dt > 0)$ (also observed in A3). In the last neap-tide the bottom remains constant $(db/dt = 0)$.
Finally, there are not enough data available at location A1 (cf. **Figure 2.22 (e)**). Towards the end of the neap-tide (06/03/2020) a vertical discontinuity is remarked which may indicate local erosion caused by the Rance river ($Q_R = 50\ (m^3/s)$) or during maintenance operations. Then, the bottom remains constant $(db/dt = 0)$.
A general trend is noted at the three locations. During neap-tide, the bottom remains $(db/dt = 0)$ but towards the end of this period a slight erosion trend is observed, possibly due to the influence of the Rance river discharge. During the spring-tide period, the bottom evolution rate seems to increase $(db/dt > 0)$, with a decreasing tendency at the end of the considered period.
Although the records at the 3 locations show vertical discontinuities and periods with insufficient data, an approximate sedimentation rate can be estimated. The 2020 Winter period (e.g. 54 days) saw sedimentation of 30 mm in A3 and 60 mm in A2, while the limited data in A1 does not allow us to determine the evolution rate of the bottom.

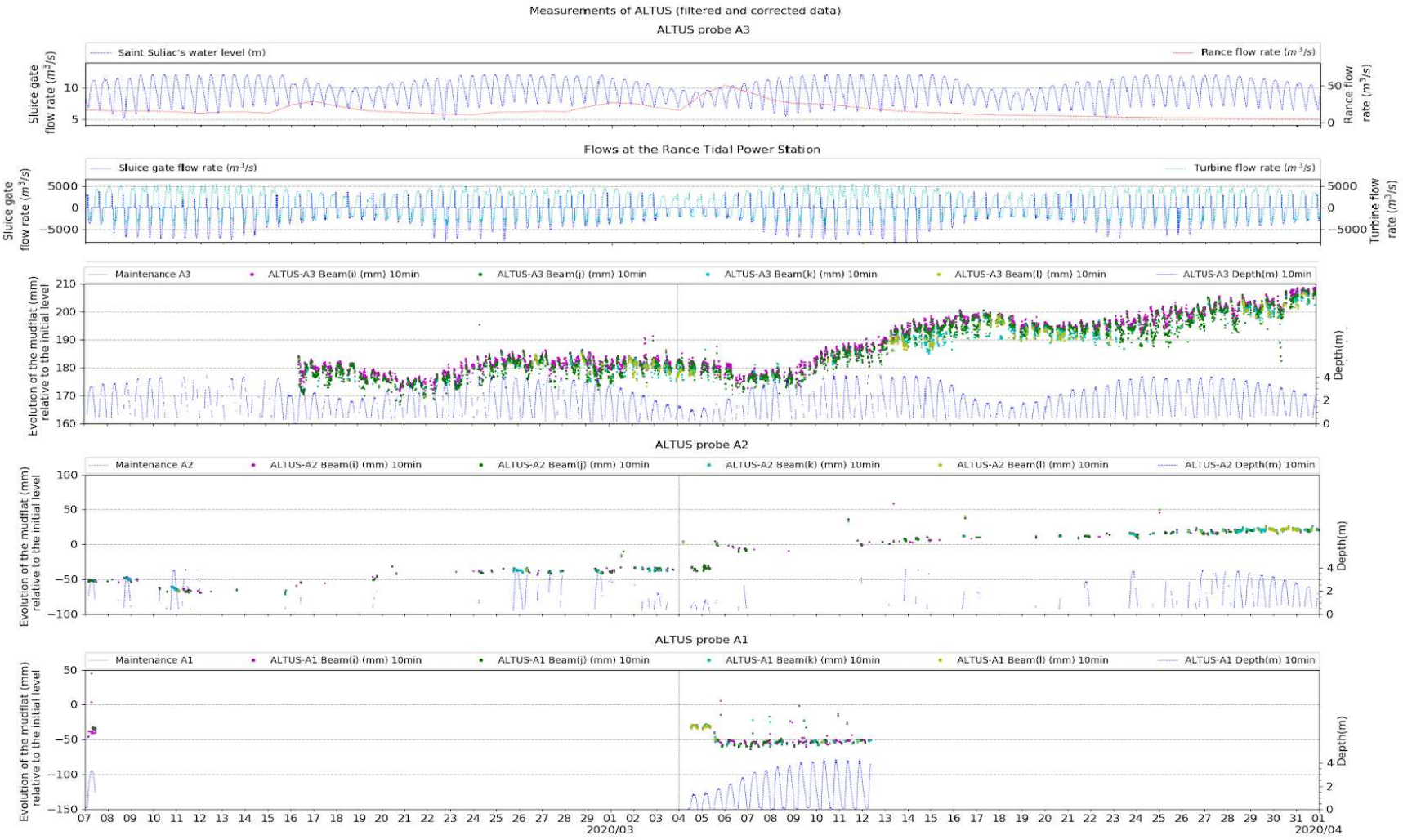

(a) On the primary axis of subplot 1: Mudflat evolution of the 4 beams at A3. On the secondary axis of subplot 1: *Depth* (m) measurements from `ALTUS` probe at location A3. **(b)** On the primary axis of subplot 2: Mudflat evolution of the 4 beams at A2. On the secondary axis of subplot 2: *Depth* (m) measurements from `ALTUS` probe at location A3. **(c)** On the primary axis of subplot 3: Mudflat evolution of the 4 beams at A1. On the secondary axis of subplot 3: *Depth* (m) measurements from `ALTUS` probe at location A1.

Figure 2.22: `ALTUS` (filtered and corrected data) in A1, A2 and A3: Winter 2020.

2.5 Conclusions

The continuous and punctual measurement of hydrodynamics, sedimentary and morphological variables provided insights on sediment dynamics and physical processes observed in the Rance estuary influenced by a tidal power station. Furthermore, this field survey provided an update of dataset of velocity field, bed evolution at mudflats, salinity and suspended solid concentration to be used for the parameterization, calibration and validation of the numerical models implemented in this thesis's work. Currents measurements are overall reliable and of high quality. However, at determined periods, continuous measurements of salinity, suspended sediment concentration and bed evolution presented high margin errors related to NTU-SSC calibration and other uncontrolled issues such as biofouling, malfunctions, battery failure and device drifts. Therefore, the related datasets needed to be cautiously selected on short and reliable time windows.

Acknowledgements

This work was funded by the French National Association of Research and Technology (ANRT) and EDF R&D with the Industrial Conventions for Training through REsearch (CIFRE grant agreement 2018/1653). Christine Bertier, Matthieu Le Brun, EDF R&D-MMN team, measurements crew of EDF-DTG and EPOC-University of Bordeaux are gratefully acknowledged for carrying out the field measurements. Luca Parquet and Marine Vandenhove are deeply appreciated for pre- and post-processing and analysing the collected field data thought internships performed respectively at EDF R&D and EPOC-University of Bordeaux.

CHAPTER 3

HYDRODYNAMICS PROCESSES IN THE RANCE ESTUARY

The work presented in this chapter has been published in
Estuarine, Coastal and Shelf Science Journal on 2nd January 2021, entitled
Hydrodynamics of a hyper-tidal estuary influenced by the world's second largest tidal power station (Rance estuary, France)

by
Rajae Rtimi[a,b], Aldo Sottolichio[b] and Pablo Tassi[a,c]

[a] Electricité de France, Research and Development Departement (EDF R&D), Chatou, France
[b] EPOC Laboratory CNRS, University of Bordeaux, Pessac, France
[c] Saint-Venant Hydraulics Laboratory, Chatou, France

▷ Objectives of this chapter

The main objective of this chapter is to analyze how the hydrodynamics of the Rance estuary is influenced by the world's second-largest tidal power station through basic flow characteristics and tidal asymmetry parameters. To this goal hydrodynamics and tidal wave patterns were analyzed, based on a calibrated and validated two-dimensional (2D), depth-averaged shallow-water hydrodynamic model of the Rance estuary. Afterwards, the influence of the plant on the propagation and the asymmetry of the tidal wave inside the estuary was quantified. Therefore, this chapter aims to answer the hydrodynamic-related topic of research questions formulated in Chapter 1:

- *How relevant are 2D and 3D numerical models at reproducing the main features of hydro-sedimentary dynamics observed in macrotidal estuaries influenced by the presence of a tidal power station?*
- *How hydrodynamics, sediment transport and morphodynamics processes are influenced by the presence of the world's second-largest tidal power station?*

Highlights

- Quantitative analysis of hydrodynamics and tidal patterns of Rance estuary, influenced by a tidal power station.
- In the absence of the plant, changes in bathymetry does not have significant influence on the estuarine hydrodynamics.
- The plant decreases tidal range, currents and tidal prism inside the estuary.
- The tidal power station increases the estuarine low-water level and elongates period of slack water and residence time.
- Tidal patterns analysis suggest that the tidal power plant does not impact the origin of sediments present inside the basin.

Abstract

The Rance estuary is a relatively small low-discharge steep-sided *ria*, located along the Brittany coast in northern France, with a maximum spring tidal range of 13.5 m. Taking advantage of this hyper-tidal regime, the first and currently the second largest operational tidal power station in the world was built at the estuary's mouth and has been in operation since the 1960s. Despite the well-known effect of damping of estuarine water levels, little attention has been given to quantifying the influence of the plant on the propagation and asymmetry of the tidal wave inside the estuary. In this study, hydrodynamics and tidal wave patterns were analyzed in this anthropogenically influenced estuarine system. A two-dimensional depth-averaged numerical model of the Rance estuary was developed. Two scenarios without the tidal power plant involving the dam's pre- and post-construction bathymetry (1957 and 2018 respectively) and present-day conditions scenarios were designed, to highlight the impact of bed evolution and the tidal power station on hydrodynamics and tidal asymmetry. Numerical results showed that, without the structure, bathymetric evolution did not substantially influence estuarine hydrodynamics. Nevertheless, on the estuary-side of the dam, the presence of the tidal power plant induced (i) a decrease in both tidal range and tidal prism, (ii) an increase of low water levels, and (iii) a decrease in both flood and ebb currents. Contrastingly, the region close to the structure reacted differently to plant operating modes, with an increase in flood currents (ebb currents) upstream of the sluice gates (downstream of the turbines). For both the natural condition and the artificially-induced hydrodynamic forcing due to the presence of the plant, numerical results showed that the Rance estuary mainly exhibits flood-dominant behavior, with a longer duration of falling than rising water and stronger peak flood currents than ebb currents. Spanning a period of approximately 60 years, this study presents a quantitative analysis of the influence of the tidal power station on the hydrodynamics in the Rance estuary, and its possible consequences for sediment dynamics. This approach is novel for this particular enclosed water body, characterized by the presence of a dam at its mouth and a lock at its uppermost limit.
Keywords: Tidal power station, Rance estuary, hydrodynamic processes, tidal asymmetry, numerical modeling.

3.1 Introduction

Hyper-tidal estuaries exhibit large tidal range (i.e., mean tidal range>6 m) and strong tidal currents, making them ideal for tidal renewable energy projects. Tidal energy is a form of hydro-power with potential as one of the future sources of renewable energy. However, a tidal power project can modify local hydrodynamics significantly, with impact on sediment dynamics, water quality and ecosystems [Xia et al., 2010; Cornett et al., 2013; Kirby and Retière, 2009]. Therefore, understanding the impact on hydrodynamics induced by tidal projects is crucial for predicting possible environmental impacts.
In estuaries, hydrodynamic behavior is influenced by several factors [Stark et al., 2017b,a; Thurman, 1994; Sumich, 1996]: (i) the gravitational forces of the Moon and the Sun combined with the rotation of the Earth; (ii) the estuary's morphology, and (iii) the freshwater input discharge. In macro-tidal estuaries, hydrodynamics is mainly governed by tides which, have a profound impact on residual sediment dynamics and consequently on morphological evolution [Zhang et al., 2018]. As examined by several authors [Aubrey and Speer, 1985; Speer and Aubrey, 1985; Friedrichs and Aubrey, 1988; Nidzieko and Ralston, 2012; Guo et al., 2018], tidal asymmetry plays an important role, causing residual sediment transport in estuarine systems [Wang et al.,

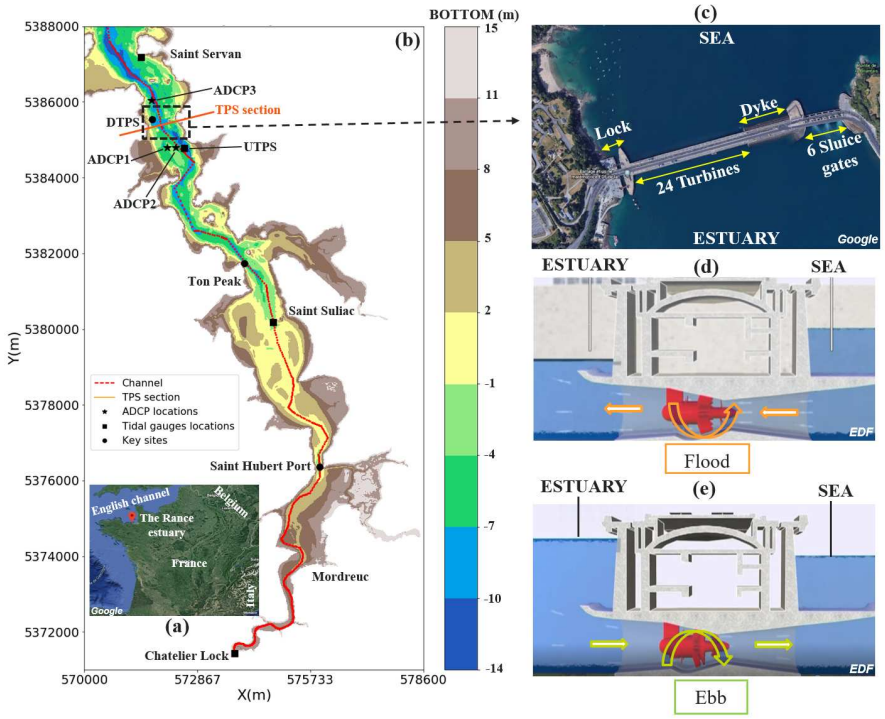

Figure 3.1: The Rance estuary: (a) location map, (b) zoom on the estuary with filled contours of 2018 bathymetry, (c) zoom on the tidal power station (TPS). Vertical plan view of the turbine generators during (d) flood and (e) ebb. Sketches (d) and (e) © EDF (modified).

1999; McLachlan et al., 2020; Mandal et al., 2020], and can be computed from flow velocity and water elevation [Friedrichs and Aubrey, 1988; Nidzieko and Ralston, 2012; Bolle et al., 2010]. The former identifies the nature of the asymmetry: *i.e.*, ebb- or flood-dominance in the estuary. The latter compares the durations of rising and falling tides. This indicates the predominant direction of residual transport of coarse sediment (gravel and sand) carried by bedload and of fine sediment (silt and clay) carried by suspension. Asymmetry in low and high slack water duration is also relevant to the net transport of the finer sediment fraction in the water column [Dronkers, 2005]. A human intervention such as a dam located at a seaward boundary modifies the hydrodynamic regime and significantly alters non-linear tidal interactions [Aubrey and Speer, 1985; Speer and Aubrey, 1985; Vellinga et al., 2014; Hoitink et al., 2003], which can be relevant to sediment transport and accumulation in highly anthropized estuarine systems.

Located on the Brittany coast of northern France (Figure 5.1.a), the Rance estuary is a relatively small steep-sided, 20 km long *ria* [Evans and Prego, 2003]. Its maximum perigean spring tidal range reaches 13.5 m at the mouth (Saint Servan, Figure 5.1.b). Taking advantage of this hyper-tidal regime, the first ever tidal power station in the world was built at the estuary mouth (Figure 5.1.b). The plant has been in operation and managed by Electricité de France (EDF) since 1966 and is currently the second largest operational tidal power station in the world [Pelc and Fujita, 2002]. With a peak (mean) output capacity of 240 MW (57 MW), it supplies 0.12% of the power demand in France, which is equivalent to a medium-size city such as Rennes (*c.* 225,000 in habitants) [EDF, 2020].

Experimental and numerical studies were conducted, mainly focusing on qualitative analysis

of sediment dynamics or ecosystem evolution in the estuary, without prior investigation of how hydrodynamics was influenced by the tidal barrier [Kirby and Retière, 2009; Bonnot-Courtois et al., 2002; Guesmia, 2001; Guesmia et al., 2001; Thiebot, 2008]. Despite a well-known effect on estuarine water levels [Bonnot-Courtois et al., 2002], little attention has been given to quantifying the influence of the plant on the propagation, and vertical and horizontal tidal asymmetry of the tidal wave. The first numerical hydrodynamic model of the Rance estuary was developed in 2001 [Guesmia et al., 2001]. It consisted in a two-dimensional (2D) model used to separately study the sea-side and estuary-side regions of the dam. The aim was to determine hydrodynamic parameters for morphological simulations [Thiebot, 2008]. Although it provided good results with respect to measurements [Guesmia et al., 2001], the approach did not evaluate the influence of the power plant on flow characteristics and tidal asymmetry, which could have significant implications for sediment dynamics and morphological changes in the estuary. In 2018, 2D and 3D numerical models were developed, to evaluate bacteriological impact in the estuary [Chevé and Le Noc, 2018]. The study area included both the basin and the offshore region. However, mesh resolution was constant over the computational domain, which was insufficient to capture flow structure close to the plant and between Mordreuc and Chatelier lock (Figure 5.1.b). The main conclusions of this study were based on the 2D model results, without any further hydrodynamic analysis.

Both 2D and 3D numerical models are used to assess hydrodynamic impacts of existing or planned tidal power plant projects. With the third highest tidal range in the world (15m maximum in spring tide), the Severn estuary (United Kingdom) would be an optimal location for tidal power projects. A 2D numerical model was developed by Xia et al. [2010] to estimate the impact of three renewable-energy projects: Cardiff–Weston, Fleming lagoon and Shoots dams. The basic dam operation regime adopted was ebb generation only. It was concluded that the Fleming Lagoon project would have little influence on hydrodynamic processes in the Severn estuary, however dam construction would have significant environmental impact [Xia et al., 2010]. Young *et al.* developed a 2D hydrodynamic model to highlight the impact of the world's largest tidal power station, the Sihwa Lake tidal power plant in South Korea [Young et al., 2010]. The tidal energy scheme of this plant is a single flood-generation mode. The study established that limiting water surface elevation would modify the estuary's ecosystem [Young et al., 2010]. Another optimal location for a tidal power plant would be the Bay of Fundy, located on the Atlantic coast of North America, where tidal range can exceed 16 m during spring tides. 2D and 3D hydrodynamic models [Cornett et al., 2010, 2013] simulated a range of hypothetical development scenarios with three different operating modes: ebb generation only, flood generation only, and ebb-flood generation. It was concluded that operating mode had considerable influence on local velocities near the lagoon, and particularly near the powerhouse, but seemed to have little influence on the magnitude of far-field hydrodynamic impact [Cornett et al., 2010, 2013]. One common feature of these studies was that they were all conducted ahead of plant construction, and consequently the impact assessments were only estimations.

The main objective of this paper is to analyze how the hydrodynamics of the Rance estuary is influenced by the world's second-largest tidal power station through basic flow characteristics and tidal asymmetry [Nidzieko and Ralston, 2012; Friedrichs and Aubrey, 1988]. For this, a two-dimensional depth-averaged model was developed corresponding to both ebb generation and flood-ebb generation schemes (section 5.3.2). The numerical model was first calibrated and validated on measurement datasets (section 5.4) and then employed to assess present-day hydrodynamic conditions in the Rance estuary (section 3.4.2). Application of the numerical model on diverse scenarios involving past/present bed elevations and presence/absence of

the dam analyzed the impact of the plant on flow patterns and tidal asymmetry (section 3.4.3). Finally, section 6.4 discusses the impact of the Rance tidal power station on hydrodynamic processes and its potential impact on sediment dynamics.

3.2 Study area

3.2.1 Rance tidal power station

The main characteristics of the Rance tidal power plant are as follows (Figure 5.1.c): (i) a 65 m lock, with 20,000 vessels per year passing through; (ii) 24 Kaplan bulb turbines appropriate for very low head and high flow rates [Hydrelect, 2012], 323 m long and 33 m wide, each unit producing 10MW; (iii) a rockfill dyke 165 m long; (iv) 6 sluice gates composing 114x15 m dam; and (v) a road on which 30,000 (60,000 in summer) vehicles per day travel between the cities of Dinard and Saint Malo. The particularity of the Rance tidal power plant is its ability to produce electricity during both falling and rising tides (Figures 5.1.d & 5.1.e), operating by one- and two-way generation modes thanks to the capacity of its Kaplan bulb turbines to rotate in both directions [Charlier, 2007; Young et al., 2010]. The Rance River drains a small catchment area, with an average river discharge of 7 m^3/s, low water flow rate of 0.5 m^3/s and a decennial flood of 80 m^3/s. These magnitudes are small compared to the tidal flux observed upstream of the plant, with about 9,000 m^3/s maximum in neap tide and 18,000 m^3/s in spring tide (Figure 5.1.b). Further information on the estuary's morphology, sedimentary and hydrological characteristics can be found in [Bonnot-Courtois et al., 2002].

3.2.2 Evolution of bed elevation between 1957 and 2018

During the last 58 years, between 1960 (before plant construction) and 2018, the Rance estuary has been subject to natural and artificial sedimentary processes governing its morphological evolution. In the present study, two bathymetry configurations were used for digital elevation models (DEMs), corresponding to the available datasets. The first DEM corresponds to the year 1957, prior to the plant's construction (Figure 3.2.a), and the second to the year 2018, which is the most recent bathymetric survey (Figure 3.2.b). For both 1957 and 2018 datasets, spatial coordinates were expressed according to the World Geodetic System 1984 (WGS84). Altitude was adjusted to the zero-level provided by the National Hydrograph Service (chart datum).

Bathymetry for 1957 was reconstructed using historical maps and data surveyed by EDF, consisting of isobaths and echo-sounder point data at specific locations. To build the Digital Elevation Model, isobaths and point data were vectorized using Global Mapper® and projected in 3D by TerraModel®. The estimated horizontal and vertical uncertainties were of the order of 1m and 0.1m, respectively [Trubert and Ichstchenko, 2016].

From May 29 to June 6 2018, a field survey was carried out to collect bathymetric and topographic data in the estuary. High-frequency multibeam echo-sounder measurements were performed to map the estuary bottom. Intertidal zone topography was measured on a light detection and ranging system (LIDAR) [EDF, 2018]. The mean uncertainties of the horizontal and vertical measurements were of the order of 0.01m.

Downstream of the tidal power station, both DEMs employed the same bathymetry, extracted from the SHOM HistoLitt® surveys carried out between 1970 and 2005 [SHOM, 2015]. For seabed depths up to 50m, vertical resolution ranged from 0.3m to 1m and horizontal resolution from 1m to 20m. Beyond 50m, vertical resolution ranged from 1% to 2% of depth and horizontal resolution was few tens of meters [SHOM, 2015].

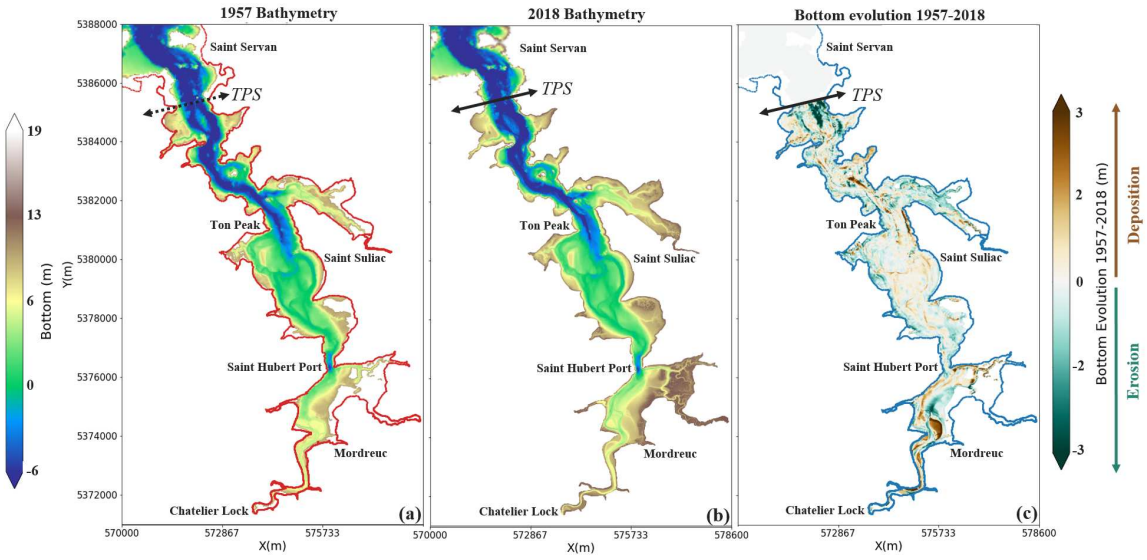

Figure 3.2: (a) Bathymetry of 1957 (before the construction of the tidal power station). Blank area represents the zones where the bathymetry is less reliable. (b) Bathymetry of 2018. Bathymetry evolution between 1957 and 2018.

According to bed evolution depicted in Figure 3.2.c, there was an erosional zone upstream of the sluice gates. Conversely, in the lower part of the estuary, sediment accretion occured in the meandering reach downstream of Mordreuc. Furthermore, in the middle-estuary region between Ton peak and Saint Hubert port, little difference was observed between the 1957 and 2018 bathymetries. The changes in bathymetry may present inaccuracies due to measurement uncertainty in the older maps.

3.3 Numerical modeling

3.3.1 Hydrodynamic model

The TELEMAC-2D module, belonging to the open-source TELEMAC-MASCARET modeling system (www.opentelemac.org) was used to study hydrodynamics in the Rance estuary and to investigate changes in flow characteristics induced by the tidal power plant. This module solves the two-dimensional, horizontal shallow water equations (2DH), which implicitly assume hydrostatic pressure distribution, constant fluid density and depth-averaged velocity components [Lane, 1998; Vreugdenhil, 2013]. This modeling approach has been applied to other shallow and vertically well-mixed estuaries [Xie et al., 2017; Angeloudis and Falconer, 2017; García-Oliva et al., 2017; Neil et al., 2018; Cornett et al., 2013]. The numerical tool has been assessed in applications in several coastal and estuarine cases [Bi and Toorman, 2015; Brown and Davies, 2010; Santoro et al., 2013; Van, 2012; Orseau et al., 2020]. Two relationships were specified to close the governing equations: a classical squared function dependency on depth-averaged velocity for bed resistance, and the Boussinesq approximation for turbulence parameterization [Lane, 1998]. This study used the Strickler law for bottom friction and a zero-equation turbulence model with constant eddy viscosity. The Strickler coefficient and eddy viscosity values were assumed to be constant over the whole computational domain. They were calibrated using

Acoustic Doppler Current Profiler (ADCP) observed data from 2012 [Bizien and Soenen, 2012] and validated with measurements of water surface elevation from tidal gauges during 2019. The computational domain covered the sea-side and the estuary-side areas extending from the oceanic open boundary ($\sim$ 20km from the tidal power plant) to the upstream limit (Chatelier lock). It was discretized with an unstructured mesh generated by the BlueKenue® pre- and post-processing tool [Barton, 2019]. The mesh consisted of 399,512 triangular elements and 204,565 nodes with variable resolution ranging between 1000m offshore, 250m near the coastline, 50m around the estuary mouth, 20m inside the estuary and 5m close to power station and within the lower estuary between Mordreuc and Chatelier lock, see Figure 5.1 [Cochet and Lambert, 2017]. The topo-bathymetric information contained in the DEM was projected onto the finite element mesh using the inverse distance weighting interpolation algorithm [Achilleos, 2011]. Boundary conditions were set as follows:

(i) At the oceanic open boundary (offshore), water levels and velocity component values were imposed through 11 tidal constituents (M2, S2, N2, K2, K1, O1, P1, Q1, M4, MS4 and MN4) from the OSU TPXO European Shelf 1/30 regional model [Egbert and Svetlana, 2002].

(ii) At the upstream limit (Chatelier lock, Figure 5.1), freshwater input from the Rance river was set up as varying between $5m^3/s$ and $30m^3/s$. The configuration of this boundary is complex: in addition to the lock, 2 sluice gates maintain constant water level at the port located upstream of the Chatelier lock. As the flow passing through these structures is not measured, flow discharge was estimated from the mean Rance river flowrate, collected from the nearest hydrometric station located $\sim$ 33km upstream of Chatelier lock.

(iii) The tidal power station was represented by two weirs: the first depicts the turbines structure and the second depicts the sluice gates structure. Unlike existing tidal power station models (TPS models) [Angeloudis et al., 2016; Cornett et al., 2013; Xia et al., 2010], the operation modes of the turbines and sluice gates were calculated by an external optimization algorithm Software named AGRA [Libaux and Drouot, 2020] and not by the head difference seen on TELEMAC-2D. AGRA Software, based on the dynamic programming method [Bellman, 1954], is used by operators in charge of the plant to simulate optimal energy generation and the resulting hydraulic conditions (flowrates, start and stop times, *etc.*), notably according to head difference and equipment availability [Libaux and Drouot, 2020]. In order to be consistent with the actual regime of the power plant, the AGRA output was used as input in the TELEMAC-2D model to define the operating mode of the turbines and sluice gates. Following studies by Xia et al. [2010]; Cornett et al. [2013]; Angeloudis et al. [2016], the turbines and sluice gates were treated separately with their corresponding flowrates, to ensure good representation of the complex flow structure in the zone around the dam; the approach of imposing a single flowrate throughout the whole plant boundary was not adopted. In TELEMAC-2D, a weir is considered as a linear singularity, represented by an island in the mesh [Telemac-Mascaret Modelling System, 2018]. Standard weir discharge equations already exist in TELEMAC-2D [Telemac-Mascaret Modelling System, 2018], but were adjusted as follows to suit the Rance tidal plant's operation:

- Flowrate through turbines was computed by three methods depending on operating mode: (a) For direct-, inverse-turbining and direct pumping (D.T., I.T. and D.P. in Table 6.2), flowrate was interpolated using discharge data generated by the AGRA Software, based on hill charts where flowrate is computed according to turbine

Table 3.1: Operating modes of sluice gates and turbines.

Structure	Sluice gates		Turbines					
Operating mode	G.O.	G.C.	F.O.	D.O.	I.T.	D.T.	D.P.	T.O.
Definition	Gates Open	Gates Close	Filling On	Draining On	Inverse Turbining	Direct Turbining	Direct Pumping	Turbines Off
Tidal phase	Flood Ebb	Flood Ebb	Flood	Ebb	Flood	Ebb	Flood	Flood Ebb

blade incidence, which in turn depends on real head difference and tidal power. (b) For filling and draining phases (F.O. and D.O. in Table 6.2), flowrate $Q_{turbines}$ was computed according to standard orifice equation 3.1. (c) For Turbines Off phase (T.O. in Table 6.2), flowrate $Q_{turbines}$ was set to 0.

$$Q_{turbines} = N_{turb} \cdot A(|\zeta_{estuary} - \zeta_{sea}|)^{1/2} \tag{3.1}$$

- Flowrate through sluice gates in the Gates Open stage (G.O. in Table 6.2) was computed by equation 3.2, adjusted from the standard orifice equation ($Q \propto C_d H^{0.5}$) using a variable instead of a constant discharge coefficient. This approach was adopted since the sluice gates in the Rance power plant are large and appropriate for low head differences, and thus the discharge coefficient varies significantly according to downstream water level. For the Gates Closed stage (G.C, Table 6.2), flowrate $Q_{sluices}$ was set to 0.

$$Q_{sluices} = N_{sg}(B\zeta_{downstream}^{1/4} - C)(|\zeta_{estuary} - \zeta_{sea}|)^{1/2} \tag{3.2}$$

In the above equations, $\zeta_{estuary}$ and ζ_{sea} are surface water elevations at Saint Suliac and Saint Servan respectively (see Figure 5.1 for locations). N_{turb} and N_{sg} are numbers of available turbines and sluice gates respectively. A, B and C are discharge coefficients and $\zeta_{downstream}$ is downstream water surface elevation. Table 3.2 summarizes values of these parameters (A, B, C, $\zeta_{downstream}$) according to tidal phase (flood and ebb).
Turbine flowrate, $Q_{turbines}$, was then distributed homogeneously across the 24 turbines. Likewise, for sluice gates, $Q_{sluices}$ was distributed homogeneously across the 6 sluice gates. This assumes that all the plant's equipment is available, which is not always the case. However, given that the outage rate for hydroelectric units is low, this assumption would not significantly influence the numerical results. In this study, both water surface elevation and bottom elevation are relative to the chart datum.

(iv) The rest of the domain contour was represented by a closed solid boundary.

3.3.2 Tide analysis

To analyze in depth the influence of the plant on the hydrodynamics in the estuary, four complementary metrics were evaluated:

(i) Tidal prism (TP), defined as the volume of water leaving the estuary at ebb tide [Davis and Fitzgerald, 2004]. This parameter was deduced from flowrate passing through the

Table 3.2: Turbines and sluice gates flowrate parameters

Tidal phase	A	B	C	$\zeta_{downstream}$
Flood	-132.61	-948.22	-900.9	$\zeta_{estuary}$
Ebb	161.98	960.96	912.73	max(1,ζ_{sea})

TPS section ($Q_{\sum_{TPS}}$) located upstream of the plant (Figure 5.1.b) and was calculated from Eq.3.3:

$$TP = \int_{t \in ebb} Q_{\sum_{TPS}}(t)\, dt \tag{3.3}$$

Tidal prism was further analyzed over a fortnightly tidal cycle to assess its evolution over neap/spring tidal periods.

(ii) Mean residence time (T_r), defined as the time taken by a water parcel to leave a defined region through its outlets to the sea [De Brauwere et al., 2011]. Following studies by [Sanford et al., 1992; Marsooli et al., 2018; Monsen et al., 2002], mean residence time can be computed from the theoretical tidal prism method as in Eq.3.4:

$$T_r = \frac{VT}{(1-b)TP} \tag{3.4}$$

where V is the mean volume of water in the system, T is the tidal period, TP is the tidal prism, and b is the return-flow factor, defined as the fraction of ebb water returning to the system during the flood tide ($0 < b < 1$) [Sanford et al., 1992].

(iii) Ebb/flood tidal current asymmetry $\gamma_0(n = u)$, and tidal duration asymmetry $\gamma_0(n = \frac{\partial \zeta}{\partial t})$, were quantified by computation of skewness as defined by Nidzieko and Ralston [2012]:

$$\gamma_0(n) = \frac{\mu_3(n)}{\mu_2^{3/2}(n)} \tag{3.5}$$

where the m-th moment about zero, μ_m, is:

$$\mu_m(n) = \frac{1}{N-1} \sum_{i=1}^{N} n_i^m \tag{3.6}$$

and N is the number of samples n_i and ζ is the water surface elevation.
The Rance estuary does not have a single along-channel velocity direction. For instance, the flow is mainly aligned north-south upstream of Ton peak, and east-west downstream. Hence, the current field can be defined as the velocity magnitude affected by the sign of the North-South velocity component. Parameters ($\gamma_0(u)$;$\gamma_0(\partial\zeta/\partial t)$) were computed as the median over a neap-spring tidal period to analyze their spatial distribution upstream and downstream of the plant; Nidzieko and Ralston [2012] showed that the tide is ebb dominant for $\gamma_0(u) < 0$ and flood dominant for $\gamma_0(u) > 0$. They reported that the duration of falling water is shorter than rising water for $\gamma_0(\frac{\partial \zeta}{\partial t}) < 0$ and longer for $\gamma_0(\frac{\partial \zeta}{\partial t}) > 0$.

(iv) Asymmetry metrics were analyzed by computing the amplitude ratio $\alpha = a_{M_4}/a_{M_2}$ and phase difference $\beta = 2\phi_{M_2} - \phi_{M_4}$ on both water surface elevation (ζ) and current (u). As the Rance estuary is dominated by the $M2$ semidiurnal tide, this approach is

appropriate for quantifying tide asymmetry. According to Friedrichs and Aubrey [1988], the amplitude ratio α indicates the degree of non-linearity: *i.e.*, the capacity of the estuary to generate/amplify secondary harmonics (M4, M6, *etc*). As for phase difference β, it illustrates the asymmetry direction, flood or ebb dominance. Least squares harmonic analysis of water surface elevation and current was performed on a record of 20 days using the T-TIDE toolbox [Pawlowicz et al., 2002]. Asymmetry metrics were then computed at selected locations in the estuary and further analyzed with Nidzieko and Ralston [2012] asymmetry parameters ($\gamma_0(u)$;$\gamma_0(\partial\zeta/\partial t)$).

3.4 Results

In this section, the numerical model was calibrated and validated using respectively ADCP measurements collected for five tide cycles in 2012 and a water level dataset recorded from tidal gauges for a period of a fortnight in 2019 (subsection 5.4). Numerical model results were then analyzed to better understand the hydrodynamics in the estuary and to highlight the influence of the power plant on the estuarine system. Subsection 3.4.2 provides a description of the hydrodynamics in the estuary today. Tide propagation and asymmetry are analyzed for three scenarios in subsection 3.4.3.

3.4.1 Model calibration and validation

To calibrate the numerical model and validate its capacity to predict water surface elevation and tidal currents, two datasets from 2012 [Bizien and Soenen, 2012] and 2019 were used. Firstly, the numerical model with the recent bathymetry of 2018 (Figure 3.2), was calibrated using a dataset consisting of Acoustic Doppler Current Profiler (ADCP) measurements for five tide cycles (June $4-6$ 2012) collected at three locations near the power station: upstream of the turbines (ADCP 1), upstream of the sluice gates (ADCP 2) and downstream of the power station (ADCP 3). Secondly, the numerical model was validated using a larger dataset of water surface measurements from tidal gauges for the period August $15-28$ 2019. This validation was needed to assess the capacity of the model to propagate the tide along the estuary from upstream (Chatelier Lock) to mouth (Saint Servan), over a continuous period of a fortnight. For velocity validation, Root Mean Square Error (RMSE) on current magnitude and direction was calculated. To validate water surface elevation, RMSEs were computed on the entire water-level signal, at high- and low-water levels. Since the model was further used for harmonic analysis, water level validation was complemented by error computation on the amplitude and phase of the M2 and M4 tide constituents.

3.4.1.1 Model calibration and validation for the year 2012

Imposing a Strickler coefficient of 60 $m^{1/3}/s$ and constant eddy viscosity of 10^{-4} m^2/s over the whole computational domain, numerical results were compared with ADCP measurements at three locations indicated in Figure 3.3. As shown in Figures 3.3.a;b;c, the model effectively reproduced water surface elevation with RMSE $\approx$ 8 cm upstream of the TPS and $\approx$ 5 cm downstream (Table 3.3). High- and low-water levels are also effectively computed by the model with RMSE below 4 cm upstream of the dam and 3 cm downstream of the structure (Table 3.3). For both stations upstream of the TPS (ADCP1 and ADCP2), high-frequency oscillations of the order of $\sim$ 10cm are clearly seen at low and high water, and the tidal range is approximately 50% less than in the station downstream of the TPS. The numerical model effectively represented

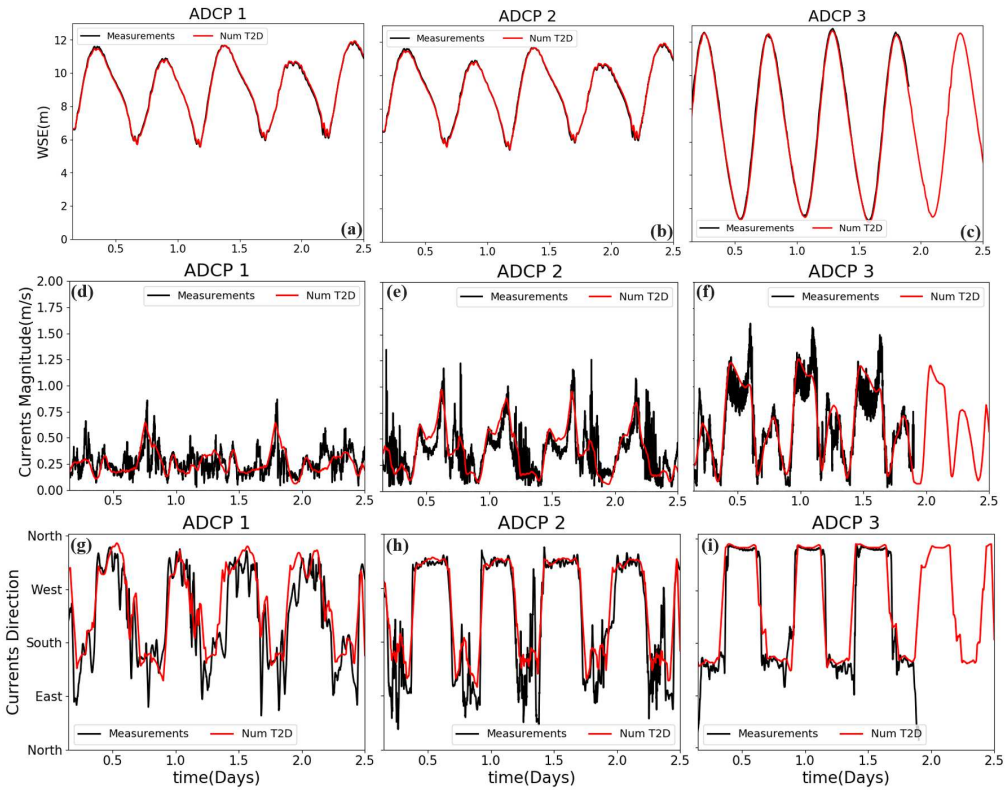

Figure 3.3: Comparison of numerical results and measured data from data set of 2012: water surface elevation, current magnitude and current direction respectively at positions (a;d;g) ADCP 1 upstream of the turbines, (b;e;h) ADCP 2 upstream of the sluice gates and (c;f;i) ADCP 3 downstream of the tidal power station (see locations in Figure 5.1).

water-level oscillations and tidal wave damping inside the estuary caused by the operation of the TPS. It is also able to reproduce satisfactorily velocity magnitude and direction at the three ADCP locations, with RMSE values below 0.2 m/s for current magnitude and 12° for current direction, as shown in Figures 3.3.d-i) and Table 3.3. Upstream of the turbines and downstream of the TPS, flood-currents are stronger than ebb-currents, while they are equivalent upstream of the sluice gates. For the latter, the velocity magnitude decreases by 15% and 6% during flood and ebb respectively with respect to velocity magnitude in the sea-side of the dam. However, this reduction is greater upstream of the turbines (ADCP 1), at 48% and 62% for flood and ebb currents respectively. The flood-current measurements exhibited a peak at the beginning of the flood, which is clearer at stations ADCP 2 and ADCP 3 (Figures 3.3.e;f). The peak upstream of the plant, directly related to turbine operation, is well represented by the numerical model. However, the peak observed downstream of the TPS (ADCP 3), which could be generated by a combination of TPS operation modes and hydrodynamic forcing (*i.e.*, wind and waves) not considered in this study, is not captured by the model. For the three ADCP locations, ebb currents are mainly oriented north-west and flood currents are mainly directed south-east.

Table 3.3: Root Mean Square Error (RMSE) computation between numerical results and measurements for years 2012 and 2019.

Data set year	2012			2019			
RMSE	ADCP 1	ADCP 2	ADCP 3	Saint Servan	upstream of TPS	Saint Suliac	Chatelier Lock
Water Surface Elevation (cm)	8.11	8.13	5.04	6.22	9.12	8.74	8.08
High Water Level (cm)	4.44	4.46	3.08	5.42	4.38	4.24	4.05
Low water Level (cm)	2.41	2.26	2.05	9.58	8.24	8.78	—
Current magnitude(m/s)	0.1	0.18	0.2		—		
Current direction (°)	12	11	8		—		

3.4.1.2 Model validation for the year 2019

To assess numerical model reliability and robustness with respect to the current operating mode of the power station, a numerical simulation was performed over a period of a fortnight from August 15 – 28 2019. For this scenario, only water surface measurements were available. Figures 3.4.a;b;c;d present a comparison between numerical results and measurements at Saint Servan, upstream of the TPS, Saint Suliac and Chatelier Lock respectively (see Figure 5.1 for tidal gauge locations). The numerical model demonstrated its ability to reproduce satisfactorily the tidal distortion caused by the TPS, as well as to correctly propagate the tidal wave along the estuary, with RMSE below 10 cm (Table 3.3). Although the model's error on low water levels is slightly higher than error on high water levels, it is still below 10 cm, which is considered satisfactory. Furthermore, the reduction in tidal range inside the estuary is well represented. The model is also able to reproduce the seiche-like oscillations, which are stronger at stations upstream of TPS and Chatelier Lock. Moreover, the amplitude and phase of the M2 and M4 components are well computed, with error below 5 cm and 9° for amplitude and phase respectively (see Table 3.4).

3.4.2 Present-day conditions of the Rance estuary

This section focuses on the fortnight's simulation in August 2019. Numerical results were validated for a large dataset of measurements and represent the current mode of plant operation. High and low tides, mean water level and tidal range along the estuary's channel were analyzed. Then, the evolution of the water surface elevation and currents was studied at particular locations in the estuary for both neap and spring tides.
Figure 3.5.a shows a comparison between spring and neap tide for low water (LWL), high water (HWL) and mean water (MWL) levels along the estuary channel, defined respectively as minimum, maximum and mean water surface elevation during one tide cycle (12 h 25 min). These results suggest that the estuary could be divided into two zones: one from the Chatelier lock to the TPS ($\sim$ 18 km) and one from the TPS downstream to the sea ($\sim$ 5 km). In the latter zone, there is a difference between HW levels (blue lines) at spring and neap tide (and similarly for LW levels, red lines), while, for the same tidal conditions, MW levels (green lines) remain

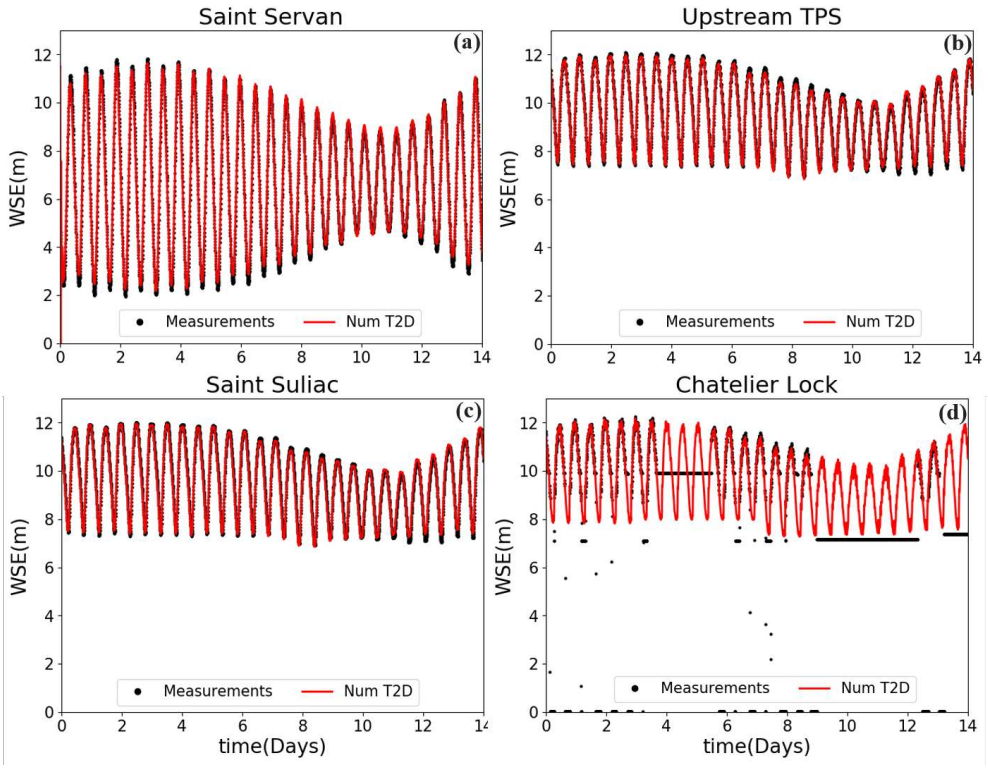

Figure 3.4: Comparison of water surface elevation between numerical and measured data, over a period of a fortnight from August 15 to 28 2019, at (a) Saint Servan, (b) upstream of tidal power station, (c) Saint Suliac and (d) Chatelier lock (see locations in Figure 5.1). Red lines and black dots indicate respectively numerical results and measured data. The measurements are not reliable at low tide at Chatelier Lock station because of technical difficulties of the gauge.

constant. In the former zone, HWL at spring tide is naturally higher than HWL at neap tide (blue lines); however, LW levels (red lines) are nearly coincident. Therefore, MW level (green lines) is not constant between spring tide and neap tide in this zone. In fact, the operating mode of the TPS requires keeping the yacht harbor upstream of the Chatelier Lock navigable, so a minimum of 2 meters is required in the channel [Caude et al., 2017], and thus, minimum water level in the estuary channel could not reach its natural value, in contrast to the zone downstream of the TPS. Moreover, LWL, HWL and MWL are always higher in the estuary side than in the sea side. This difference is more significant for LWL, and mainly at spring tide. Consequently, tidal range (Figure 3.5.b) is decreased in the zone upstream of the TPS by nearly 50% at spring tide and 33% at neap tide compared to the sea-side region.

Water surface elevations and currents were analyzed simultaneously with power station operating modes during a spring tide period (Figures 3.6.a-h). As seen previously, tidal range is reduced in the estuary and high-frequency oscillations are observed at high and low tide during the Off period of both turbines and sluice gates (T.O. and G.C. stages, Table 6.2). These oscillations are stronger at the Chatelier Lock, considering the tidal wave reflecting on the upstream boundary condition [Duclercq, 2020]. Moreover, a lag of $\sim$ 2 hours is observed at high and low tides (and similarly for ebb and flood currents) between Saint Servan (sea) and the other locations along the estuary. After reaching the natural water level maximum ($t = 2.4$ d), the pump units raise the estuary water level (D.P. phase) to allow a greater drop in the next

Table 3.4: Computation of harmonics amplitude and phase errors based on tidal constituents of water surface elevation between numerical results and measurements for year 2019. All results were obtained with the T-TIDE toolbox [Pawlowicz et al., 2002]

Tidal constituents	M2		M4	
Error on	Amplitude (cm)	Phase (°)	Amplitude (cm)	Phase (°)
Saint Servan	3.02	3	2.41	8
Upstream of TPS	4.21	4	3.89	9
Saint Suliac	4.15	4	3.77	9

low tide, maximizing electricity production (D.T. stage). For the same purpose, the high water (resp. low water) slack period lasts for ∼1h 20 minutes (resp. ∼ 25 minutes), allowing operating modes to be switched from direct pumping to direct turbining (resp. direct turbining to inverse turbining). During spring tide, the TPS can operate in two-way generation, so that the electricity is produced not only during ebb (D.T. stage) but also during flood (I.T. stage). Furthermore, Figures 3.6.e;f;g show that the TPS amplifies the peak-flood current in the estuary, mainly by the opening of the sluice gates (G.O. stage). This amplification is then reduced toward the estuary's upstream limit (Chatelier Lock). Moreover, flood currents are stronger than ebb-currents on both sea and estuary sides, except near Chatelier Lock (Figure 3.6.h) where river currents (negative currents) are dominant.

A similar analysis was performed for a neap tide period, as shown in Figures 3.7.a-h. Since tidal range in the sea side is naturally lower than in spring tide, the operating mode of the TPS is obviously different to ensure electricity production during neap tides as well. Presently, the TPS operates only in one-way generation during this period, so electricity is produced only during ebb (D.T. stage). Thus, in order to meet navigation requirements and ensure a sufficient drop between sea and estuary levels for a long enough time, the direct pumping stage (D.P.) is longer than in spring tide. Consequently, the high-water level in the estuary is clearly higher than in the sea. In addition, the maximum flood-current upstream of the TPS is amplified by pumping through the turbines and sluice gates rather than the sluice gates only, as is the case at spring tide. However, this amplification is quickly dissipated, since currents at Saint Suliac (∼ half the estuary) are weaker than those at Saint Servan (Figures 3.7.e;g).

3.4.3 Influence of the tidal power station on hydrodynamics and tide asymmetry

To evaluate the impact of the tidal power station on hydrodynamics and tide asymmetry, three configurations were designed (Table 3.5) for the fortnight of August 15 – 28 2019. The first (C1) was based on the DEM for 1957 (Figure 3.2.a). It represents a real configuration of the estuary in the past, specifically before the construction of the dam. The second (C2) is a virtual configuration: the present estuary configuration but without the power station. It was recreated from the DEM for 2018 by removing the dam and smoothing the bottom elevation upstream and downstream of the TPS. The third configuration (C3) represents the present estuary configuration, with the TPS and the DEM for the year 2018 (as presented in section 3.4.2). Comparison between C1 and C2 scenarios highlights the influence of the bathymetry, spanning ∼ 52 years of TPS operation. Comparison between the C2 and C3 configurations emphasises the impact of the TPS over a period of a fortnight. These comparisons are complemented by asymmetry analysis, providing preliminary insights at a larger time scale.

All three numerical simulations were performed using the same hydrological condition (river

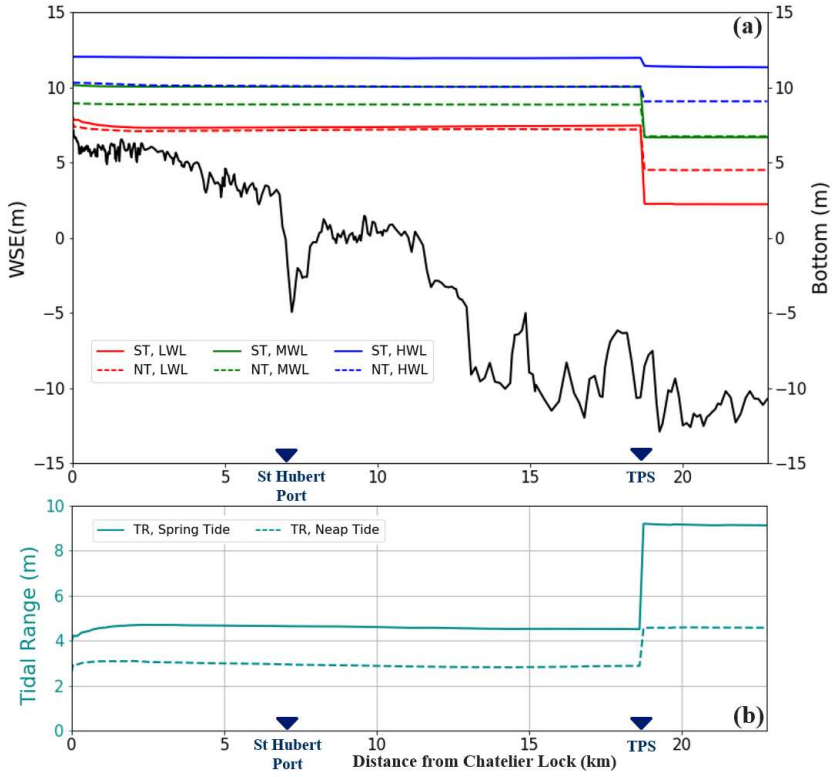

Figure 3.5: Comparison of (a) low, mean, high water levels and (b) tidal range at neap and spring tide along the estuary channel (see Figure 5.1 for channel position). The black line indicates bed elevation.

Table 3.5: Modeling scenarios

Name	Bathymetry	Type
C1	1957	Without power station
C2	2018	Without power station
C1	2018	With power station

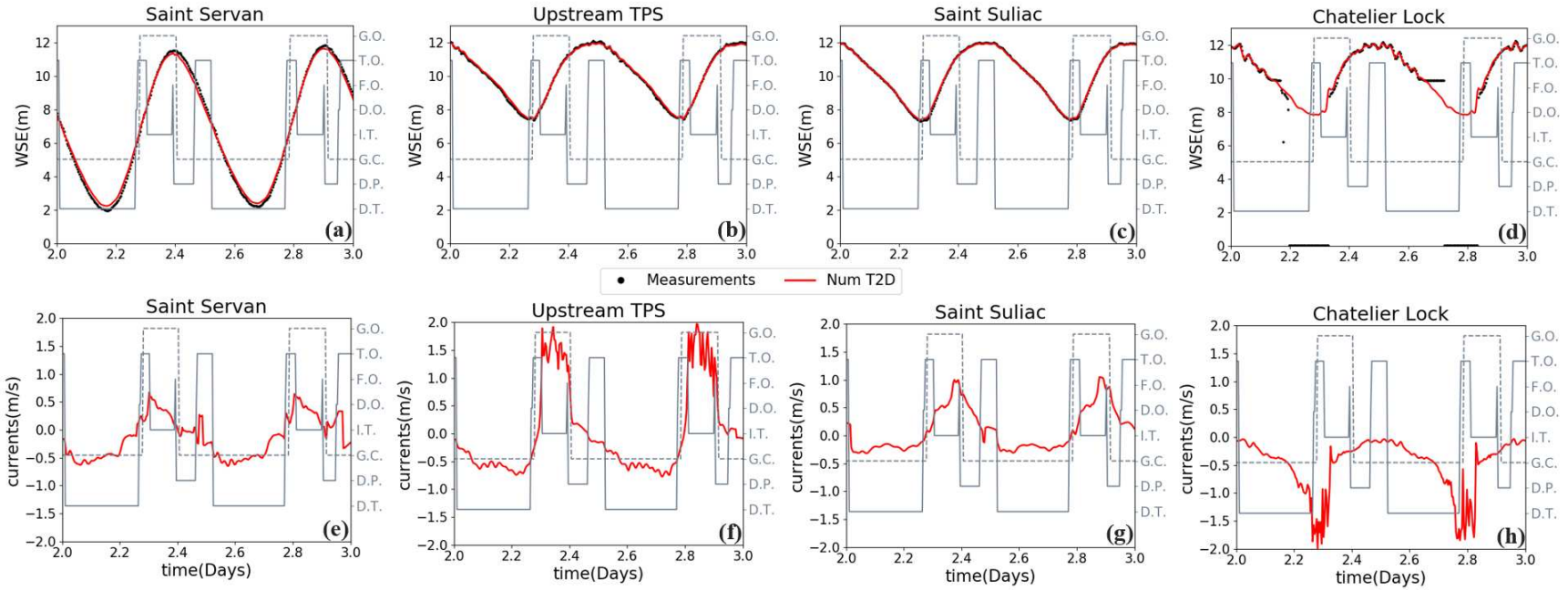

Figure 3.6: Hydrodynamic variables during spring tidal period: water surface elevation and currents respectively at locations (a;e) Saint Servan, (b;f) upstream of TPS, (c;g) Saint Suliac and (d;h) Chatelier Lock. Black dots and red lines indicate respectively measurements and numerical simulation. Gray solid- and dashed-lines represent operating modes of the TPS (see Table 6.2).

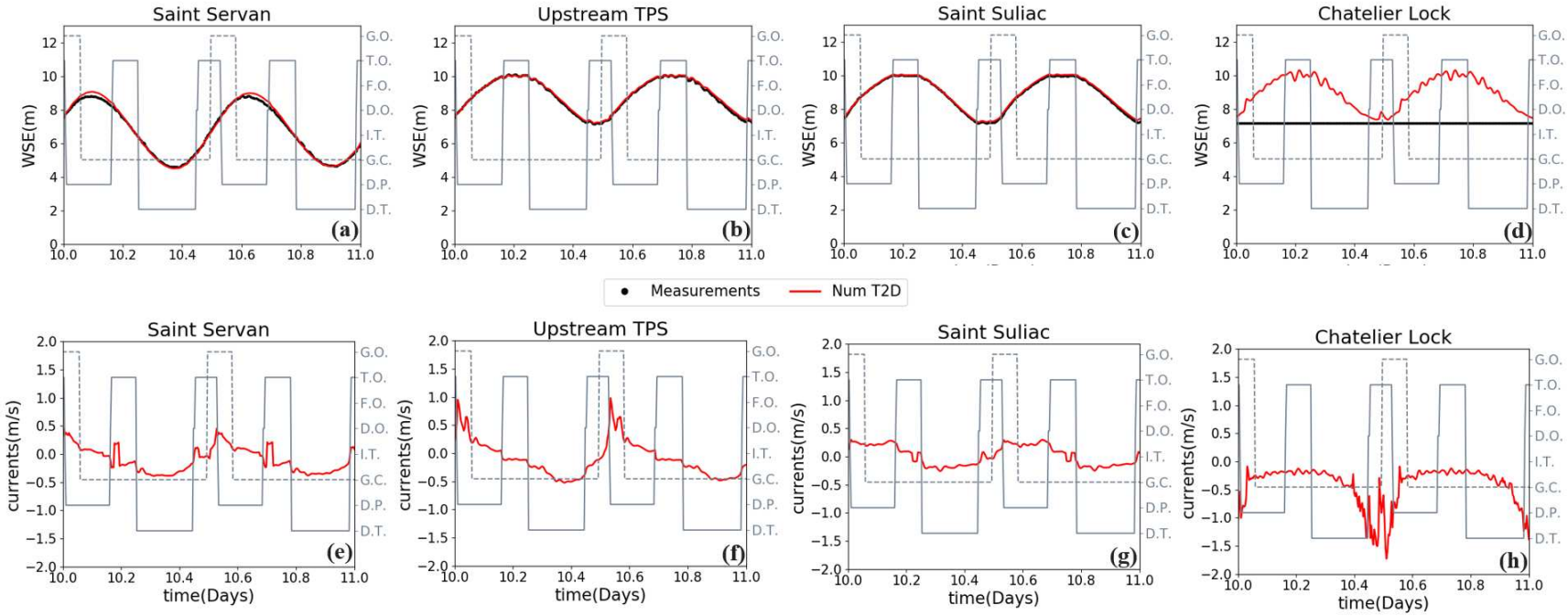

Figure 3.7: Hydrodynamic variables during neap tidal period: water surface elevation and currents respectively at locations (a;e) Saint Servan, (b;f) upstream of TPS, (c;g) Saint Suliac and (d;h) Chatelier Lock. Black dots and red lines indicate respectively measurements and numerical simulation. Gray solid- and dashed-lines represent operating modes of the TPS (see Table 6.2).

discharge at Chatelier lock), the same tidal condition (mean sea level and tidal amplitude and phase), and the same physical parameters. The scenarios were first analyzed in terms of hydrodynamic variables along the estuary's main channel. Then, tidal wave propagation and the spatial distribution of currents at neap and spring tide were discussed. Finally, asymmetry parameters were compared for the three configurations to quantify the tidal distortion caused by both artificial hydrodynamic forcing by the TPS and the estuary's morphology.

3.4.3.1 Hydrodynamic variables

Morphological changes in estuaries may have an important influence on hydrodynamic variables such as low, high, and mean water levels (LWL, HWL, MWL respectively) and tidal range. These quantities were compared along the estuary's channel at spring tide between the configurations without the TPS: C1 with the bathymetry for 1957 and C2 with the bathymetry for 2018 (Figures 3.8.a-b). Overall, bathymetry does not have a significant impact on the spatial distribution of water level indicators or on tidal range. However, it is noteworthy that the estuary could be split into two parts in which hydrodynamic variables behave differently. In the first zone, between Chatelier lock and Saint Hubert port ($\sim 6\ km$), the channel is partially uncovered at low tide but keeps the same level at high tide; thus the tidal range is variable and increases according to bottom depth. At spring tide, where differences between low and high tide are large, the limit of tidal range rise occurs approximately at the Saint Hubert port, in contrast to neap tide, where the limit is slightly ($\sim 2\ km$) upstream. In the second zone, from Saint Hubert port to the mouth ($\sim 17\ km$), the channel is always covered, at both neap and spring tides. Moreover, despite some local changes in the channel bottom between 1957 (before the dam construction) and 2018, for instance directly upstream of the TPS, the water level indicators and tidal range do not seem to be influenced. Furthermore, tidal range in this second zone is variable (variation of $\sim 0.5m$ at spring tide and $\sim 0.1m$ at neap tide), as it slightly decreases according to bed position.

As presented in section 3.4.2, values of LWL, HWL, MWL and tidal range are highly sensitive to dam operations. Comparison of these values for configurations C2 and C3 (respectively with and without the TPS, in Table 3.5) provides a deeper overview of the influence of the TPS on water level indicators (Figures 3.8.c-d). Downstream of the dam, the impact of the TPS on water levels and tidal range seems to be negligible, but is more significant upstream. In the last region, the plant amplifies the high-water level (continuous blue line in Figure 3.8.c) at neap tide by $\sim 10\%$ but maintains approximately the natural maximum level at spring tide. Thus, the dam does not necessarily influence the flooded areas. Low-water level (red line), is strongly increased by the TPS and kept constant along the basin. It nearly reaches the natural mean water level without the structure (green dashed line). Thus, the region between Chatelier lock and Saint Hubert port switches from being an intertidal zone in the configuration without the TPS (C2) to a permanently flooded zone in the configuration with the TPS (C3). In the current study, a mean spring tide cycle was chosen; hence the area between Saint Hubert port and the plant was continually submerged. This behavior might be influenced by the TPS, and especially the area directly downstream of Saint Hubert port (between $8km$ and $12km$ from the Chatelier lock), which may be naturally uncovered during an extreme spring tide but switched to a flooded zone by the plant. Therefore, the dam ensures the continuity and uniformity of water level at low tide along the estuary's channel for the purpose of maintaining navigation to the yacht harbor located upstream of the Chatelier lock. Moreover, mean water levels (green lines) at both spring and neap tidal periods are amplified by the presence of the plant. Furthermore, in the area upstream of the TPS, the difference in tidal range between configurations without and with the dam (Figures 3.8.b & 3.8.d) increases according to bed elevation, peaking at $\sim 5.25m$ at

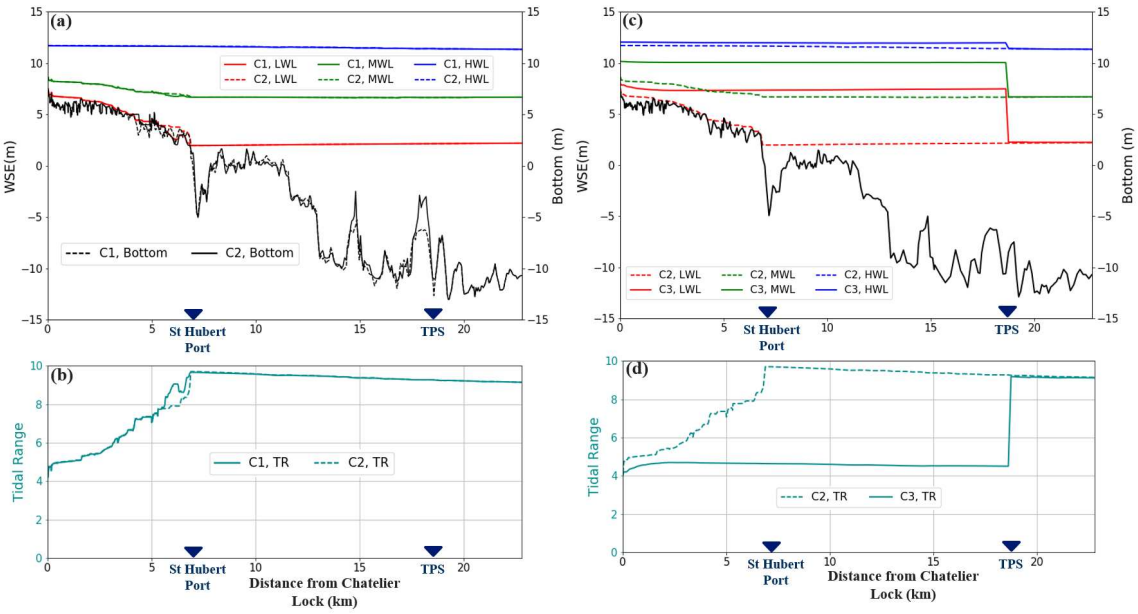

Figure 3.8: Spatial comparison of hydrodynamic parameters between configurations C1, C2 and C3 along the estuary channel at spring tide (see Figure 5.1 for channel location). (a;b) For low, mean, high water levels and tidal range respectively between configurations C1 and C2. (c;d) For low, mean, high water levels and tidal range respectively between configurations C2 and C3. Black dashed- and solid-lines indicate bed elevation in 1957 and 2018 respectively.

spring tide near Saint Hubert port. Thus, the dam reduces the tidal range by at least $\sim$ 13% at neap tide and at most $\sim$ 50% at spring tide.

3.4.3.2 Tide and current distributions and propagation

The construction of the tidal power station at the estuary's mouth induces a considerable decrease in tidal range, reducing water volume entering and exiting the basin. Also, the Rance dam operates in both one- and two-way generation modes. Therefore, maximum tidal current at both flood and ebb are potentially influenced by the TPS. It is interesting to compare maximum flood and ebb current distributions between scenarios with different bathymetries (C1 and C2 in Table 3.5), and configurations with and without the dam (C2 and C3 in Table 3.5), over a spring tide cycle (Figures 3.9.a-f).

Bathymetry does not seem to have a major impact on maximum flood current distribution (Figures 3.9.a;b). However, a slight amplification of maximum ebb current occurs in the main channel of the upper estuary from Ton Peak to Saint Servan (Figures 3.9.d;e). This amplification may be caused by the channel's morphological development over the past 52 years: construction of the TPS to 2018, the main channels upstream of the dam expanded slightly and deepened (Figure 3.2), allowing faster ebb-current propagation.

Scenarios with and without the TPS showed that the maximum flood current is amplified by the dam directly upstream of the sluice gates, but significantly reduced in the rest of the estuary (Figures 3.9.b;c). Maximum flood currents upstream of the sluice gates increased from $0.8m/s$ without the TPS to $1.75m/s$ with: *i.e.*, an amplification factor of $\sim$ 2.2. In other words, locally in

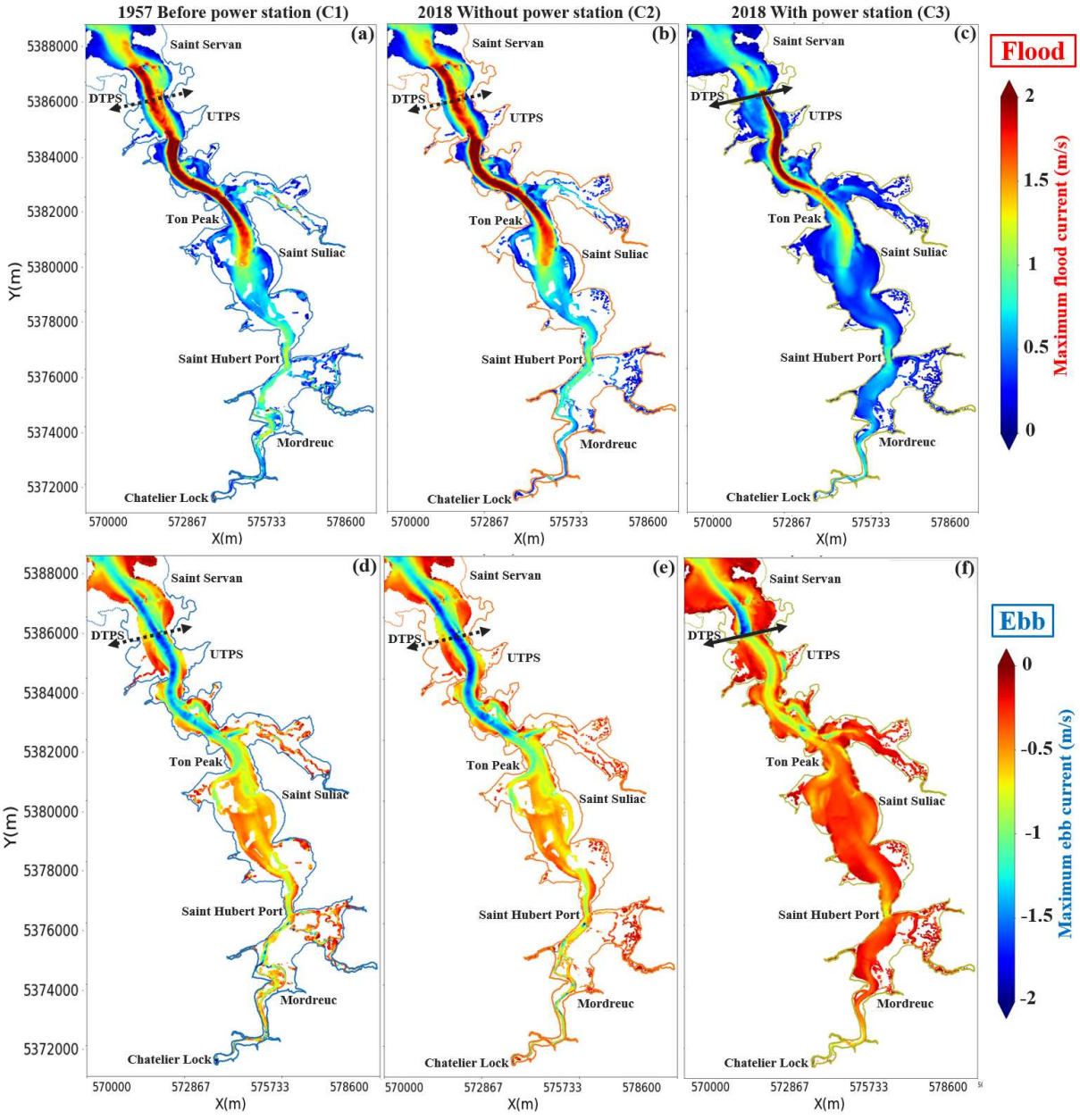

Figure 3.9: Spatial distribution of (a;b;c) maximum flood currents and (d;e;f) maximum ebb currents for the three studied scenarios respectively. Dry zones at ebb are blanked.

the region upstream of the dam, the main channel with maximum flood current is controlled by both the modified bathymetry and geometry, and the artificially-induced hydrodynamic forcing by the plant. Nevertheless, the maximum flood current is decreased in the rest of the estuary, from $1.75 m/s$ without the TPS to $1.25 m/s$ with: *i.e.*, reduction by a factor of ~ 0.7. The same behavior applies for maximum ebb-current: amplification by the TPS directly downstream of the turbines by a factor of ~ 3.1 and reduction in the rest of the estuary by a factor of ~ 0.4. Complementary comparisons of current differences between the three modeled scenarios are given in appendix B.2.

On the basis of the foregoing remarks, four locations (downstream of TPS, upstream of TPS, Ton peak and Saint Hubert port, Figure 5.1) were selected to further analyze the influence of dam operating modes on current distribution. The temporal evolution of water surface elevation and currents was analyzed for a mean spring tide on the three scenarios (C1, C2 and C3: Table 3.5, Figures 3.10.a-h). As expected, differences are negligible between configurations C1 and C2, with different bottom elevation levels (red and green dashed lines) on both water surface elevation and currents. Comparison between configurations C2 and C3, without and with the TPS (green dashed line and blue continuous line, respectively) showed that, while the dam does not modify water surface elevation downstream of the TPS (Figure 3.10.a), it distorts the currents. At this location, peak ebb current is equivalent to peak flood current in the absence of the TPS, while the presence of the TPS leads to a substantially higher peak ebb current than peak flood current. Also, maximum ebb current occurs during the D.T. phase of electricity generation by the turbines, with sluice gates closed. This explains the amplification of maximum ebb current by the TPS directly downstream of the turbines rather than downstream of the whole structure (cf. Figure 3.9.f). Furthermore, upstream of the TPS, peak ebb current is higher than peak flood current for the configuration without the dam, while the opposite is true for the configuration with the dam (green dashed line and blue line in Figure 3.10.f). Flood current is maximized by opening the sluice gates during flood (G.O. stage). This is explained on the one hand by the fact that the estuary is filled mostly via sluice gates rather than turbines, and on the other hand sluice gates width ($114 m$) is considerably smaller than turbines width ($323 m$). Since higher flow through a smaller section induces higher velocity, flood currents upstream of sluice gates are faster than upstream of turbines. Similarly, peak flood currents are significantly greater with the TPS than without. However, this amplification caused by the TPS is remarkably reduced further upstream (for instance, at Ton Peak and Saint Hubert port), as a result of the reduction in tidal range and hence in tidal prism (Figures 3.10.g;h). In addition, the difference in current magnitude between scenarios with and without TPS also decreases along the estuary, from $0.65 m/s$ at Ton Peak for maximum flood current ($0.4 m/s$ for maximum ebb current) to $0.25 m/s$ at Saint Hubert port for maximum flood current ($0.25 m/s$ for maximum ebb current). Moreover, a lag of approximately 2 hours is caused by the TPS for both water elevation and current on the estuary side of the dam. This time lag is related to the elongation of high- and low-water slack periods induced by the operating mode of the turbines to enable efficient electricity generation (see section 3.4.2). The high-tide slack period changes from 20 minutes for the scenario without the TPS to 1 hour 20 minutes for the scenario with TPS, although the difference is less significant for low-tide slack period. These analyses were carried out over a spring tide period, where the dam operates on two-way generation. Next, a similar analysis was performed over a neap tide period, where the plant is in one-way generation mode (Figures 3.11.a-h). Overall, the TPS induces a similar impact on water surface elevation and currents during neap and spring tide, except for a few details presented hereafter. On the estuary side of the dam (for instance, upstream of the TPS: Figure 3.11.b), there was no difference during flood between configurations

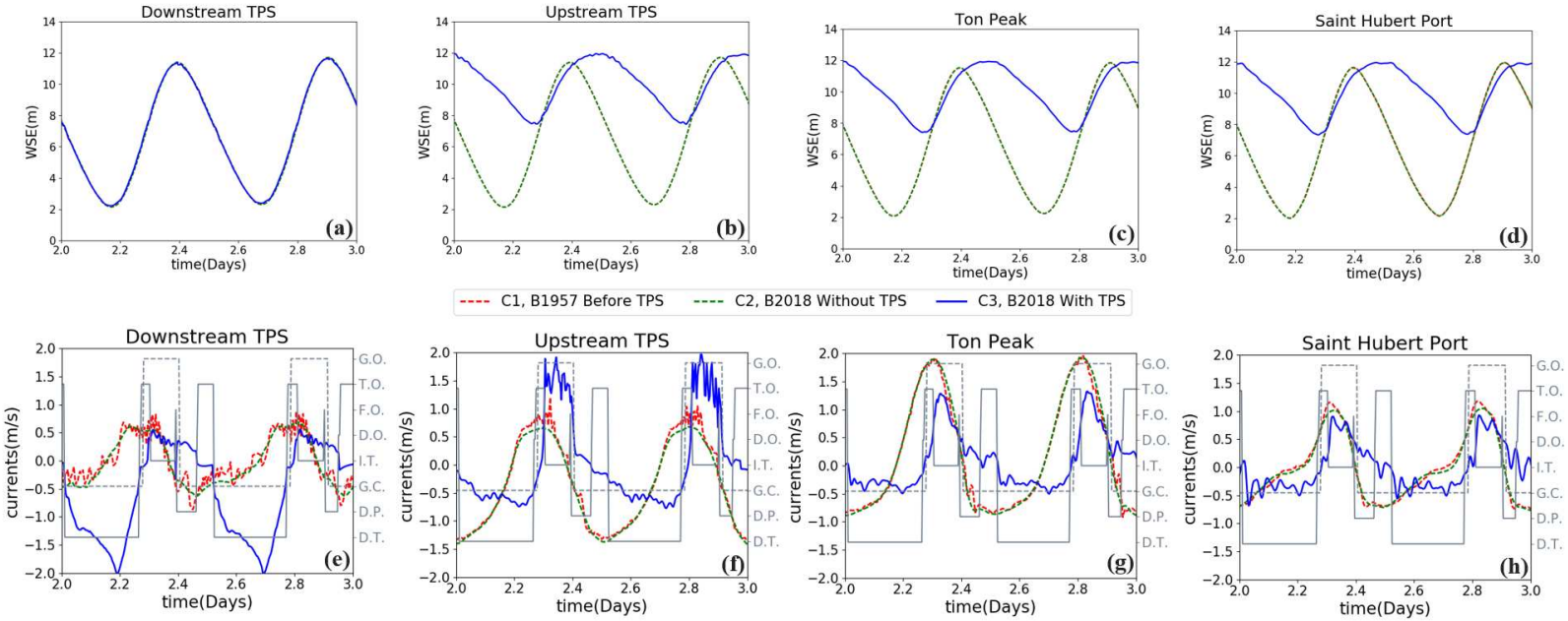

Figure 3.10: Hydrodynamic variables of the three scenarios during spring tidal period: water surface elevation and currents respectively at locations (a;e) downstream of TPS, (b;f) upstream of TPS, (c;g) Ton Peak and (d;h) Saint Hubert Port. Gray solid- and dashed-lines represent operating modes of the TPS (see Table 6.2).

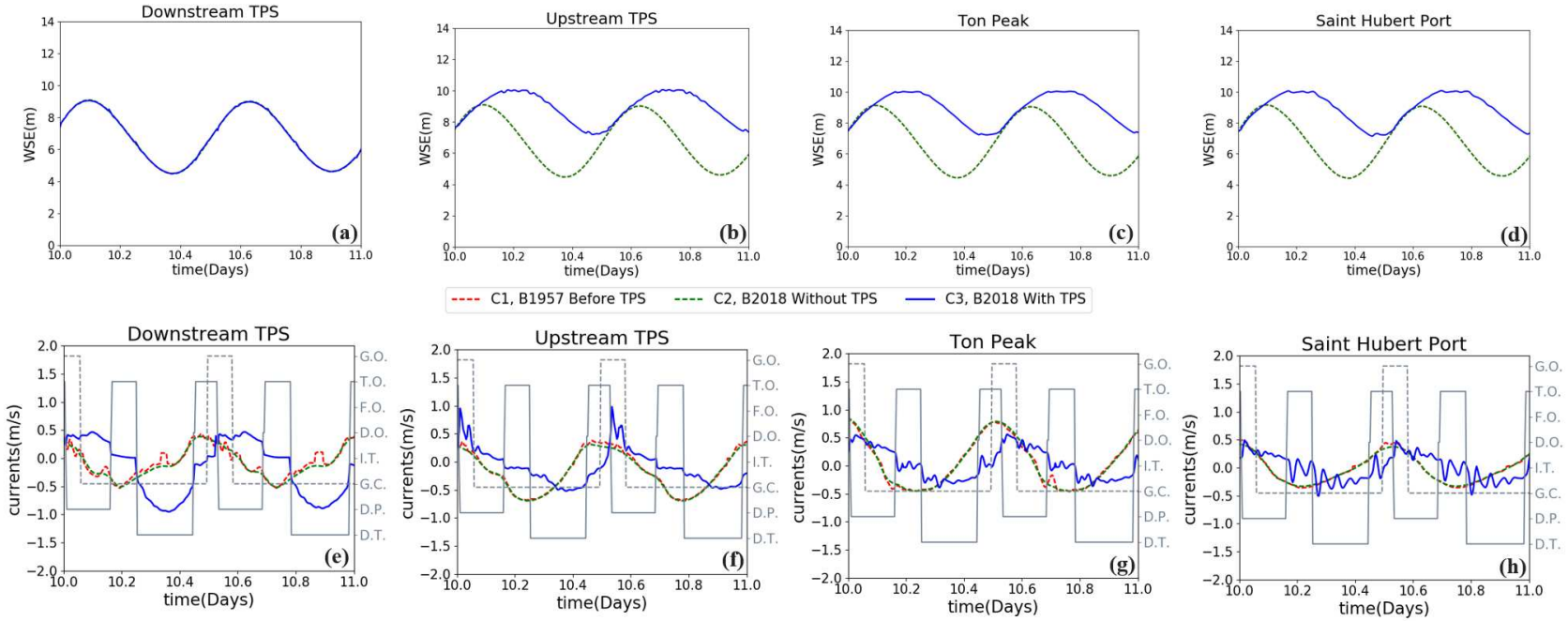

Figure 3.11: Hydrodynamic variables of the three scenarios during neap tidal period: water surface elevation and currents respectively at locations (a;e) downstream of TPS, (b;f) upstream of TPS, (c;g) Ton Peak and (d;h) Saint Hubert Port. Gray solid- and dashed-lines represent operating modes of the TPS (see Table 6.2).

without (green dashed line) and with the TPS (blue continuous line), unlike during the spring tidal cycle (Figure 3.10.b). Thus, at neap tide the plant could operate only on one-way generation, which means electricity is generated only during ebb (D.T. stage) and not during flood as is the case during spring tide. Moreover, to ensure a sufficient water head between the basin and downstream sea level, the D.P. phase is longer during neap than spring tide, resulting in a high tide that is greater than the natural high tide (configuration C2 without TPS). Furthermore, peak flood current upstream of TPS (Figure 3.11.f) for the configuration with TPS (C3) occurs at the junction between the D.P. phase of the turbines and the G.O. phase of the sluice gates (Table 6.2) and not during an electricity production phase (D.T. or I.T.) as is the case at spring tide.

To complement tidal current analysis, investigations were conducted on the temporal evolution of flowrate across the section upstream of the TPS (Figure 5.1) and on tidal prism during a neap-spring tide period for the three simulated scenarios (Figures 3.12a-d). Over the fortnight period, the TPS reduces discharge both entering (flood) and exiting (ebb) the estuary. Particularly, at spring tide (Figure3.12.b) maximum flood discharge (ebb discharge) decreases from 10,600m^3/s ($-$7,500m^3/s at ebb) without the TPS to 7,000m^3/s ($-$5,000m^3/s at ebb) with the TPS: *i.e.*, a reduction of 34% (33% at ebb). At the neap tide (Figure3.12.c), the decrease induced by the dam is slightly less: at most 25% at flood and 22% at ebb. It should be borne in mind that the estuary is filled mostly via the sluice gates at spring tide, whereas at neap tide the contributions of sluice gates and turbines are equivalent. Moreover, bathymetry did not seem to have a significant influence on tidal prism (red and green lines in Figure 3.12.d). However, the presence of the dam (blue line) induces a major decrease in tidal prism, from 1.22×10^8 m^3 without the structure over spring tide (0.6×10^8 m^3 over neap tide) to 0.8×10^8 m^3 with (0.4×10^8 m^3 over neap tide). To evaluate flushing rate in the estuary, tidal prism needs to be compared to the volume of water contained in the basin at high tide, estimated at 1.84×10^8 m^3. Thus, tidal prism accounts for 66% without the TPS at spring tide (33% at neap tide) versus 43% with the TPS at spring tide (22% at neap tide). Theoretical mean residence times in the estuary for scenarios without and with the dam showed that the presence of the TPS could multiply the natural water residence time by a factor of 1.52 at most. Therefore, the presence of the plant causes a lower flushing rate and longer water residence time.

3.4.3.3 Tide asymmetry parameters

To quantify the distortion and asymmetry of the tidal signal as it crosses the dam and propagates along the basin, two complementary approaches were applied in the three scenarios: C1 configuration from 1957 before TPS construction, C2 configuration of 2018 without the TPS, and C3 configuration of 2018 with the TPS (Table 3.5).

The first approach focuses on tidal velocity and duration skewness [Nidzieko and Ralston, 2012]. These parameters ($\gamma_0(u)$;$\gamma_0(\frac{\partial \zeta}{\partial t})$) were computed as the median over a neap-spring tidal period to analyze their spatial distributions in the three scenarios (Figures 3.13.a-f). Despite the presence of the dam and the morphological evolution in the Rance estuary, tide is flood-dominant in the main channel and ebb-dominant in the secondary channels (Figures 3.13.a-c). The presence of the power plant slightly decreases the flood-dominance by $5-7\%$ throughout the estuary. Nevertheless, local impacts of the plant on maximum flood and ebb currents (Figures 3.6; 3.7 & 3.9;) also appears in the spatial distribution of velocity skew near the plant: (i) upstream of the sluice gate, the tide is switched from ebb-dominant without the TPS to flood-dominant with, (ii) downstream of the turbines, the tide is switched from flood-dominant without the dam to ebb-dominant with. Complementary comparisons of velocity skew ratios are given in

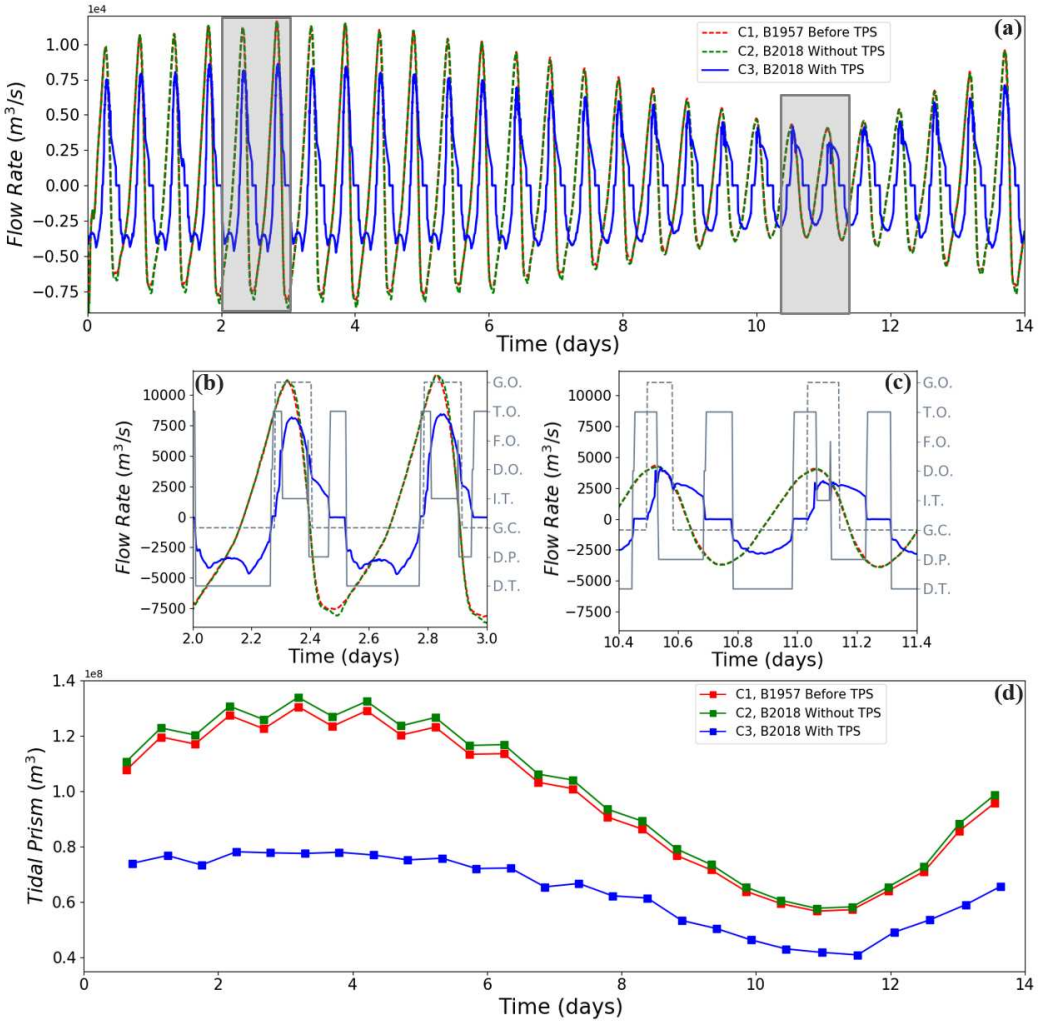

Figure 3.12: Temporal evolution at TPS section of (a) flowrate during a fortnight period, (b) zoom on flowrate during spring tide (two-way generation mode), (c) zoom on flowrate during neap tide (one-way generation mode) and (d) tidal prism for the three scenarios. (see Figure 5.1 for section location).

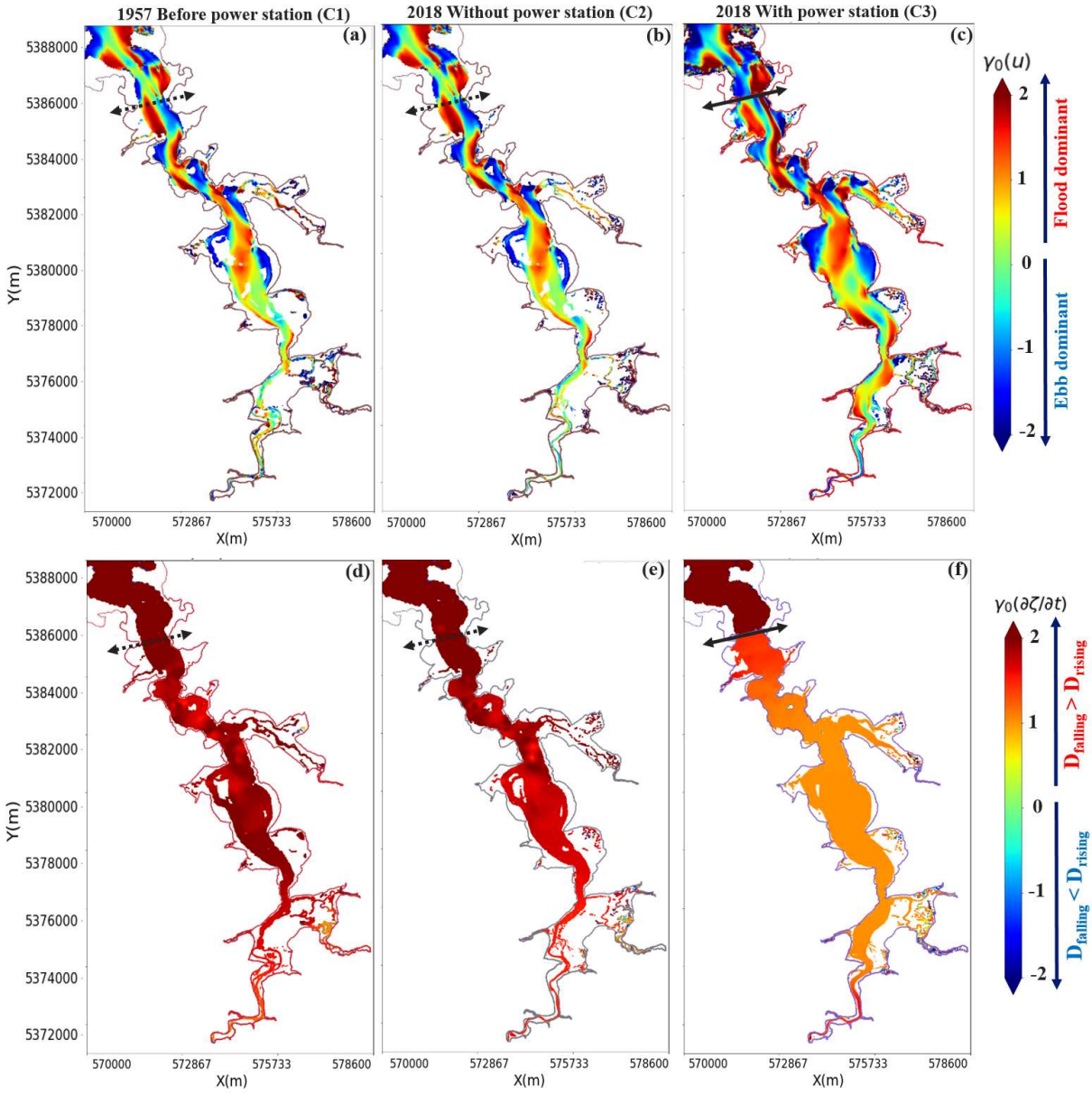

Figure 3.13: Spatial distribution of (a;b;c) velocity skewness parameter $\gamma_0(u)$ and (d;e;f) tidal duration asymmetry parameter $\gamma_0(\frac{\partial \zeta}{\partial t})$ for the three scenarios respectively. Dry zones at ebb are blanked.

appendix B.2. Furthermore, in the Rance estuary, with and without the TPS, duration is always longer for falling than rising water. As expected, bathymetry does not induce any significant changes in duration skew. Likewise, the plant does not influence tidal duration asymmetry downstream of the TPS, as seen previously in Figures 3.6.a & 3.7.a. Although upstream of the TPS the magnitude of this typical skew is substantially decreased by the TPS, it still maintains the same trend. This behavior could be related to the operating modes of the plant, which tend to extend high tide and low tide slack periods, so that the temporal variation in water surface elevation $\frac{\partial \zeta}{\partial t}$ is equal to zero over this period, in turn decreasing duration asymmetry (cf. Figures 3.6.b-d & 3.7.b-d).
The second approach quantifies tidal asymmetry through harmonic analysis using the amplitude ratio $\alpha = a_{M_4}/a_{M_2}$ and phase difference $\beta = (2\phi_{M_2} - \phi_{M_4})$ [Friedrichs and Aubrey, 1988]. This method is suitable for the present case study, as the Rance estuary is a system dominated by the M2 semidiurnal tide [Bauer, 1993]. Asymmetry metrics derived from harmonic analysis of both water surface elevation $(\alpha_\zeta; \beta_\zeta)$ and currents $(\alpha_u; \beta_u)$ were computed over the spring-neap tidal period using the T-TIDE toolbox [Pawlowicz et al., 2002], for the three configurations at six locations: Saint Servan, downstream of TPS, upstream of TPS, Ton peak, Saint Hubert port and Chatelier lock (see Figure 5.1 for locations and Table 3.6 for asymmetry metrics). As expected, bathymetry does not have any significant impact on these tidal distortion parameters. For configurations without the TPS (C1 & C2), tide is hardly distorted along the estuary, with α_ζ between 0.048 and 0.05. Moreover, the presence of the plant does not affect asymmetry metrics related to water surface elevation $(\alpha_\zeta; \beta_\zeta)$ for stations on the sea side of the dam (Saint Servan and downstream of TPS). However, phase difference related to currents (β_u) in this zone is modified from 352° without the TPS to 171° with. Hence, location downstream of the TPS switches from flood dominant ($0° < \beta_u < 90°$ or $270° < \beta_u < 360°$) to ebb dominant ($90° < \beta_u < 270°$) [Friedrichs and Aubrey, 1988]. Upstream of the TPS, the presence of the dam modifies the tide from ebb dominant with $\beta_u = 173°$ without the plant to $\beta_u = 355°$ with. Furthermore, Table 3.6 indicates that the dam induces a substantial decrease in both amplitude ratios α_ζ and α_u by $\sim 70\%$ in the basin side of the plant, but does not modify the flood-dominance behavior of the estuary, except locally near the TPS. These findings are in agreement with the analysis based on Nidzieko and Ralston's parameters [Nidzieko and Ralston, 2012].

3.5 Discussion

Investigations carried out based on comparison of hydrodynamic and asymmetry parameters between three scenarios with different DEMs and with presence/absence of the TPS, helped to evaluate the impact of the plant on hydrodynamics in the Rance estuary. It was shown that high tide is slightly increased by the presence of the dam in the estuary side of the plant (Figures 3.5 & 3.12). However, this amplification occurs specifically at neap tide. At present, maximum water level upstream of the plant is limited to 12 m [Caude et al., 2017]: *i.e.*, although during an extreme spring tide where maximum high-water level seaward is above 12 m, the high tide inside the estuary will not exceed 12 m. Hence, the plant effectively protects the estuary from storms and risk of marine flooding. This was also seen in studies of other tidal power plant projects: *e.g.*, the Sihwa Lake TPS [Young et al., 2010], the Severn dam, the Flemming Lagoon, the Shoots dam [Xia et al., 2010] and others [Neil et al., 2018]. The plant's impact on low tide, however, is more significant. The higher low-water level in the configuration including the TPS (Figures 3.5 & 3.12) modifies a large part of the intertidal areas in the basin (present in the scenario without the TPS), which are permanently submerged: *e.g.*, the area between Chatelier

Table 3.6: Asymmetry metrics derived from the harmonic analysis of water surface elevation (ζ) and current (u) at six selected positions along the estuary (Figure 5.1 for locations) for the three modeling scenarios (Table 3.5). All results were obtained with the T-TIDE toolbox [Pawlowicz et al., 2002].

Scenarios	C1, B1957 Before TPS				C2, B2018 Without TPS				C3, B2018 With TPS			
Variables	WSE		Current		WSE		Current		WSE		Current	
Locations	$\alpha_\zeta(-)$	$\beta_\zeta(°)$	$\alpha_u(-)$	$\beta_u(°)$	$\alpha_\zeta(-)$	$\beta_\zeta(°)$	$\alpha_u(-)$	$\beta_u(°)$	$\alpha_\zeta(-)$	$\beta_\zeta(°)$	$\alpha_u(-)$	$\beta_u(°)$
Saint Servan	0.048	82	0.1	23	0.049	82	0.1	24	0.05	83	0.1	14
Downstream of TPS	0.05	106	0.09	350	0.05	107	0.092	352	0.047	110	0.093	171
Upstream of TPS	0.051	85	0.096	175	0.05	85	0.1	173	0.013	175	0.024	355
Ton Peak	0.05	90	0.098	50	0.05	90	0.096	48	0.015	171	0.028	290
Saint Hubert Port	0.05	126	0.1	281	0.05	128	0.098	285	0.012	170	0.021	287
Chatelier Lock	0.08	88	0.15	197	0.07	87	0.14	196	0.017	169	0.031	157

lock and Saint Hubert port. This could be directly related to the evolution of the estuary's ecosystems. Kirby and Retière [2009] discussed the post-closure environmental effects of the Rance dam and measurements demonstrated that an increase in permanent subtidal area leads to changes in the estuary's ecosystem, with richer biodiversity, increased habitat variety, greater abundance of fish species and greater variety and density for birdlife. Moreover, higher low tide allows navigation to the yacht harbor next to the Chatelier Lock during ebb. As the tide passes through the dam and propagates along the estuary, it becomes more distorted and more asymmetric. This effect has both natural and artificial origins, due to the estuary's morphology and to hydrodynamic forcing by the plant. Simultaneously analyzing tide propagation (Figures 3.10 & 3.11), skewness parameters (Figure 3.13) and asymmetry (Table 3.6), shows the area near the dam ($\sim$ 1.5km upstream and $\sim$ 0.5km downstream) to be highly sensitive to the presence of the TPS. Amplification of flood current upstream of the sluice gate can cause local bed scouring, which may explain the high erosion rate seen in the same area in Figure 3.2. Furthermore, with and without the dam, the Rance estuary is mainly flood-dominant with longer duration of falling than rising water and stronger peak flood current than peak ebb current [Nidzieko and Ralston, 2012; Friedrichs and Aubrey, 1988; Aubrey and Speer, 1985; Speer and Aubrey, 1985]. All this enhances the tendency of residual sediment transport to be in the landward direction: *i.e.,* sediments are carried from the coast toward the estuary [McLachlan et al., 2020]. It noteworthy that similar behavior is observed before TPS construction, as confirmed by the C1 results presented in Figure 3.13. Thus, the plant does not impact the source of sediments present inside the basin. These results are in agreement with measurements performed 15 years after TPS construction, showing that more than 90% of the Rance estuary's sediments came from the sea [LCHF, 1982; Bonnot-Courtois et al., 2002; Thiebot, 2008]. In addition, flow velocity away from the TPS zone is substantially lowered by the presence of the dam. This may significantly reduce in the suspended sediment concentrations and thus impact the dynamics of the estuarine turbidity maximum (ETM). Furthermore, prolonging high- and low-water slack periods, due to the presence of the power plant, may impact tidal transport of fine sediment with consequences for the settling, re-suspension and diffusion of fine particles in the water column [Dronkers, 2005]. However, these interpretations need to be analyzed closely with respect to local conditions of sediment bed composition, since the suspended load carried in the seawater is related to tidal current magnitude if the bed includes unconsolidated sediments [Van Rijn, 1984; Falconer and Chen, 1991]. Therefore, the impact of the dam on sedimentation needs further investigation. Furthermore, analysis of tidal prism and flowrate passing through the TPS (Figure 3.12) showed that the plant significantly reduced flushing rates and hence increases the resident time of water containing suspended sediments and pollutants. This was also reported in other tidal power plant projects [Young et al., 2010; Xia et al., 2010; Cornett et al., 2013]. On the other hand, since a greater volume of sediment enters from the sea, reducing the water volume flowing into the estuary during flood might reduce the amount of sediment entering the basin. These interpretations need to be supported by complementary sediment transport simulations or *in-situ* observations.

3.6 Conclusions

This study presents a detailed analysis of the hydrodynamics of the Rance estuary, influenced by the world's second largest tidal power station. This closed-estuary type exhibits an original configuration due to (i) the presence of the Chatelier lock upstream of the basin and the tidal power station downstream and (ii) the plant's hybrid tidal energy schemes of ebb-generation

and ebb-flood generation. A two-dimensional depth averaged model of the Rance estuary was developed and successfully validated against water level observations and velocity field measurements for many tidal stations throughout the estuary. The model was then applied to simulate the tidally-driven hydrodynamic processes for the present-day conditions of the Rance estuary and two other scenarios featuring: 1) an artificial condition of the estuary without the dam and 2) the historic conditions of the basin (in 1957), before the dam's construction. Then, the simulations were analyzed in terms of basic flow characteristics and tide asymmetry parameters. Numerical results indicated that, in the absence of the TPS, bathymetry does not have any significant impact on hydrodynamics. However, the presence of the dam substantially modifies tidal patterns. The main consequences of the presence of the dam at the estuary mouth can be summarized as follows. (i) A major decrease in tidal range and tidal prism along with the amplification of the estuary's low-water level switches a large part of intertidal zones, which become permanently submerged, which seems to help the estuary's ecosystem. (ii) A limitation of the high-water level inside the estuary up to 12m protects the basin against marine flooding. (iii) There is an overall decrease in tidal currents in the estuary, except upstream of the sluice gates and downstream of the turbines. (iv) Flood currents and ebb currents are locally amplified upstream of the sluice gates and downstream of the turbines respectively. The study also revealed that the Rance estuary, with and without the TPS, is flood-dominant, with a shorter duration of rising than falling water. These findings suggest that sediment transport tends to be in the landward direction: *i.e.*, the plant does not impact the source of sediment present inside the basin. Finally, the study highlights the need to couple hydrodynamics to sediment transport processes to further quantify the impact of the dam on sediment dynamics and morphological changes in the Rance estuary. The effect of sea level rise, estimated to be $\sim$ 10cm between 1957 and 2019 [SHOM, 2020], could also be evaluated to have a more consistent overview of the long term evolution of this particular estuarine system.

Acknowledgments

The authors are grateful to Christophe Cochet and Malo Lambert for providing the preliminary version of the model used in this work. Antoine Libaux, Marion Duclercq and Florian Boucard are warmly acknowledged for supplying data from the AGRA Software and feedback on the tidal power station operating modes. We would like to acknowledge Chi-Tuân Pham and Sébastien Bourban for giving advice on the tidal model's validation. Finally, we thank the three reviewers, whose comments and suggestions helped improve and clarify this manuscript.

Notation

Q_{river}	=	River flow rate (m^3/s);
$Q_{turbines}$	=	Flow rate passing through turbines (m^3/s);
$Q_{sluices}$	=	Flow rate passing through sluice gates (m^3/s);
A, C	=	Discharge coefficients ($m^{5/2}/s$);
B	=	Discharge coefficient ($m^{9/4}/s$);
$Q_{\sum_{TPS}}$	=	Flow rate passing through section upstream of the TPS(m^3/s);
ζ, WSE	=	Water surface elevation (m);
T_r	=	Mean Residence Time (s);
V	=	Mean volume of water in the system (m^3);
T	=	Tidal period (s);
b	=	Return flow factor (-);
TP	=	Tidal Prism (m^3);
μ_m	=	The m-th moment about zero ($(m/s)^m$);
$\gamma_0(u)$	=	Tidal current asymmetry (-);
$\gamma_0(\frac{\partial \zeta}{\partial t})$	=	Tidal duration asymmetry (-);
$a_{M_2}(\zeta)$	=	M2 amplitude of water surface elevation (m);
$a_{M_4}(\zeta)$	=	M4 amplitude of water surface elevation (m);
$a_{M_2}(u)$	=	M2 amplitude of current (m/s);
$a_{M_4}(u)$	=	M4 amplitude of current (m/s);
α_ζ	=	Surface amplitude ratio (-);
α_u	=	Current amplitude ratio (-);
$\phi_{M_2}(\zeta)$	=	M2 phase of water surface elevation (°);
$\phi_{M_4}(\zeta)$	=	M4 phase of water surface elevation (°);
$\phi_{M_2}(u)$	=	M2 phase of current (°);
$\phi_{M_4}(u)$	=	M4 phase of current (°);
β_ζ	=	Surface phase difference (°);
β_u	=	Current phase difference (°);

CHAPTER 4

FURTHER INSIGHT INTO HYDRODYNAMICS PROCESSES IN THE RANCE ESTUARY

The work presented in this chapter has been published in
Hydroscience Journal - La Houille Blanche on 27th January 2022, entitled
Three-dimensional hydrodynamic model of the Rance estuary (France) influenced by the world's second largest tidal power plant

by
Rajae Rtimi[a,b], Aldo Sottolichio[b], Pablo Tassi[a,c], Christine Bertier[a], Matthieu Le Brun[a], Marine Vandenhove[b] and Luca Parquet[a]

[a] Electricité de France, Research and Development Departement (EDF R&D), Chatou, France
[b] EPOC Laboratory CNRS, University of Bordeaux, Pessac, France
[c] Saint-Venant Hydraulics Laboratory, Chatou, France

▷ Objectives of this chapter

This chapter focuses on the three-dimensional (3D) aspects of the flow field distribution along the horizontal and vertical directions, as well as the impact of the plant on the dynamics of the freshwater-saltwater interface. Therefore, this chapter addresses the 3D hydrodynamics-related topic of the research questions formulated in Chapter 1:

- *How relevant are 2D and 3D numerical models at reproducing the main features of hydro-sedimentary dynamics observed in macrotidal estuaries influenced by the presence of a tidal power station?*
- *How hydrodynamics, sediment transport and morphodynamics processes are influenced by the presence of the world's second-largest tidal power station?*

Highlights

- The implemented 3D hydrodynamic model reproduces satisfactorily temporal and spatial distribution of currents inside the Rance basin.
- The estuary's morphology plays an important role on currents distribution and direction, particularly at the narrowing of Saint-Hubert-Port.
- The plant pushes the freshwater-saltwater interface roughly 5km upstream in the estuary. This position is also sensitive to seasonal river discharge variation.

Abstract

The Rance estuary is a small steep-sided *ria*, located in the Brittany coast of northern France,with a maximum perigean spring tidal range of 13.5m and an average river discharge of 7m^3/s. Taking advantage of this significant tidal range, the Rance tidal power station (RTPS) was built in the 1960s as the world's first and largest tidal power plant, with peak output capacity of 240Megawatts. It is currently the second world's largest tidal power installation after the Sihwa Lake tidal barrage (South Korea). The Rance TPS is 750m long with two active parts: (i) a barrage of 6 sluice gates and (ii) a structure of 24 bulb turbines. Despite a well-known effect of the plant on the damping of estuarine water levels, little attention has been given to currents vertical distribution and the impact of the plant on the dynamics of the freshwater-salt water interface. To this goal, a three-dimensional (3D) model of the Rance estuary has been developed in the TELEMAC-MASCARET modelling system. Moreover, Acoustic Doppler Current Profiler (ADCP) and continuous salinity measurements were carried out to validate the numerical model. Simulated and measured currents showed that (i) the presence of the RTPS induces an acceleration of flood currents directly upstream of the sluice gates and (ii) ebb currents are strengthened by the narrowness of the Saint-Hubert-Port. Finally, simulated and measured salinity assessed the dynamics of the freshwater-saltwater interface which is shifted to 2km from the Chatelier Lock during summer.
Keywords: Numerical modelling, tidal power station, estuarine hydrodynamics, salinity.

4.1 Introduction

Estuaries are transitional water bodies found in continuously changing dynamic systems, dominated by cyclically tidal forcing, inputs of freshwater, and other natural constraints. Hydrodynamic and morphological attributes observed in estuaries strongly depend on these driving forces, which in turn might be influenced by the combined effect of multiple human pressures. The presence of a dam built across the estuary's mouth and/or a lock regulating the natural freshwater discharge can have considerable effects on the natural variability and equilibrium of these systems [Kim et al., 2017]. In consequence, static features such as estuarine mean water level as well as dynamic processes such as tidal wave propagation and distortion are expected to be affected as a result of the human pressure on the semi-enclosed body of water [Angeloudis and Falconer, 2017].

Owing to the region's hyper-tidal regime and its narrow and confined characteristics, the Rance estuary, located in Brittany, France, hosts the Rance Tidal Power Station (RTPS). Opened in 1966, this large-scale tidal power plant was for 45 years the largest marine energy facility in the world by its installed capacity, surpassed in 2011 by the South Korean Sihwa Lake Tidal Power station. Currently operated by Electricité de France, the dam is 750 m long, with a power plant portion equal to 332.5 m housing 24 bulb turbines [Charlier, 2007]. By reaching a peak output of 240 megawatts (MW) and average 57 MW, the RTPS supplies 0.12% of the power demand of France, which is the averaged electric energy consumption equivalent to a medium-size city like Rennes, with a population of approx. 360,000 inhabitants in the urban area.

To better understand the influence of the RTPS on the hydrodynamics and its consequences on sediment dynamics and morphological changes, Rtimi et al. [2021a] (Chapter 3) studied flow patterns and tidal asymmetry for diverse scenarios involving past and present bed elevations, the presence/absence of the dam and the existence of a lock at the estuary's upper limit. The

two-dimensional (2D), depth-averaged numerical model implemented by Rtimi et al. [2021a] (Chapter 3) provided detailed analysis on the flood-dominant characteristics of the estuary's dynamics for both spring and neap tides. Nevertheless, the understanding of the flow through the water body, and the effect of the functioning of the sluice gates and turbines of the RTPS, did not account for three-dimensional (3D) processes. The comprehension of three-dimensional hydrodynamic processes is important for a better prediction of the water circulation, salinity distribution and velocity gradients within the body of water. These hydrodynamic processes influence, for example, the concentration of suspended particulate matter and therefore, the estuarine turbidity maximum [Amoudry et al., 2014; Burchard et al., 2018; Hesse et al., 2019]. Due to the natural and anthropogenic-influenced variability of the Rance estuary, these processes are crucial for accurate sediment transport and morphodynamic predictions and may have profound implications on the estuarine ecosystem [Bonnot-Courtois et al., 2002; Kirby and Retière, 2009].
In this work, a 3D Reynolds-averaged Navier-Stokes model of the Rance estuary is implemented. This model accounts for the influence of the RTPS and solves the flow velocity and water salinity fields. It is calibrated and validated with a set of continuous recording probes and high-resolution field survey campaigns over a 10 days period. The 3D flow field and salinity distribution are validated with datasets collected from Acoustic Doppler Current Profiler, STPS and SAMBAT probes, respectively. Field surveys and probes data, in combination with 3D model results, allowed to better understand (a) the complex flow behavior at specific zones of the Rance estuary; and (b) the mixing processes and salinity distribution within this particular body of water regulated by the presence of the RTPS at the estuary's mouth and a lock at its upper limit.

4.2 Material and methods

4.2.1 Site description

The Rance estuary is a small steep-sided ria [Evans and Prego, 2003] located on the Brittany coast of northern France. It is 20 km long and has variable irregular width, with a maximum value of $2km$ at $10km$ upstream from the mouth. Its maximum spring tidal range reaches $13.5m$ at the mouth. Taking advantage of this hyper-tidal regime, the first ever tidal power station in the world was built at $3km$ from the estuary mouth (Figure 4.1). The plant has been in operation and managed by Electricité De France (EDF) since 1966 and is currently the second largest operational tidal power station in the world [Pelc and Fujita, 2002]. The head of the estuary is located at the Chatelier Lock, which delimits the upstream limit of tide propagation. The Rance river drains a small catchment area, with an average river discharge of $7m^3/s$, low water flow rate of $0.5m^3/s$ and a decennial flood of $80m^3/s$.

4.2.2 Field measurements

4.2.2.1 Currents

Surveys of current velocities were conducted at four locations along the estuary, on 14^{th}, 15^{th} and 21^{st} October 2020. At each location, horizontal current velocities were collected through cross-sectional transects with a vessel-towed $1200kHz$ RDI Workhorse Acoustic Doppler Current Profiler (ADCP) in $0.25m$ bins. At locations of transects 1, 2 and 3 (Figure 4.1), currents were collected throughout a semidiurnal tidal cycle (12.42 h), with a total of 30 full transects being

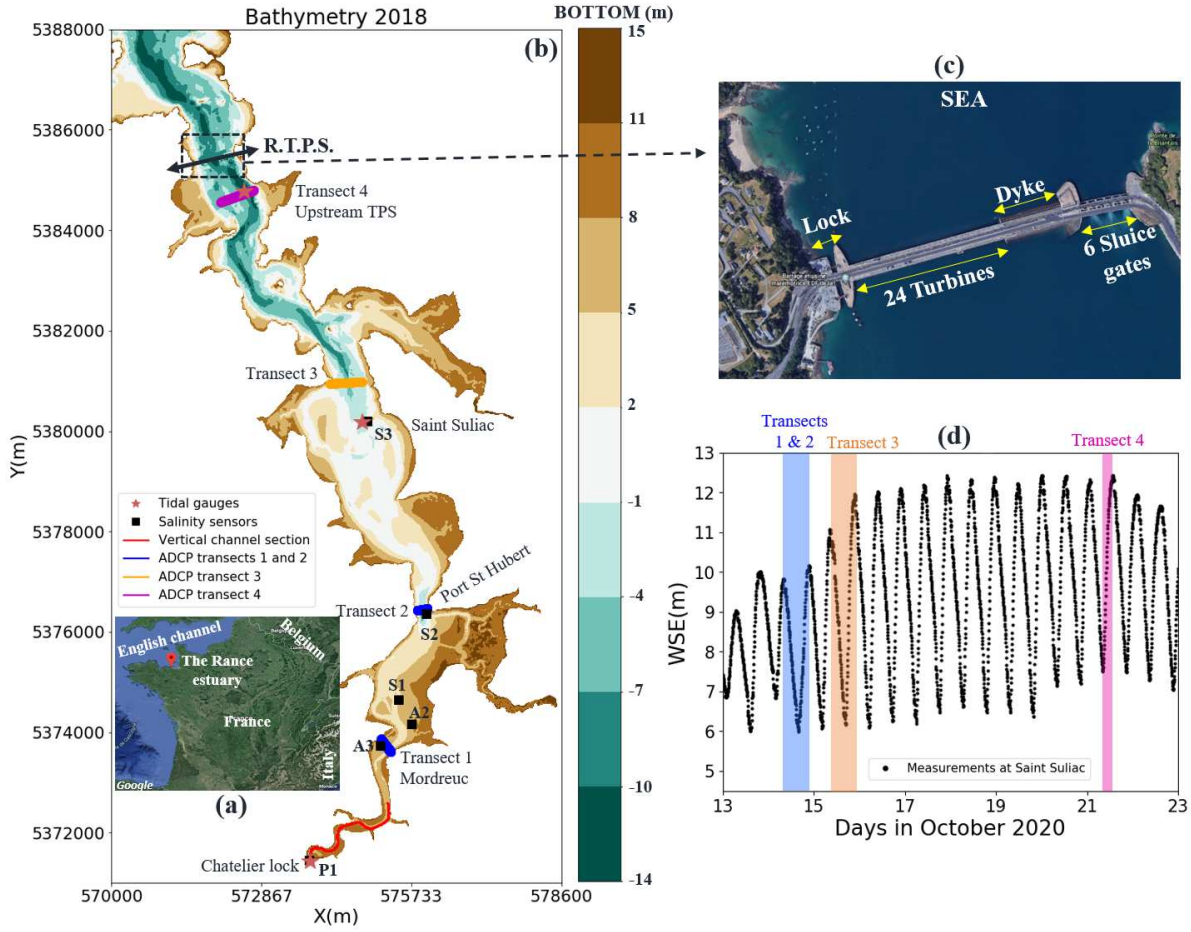

Figure 4.1: The Rance estuary: (a) map location, (b) bathymetry of 2018 with locations of tidal gauges, salinity sensors and ADCP transects, (c) zoom on the constituents of the Rance Tidal Power Station (RTPS) and (d) measured water level at Saint-Suliac over a 10 days period during October 2020. Blue, orange and magenta rectangles in Figure (d) indicate period measurements at transects (1,2), 3 and 4 respectively.

completed at each location. At transect 4, close to the RTPS, measurements were limited to a period of 3 hours during flood tidal stage and 10 full transects were completed. For each completed transect, measurements were then averaged over 20 ensembles to reduce noise.

4.2.2.2 Salinity

Salinity data used in this study was obtained through continuous measurements collected at six stations along the estuary from June 2019 to December 2020 (Figure 4.1). At stations P1, A2 and A3, a STPS probe by NKE was deployed at fixed height above the bottom. At P1, the probe was fixed at a pier close to the Chatelier Lock. At A2 and A3, probes were fixed at 30cm above the bed on intertidal mudflats. At these three stations, the probes emerged during part of the tidal cycle. As for S1, S2 and S3, salinity was measured by a SAMBAT probe (by NKE) permanently submerged at $80cm$ below the water surface and attached to a floating buoy. At the six stations, salinity was recorded continuously with a time step of 10 minutes. The probes were deployed continuously for more than 18 months. Raw data was carefully verified in order to select valid shorter time series, discarding malfunctions, battery failure or device drifts.

4.2.3 Mathematical and numerical model

Flow and the salinity fields are computed by solving the conservation equation of fluid mass, the Reynolds-averaged Navier-Stokes (RANS) momentum equations and a passive scalar equation accounting for the salinity, where the Boussinesq approximation is used. The solution variables are the horizontal velocity $u = (u, v)$, the vertical velocity w, the free-surface elevation $H = h + b$, with h the water-depth and b the bottom elevation above datum, the pressure p, and the water salinity S. These variables are functions of the Cartesian coordinate space $x = (x, y, z)$ and time t. Initial and boundary conditions as well as the representation of the RTPS are imposed as described by Rtimi et al. [2021a]. The latter consisted on modelling the array of turbines and sluice gates by couples of sources and sinks from each side of the plant. For instance, during filling phase (Table 6.2), nodes representing the turbines on the sea-side of the plant are seen by the model as sinks, and nodes representing the turbines on the estuary-side of the plant are seen by the model as sources. This methodology showed its capacity to correctly simulate 2D depth-averaged hydrodynamics in the Rance estuary [Rtimi et al., 2021a]. It was thus adopted in this work. Sources and sinks representing the turbines and sluice gates were placed at a fixed elevation, equal to $1m$, which represents approximately the middle of the water column. Furthermore, salinity is imposed explicitly according to flow's direction. Indeed, during flood, flow rates at the RTPS are positive (into the estuary), salinity at nodes on the sea-side of the plant are implicitly computed by the numerical model, their values are imposed thus at corresponding nodes on the estuary-side of the plant. Vice versa during ebb, flow rate at the RTPS are negative (into the sea), salinity at nodes on the estuary-side of the plant are thus implicitly computed by the numerical model, their values are imposed then at corresponding nodes on the sea-side of the plant.

To close the hydrodynamic system, a standard $k - \epsilon$ turbulence model for both horizontal and vertical directions was used. Energy losses due to friction are parameterized with the Strickler roughness closure relationship. The Coriolis force is considered in the model, with the Coriolis parameter equal to $1.0909970 \times 10^{-4}\ s^{-1}$. The water density varies with salinity and its average value is equal to $999.972\ kg/m^3$. For the active scalar accounting for the salinity, the horizontal and vertical diffusion coefficients are set to $2.70 \times 10^{-4}\ m^2/s$.

The numerical solution of the governing equations is performed with the module TELEMAC-

3D (T3D), belonging to the TELEMAC-MASCARET modelling system (`www.opentelemac.org`) Dutta et al. [2017]. TELEMAC-3D's basic algorithm splits the solution into three steps, namely (i) calculation of the advected velocity components, (ii) update of the velocity field by incorporating the diffusion and source terms, and (iii) the water-depth calculation from the vertical integration of the continuity equation and the momentum equations by only including the pressure-continuity terms. An algorithm that deals with wetting and drying processes at the intertidal zones is incorporated in the numerical solution procedure. The computational domain is discretized with an unstructured triangular mesh in the horizontal directions, extruded along the vertical direction to form triangular prisms, covering the volume delimited by the bottom and the water surface elevation. The horizontal mesh of the Rance estuary and its adjacent coastal sea area consists of 389,766 elements and 199,625 nodes. The mesh size varies from $50m$ in the offshore zone, down to $5m$ m in estuary's basin near the RTPS and between Mordreuc and the Chatelier Lock (Figure 4.1). The mesh size is $20m$ elsewhere. Along the vertical direction, 8 layers were specified at each horizontal mesh, i.e. each prismatic element's thickness depends on the bottom elevation. The nodes of the horizontal mesh contain the bathymetric information, where the digital elevation dataset is identical to the high-resolution data (Lidar and field survey records) used by the model of Rtimi et al. [2021a].

4.3 Results

4.3.1 Tide propagation

Prior to the analysis of currents distribution and salinity variations, the tide propagation is first validated through field data from three tidal gauges for periods spanning neap and spring tides: July 20^{th}-30^{th}, 2020 and October 13^{th}-23^{rd}, 2020. The numerical model reproduces well the tidal distortion produced by the RTPS as well as the tidal propagation along the estuary (Figure 4.2) with Root Mean Square Errors (RMSEs) below 10cm. Moreover, high frequency oscillations of $\sim$10cm are observed during high tide, and are amplified at both Chatelier Lock and upstream of the RTPS stations. This seiche-like phenomenon was also noticed by Rtimi et al. [2021a] over a fortnight period in 2019.

4.3.2 Currents

This section focuses on the period of October 13^{th}-23^{rd}, 2020 when ADCP measurements were performed. Maximum flood and ebb currents (magnitude, along-channel, cross-channel and vertical components) were first compared between numerical model and ADCP data for transects 1, 2 and 3 (see Figure 4.1 for transects locations) given the availability of measurements within a complete tidal cycle. Then, the magnitude of maximum current was analyzed locally at transect 4 (upstream of the RTPS) during the opening period of the sluices. Afterwards, simulated and measured temporal evolution of the depth-averaged along-channel and the cross-channel velocities were compared at selected locations of each transect.

4.3.2.1 Vertical and horizontal current variations

The numerical model reproduces satisfactorily the vertical and cross-section distributions of maximum flood current along the estuary (Figure 4.3). Indeed, the outflow at Mordreuc (transect 1) is accelerated in the main channel (200-300m from left bank) due to the morphology of the transect, then it is decelerated by the center shoal, which extends between 50 and 150m from

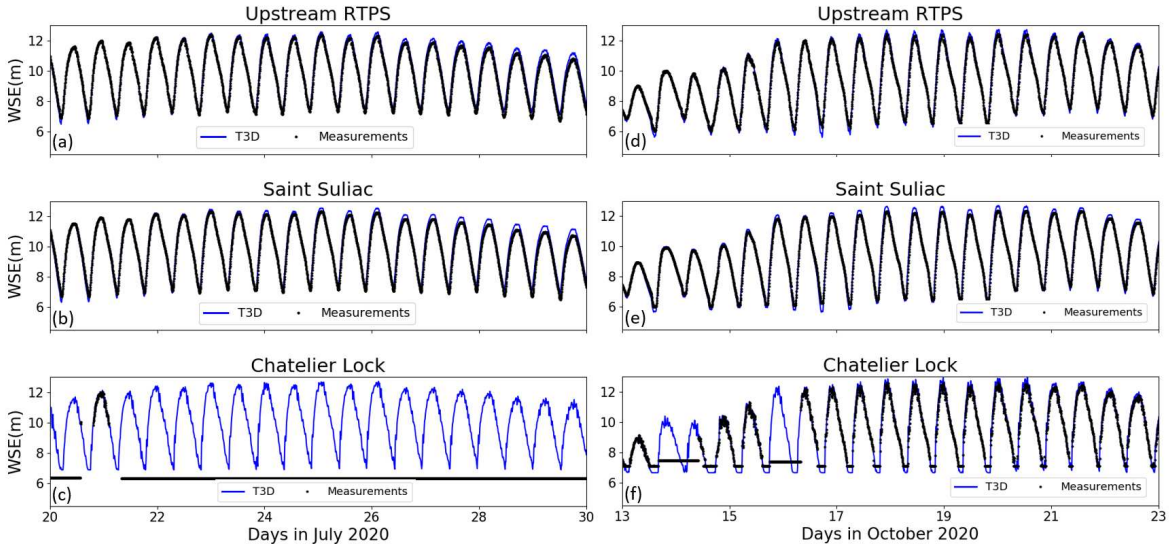

Figure 4.2: Comparison of simulated and measured water surface elevation within two periods: (a,b,c) July 20-30, 2020 and (d,e,f) October 13th-23rd, 2020. Blue lines and black dots indicate respectively T3D and measured data. The measurements are not reliable during low tide at Chatelier Lock station because of low water levels.

left bank, to finally reach magnitudes below 0.25m/s in the secondary channel (0-50m from left bank). However, the maximum current magnitude simulated at transect 1 is slightly greater than the one measured. This could be explained by the lack of reliable measurements at the exact time as the numerical model. Actually, maximum flood current in transect 1 occurred at 5 p.m. (UTC), however reliable ADCP measurements are available only at 4:30 p.m. (UTC) and 5:30 p.m. (UTC). Therefore, Figure 4.3.a corresponding to 5:30 p.m. was chosen to represent the ADCP maximum flood currents even though it is delayed by $\sim$ 30 minutes compared to the actual moment of maximum flood current. The along-channel current is sped up by the narrowness of the cross-section at Saint-Hubert-Port (transect 2), with a peak current magnitude of 1m/s against 0.8m/s at transect 1. Interestingly, the complex pattern of flow velocity measured at transect 3 is well reproduced by the numerical model (Figures 4.3.c and 4.3.f). The strongest flood currents of $\sim$1.2m/s are observed in the eastern side of the main channel (200-650m from left bank), then the flow is slowed down toward the western channel. It is noteworthy the logarithmic-like vertical velocity distribution in the eastern region (450-550m) with a maximum (respectively minimum) current magnitude at the surface (respectively near the bed). Finally, maximum flood currents are increased going from the estuary upstream (transect 1) towards its downstream (transect 3).
To further analyze the flow's three-dimensional structure, maximum along-channel flood currents were plotted with vectors of the cross-channel and vertical velocity components at transects 1, 2 and 3 (Figure 4.4). Color map indicates the direction of the along-channel velocity, with positive values (red color) for currents oriented upstream, and negative values (blue color) for currents oriented downstream. The numerical model captures the main patterns of currents vertical and cross-channel structure along the estuary. Indeed, at Saint-Hubert-Port (transect 2) maximum flood current is oriented upstream over the whole cross-section, and the flow's structure revealed the convergence of cross-section currents (Figures 4.4.b and 4.4.e). Interestingly,

the convergence area is not located in the middle of the cross-section $\sim 95m$ from the left bank, but is located $\sim 65m$ from the left bank and it varies along the water column, from $50m$ near the surface to $70m$ near the bed. This flow behavior can be explained from the geomorphology of the estuary near Saint-Hubert-Port area (Figure 4.1.b). Actually, the narrowness of this zone drives the convergence of flood currents. Also, the zone downstream of Saint-Hubert-Port is asymmetric with wider opening towards the right bank comparing to left bank, which favored the localisation of the convergence nodes at transect 2 to be near the left bank. Further upstream (transect 1), measurements depicted an along-channel velocity oriented upstream over the whole transect (Figure 4.4.a) while the numerical model revealed a spatial variation with negative (oriented downstream) along-channel currents in the secondary channel (0-$50m$ from left bank) and positive (oriented upstream) along-channel currents from the central shoal to the main channel (50-$300m$ from left bank) (Figure 4.4.d). This is related to the 30 minutes delay between measurements (Figure 4.4.a) and numerical simulation (Figure 4.4.d) explained in the previous paragraph. Furthermore, the co-existence of inflow and outflow currents along transect 1 is explained from the morphology of the area near Mordreuc (Figure 4.1.b) as strong flood currents could be reflected by the bend upstream Mordreuc and generated hence negative along-channel currents at the secondary channel. It should be noted that the vertical gradient of cross-channel velocity vectors is well captured by the numerical model with high acceleration near the bed (Figures 4.4.a and 4.4.d). Further downstream (transect 3), both simulated and measured along-channel currents showed an outflow (towards the downstream) in the eastern region (0-$100m$ from the left bank) and an inflow in the central and western region (Figures 4.4.a and 4.4.f). Indeed, the bifurcation of the main channel by the shoal present upstream of transect 3 (Figure 4.1.b) induced a horizontal recirculation of flood currents which generated an outflow in the eastern area of transect 3.

Similar analysis was performed on maximum ebb currents at the same transects (Figures 4.5 and 4.6). The numerical model reproduces well the distribution of maximum ebb velocity magnitude along the estuary. Indeed, an interesting pattern of vertical velocity distribution is observed at Saint-Hubert-Port (transect 2), with flow increase from the bottom to the surface. Contrastingly to maximum flood currents noticed at the most downstream transect (Saint-Suliac, transect 3), maximum ebb currents are observed at Saint-Hubert-Port transect (Figures 4.3.c and 4.5.b) where the morphology of the estuary impacts considerably currents variation. Furthermore, for all transects, flood currents maxima (at the most $1.2m/s$) are stronger than ebb currents maxima (at the most $0.7m/s$). Indeed, this could be explained by the tidal asymmetry in the Rance estuary assessed by Rtimi et al. [2021a], in addition to the low river discharge at the uppermost limit (Chatelier Lock).

Contrastingly to the along-channel flood currents (Figure 4.4), along-channel ebb currents are always oriented toward the sea (Figure 4.6). At Saint-Hubert-Port (transect 2), cross-channel vectors are directed toward the transect edges to be distributed to the widening downstream of Saint-Hubert-Port zone. Further downstream (transect 3), cross-channel vectors are converging to the deepest zone of the transect (300-$400m$ from the left bank) with stronger cross-channel currents in the western region (0-$300m$ from the left bank) comparing to the eastern region (400-$650m$ from the left bank).

The depth-averaged numerical model implemented in Rtimi et al. [2021a] (Chapter 3) assessed that the location of maximum flood current across the section upstream of the RTPS is highly sensitive to the operating modes of the dam. Indeed, ADCP measurements support this modification induced by the plant and is also well reproduced by the three-dimensional numerical model (Figures 4.7.a and 4.7.b). The strongest along-channel velocities (at the most $2.5m/s$)

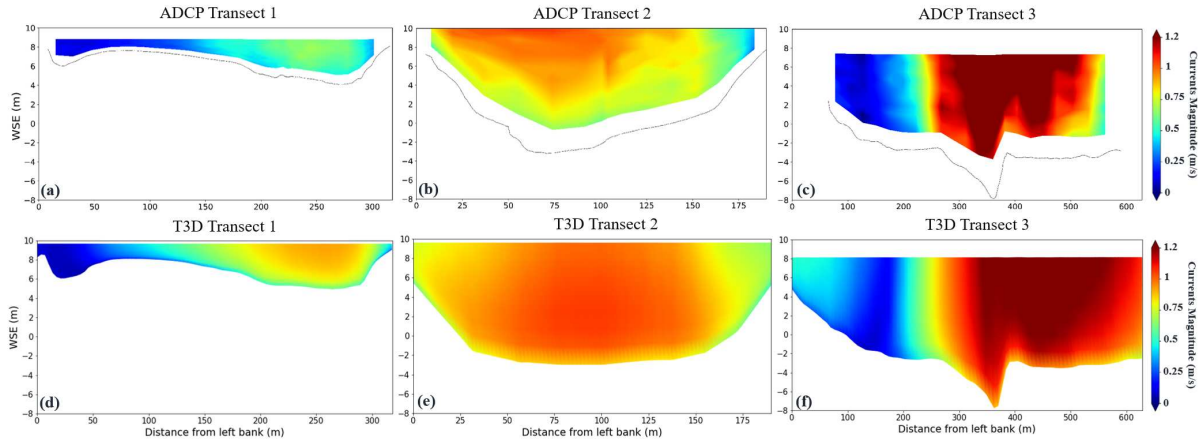

Figure 4.3: Comparison of maximum flood current magnitude between (a,b,c) ADCP measurements and (d,e,f) numerical model T3D at transects 1, 2 and 3 respectively (see Figure 1.5 for transects locations).

occurred in the eastern region, between 350m and 550m from the left bank, corresponding to the zone directly upstream of the sluices. In the western region (0-70m) corresponding to a part of the turbines upstream, weaker currents (at the most 0.75m/s) are noticed due to the operating mode of the turbines. Finally, the center shoal (200-300m) and the presence of a dike (Figure 4.1) significantly reduce the currents to magnitudes below 0.25m/s. Analyzing simultaneously maximum flood currents distributions along the estuary (Figures 4.3 and 4.7), the RTPS generates a jet-like flow during the opening of the sluices with peak outflow of 2.5m/s, which will be reduced by $\sim$40% 5km upstream.

4.3.2.2 Temporal variation

To complement analyses performed on maximum ebb and flood currents, key stations were selected at each transect to assess the temporal variation over a semidiurnal tidal cycle of the depth-averaged along-channel and cross-channel velocities.
At the most upstream transect (transect 1), the central channel location (Figure 4.8.a) was selected due to the availability of measurements over the semidiurnal tidal cycle. Depth-averaged along-channel (cross-channel) velocity is mainly oriented toward the sea (toward the right bank) during ebb and toward the river (toward the left bank) during flood (Figures 4.8.b and 4.8.c). The simulated velocity components depicted oscillations that could not be validated from ADCP data due to measurements low frequency, but peak values where measurements are available are well captured by the numerical model.
Further downstream, two relevant locations were selected at transect 2 (Saint-Hubert-Port), the channel's western and central sides (Figure 4.9.a). Depth-averaged cross-channel velocity is mainly directed to the right bank during ebb and to the left bank during flood (Figure 4.9.c). Unfortunately, the position of the station W.C. could not highlight the convergence of cross-channel vectors illustrated in Figures 4.4.e and 4.6.e. ADCP measurements revealed oscillations of the depth-averaged along-channel velocity over the whole semidiurnal tidal cycle. These oscillations are also captured by the numerical model (Figure 4.9.b). This behavior may be induced by the morphology of the estuary at Saint-Hubert-Port (Figure 4.1.b) as the narrowness of this zone generated recirculation that influences the amplitude of the along-channel currents.

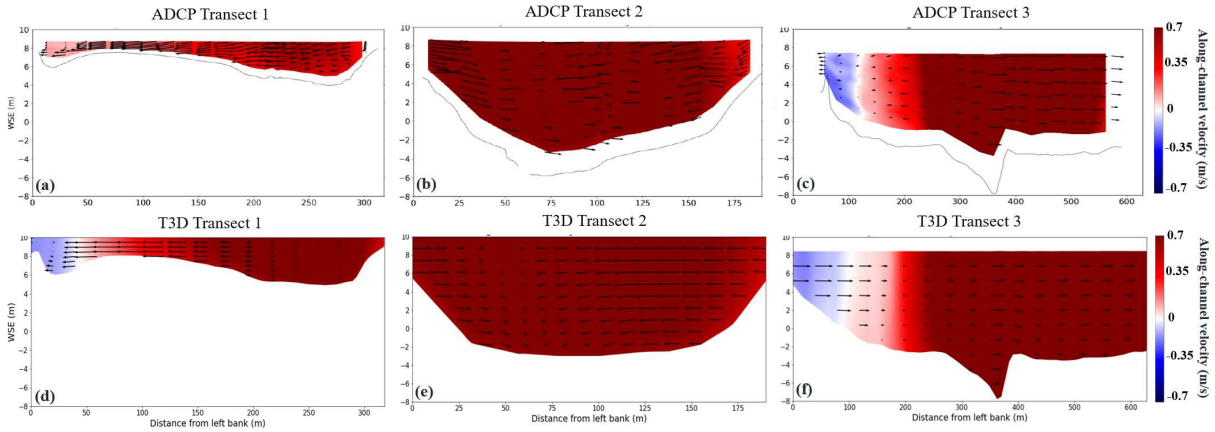

Figure 4.4: Comparison of maximum along-channel flood current and cross-channel recirculation vectors between (a,b,c) ADCP measurements and (d,e,f) numerical model T3D at transects 1, 2 and 3 respectively (see Figure 4.1 for transects locations). Positive values (red color) represent currents oriented upstream, and negative values (blue color) represent currents oriented downstream.

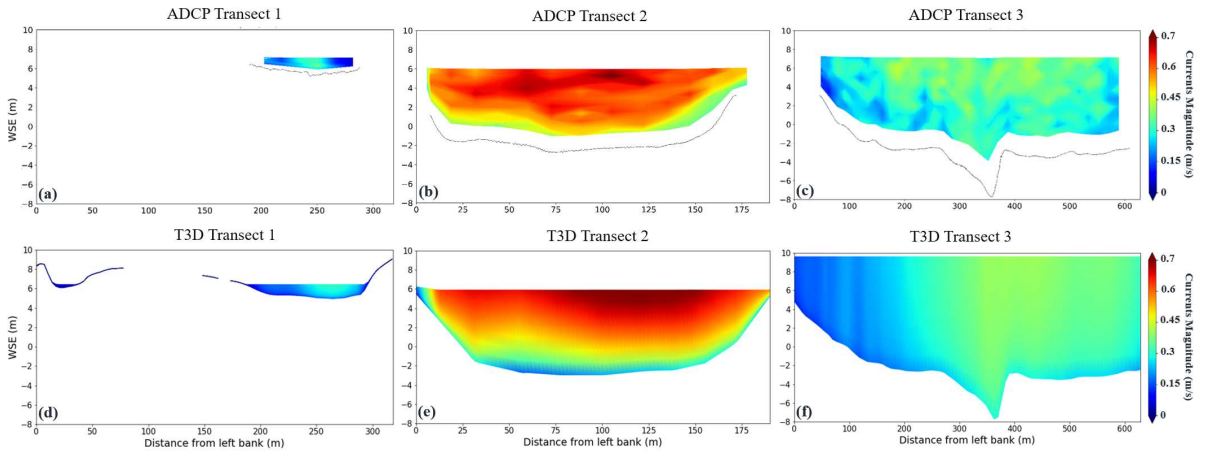

Figure 4.5: Comparison of maximum ebb current magnitude between (a,b,c) ADCP measurements and (d,e,f) numerical model T3D at transects 1, 2 and 3 respectively (see Figure 4.1 for transects locations).

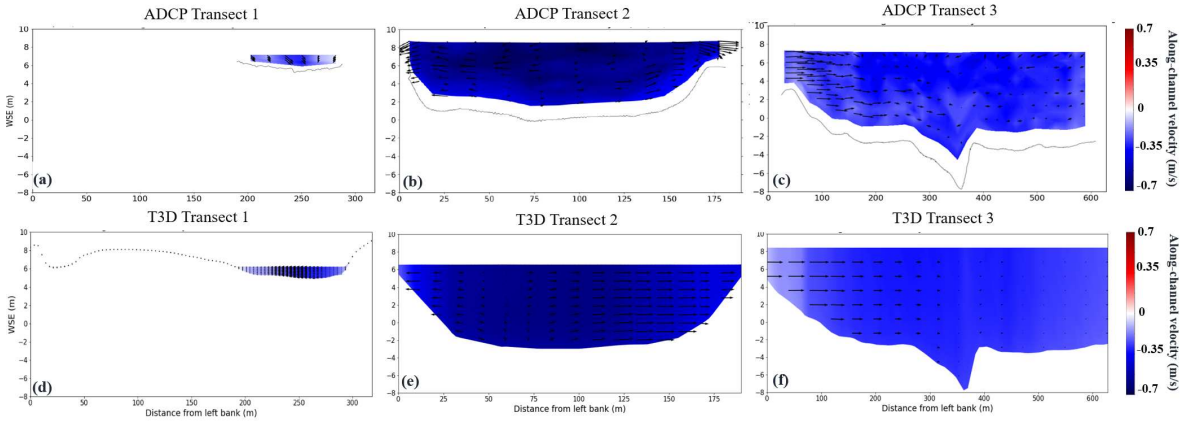

Figure 4.6: Comparison of maximum along-channel ebb current and cross-channel recirculation vectors between (a,b,c) ADCP measurements and (d,e,f) numerical model T3D at transects 1, 2 and 3 respectively (see Figure 4.1 for transects locations). Positive values (red color) represent currents oriented upstream, and negative values (blue color) represent currents oriented downstream.

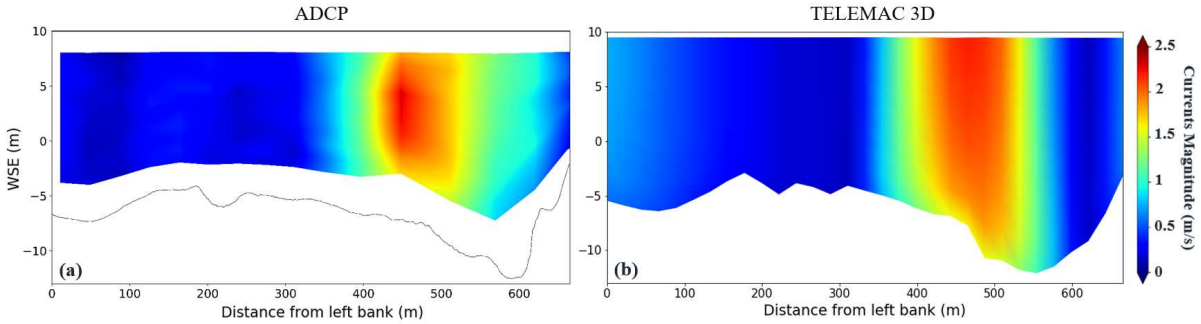

Figure 4.7: Comparison of maximum current magnitude between (a) ADCP measurements and (b) numerical model T3D at the T.P.S. upstream (transect 4, see Figure 4.1 for location).

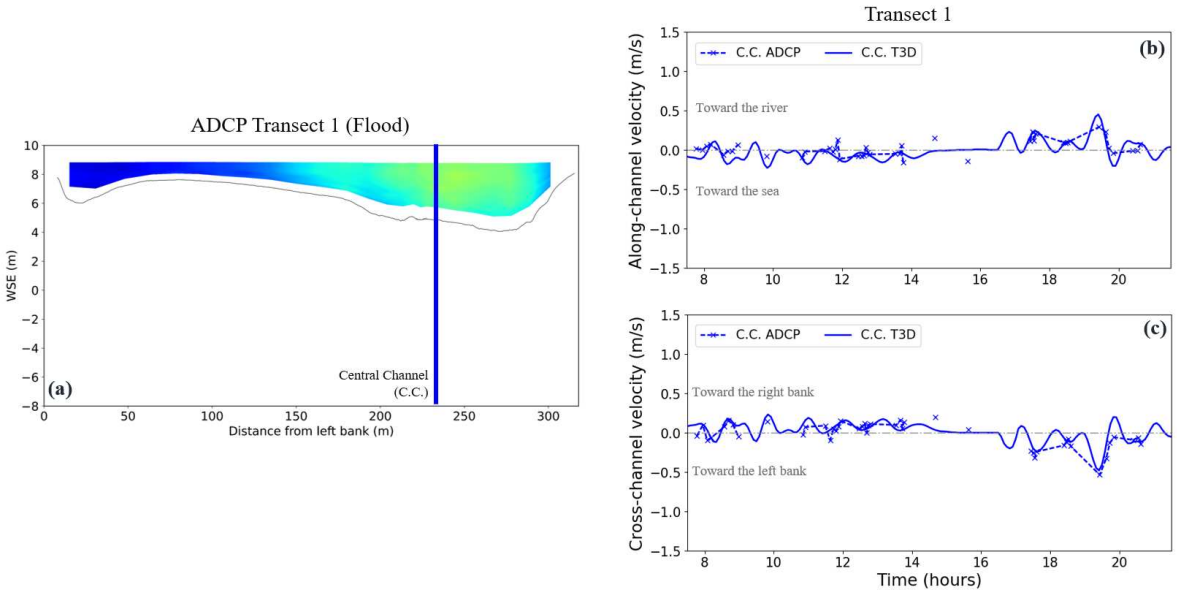

Figure 4.8: Velocity components at transect 1. (a) ADCP maximum flood current magnitude with location of central channel (C.C.) location. Temporal evolution of measured and simulated depth-averaged (a) along-channel velocities and (b) cross-channel velocities at the C.C.

These variations are stronger during flood comparing to ebb, specially during the beginning of the flood (around 17 hours) where the along-channel current direction is switched from landward to seaward.
Further downstream, three relevant locations were selected at transect 3 (Saint-Suliac), the channel's western, central and eastern sides (Figure 4.10.a). Depth-averaged along-channel ebb currents are mainly uniform along the transect and oriented toward the sea with amplitudes below $0.5m/s$ (Figure 4.10.b). Interestingly, depth-averaged cross-channel velocity illustrated a heterogeneity along transect 3. Indeed, depth-averaged cross-channel velocity is mainly directed towards the right bank over the whole ebb period in the western channel, while it is oriented toward the right bank at the beginning of the ebb (8-10 hours) in central and eastern channels, then switched toward the left bank for the rest of the ebb period (10-17 hours) (Figure 4.10.c). Afterwards, flood period initiated (17 hours) with strong currents acceleration due to the opening of sluice gates. This flood currents increase is more important in the eastern side comparing to the western side with peak values of $1.2m/s$ and $0.75m/s$ respectively. Two hours later, an overall tendency of flood currents deceleration is noticed over the whole transect. The orientation switch of flood currents starts in the western zone to end in the eastern zone. Furthermore, the depth-averaged cross-channel velocity is uniform along the transect during flood with amplitudes below $0.5m/s$. In summary, along-channel and cross-channel components analysis revealed the heterogeneity of the along-channel component during flood and cross-channel component during ebb according to the position along the transect. This currents pattern is well captured by the numerical model.

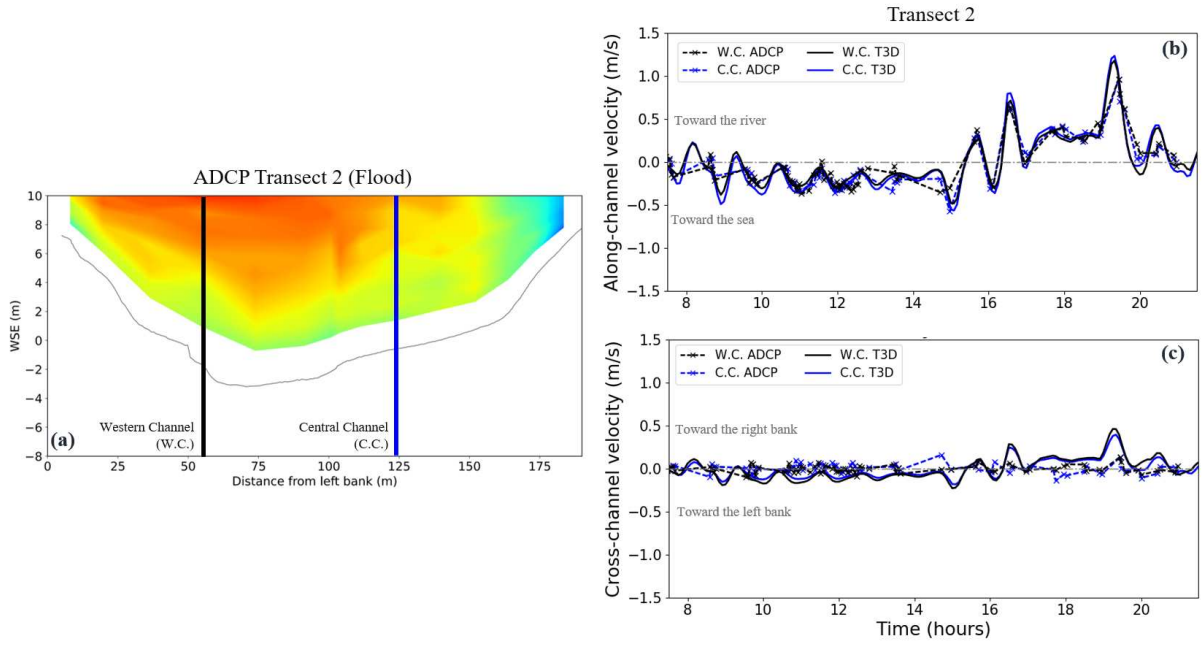

Figure 4.9: Velocity components at transect 2. (a) ADCP maximum flood current magnitude with location of two stations: Western channel (W.C.) and central channel (C.C.). Temporal evolution of measured and simulated depth-averaged (a) along-channel velocities and (b) cross-channel velocities at W.C and C.C.

4.3.3 Salinity

The validation of simulated salinity was carried out using ten days period's dataset (July 20th-30th, 2020) provided by six salinity gauges located along the estuary (black squares in Figure 4.1). The examination of numerical and measured salinity revealed a good agreement between the model and the observations (Figure 4.11). At stations S1, S2 and S3, salinity is oscillating between 33 and 35g/l as the probes are constantly submerged. Therefore, the lower estuary is mainly dominated by salt water (35g/l). Contrastingly, stations P1, A2 and A3 revealed a temporal variation between 0 during low tide and 34g/l otherwise. This pattern is explained by the emergence of the probes at low water, noticed from water levels at each station (grey lines in Figures 4.11.d, 4.11.e and 4.11.f). However, the model tends to overestimate the salinity at the uppermost limit (P1) between the 7th and the 10th day (Figure 4.11.f). Actually, the salinity in this region is highly sensitive to the river discharge at the Chatelier Lock. Since this latter is not measured, it made it difficult to predict the salinity decrease at P1. Moreover, this variation could also be explained by the presence of the rain which is not taken into account in the simulations. Nevertheless, the model reproduces satisfactorily the overall salinity dynamics in the Rance estuary.

To analyze the freshwater-saltwater interface in the Rance estuary, simulated salinity during July 2020 is compared with historical measurements from Bonnot-Courtois et al. [2002] before and after the construction of the plant (Figure 4.12). Before the RTPS, the freshwater-saltwater interface could be flushed up to Saint-Suliac, but after the RTPS operation, saltwater penetrates further upstream the estuary, up to Saint-Hubert-Port. In July 2020, horizontal salinity distri-

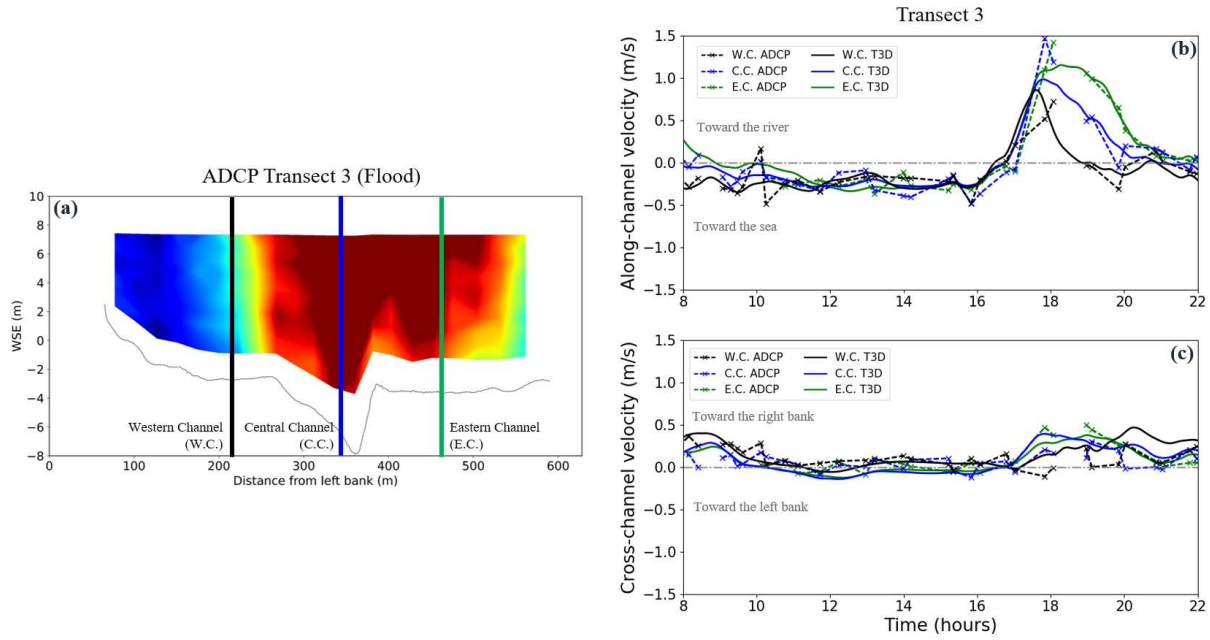

Figure 4.10: Velocity components at transect 3. (a) ADCP maximum flood current magnitude with location of three stations: Western channel (W.C.), central channel (C.C.) and eastern channel (E.C.). Temporal evolution of measured and simulated depth-averaged (a) along-channel velocities and (b) cross-channel velocities at W.C, C.C. and E.C.

bution (Figure 4.12.c) revealed that the freshwater-saltwater interface is indeed pushed by the barrage toward the lower estuary. However, the mixing area between fresh and salt waters does not exceed 2km downstream of the Chatelier Lock, while it could cover, during winter, a larger portion, up to 5km from the Chatelier Lock [Bonnot-Courtois et al., 2002]. Examination of the vertical salinity distribution along the channel (see Figure 4.1 for exact location) assessed that the Rance estuary could be divided into three regions (Figure 4.12.d): (i) 0-200m from the Chatelier Lock where salinity is below 20g/l; (ii) 200-1800m from the Chatelier lock where the channel becomes deeper, salinity is increased and varies between 25 and 30g/l, and (iii) above 1800m from the Chatelier Lock where salinity is around 35g/l.

4.4 Discussion

The present work aims to validate the 3D flow structure and salinity simulated along the Rance estuary influenced by the world's second largest tidal power plant.
Comparisons between simulated and measured velocities revealed the ability of the numerical model to reproduce the 3D flow structure from the lower estuary (transect 1) to the upstream of the RTPS (transect 4). Flood currents are mainly modulated by the operation modes of the RTPS, specifically the opening of sluice gates. Locally, the flow is substantially accelerated near the eastern channel upstream of the plant, with a homogeneous distribution along the water column. These findings confirm the predictions of the 2D depth averaged model of Rtimi et al. [2021a]. Furthermore, the morphology of the estuary significantly influences the propagation of ebb currents, with the strongest flow velocity observed in the narrowing at Saint-Hubert-Port.

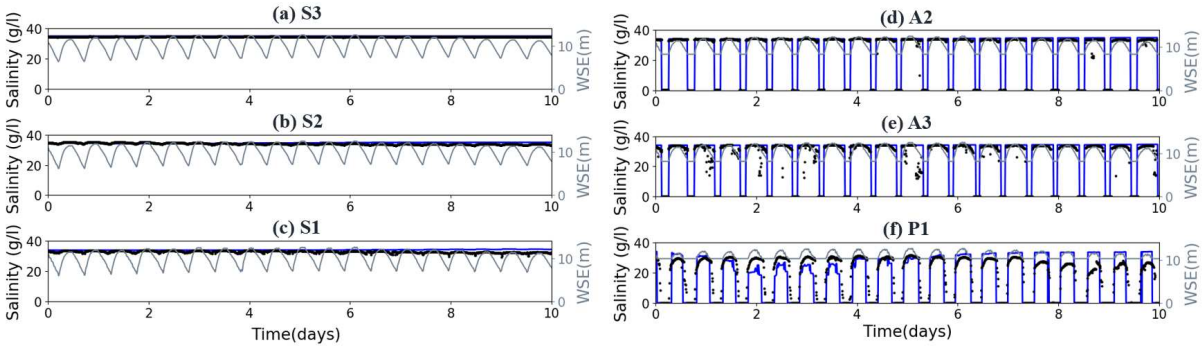

Figure 4.11: Temporal evolution of salinity at different stations along the estuary (see Figure 4.1 for location) between measurements and numerical model within the period of July 20th-30th, 2020. Blue and grey lines represent the simulated salinity and water surface elevation respectively at the referred station. Black dots indicate salinity measurements.

This geometrical configuration drives the convergence of cross-channel currents during flood and their divergence during ebb. On a semidiurnal tidal time scale, it could generate oscillations of the along-channel velocity, that could switch the currents direction from landward to seaward. In addition, Saint-Suliac zone is characterized by the heterogeneity of the along-channel and cross-channel components distribution along the along the transect. Moreover, currents do not seem to considerably vary along the water column except at Saint-Hubert-Port (transect 2) and Saint-Suliac (transect 3) during floods.
After over 50 years of service, the Rance hydro-electric power station induces modification in the natural hydraulic regime which led to a different distribution of salinity compared to that before the dam's construction. Dynamics of freshwater-saltwater interface is sensitive to seasonal river discharge variation, hydraulic flushes occurred at the Chatelier Lock and plants operating cycles. Seasonal variability of this interface ranges between 2km in summer (5km in winter, [Bonnot-Courtois et al., 2002]) from the Chatelier Lock.
In addition to tidal asymmetry depicted from flood and ebb currents [Friedrichs and Aubrey, 1988], density variation induced by salinity gradient and cross-channel flow could influence the estuarine turbidity maximum as well as sediments transport and deposition in the basin [Sottolichio et al., 2000; Amoudry et al., 2014; Burchard et al., 2018; Hesse et al., 2019]. Further analysis of the hydrodynamics coupled with sediment transport processes is therefore necessary to investigate the impact of the RTPS on the sedimentation in the estuary.

4.5 Conclusions

Analyses of the three-dimensional flow field and salinity distribution, along the estuary over a 10 days period, collected by acoustic Doppler current profiler and continuous measurements probes respectively, have enabled the validation of a 3D numerical model accounting for the presence of the RTPS. The model correctly reproduces the spatial distribution and temporal evolution of ebb and flood currents along the estuary. Moreover, salinity patterns are also satisfactorily captured, with a freshwater-saltwater interface expected 2km downstream of the Chatelier Lock during summer. Furthermore, these results highlight the added-value of 3D numerical modeling of the Rance estuarine system with respect to the 2D depth-averaged model.

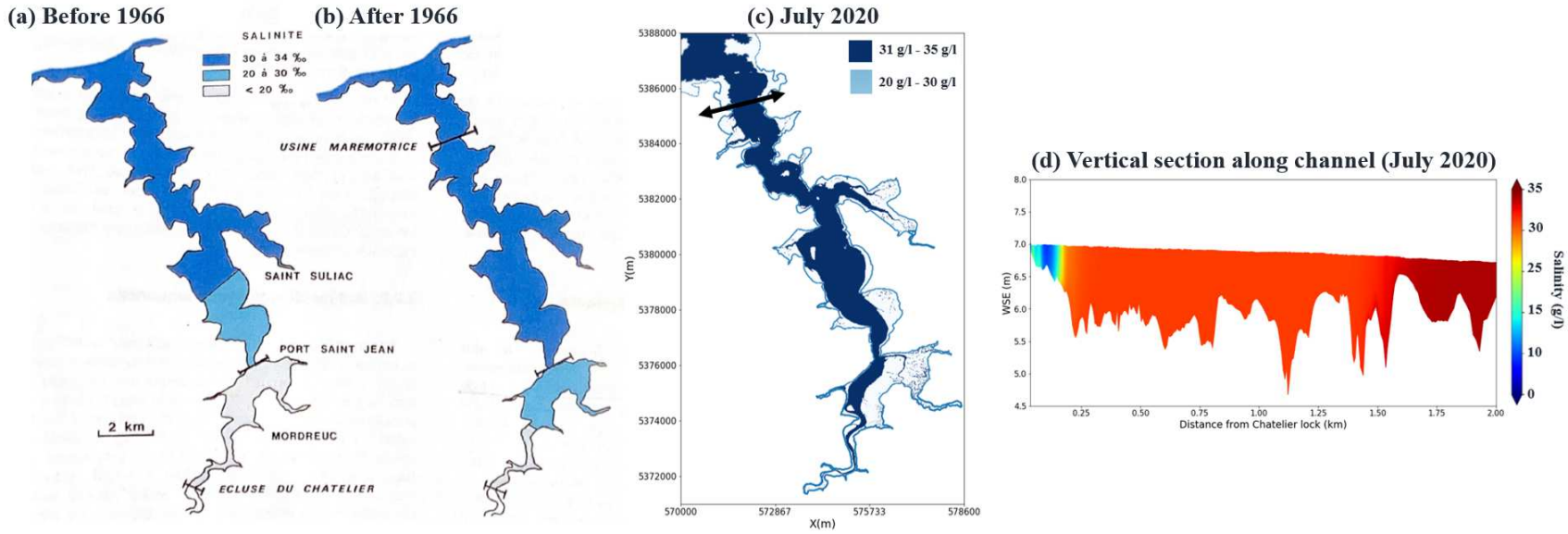

Figure 4.12: Salinity distribution in the Rance estuary (a) before 1966 from Bonnot-Courtois et al. [2002], (b) after 1966, i.e. after the operation of the plant, (c) in July 2020 and (d) detail on vertical section along the lower estuary channel, 2km downstream from the Chatelier Lock (see Figure 1.5 for section's location). Figures (a) and (b) were adapted from Bonnot-Courtois et al. [2002].

The RTPS modifies tidal patterns and the flow structure within the water body, which in turn might influence the sediment transport and estuarine morphological evolution. This subject has not been studied extensively and warrants further investigation.

Acknowledgements

This work was funded by the French National Association of Research and Technology (ANRT) and EDF R&D with the Industrial Conventions for Training through REsearch (CIFRE grant agreement 2018/1653). Authors would like to thank the crew members from the MNT team at EDF R&D, EDF DTG and EPOC who performed the field measurements and pre-analyzed the collected data.

CHAPTER 5

SEDIMENT DYNAMICS AND MORPHOLOGICAL PROCESSES IN THE RANCE ESTUARY

The work presented in this chapter is submitted to
Renewable Energy Journal, entitled
The Rance tidal power station: toward a better understanding of sediment dynamics in response to power generation

by
Rajae Rtimi[a,b], Aldo Sottolichio[b] and Pablo Tassi[a,c]

[a] Electricité de France, Research and Development Departement (EDF R&D), Chatou, France
[b] EPOC Laboratory CNRS, University of Bordeaux, Pessac, France
[c] Saint-Venant Hydraulics Laboratory, Chatou, France

▷ Objectives of this chapter

This chapter aims to improve the understanding of sediment dynamics in response to power generation and to quantify the impact of the tidal plant on sediment transport and morphodynamics. To reach this goal, the implementation, calibration and validation of a 3D hydro-morphodynamic model of the Rance estuary were performed. Then, numerical results were analyzed to assess the present-day sediment dynamics in response to power generation. Afterwards, comparison between scenarios in the presence/absence of the power station evaluated the impact of the dam on sediment transport and bed level evolution in the estuary. Therefore, this chapter aims to answer sediment transport and morphodynamics relative topics of research questions formulated in Chapter 1:

- *How relevant are 2D and 3D numerical models at reproducing the main features of hydro-sedimentary dynamics observed in macrotidal estuaries influenced by the presence of a tidal power station?*
- *How hydrodynamics, sediment transport and morphodynamics processes are influenced by the presence of the world's second-largest tidal power station?*
- *Which are the dominant physical mechanisms driving the sediment dynamics in the Rance estuary?*

Highlights

- Quantitative analyses of sediment dynamics in the Rance estuary, influenced by a tidal power station.
- Peak flood suspended sediment concentration (SSC) are noticed during the sluice gates opening phase.
- Sediment could be resuspended locally during ebb, particularly during the turbining phase.
- Significant sedimentation rates are observed in the upper estuary.
- The upper's estuary sedimentation is also observed in the absence of the plant, but with lower rates.

Abstract

A three-dimensional coupled hydrodynamic and morphodynamic numerical model was developed to analyse sediment dynamics in the Rance estuary in response to the tidal power station (TPS) built near the mouth in the 1960s. The Rance estuary is a relatively small low-discharge steep-sided *ria*, located along the Brittany coast in northern France, with a maximum spring tidal range of 13.5 m. Taking advantage of this significant tidal regime, the first and currently the second largest operational tidal power station in the world was built at the estuary's mouth, with a peak output capacity of $240MW$. After calibration and validation of the model for present-day conditions, suspended sediment concentration (SSC) and bed level evolution were evaluated at tidal and fortnightly scales for different scenarios, with and without TPS. Peak SSC are reached during spring tides and specifically during the estuary's filling (flood) stage where both turbines and sluice gates are open. Unbalanced with sediment transport during ebb, sediments are accumulated in the main channel of the upper estuary. Under natural tidal forcing (i.e. without TPS), simulations show that an estuarine turbidity maximum forms in the upper estuary, and sediment deposition is significant. However, sedimentation rates are two times lower than those observed in the presence of the TPS. A possible alternative for reducing sediment accumulation in the upper estuary would the opening of sluice gates simultaneously with the turbines during falling tide to enhance ebb currents that would allow particles transport towards the estuary's downstream.
Keywords: Tidal power station, sediment dynamics, morphodynamics, numerical modeling, TELEMAC-MASCARET system, the Rance estuary.

5.1 Introduction

Tidal power is a potential future renewable source of energy as electricity is produced by the surge of ocean waters during the rise and fall of tides [O'Rourke et al., 2010]. There are currently three different ways to generate tidal energy: tidal streams, barrages, and tidal lagoons. Although they have great potential to provide predictable renewable energy resources [Neil et al., 2018], they could have impact on hydrodynamics, sediment dynamics, water quality and ecosystems [Ng et al., 2013; Kirby and Retière, 2009; Xia et al., 2010; Cornett et al., 2013]. As a tidal power station (TPS) is usually constructed across the estuary's mouth, this anthropogenic disturbance is added to natural factors, such as river discharge, tidal forcing and sediment distribution, that control sediment transport and morphodynamics in typical estuarine systems [Grasso et al., 2018; Grasso and Le Hir, 2019]. Therefore, understanding the impact on sedimentary processes in response to power generation is crucial for the assessment of the plant's environmental impact [Wu et al., 2017] and it is equally important for the estuary management. The understanding of sediment processes in estuaries relies on analyses of suspended sediment matter and morphodynamics [Dronkers, 2005]. The former can be characterized from suspended sediment concentration (SSC) values, examined on timescales from a semidiurnal tidal cycle to fortnightly periods, in order to (i) assess estuarine turbidity maximum (ETM) dynamics [Sottolichio et al., 2011; Toublanc et al., 2016; Grasso et al., 2018], (ii) reveal transport processes [Grabemann, 1989], and (iii) evaluate residual sediment fluxes [Geyer et al., 2001; Burchard et al., 2018]. Furthermore, morphodynamics are analyzed in terms of bed level change over timescales ranging from a fortnight to decades [Fairley et al., 2015; Brand et al., 2021].
Net siltation and sediment accumulation were observed in the Rance estuary where the second world's tidal power station was built [Pelc and Fujita, 2002]. The Rance barrage is located on

the Brittany coast of northern France (Figure 5.1.a). The maximum perigean spring tidal range reaches 13.5m at the mouth (Saint-Servan, Figure 5.1.b), allowing a peak output capacity of 240MW. The Rance tidal power plant supplies 0.12% of the power demand in France, which is equivalent to a medium-size city with 360,000 inhabitants [EDF, 2020]. Bonnot-Courtois *et al.* reported qualitative influence of the plant on sediment dynamics in the Rance estuary mainly based on measurements performed after the construction of the barrage [Bonnot-Courtois, 1993; Bonnot-Courtois and Le Vot, 1993; Bonnot-Courtois et al., 2002]. Similarly, Kim *et al.* conducted observational studies on the unbalanced sediment transport by the Sihwa Lake tidal power plant [Kim et al., 2021]. Such studies allow to assess the present-day sediment dynamics in an estuarine system, but are unable to quantify the impact of the plant on sedimentary processes. Furthermore, Thiebot [2008] developed a two-dimensional (2D) hydro-sedimentary model of the Rance estuary but the simulated bed level changes could not be validated due to lack of bathymetry survey data [Thiebot, 2008]. In addition, only cohesive sediment was considered in this model [Thiebot, 2008]. Therefore, Thiebot's model did not address sediment processes related to the mixture between cohesive and non-cohesive matter. Recently, Rtimi *et al.* developed 2D and 3D hydrodynamics models of the Rance estuary which assessed quantitatively the impact of the TPS on the hydrodynamics in this particular estuarine system [Rtimi et al., 2021a,b]. The former work addressed also the concept of tidal asymmetry [Nidzieko and Ralston, 2012; Friedrichs and Aubrey, 1988] that provided preliminary insights on sediment dynamics but needed to be supported by sediment transport and morphodynamics simulations [Rtimi et al., 2021a]. Three-dimensional (3D) hydrodynamic processes such as water circulation, velocity and density gradients within the water body are important to correctly predict SSC and therefore sediment fluxes [Amoudry et al., 2014; Burchard et al., 2018; Hesse et al., 2019]. Robins et al. [2014] and Fairley et al. [2015] highlighted that 3D modelling would provide more accurate results in configurations evolving tidal energy. Indeed, these models allow more realistic representation of hydrodynamics processes which are strongly linked to sediment dynamics. However, numerical results from Fairley et al. [2015] were only validated in terms of hydrodynamics and lacked morphodynamics validation on the basis of measured bed level data.
The main objective of this work is to improve the understanding of sediment dynamics in response to power generation and to quantify the impact of the tidal plant on sediment transport and morphodynamics. To this goal, a 3D hydro-morphodynamic model of the Rance estuary was developed (section 5.3.2). The numerical model was calibrated and validated in terms of sediment transport and bed level evolution on the basis of measurements captured from field survey campaigns and probes installed in the Rance estuary's basin during 2018-2021 (section 5.4). Then, numerical results were analyzed to assess the present-day sediment dynamics in response to power generation (section 5.5). Afterwards, comparison between scenarios in the presence/absence of the power station evaluated the impact of the dam on sediment transport and bed level evolution in the estuary (section 5.6). Finally, section 6.4 discusses the Rance study case in a global context.

5.2 Study site

The Rance estuary is a small steep-sided *ria* [Evans and Prego, 2003] located on the Brittany coast of northern France (Figure 5.1.a), characterised by the presence of a tidal power plant on its mouth. The Rance tidal power station can operates on a ebb- and two-way generation modes [Neil et al., 2018]. In other words, It is distinguished by its ability to produce electricity during both ebb and flood. Active parts of the Rance tidal power station are : (i) 24 turbines extending

on 323m long and 33m wide, each unit producing 10MW; (ii) 6 sluice gates composing 114m long and 15m wide dam (Figure 5.1.c). The head of the estuary is located at the Chatelier lock (Figure 5.1.b), which delimited the upstream limit of tide propagation. The Rance river drains a small catchment area, with an average freshwater discharge of $7m^3/s$, low water flow rate of $0.5m^3/s$ and a decennial flood of $80m^3/s$.
Bonnot-Courtois et al. [2002] assessed the distribution of superficial sediment in the Rance estuary from around 150 samples conducted in 1994 (Figure 5.2.a). On the basis of this map and recent localized samples performed in 2021, four classes of sediments were retained for numerical modelling: gravel, fine sand with a representative median diameter equal to $200\mu m$, very fine sand with a representative median diameter equal to $100\mu m$ and mud with representative median diameter equal to $20\mu m$. In order to optimize computational time, gravel zones, namely the main channel upstream of the TPS and area around Saint-Hubert Port, were represented by a non-erodible bottom. Following the map of 1994, a schematic simplified distribution of the 3 retained sediment classes was used to initialize the numerical model developed in Section 5.3.2. Then, a spin-up period of two fortnights was sufficient to obtain the main patterns of sediment distribution observed in the map of 1994 (Figure 5.2). Downstream of the tidal power station, coves are mainly composed of mud or a mixture between fine sand and mud. Upstream of the plant, coves bed is recovered mainly by pure mud, while the main channel, between Saint-Suliac and the barrage, can be recovered by coarser sediment, predominantly fine sand of $200\mu m$. Further upstream, between Saint-Suliac and Saint-Hubert port, the eastern region is composed by pure mud and western region by sandy mud. Then, sediments become finer from Saint-Hubert port to the Chatelier lock, with (i) presence of pure mud on the wider areas of coves to the most upstream channel south of Mordreuc, (ii) presence of fine sand of $200\mu m$ directly upstream of Saint-Hubert port and (iii) mixture of fine and very fine sand of 200 and $100\mu m$ respectively in the channel of area near Mordreuc. The former is not noticed in the 1994 sediment distribution, but was observed in recent sediment samples from 2021. The obtained sediment distribution (Figures 5.2.b-d) was the initial state of all numerical simulations presented further after.

5.3 Material and methods

5.3.1 Field measurements

A field hydro-sedimentary survey was performed in the Rance estuary from June 2019 to May 2021. Two types of field measurements were deployed to calibrate and validate the numerical model: suspended sediment concentration and bed level evolution. Further details on data acquisition and data pre- and post-processing is provided in Chapter 2.

5.3.1.1 Suspended Sediment Concentration

Continuous turbidity measurements were carried out by mono-parameter STBD probe (Figure 5.1.d) and multi-parameter probe SAMBAT (Figure 5.1.e) from NKE [Bertier, 2020b] at four different locations along the estuary: T1, T2, S1 and S2 (Figure 5.1.b). STBD probes are equipped with an external automatic wiper brush and a sensor emitting a modulated light at $880nm$ (Figure 5.1.d). The light reflected by the particles is detected by a cell which provides a signal proportional to particles concentration. STBD probes record (i) turbidity up to $3000NTU$, (ii) depth up to $6m$ and (iii) temperature ($-2° < C < 35°$) [Bertier, 2020b]. These probes were installed at T1 and T2 (Figure 5.1.b) on buoys located at $80cm$ and $90cm$ below the water surface,

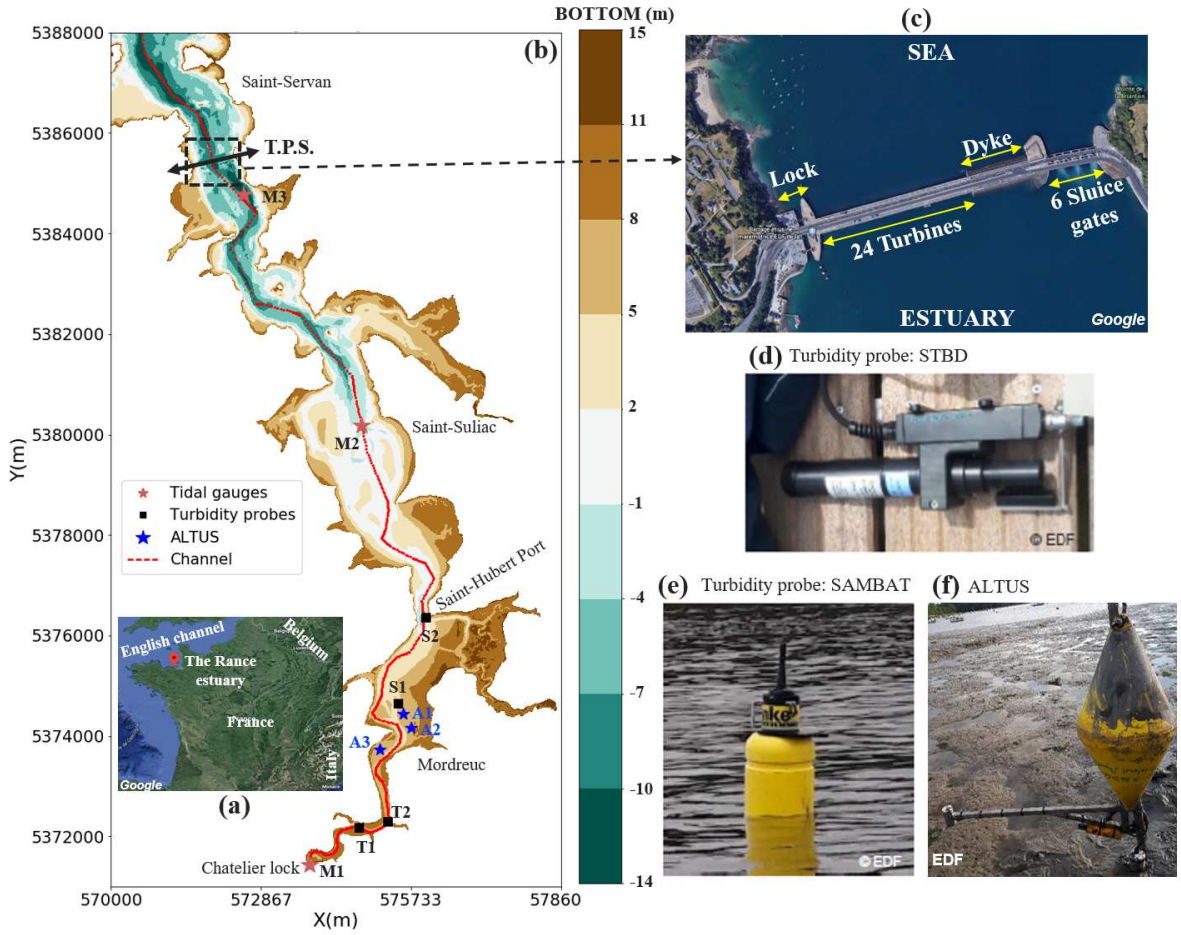

Figure 5.1: The Rance estuary: (a) location map, (b) zoom on the estuary with bathymetry of 2018, (c) zoom on the tidal power station (TPS). Turbidity probes :(d) STBD corresponding to stations T1 and T2; and (e) SAMBAT corresponding to stations S1 and S2. (f) Bed evolution probe ALTUS corresponding to stations A1, A2 and A3.

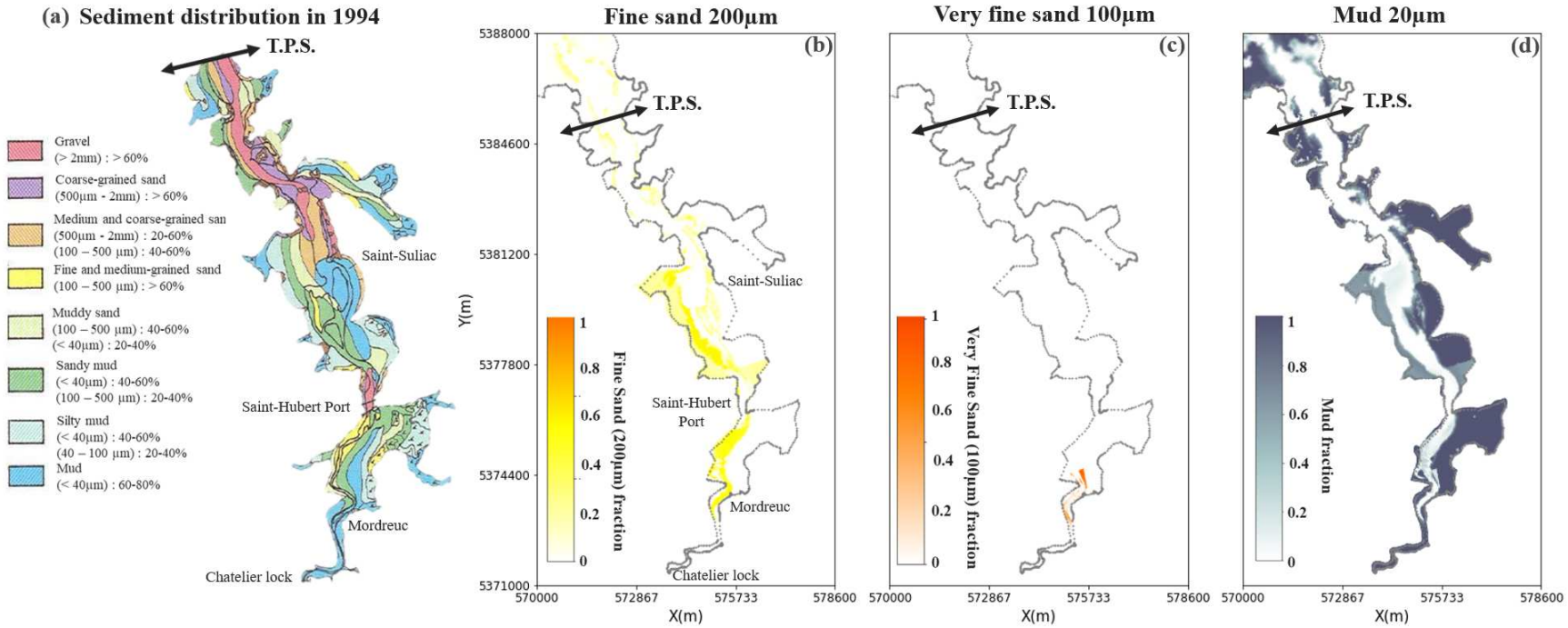

Figure 5.2: Distribution of superficial sediments in the Rance estuary: (a) map drown up from samples taken in 1994 [Bonnot-Courtois et al., 2002], (b,c,d) fractions of fine sand (200μm), very fine sand (100μm) and mud (20μm) respectively after a spin-up simulation of 2 fortnights.

respectively. SAMBAT probe is an autonomous multi-parameter probe fixed on a buoy, equipped with a GPS, a remote transmission, a fast wireless configuration thanks to a communication interface (Radio Data Pencil), and uses a brush to protect optical sensors from biofouling [Bertier, 2020b]. This instrument measures the main physicochemical water parameters: temperature, depth, conductivity for the calculation of salinity, turbidity, dissolved oxygen and pH. SAMBAT probes were deployed at S1 and S2 to measure turbidity 80cm below the water surface (Figure 5.1.b).
Turbidity is expressed in Nephelometric Turbidity Unit (NTU). In order to determine the corresponding Suspended Sediment Concentration (SSC), NTU-SSC calibration of STBD and SAMBAT probes was performed. NTU-SSC conversion equations presented high uncertainties since 70% of SSC samples were above 1000mg/l while SSC values in the Rance estuary are below 300mg/l [Parquet, 2021; Bertier, 2020a]. Therefore SSC measurements deployed in this work are associated to margin errors of 50% [Parquet, 2021].
SSC survey was conducted over 18 months period (June 2019 - May 2021) with recording frequency of 10 minutes. Beyond margin errors related to NTU-SSC calibration, other issues as biofouling, malfunctions, battery failure and device drifts were observed [Bertier, 2020b]. Therefore, SSC measurements used in this work were cautiously selected on short and reliable time windows.

5.3.1.2 Bed evolution

Bed evolution measurements used in this work were performed by ALTUS system «*ALTimètre à Ultrasons Submersible*»probe from NKE (Figure 5.1.f) installed on three different locations, A1, A2 and A3, mainly localized in the uppermost part of the estuary (Figure 5.1.b). ALTUS system was developed in order to accurately measure the bed level variations in muddy dominant environments, mudflats and shallow waters such as bays and estuaries [Jestin et al., 1998]. The ALTUS altimeter (Figure 5.1.f) is an autonomous self-contained device equipped with:

- a 2MHz acoustic transducer positioned about 30 cm above sediment and facing downwards,
- a recording module. The travel time from the emission of the acoustic wave and its reception by the transducer is converted into distance. These speed of sound depends on the temperature and salinity of the environment,
- a pressure sensor buried on the surface of the bed, which measures water depth.

The ALTUS system records (i) four distances between the transducer and the bed through 4 beams (1, 2, 3, 4), (ii) «*Maximum echo* »value to assess the quality of measurements, and (iii) absolute pressure for water depth measurements.
ALTUS system were deployed on 3 locations in the Rance estuary, A1 A2 and A3 (Figure 5.1.b). The choice of installations sites focuses mainly on the upstream part of the estuary as this zone corresponds to a dynamically active region, with an energetic sediment dynamics. Continuous measurements of bed evolution were collected from June 2019 to May 2021 with a recording frequency of a cycle of 10 measurements every 0.5 seconds repeated every 10 minutes.
The raw data presented anomalies that need to be filtered in order to avoid wrong interpretations [Parquet, 2021; Bertier, 2020b]. Thus, the following filters were applied: (i) negative distances measured between the transducer and the bottom, (ii) negative depth measurements and (iii) maximum echo (%) below 20%. Then, the measured bed levels are corrected with Equation

5.1 given the speed of sound V_s in saline waters as a function of temperature T and salinity S [Coppens, 1980].

$$V_s(S,T) = 1449.05 + 45.7\,T - 0.0521\,T^2 + 0.00023\,T^3\left(1.333 - 0.0126\,T + 0,00009\,T^2\right)(S-35). \tag{5.1}$$

Following analyses conducted by Parquet [2021], measured bed evolution data were carefully selected on valid short time series, discarding battery failure, vertical discontinuities and malfunctions.

5.3.2 Numerical modelling

5.3.2.1 Hydrodynamic model

The TELEMAC-3D module, belonging to the open-source TELEMAC-MASCARET modelling system[1], solves the Reynolds averaged Navier–Stokes equations. The hydrostatic approximation used here eliminates the need to solve the three-dimensional Poisson equation for the dynamic pressure, thereby decreasing computational resources. A number of relationships must be specified to close the governing equations. The classical squared function dependency is used to set the bed resistance. In this work, the Strickler friction coefficient is used. The Boussinesq approximation is used for the turbulence parameterization, with eddy viscosities values calculated with the $k-\epsilon$ model. The Coriolis force is considered in the model, with the Coriolis parameter equal to $1.0909970\times10^{-4}\ s^{-1}$. The computational domain is discretized with a triangular element mesh over an horizontal plane, followed by extruding each triangle along the vertical direction into linear prismatic columns spanning the water column from the bottom to the free surface. Each column is composed of a fixed number of prismatic elements whose resolution can be adjusted accordingly, e. g. near the bottom and the free surface. Further details on the 3D hydrodynamics model and validation procedure are given by Rtimi et al. [2021b].

5.3.2.2 Sediment transport model

The hydrodynamic model was coupled with the sediment transport and bed evolution module GAIA [Audouin et al., 2019] of the TELEMAC MASCARET modeling system. This module deals efficiently with both 2D and 3D sediment transport processes and improves the treatment of graded and mixed sediments. Following the classical approach to modelling estuarine morphodynamics that consists on dividing the sediment-water domain into two overlapping subdomains. The upper one describes the mobile suspension dynamics where sediments are transported by water motion, the lower one is the bed where sediments dynamics processes are governed by erosion, deposition, consolidation and other processes. Sediment exchanges between the bottom and the water column are computed by erosion and deposition fluxes. In the Rance estuary, non-cohesive sediments are mainly transported by suspension as justified in Appendix C.1 by the Bagnold criterion [Bagnold, 1966]. Therefore, bedload transport is not considered here.
In the water column, the 3D suspended sediment transport is modelled by Equation 5.2:

$$\frac{\partial C}{\partial t} + \frac{\partial (uC)}{\partial x} + \frac{\partial (vC)}{\partial y} + \frac{\partial ((w-w_s)C)}{\partial z} = \frac{\partial}{\partial x}\left(\epsilon_{sh}\frac{\partial C}{\partial x}\right) + \frac{\partial}{\partial y}\left(\epsilon_{sh}\frac{\partial C}{\partial y}\right) + \frac{\partial}{\partial z}\left(\epsilon_{sv}\frac{\partial C}{\partial z}\right) + S, \tag{5.2}$$

[1] www.opentelemac.org

where $C = C(x, y, z, t)$ is the suspended sediment concentration, (u, v, w) are the components of the velocity along the x, y and z directions, respectively, $(\epsilon_{sh}, \epsilon_{sv})$ are the diffusion coefficients in the horizontal and vertical directions, respectively, w_s is the sediment settling velocity, and S includes source and/or sink terms.

In Equation 5.2, z ranges from the water surface elevation $WSE(x, y, t)$ to the lowest limit where the water is undisturbed $-H(x, y, t)$ (where H is the water depth). At this position, the boundary condition is given by Equation 5.3, where D, E are deposition and erosion fluxes respectively:

$$w_s C + \epsilon_{sv} \frac{\partial C}{\partial z} = D - E \tag{5.3}$$

For a single class of cohesive sediment, the deposition and erosion fluxes are computed by Equations 5.4 and 5.5, respectively.

$$D = w_s C_{z_{ref}} \left[1 - \left(\frac{\tau_b}{\tau_{cd}} \right) \right], \tag{5.4}$$

$$E = \begin{cases} M \left[\left(\frac{\tau_b}{\tau_{ce}} \right) - 1 \right] & \text{if } \tau_b > \tau_{ce} \\ 0 & \text{otherwise} \end{cases} \tag{5.5}$$

Above, $C_{z_{ref}}$ is the near-bed concentration, τ_b is the bed shear stress, τ_{cd} is the critical shear stress for mud deposition, M the Krone-Partheniades erosion law constant and τ_{ce} the critical bed shear stress for mud erosion. For a single class of non-cohesive sediment, the deposition flux is computed by Equation 5.6:

$$D = w_s C_{z_{ref}}, \tag{5.6}$$

with $C_{z_{ref}}$ the near-bed concentration. The settling velocity w_s is computed from the Stokes, Zanke and Van Rijn formulas (Equation 5.7).

$$w_s = \begin{cases} \frac{\alpha d_{50}^2 g}{18\nu} & d_{50} < 10^{-4} \\ 10\frac{\nu}{d_{50}}\left(\sqrt{1 + \frac{0.01 \alpha g d_{50}^3}{\nu^2}} - 1\right) & 10^{-4} \leq d_{50} \leq 10^{-3} \\ 1.1\sqrt{\alpha g d_{50}} & \text{otherwise} \end{cases} \tag{5.7}$$

where $\alpha = (\rho_s - \rho)/\rho$, with ρ_s the sediment density, ρ the water density, d_{50} is the median sediment diameter size, and ν is the water kinematic viscosity (here equal to $10^{-6}\ m^2/s$).
The erosion flux for a single class of non-cohesive sediment is computed by Equation 5.8:

$$E = w_s C_{eq}, \tag{5.8}$$

where C_{eq} is the equilibrium near-bed concentration computed from the Zyserman and Fredsoe formula [Zyserman and Fredsoe, 1994], see Equation 5.9:

$$C_{eq} = \frac{0.331(\theta' - \theta_{cr})^{1.75}}{1 + 0.72(\theta' - \theta_{cr})^{1.75}}, \tag{5.9}$$

where $\theta' = \mu\theta$ is the shear stress due to skin friction and μ is the correction factor for skin friction. This correction is not activated in this work ($\mu = 1$) as it present stability issues in very

shallow waters (*e.g.*, intertidal zones in the Rance upper estuary). The Shields parameter θ and the critical Shields parameter θ_{cr} are computed respectively from Equations 5.10 and 5.11.

$$\theta = \frac{\mu \tau_b}{(\rho_s - \rho) g d_{50}} \tag{5.10}$$

$$\theta_{cr} = \begin{cases} \frac{0.24}{d^*} & d^* \leq 4 \\ 0.14(d^*)^{-0.64} & d^* \leq 10 \\ 0.04(d^*)^{-0.1} & d^* \leq 20 \\ 0.013(d^*)^{0.29} & d^* \leq 72 \\ 0.045 & \text{otherwise} \end{cases} \tag{5.11}$$

Above, the dimensionless sediment diameter d^* is equal to $d_{50}(g\alpha/\nu^2)^{1/3}$.

For multiple classes of non-cohesive sediments, the total erosion flux is computed from the erosion flux of each class (Equation 5.12):

$$E_{total} = \sum_{i=1}^{N_{sand}} E(i) \cdot R(i), \tag{5.12}$$

where $E(i)$ and $R(i)$ are the erosion rate and the ratio of class i of non-cohesive sediment respectively (cf. Equations 5.8 and 5.13 respectively):

$$R(i) = \frac{M(i)}{\sum_{i=1}^{N_{sand}} M(i)}, \tag{5.13}$$

where $M(i)$ is the mass the non-cohesive sediment class i and N_{sand} is the total number of non-cohesive sediment classes.

For cohesive and non-cohesive sediment mixtures, the critical shear stress $\tau_c(mixture)$ and the erosion rate $E(mixture)$ are computed depending on the cohesive sediment fraction (F_{coh}) in the mixture (cf. Equations 5.14 and 5.15 respectively). Following [Le Hir et al., 2011], sediment mixtures can be characterized from three regimes separated by two critical mud fractions: (i) below 30%, the mixture behaves like pure sand, (ii) above 50% the mixture behaves like pure mud, whereas (iii) between 30% and 50% a linear interpolation from values computed from regimes (i) and (ii) is applied.

$$\tau_c(mixture) = \begin{cases} \tau_c(noncoh) = \theta_{cr} d_{50} g(\rho_s - \rho) & F_{coh} < 30\% \\ \tau_c(coh) & F_{coh} > 50\% \\ \frac{F_{coh} - 0.3}{0.5 - 0.3}(\tau_c(coh) - \tau_c(noncoh)) + \tau_c(noncoh) & 30\% \leq F_{coh} \leq 50\% \end{cases} \tag{5.14}$$

where $\tau_c(coh)$ is the critical shear stress for cohesive sediments and $\tau_c(noncoh)$ the critical shear stress for non-cohesive sediments.

$$E(mixture) = \begin{cases} E(noncoh) & F_{coh} < 30\% \\ E(coh) & F_{coh} > 50\% \\ \frac{F_{coh} - 0.3}{0.5 - 0.3}(E(coh) - E(noncoh)) + E(noncoh) & 30\% \leq F_{coh} \leq 50\% \end{cases} \tag{5.15}$$

where $E(coh)$ and $E(noncoh)$ are erosion fluxes for cohesive and non-cohesive sediments, computed respectively by Equations 5.5 and 5.8.

As evolution of deposited sediments in the bed is governed by several processes, it could be

Table 5.1: Calibrated parameters values retained for the morphodynamic model.

Sediment Class	Parameter	Definition	Value	Unity
Mud	d_{50}	Median diameter	20	µm
	w_s	Settling velocity	0.45	mm/s
	τ_{ce}	Critical shear stress for mud erosion	0.8	Pa
	M	Krone-Partheniades constant	10^{-4}	$kg/m^2/s$
	τ_d	Critical shear stress for mud deposition	1000	Pa
Very fine sand	d_{50}	Median diameter	100	µm
	ρ_s	Sediment density	2650	kg/m^3
	μ	Correction factor for skin friction	1	$--$
	λ	Sediment porosity	0.4	$--$
Fine sand	d_{50}	Median diameter	200	µm
	ρ_s	Sediment density	2650	kg/m^3
	μ	Correction factor for skin friction	1	$--$
	λ	Sediment porosity	0.4	$--$

modelled following various strategies. The simplest one consists of considering the bed as a homogeneous layer of sediment with a constant bed sediment concentration. Therefore, the thickness of the bed changes according to erosion and deposition fluxes only. In case of single class of non-cohesive sediment, bed evolution is thus computed by the Exner equation (eq. 5.16), with b is the bed elevation and λ is the non-cohesive sediments porosity. In case of sand-mud mixture, deposition fluxes D of cohesive and non-cohesive sediments are first computed respectively by Equations 5.4 and 5.6. Then, the resulted sand and mud masses are added directly to the superficial layer contributing to its thickening with respect to filling the void by cohesive sediment. More sophisticated approaches exist to model the vertical composition of the bed by a multi-layer model with variable sediment bed concentration along the considered layers and activating consolidation processes [Thiebot, 2008; Le Hir et al., 2011]. These models provide details analyses about bed dynamics and are necessary in case single layer models do not capture morphodynamics tendencies. For this work, the calibrated single-layer model was sufficient to capture the main features of bed evolution in the Rance estuary (section 5.4) and a multi-layer morphodynamic model provided complementary bed level changes, namely over neap tides (Appendix C.2). Thanks to its reasonable CPU time and reliable results, the single-layer morphodynamic model was deployed to investigate sediment dynamics in the Rance estuary.

$$(1-\lambda)\frac{\partial b}{\partial t} = D - E \tag{5.16}$$

Parameters needed for the morphodynamic model are summarized in Table 5.1.

5.3.2.3 Tidal power plant implementation and boundary conditions

The computational domain is extended from the upstream limit (Chatelier lock, cf. Figure 5.1) to the oceanic open boundary (10km downstream of the TPS). It was discretized with an unstructured triangular mesh in the horizontal direction by the BlueKenue pre- and post-processing tool [Barton, 2019], then it was extruded along the vertical direction to form triangular prisms, covering the volume delimited by the bottom and the water level. The horizontal mesh

Table 5.2: Operating modes of sluice gates and turbines.

Structure	Sluice gates		Turbines					
Operating mode	G.O.	G.C.	F.O.	D.O.	I.T.	D.T.	D.P.	T.O.
Definition	Gates Open	Gates Close	Filling On	Draining On	Inverse Turbining	Direct Turbining	Direct Pumping	Turbines Off
Tidal phase	Flood Ebb	Flood Ebb	Flood	Ebb	Flood	Ebb	Flood	Flood Ebb

consisted of 199,625 nodes and 389,766 elements. Cell length varies from $50m$ in the offshore zone, down to $10m$ in near the barrage and within the upper estuary (between Mordreuc and the Chatelier lock, Figure 5.1). The mesh size is $20m$ elsewhere. Then, 8 layers were specified at each horizontal mesh along the vertical direction, *i.e.* each prismatic element's thickness depends on the bottom elevation. Bed level information was extracted from high-resolution bathymetry dataset dating from 2018 (Lidar and field survey records) that was used by the model of Rtimi et al. [2021a]. Three sediment classes were deployed to represent the composition of the bed : (i) fine sand with a representative median diameter equal to $200\mu m$, (ii) very fine sand with a representative median diameter equal to $100\mu m$ and (iii) mud with representative median diameter equal to $20\mu m$. Initial sediment distribution for numerical simulations was obtained after a spin-up period of two fortnights and captures the main zones of sediment distribution observed in the map of 1994 (Figure 5.2).
Hydrodynamic boundary conditions were set as follows: (i) water levels and depth-averaged velocity components were imposed at each node on each vertical plan of the oceanic boundary, through 11 tidal constituents (M2, S2, N2, K2, K1, O1, P1, Q1, M4, MS4 and MN4) from the OSU TPXO European Shelf 1/30 regional model [Egbert and Svetlana, 2002]; (ii) river discharge from the Rance river was set up to $5m^3/s$ at the upstream limit (Chatelier lock). For sediment transport model, a constant suspended sediment concentration value was set to $0g/l$ at both oceanic and river boundaries.
The implementation of tidal power plant in TELEMAC-3D follows the methodology proposed by Rtimi et al. [2021a,b]. The latter consisted on modelling the array of turbines and sluice gates by couples of sources and sinks from each side of the plant. For instance, during filling phase (Table 6.2), nodes representing the turbines on the sea-side of the plant are seen by the model as sinks, and nodes representing the turbines on the estuary-side of the plant are seen by the model as sources. This methodology showed its capacity to correctly simulate 2D and 3D hydrodynamics in the Rance estuary [Rtimi et al., 2021a,b]. It was thus adopted in this work. Since particles could be transported only by suspension in this work, suspended sediment concentrations are imposed explicitly according to flow's direction. Indeed, during flood , flow rates at the TPS are positive (into the estuary), SSC at nodes on the sea-side of the plant are implicitly computed by the numerical model, their values are imposed thus at corresponding nodes on the estuary-side of the plant. Vice versa during ebb, flow rate at the TPS are negative (into the sea), SSC at nodes on the estuary-side of the plant are thus implicitly computed by the numerical model, their values are imposed then at corresponding nodes on the sea-side of the plant.

5.3.2.4 Sediment flux computation

To assess the influence of the plant on sediment dynamics in the estuary, residual advective sediment flux F_S and cumulative sediment flux F^S_{cumul} over a time period P were evaluated from Equations 5.17 and 5.18 respectively following [Geyer et al., 2001; Kim et al., 2021]:

$$F_S = < H > \int_0^1 < U(z^*) >< SSC(z^*) > dz^*; \quad z^* = z/H \tag{5.17}$$

$$F^S_{cumul} = \int_0^P F_S dt, \tag{5.18}$$

where $< H >$, $< U >$ and $< SSC >$ are tidally averages of water depth H, along-channel velocity U and suspended sediment concentration SSC respectively.

5.4 Numerical model validation

The numerical model was first validated from water level measurements at three different locations along the estuary from continuous data available over the year 2020. Then, simulated suspended sediment concentration and bed evolution over two fortnights were validated from STPS-SAMBAT and ALTUS data respectively. The following numerical results were obtained after a spin up of 28 days and with the calibrated parameters (cf. Table 5.1). Due to technical issues during field surveys, only few reliable measurements were available at several probes over a continuous neap-spring tidal cycle. Therefore, two periods were chosen to validate the hydro-morphological model: July 20th 2020 to August 3rd 2020 and November 24th 2020 to December 8th 2020.

5.4.1 Water levels

As the Rance estuary is a highly influenced environment due to the presence of the TPP [Rtimi et al., 2021a,b], the proper simulation of sediment transport mechanisms and morphological changes depends heavily on the correct simulation of flow rates passing through turbines and sluice gates. This can be characterized from water surface elevation along the estuary (Figure 5.3). Water levels are well simulated by the numerical model over both monitoring periods in the lower estuary (M1), in the middle-estuary (M2) and in the upper estuary (M3). The tide distortion caused by the presence of the plant is correctly reproduced inside the estuary. Moreover, oscillations of the water-surface elevation measured at M1 location during high-tide are also well captured by the numerical model. These seiche-like fluctuations of the water surface [Rtimi et al., 2021a] are stronger in the upper-most tidal gauge station (M1). Furthermore, computation of Normalized Root Mean Square Errors (NRMSEs) [Wikipédia, 2019] at the three locations along the estuary (Table 5.3) assessed the ability of the model at reproducing the tidal propagation, with NRMSEs values below 5%. Finally, currents validation from Acoustic Doppler Current Profiler (ADCP) survey was previously performed in [Rtimi et al., 2021b].

5.4.2 Suspended sediment dynamics

Measured and simulated tide-averaged sub-surface (80cm below the surface) SSC values are compared at four locations along the estuary (T1, T2, S1 and S2) during two fortnightly tidal cycles in Figures 5.4 and 5.5. The numerical model reproduces reasonably well the measured

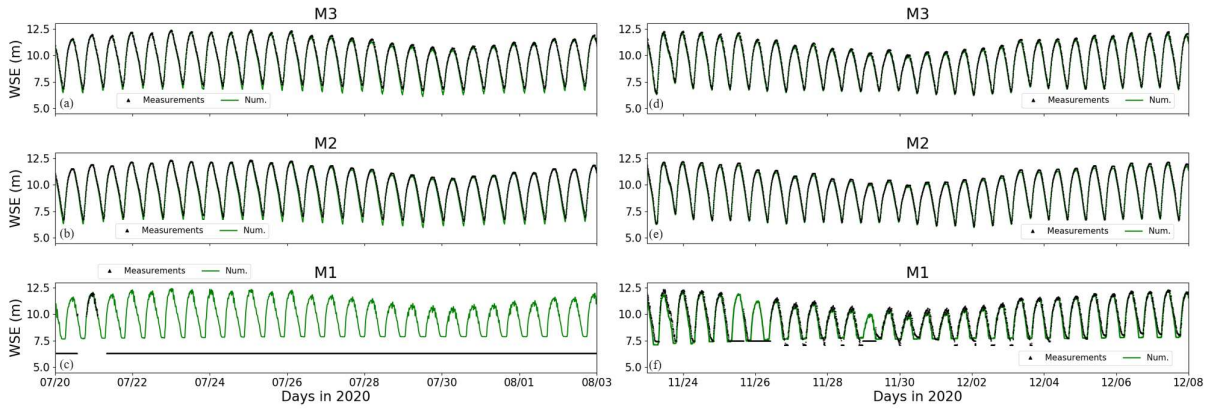

Figure 5.3: Comparison of water surface elevation between numerical and measured data within two periods: (a;b;c) July 20th - August 3rd 2020 and (d;e;f) November 24th - December 8th 2020. Green lines and black triangles indicate respectively numerical and measured data. The measurements are not reliable during July 20th - August 3rd 2020 at M1 station because of technical issues.

SSC in terms of magnitude, neap-spring variation and winter-summer phasing. SSC values at locations T1 and T2 are significantly modulated by the fortnightly hydrodynamic forcing, with an increasing resuspension during spring tides due to strong currents (Figures 5.4.c, 5.4.d and 5.5.b). Further downstream, at locations S1 and S2, the near-surface SSC values are considerably lower (below 20 mg/l) than the values measured at upstream probes (cf. Figures 5.4.b and 5.5.a), as the water column at these stations is deeper. The numerical model is also able to capture the ETM formation, which is located near the T2 probe with a maximum concentration value of $\sim$ 70 mg/l. These results are also consistent with previous studies, e.g. [Bonnot-Courtois et al., 2002; Thiebot, 2008]. Well-calibrated hydrodynamic models are usually able to predict water levels and currents with low Normalized Root Mean Square Error values (NRMSEs), see e.g. [Rtimi et al., 2021a], which is not often the case for sediment transport models. Hence, they need to be associated to margin errors to quantify the confidence interval in numerical results. NRMSE values computed at locations T1, T2, S1 and S2 were summarized in Table 5.3. Station T2 presented the higher value of NRMSEs, always below 50%, while error margins at downstream stations (S1 and S2) and the uppermost station (T1) are lower than 10%. Comparing to confidence ranges of simulated SSC in macrotidal estuaries [Grasso et al., 2018; Toublanc et al., 2016; Amoudry et al., 2014], the present error margins are considered satisfactory to investigate suspended sediments dynamics in this complex estuarine system.

5.4.3 Mudflats evolution

In the present work, high-frequency data (one measure per tidal cycle) is used to assess the capability of the model at reproducing the bed evolution at selected locations. Measured and simulated tide-averaged bed evolution are compared at locations A1, A2 and A3 in Figures 5.6 and 5.7. The measured bottom evolution is reasonably well reproduced by the numerical model during both simulated periods in terms of magnitude on the neap-spring tidal scale and winter-summer scales. A general tendency to sedimentation is noticed at the three locations, with increasing rates from probe A1, A2 to A3 and variable cumulative rate in each fortnight (*e.g.* at A3, a bottom rise of 6.5cm is observed in July against 2.75 cm in November). In addition,

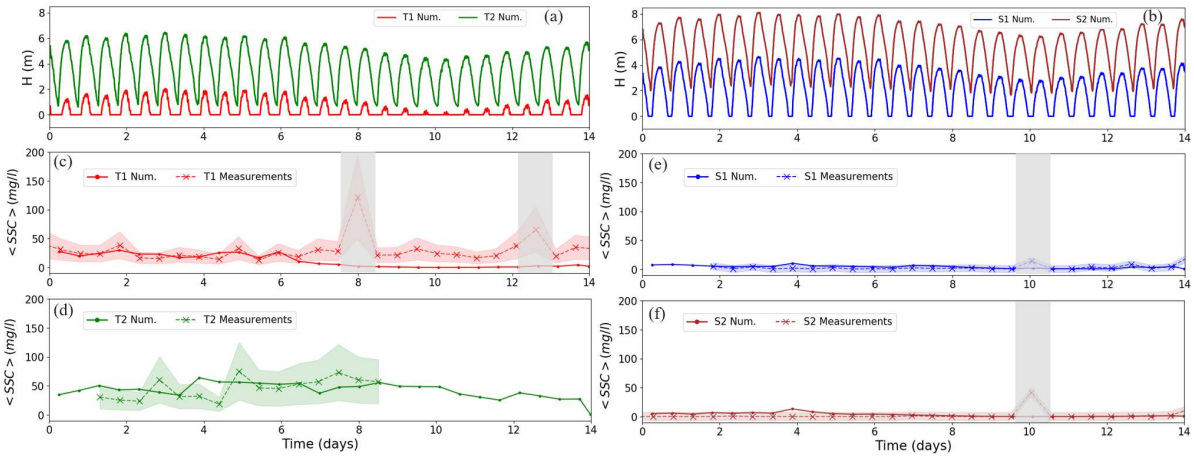

Figure 5.4: Simulated water levels at (a) T1, T2 and (b) S1, S2. Measured and simulated tide-averaged suspended mud concentration at (c) T1, (d) T2, (e) S1 and (f) S2. (see locations in Figure 5.1). Light colored areas represent measurements uncertainties. Light-grey box delimit periods where the probe is near the bottom, thus the probe measures bed mud concentration rather than suspended mud concentration. Period corresponding to July 20th - August 3rd 2020.

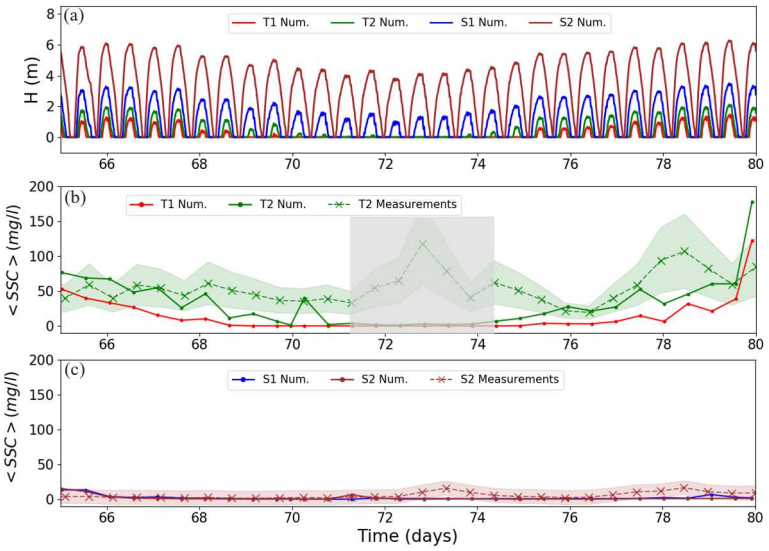

Figure 5.5: Simulated water levels at (a) T1, T2, S1 and S2. Measured and simulated tide-averaged suspended mud concentration at (b) T1, T2 and (c) S1, S2. (see locations in Figure 5.1). Light colored areas represent measurements uncertainties. Light-grey box delimit periods where the probe is near the bottom, thus the probe measures bed mud concentration rather than suspended mud concentration. Period corresponding to November 24th - December 8th 2020.

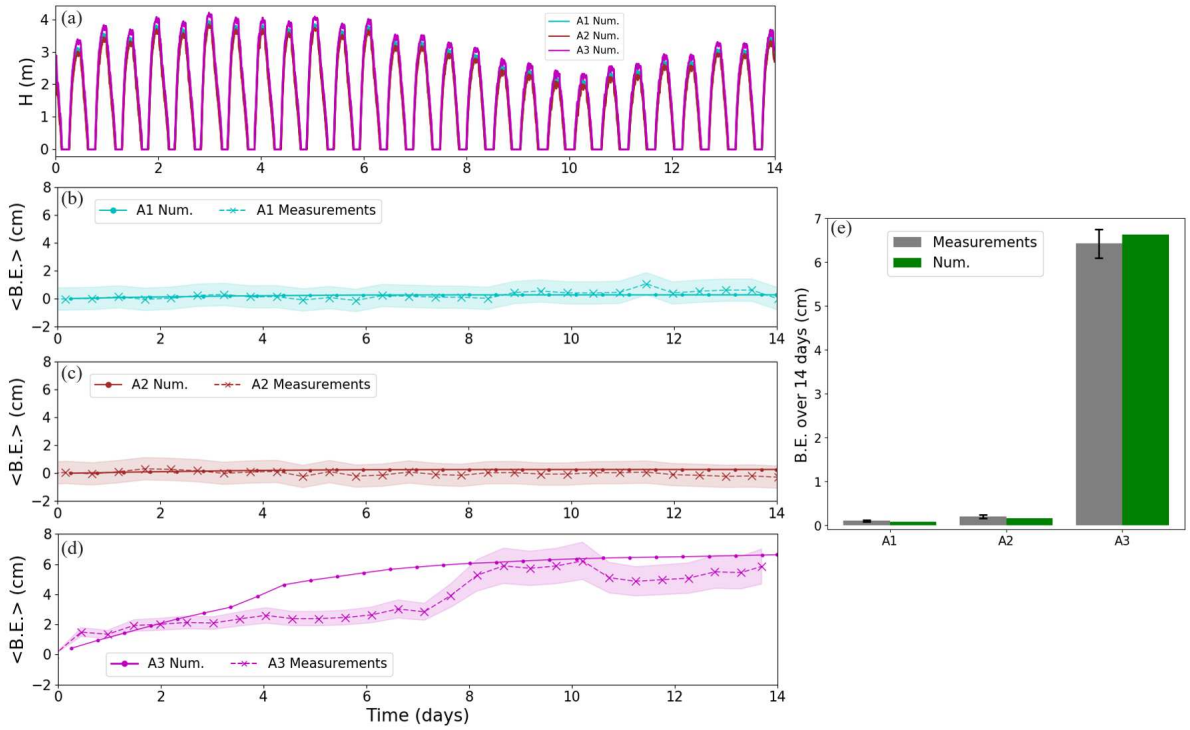

Figure 5.6: (a) Simulated water levels at A1, A2 and A3 (see locations in Figure 5.1). Measured and simulated tide-averaged bed evolution at (b) A1, (c) A2 and (d) A3 locations. (e) Cumulative bed evolution over a fortnightly tidal period. Light colored areas represent measurements uncertainties. Period corresponding to July 20th - August 3rd 2020.

the sedimentation rate during spring tide (days 1-3 in Figure 5.6.b) is more important than in neap tide (days 9-10 in Figure 5.6.b). Although the morphological model simulated well the cumulative bed evolution over the whole neap-spring tidal cycle (cf. Figures 5.6.c, 5.7.c and Table 5.3), a small scale dynamic effect such as the bottom decreasing of $\sim$ 1 cm is observed at A3 during a neap tide (day 10 in Figure 5.6.b) which was not captured by the numerical model. Indeed, according to field data analyses, this decrease might correspond to mud consolidation process that was not taken into account by the numerical model. Moreover, the computation of bed evolution NRMSE values between numerical results and measurements (Table 5.3) showed low margin errors, below 7%, at station A1 (the furthest downstream) at both tide-averaged and neap-spring tidal cycle time scales. Nevertheless, NRMSEs at stations A2 and A3 present high values between 32 - 60 % on spring tides, below 20 % on neap tides and lower margins below 10% at the time scale of a fortnight. Thus, the morphological model provides satisfactory results at reproducing bed evolution processes in this macrotidal estuary over fortnightly time scales.

5.5 Present-day sediment dynamics in the Rance estuary

This section aims to investigate the present-day sediment dynamics in the Rance estuary based on conditions of the year 2020. Representative time windows during spring tide and neap tide were selected to assess detailed SSC variations and its correlation with plant's operation modes, currents and residual components. Afterwards, the morphological evolution in the

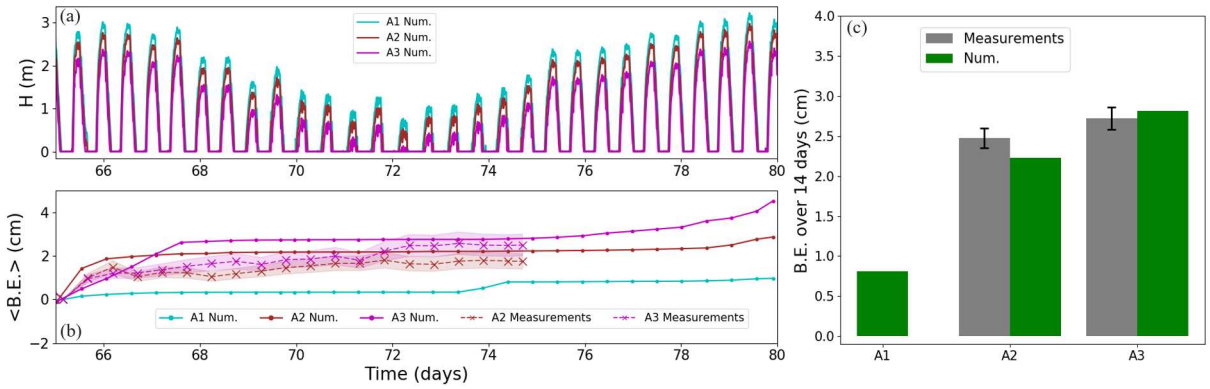

Figure 5.7: (a) simulated water levels at A1, A2 and A3. Measured and simulated (b) tide-averaged bed evolution and (c) cumulative bed evolution over a fortnight at A1, A2 and A3 locations.(see locations in Figure 5.1). Light colored areas represent measurements uncertainties. Period corresponding to November 24th - December 8th 2020.

Table 5.3: Normalized Root Mean Square Errors (NRMSE) [%] computation between numerical results and measurements in terms of water levels, tide-averaged suspended sediments concentration and tide-averaged bottom evolution.

Variables	WSE NRMSE [%]			<SSC> NRMSE [%]				<BE> NRMSE [%]		
PeriodsStations	M1	M2	M3	T1	T2	S1	S2	A1	A2	A3
Neap tides	3.3	3.4	3.6	—	—	6.1	10	6.7	6.1	16
Spring tides	4.1	4.6	4.9	9.2	41	8.4	4.5	5.1	32	60
Fortnight tidal cycle	3.7	4.1	4.3	—	—	7.2	7.4	6.1	9.8	7.5

whole estuary is tested over a short time scale (fortnight) and over a longer time scale (3 months).

5.5.1 ETM location in the Rance estuary

The upstream of the Rance estuary is characterized by the presence of shallow banks where significant local resuspension is observed. The dynamics in these specific areas is different from that governed by the estuarine turbidity maximum, which makes it difficult to correctly estimate the ETM location. Following [Bonnot-Courtois and Le Vot, 1993; Thiebot, 2008], the tide-averaged SSC over a spring tidal cycle is a relevant indicator to asses the mean zone where suspended matter is concentrated. Figures 5.8.a-c illustrate the horizontal distribution of depth-averaged tide-averaged SSC for the three sediments classes considered, namely mud (clay and silt) with representative median diameter equal to $20\mu m$, very fine sand with a representative median diameter equal to $100\mu m$, and fine sand with a representative median diameter equal to $200\mu m$, and Figure 5.8.d represents the vertical distribution of the SSC along the estuarine channel (cf. Figure 5.1 for channel's location). The ETM zone is located approximately 2km from the Chatelier lock with a peak concentration of $100mg/l$ (Figure 5.8.d). Downstream of the ETM area, SSC does not exceed $10mg/l$. In the whole estuary, the suspended matter is mainly composed of cohesive sediments and a lower contribution of non-cohesive sediments: $\sim 10\%$ of $200\mu m$ sand and less than 5% of $100\mu m$ sand (cf. Figures 5.8.a-c). Furthermore, the vertical structure of the ETM is well captured by the numerical model, with highest concentrations of $\sim 100mg/l$ near the bed, then $\sim 60mg/l$ in the middle of the water column and $\sim 40mg/l$ near the surface. High SSCs are also noticed 3km from the Chatelier lock (Figure 5.8.d). The vertical structure of suspended matter in this zone shows that these high concentrations are mainly generated by local resuspension of cohesive sediments present on the left mudflat bank near Mordreuc (cf. Figure 5.1). Historically, in 1991, the ETM was located directly upstream of the Chatelier lock (dashed orange line in Figure 5.8.d) [Bonnot-Courtois and Le Vot, 1993]. Actually, 1989 was a drought year with rare rainfall periods, the river was thus on its minimum flow discharge ($\sim 0m^3/s$). Then, significant precipitations occurred in 1992 and restored an acceptable river flow rate which allows the migration of the ETM 2km downstream in 1993 (dashed grey line in Figure 5.8.d). As the period simulated in this work represent ordinary rainfall conditions, the simulated ETM location is consistent with that measured in 1993 [Bonnot-Courtois and Le Vot, 1993]. Furthermore, this diachronic comparison between ETM locations in 1993 and 2020 shows a stable mean position of ETM under the same river discharge conditions. Consequently, the following analyses on SSC dynamics focus on the upper estuary (*i.e.*, 0-7.5km from the Chatelier lock) where the suspended matter is concentrated.

5.5.2 Impact of TPS operation modes on SSC dynamics

Hydrodynamic processes in the Rance estuary are significantly influenced by the plant's operating modes [Rtimi et al., 2021a]. Therefore, high-frequency (10 min) SSC variations are examined simultaneously with turbines and sluice gates operating modes at selected locations in the upper estuary during both spring tides (Figures 5.9.a;b) and neap tides (Figures 5.9.c;d). As probe T2 is located in the ETM area (see Figure 5.1), SSC peak values are of $200mg/l$ during spring tide ($130mg/l$ in neap tide). Upstream at T1 location, peak suspended concentrations drops to $40mg/l$ in spring tide ($10mg/l$ in neap tide). Further downstream, at S1 and S2 locations, peak SSC does not exceed $20mg/l$ in spring tide ($5mg/l$ in neap tide). These peak values are only noticed during flood and specifically during the estuary's filling phase where turbines and sluice gates are open simultaneously (F.O. and G.O. phases, Table 6.2). This could be explained

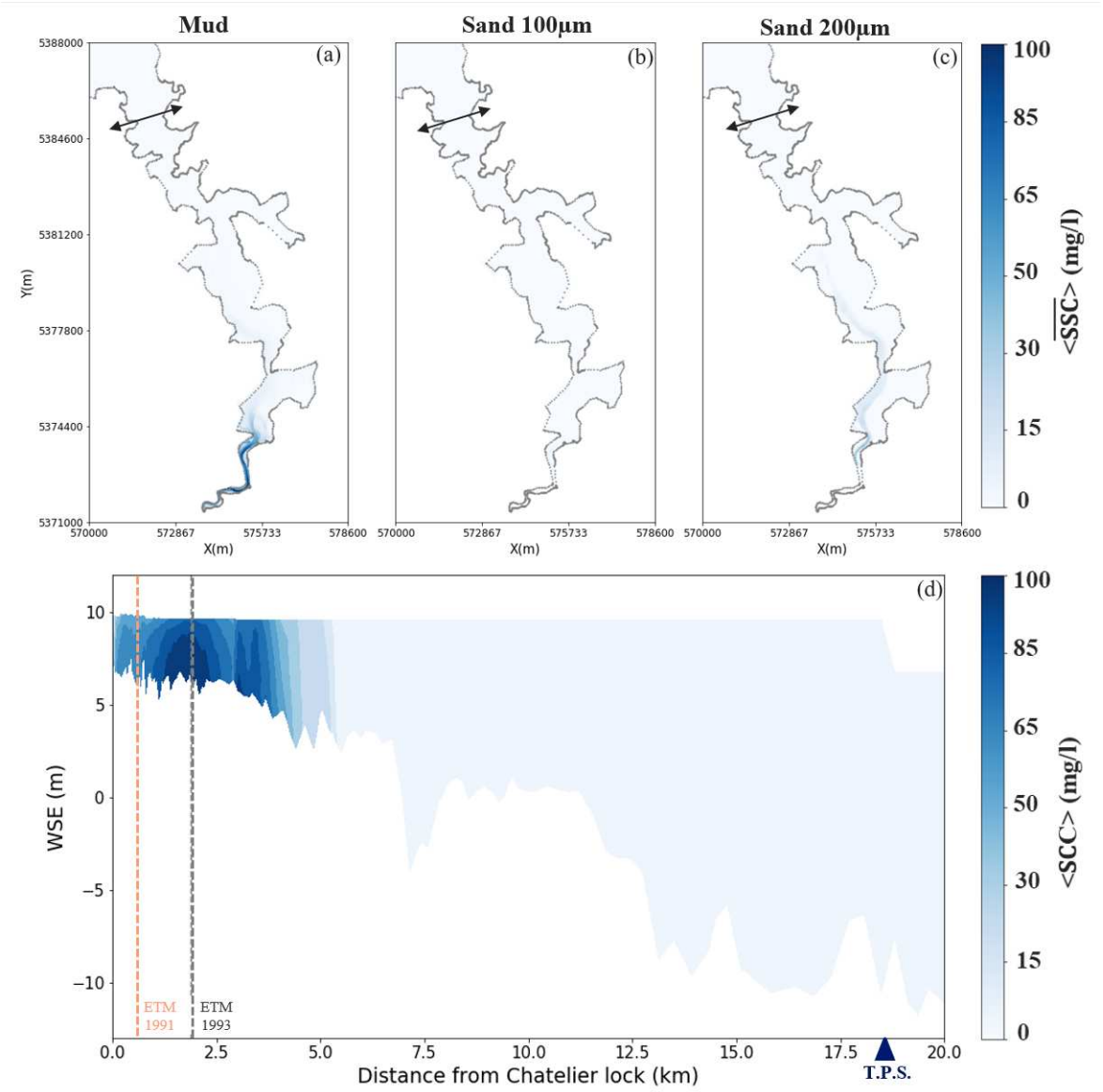

Figure 5.8: Depth-averaged and spring tide-averaged concentration of suspended (a) cohesive sediments, (b) sand of 100μm and (c) sand of 200μm. (d) Vertical distribution of spring tide-averaged SSC along the estuary's channel (see Figure 5.1 for channel's location).

by the jet generated by the sluice gates and also by peak velocities reached in the whole estuary during this time period [Rtimi et al., 2021a]. Moreover, an increase of SSC values is also observed during ebb, specifically on spring tide (Figure 5.9.b) with values 10 times lower than peak-flood SSC. Contrastingly, these peak-ebb concentrations do not occur during draining mode (D.O. phase, Table 6.2) but during the power generation mode (D.T. phase, Table 6.2). It is noteworthy that peak-flood SSC observed at the four locations follows the propagation of an advective travelling wave. Indeed, according to Figure 5.9, the first peak is noticed at location S2 which is 7.5km from the Chatelier lock, the second peak is noted at location S1 which is 5km from the Chatelier lock, the third peak is recorded at location T2 which is 2km from the Chatelier lock and finally the fourth peak is noticed at T1 located 0.5km from the Chatelier lock. This SSC propagation wave is obviously correlated to tide propagation in the estuary (cf. Figures 5.9.a;b) on one hand, and also to local currents on the other hand. Indeed, probes T1 and S1 emerge for 4 and 2 hours respectively (Figure 5.9.a), the arrival of the tidal wave during flood corresponds also to the arrival of suspended sediments that are accumulated progressively from the estuary's downstream to its upstream. Thus, the suspended matter in each location is composed of (i) local materials resuspended due to bed shear stress and (ii) advected particles from the estuary's upstream. To analyze these processes, SSC values were plotted against the along-channel velocity over one spring tidal cycle (days 5.9 - 6.4) at stations T1, T2 and S1 (Figures 5.10.a;b). At location T2 (Figure 5.10.a), increasing velocity implies a linear increase of SSC during the estuary's filling stage (flood's beginning). This trend corresponds to the resuspension of local particles. Then, a significant increase of concentration occurred (also during the basin filling phase) while currents slightly increase to reach the maximum of $0.5 m/s$. It is a combined effect of resuspension and advection. Afterwards, decreasing concentration values towards the end of the flood (during G.C. phase, Table 6.2), related to the decreasing velocity, originates sediment deposition. At S1 (Figure 5.10.b), local resuspension behavior is noticed during the first sequence of flood, followed by particle deposition with decreasing currents. This effect is observed downstream of the ETM location. At T1 (Figure 5.10.b), the considerable increase of SSC while the velocity is constant is purely an effect of particles advection only. This particular concentration behavior characterizes suspended sediments dynamics in areas upstream of the ETM zone. Furthermore, the asymmetry between flood and ebb (Figure 5.10.b) is noteworthy at all stations. Indeed, the Rance estuary is a flood dominant system [Rtimi et al., 2021a] with low river flow rate at the uppermost boundary comparing to flow rate passing through the plant. These hydrodynamic conditions made it difficult to allow sediments significant resuspension nor their transport during ebb. Moreover, as depicted previously, the simultaneous opening of sluice gates and turbines generates the peak flood currents and thus peak flood SSC. However, peak ebb currents occurs during the power generation stage (turbines on D.T. mode, Table Table 6.2) while sluice gates are closed. Consequently, lower SSC values are observed due to weaker peak ebb currents. In summary, on the scale of a tidal cycle, the operating modes of the power station modulates the suspended sediments dynamics in the Rance estuary. During times of strong flood currents, corresponding to the basin's filling phase (both turbines and sluice gates are open), resuspension and particles transport take place. During times of strong ebb currents, corresponding to electricity production phase (only turbines are open), sediments could be resuspended locally but not transported further than 3km from the uppermost limit due to insufficient ebb currents and low river discharge. But what happens on a larger time scale?

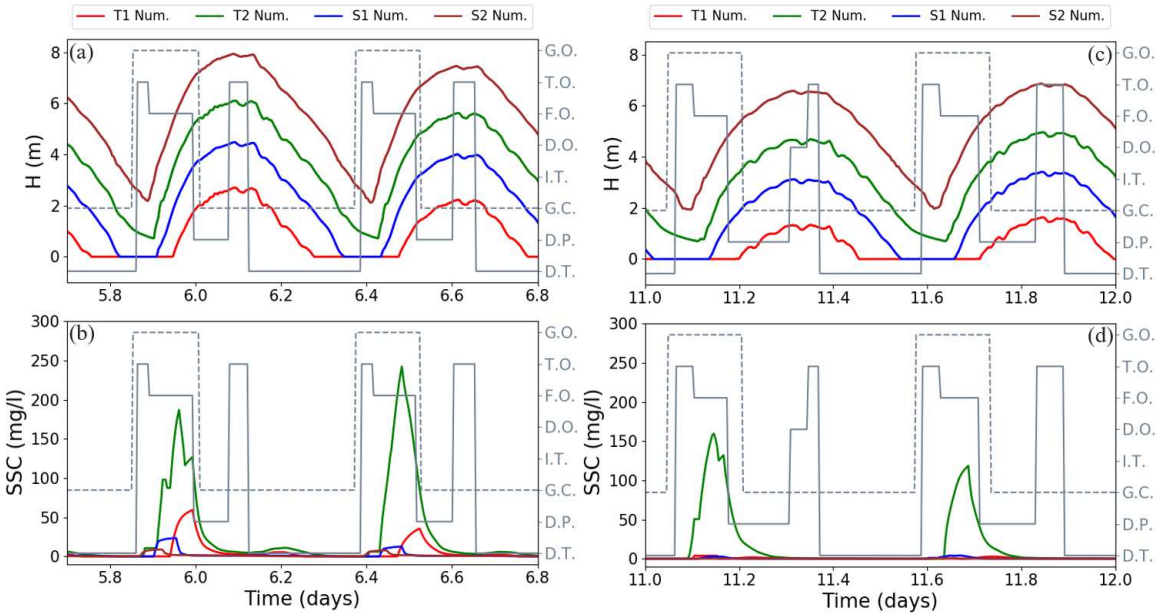

Figure 5.9: Water depth and near-surface suspended mud concentration at T1, T2, S1 and S2 (see Figure 5.1 for locations) during (a,b) spring tides and (c,d) neap tides. Grey filled- and dashed-lines represent turbines and sluice gates operation modes respectively (see Table 6.2).

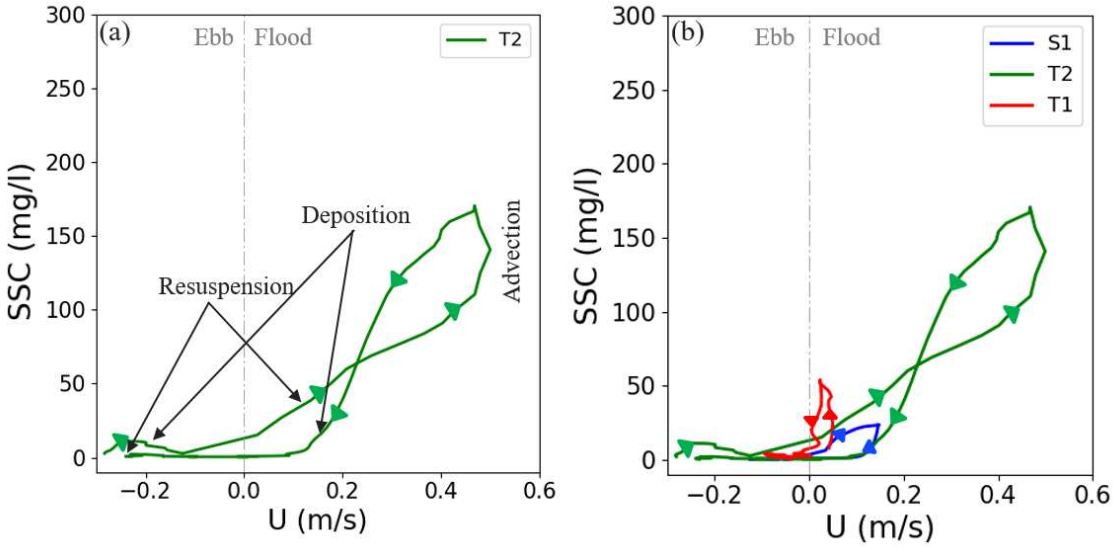

Figure 5.10: Correlation between suspended mud concentration and local currents over a spring tidal cycle at (a) location T2 and (b) locations T1, T2 and S1. (see Figure 5.1 for probes locations).

5.5.3 Residual and cumulative sediment fluxes

To assess sediment transport pathways on a fortnightly time scale or even longer time scales, residual and cumulative sediment fluxes are suitable indicators to be examined [Valle-Levinson and Guo, 2009; Rtimi et al., 2021a; Kim et al., 2021]. These quantities were computed at stations T2 and S2 (Figures 5.11.a-e) as they are always submerged (cf. Figure 5.11.a). Residual depth-averaged SSC ($< \overline{SSC} >$) at station T2 between spring tide and neap tide is showed in Figure 5.11.b. A maximum residual concentration of $52 mg/l$ on day 4.5 is observed during spring tide, and a minimum residual concentration of $20 mg/l$ on day 12.1 is noticed during the neap tide. As for station S2, the water is almost clear with residual concentrations near to $0 mg/l$. Regarding residual depth-averaged along-channel currents ($< \overline{U} >$), the distinct neap-spring tidal variation is noticed in both stations T2 and S2 (Figure 5.11.c). Residual currents are stronger at station S2 (maxima of -0.045m/s in spring tide and -0.002m/s in neap tide) comparing to T2 (maxima of -0.025m/s in spring tide and -0.011m/s in neap tide). Actually, S2 is located at the estuary's narrowness (cf. Figure 5.1) where currents are strengthen by the decrease of the wet section [Rtimi et al., 2021b]. Furthermore, as $< \overline{U} >$ is always negative, meaning that the residual flux is oriented towards the interior of the estuary. The residual advective sediment flux (F_S) is also continually negative (into the estuary) with spring tide peak reaching -0.004 $kg/m/s$ on day 4.5 at T2 (-0.003$kg/m/s$ on day 3.9 at S2) and neap tide peak close to $0 kg/m/s$ for both T2 and S2. The depth-averaged cumulative sediment flux over the period of a fortnight is thus negative, with varying slopes between spring and neap tides. Indeed, about 40 tons/m (resp., 10 tons/m) of sediment was delivered into the estuary's upstream (T2) over spring tides (resp., neap tides), between day 0 and day 7 (resp., between day 7 and day 14). Contrastingly, the cumulative sediment flux further downstream (S2) is also oriented towards the estuary but with 2 times less materials per meter (-18 tons/m at S2 versus -20 tons/s at T2 on spring tides). In a nutshell, sediments are accumulated to the inside of the upstream area (up to 7km from the river boundary) mainly during spring tides.

5.5.4 Morphological evolution of the Rance estuary

The numerical model showed its ability to simulate morphological evolution in localized points over time scales of a fortnight (section 5.4.3). In this section, its reliability and robustness is assessed over a longer time scale. To this goal, bathymetry datasets, covering the upper estuary and available on February 1st and May 13th 2021 (3 months) were deployed. The horizontal resolution of the available measurements was below $1m$ while the horizontal resolution of the numerical model is $10m$. Therefore, the measured dataset was interpolated on the numerical mesh in order to ensure fair comparison between measured data and numerical results.
Measured and simulated bed evolution between February and May 2021 were first compared in the upper estuary (Figures 5.12.a;b). The numerical model captures correctly the global morphological evolution tendency in the channel and on the banks. Indeed, $1.5km$ downstream of the Chatelier lock, a general tendency to sediments deposition in the main channel is observed while eastern and western banks are stable. To deeply analyze this behavior, measured and simulated bed evolution along with the initial bathymetry were plotted on the cross-channel profile P1 (Figure 5.13.a). Both measured and simulated bed evolution along this profile follow a log-normal distribution with significant sediments deposition in the main channel. Although the numerical model underestimates sedimentation in the channel's trough and overestimates it elsewhere, the averaged cross-channel bed evolution is well simulated, with error margins of 8% (measured $23cm$ vs simulated $25cm$). Indeed, the numerical mesh resolution in this

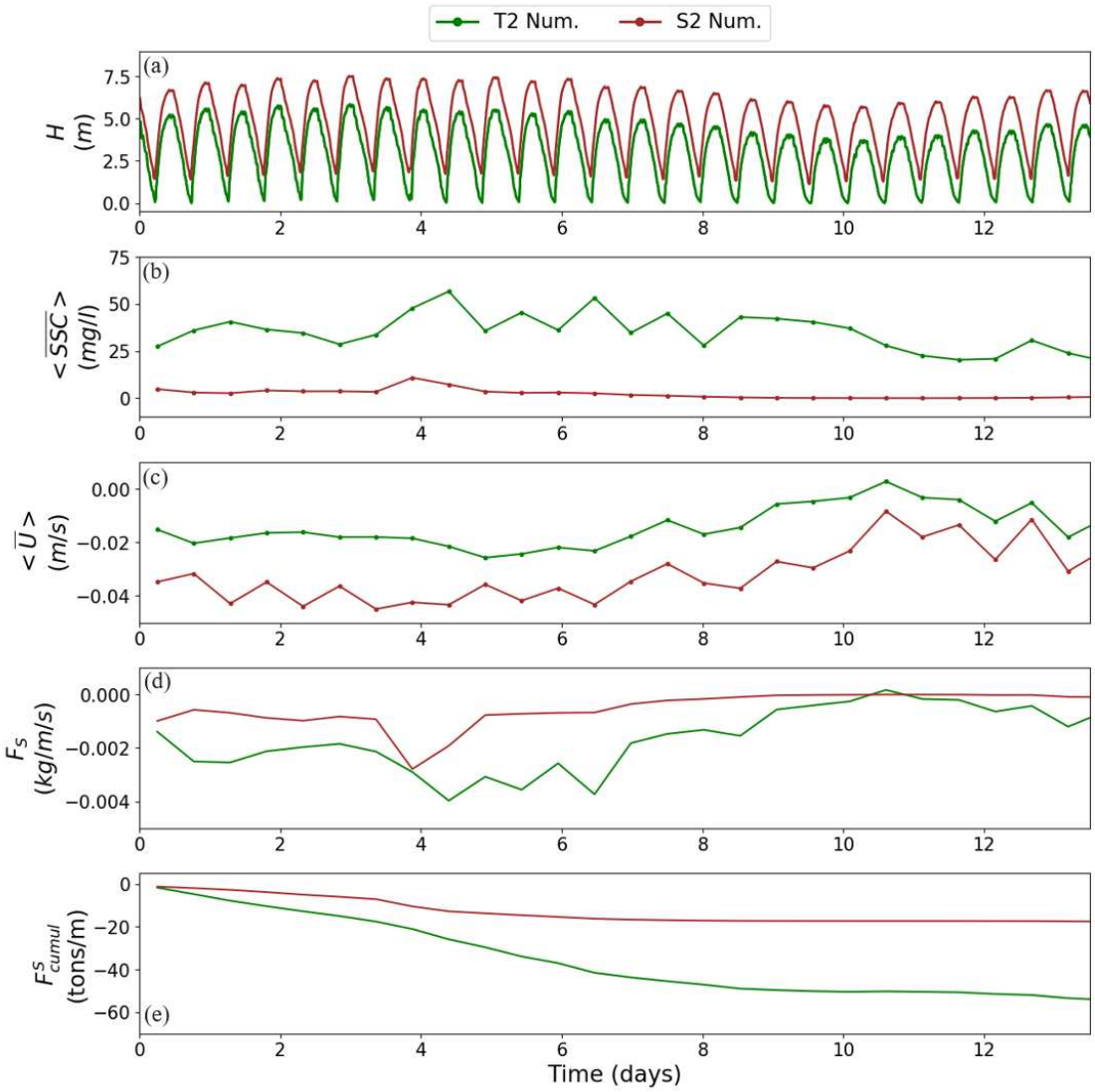

Figure 5.11: Residual components at positions T2 and S2 (see Figure 5.1 for locations): (a) water depth, (b) depth- and tide-averaged suspended sediments concentration, (c) residual depth-averaged along-channel velocity, (d) residual sediment flux (Equation 5.17), and (e) cumulative net sediment flux (Equation 5.18).

zone (equal to 10m) is not fine enough to capture the real definition of the main channel in this area. Consequently, the numerical channel is larger and less steep comparing to the real channel. Therefore, the numerical morphology promotes sediment deposition on a larger through compared to the real configuration.
Then, between 1.5 and 2.5km downstream of the Chatelier lock, dredging operations were performed between 5th and 12th March 2021 (light-grey box in Figure 5.12.a). As these occasional operations are not taken into account in the numerical model used in this work, comparison between simulations and measurements is not relevant. However, it should be noted that the numerical model exhibits a similar tendency to sediment deposition in the main channel as in the zone upstream of the dredging area.
Contrastingly, between 3.5 and 4.5km downstream of the Chatelier lock, the eastern channel is eroded and the western channel is subject to sediments deposition. Similar to profile P1, measured and numerical bed evolution are compared over the cross-channel profile P2 in Figure 5.13.b. Indeed, the sedimentation rate over 3 months can reach up to 10cm in the west secondary channel (50-150m from the left bank). Then, smaller accretion is observed on the central shoal (150-350m from the left bank) with rates below 3cm over 3 months. Further east, the main channel (350-475m from the left bank) is subject to erosion with a bulk rate of 68cm over 3 months. Margin errors related to simulated bed evolution rates are below 5% in the secondary channel and central shoal, and of 25% in the main channel. These margin errors are mainly explained by the horizontal resolution of the numerical model. Therefore, a smaller scale model focusing only on the upper estuary with a horizontal resolution of 1m would be more appropriate to simulate bed evolution upstream with lower margin errors. However, the present model is able to correctly simulate the main morphological tendencies. Thus, it was deployed to assess bed evolution over the whole estuary.
Figure 5.12.c shows that significant bed evolution occurs in the upper estuary. Indeed, between 4.5 and 5km from the Chatelier lock, an erosion rate of 40cm over 3 months is noticed in the western channel and an accretion rate of 10cm is observed in the eastern mudflat. Further downstream, between 8.5 and 11.5km downstream of the Chatelier lock, erosion rates are below 15cm over the 3 months period. Finally, there isn't any substantial bed evolution elsewhere. In summary, the numerical model is able to reproduce relevant morphological changes in the estuary over a time period spanning 3 months. Moreover, the important morphological changes are concentrated in the upper estuary.

5.6 Influence of the tidal power station on sediment dynamics

Two configurations were proposed to evaluate the influence of the tidal power plant on the sediment dynamics. The first is the present configuration of the Rance estuary with the tidal power station (as presented in section 5.5). The second is an hypothetical configuration consisting on removing the plant from the estuary's mouth. Both simulations were performed using the same tidal and hydrological conditions, and the same physical parameters. As seen in section 5.2, a spin-up period of two fortnights is sufficient to correctly initialize sediment distribution in the Rance estuary. Consequently, analyses of TPS impact on sediment dynamics are performed after three fortnights to ensure a stabilisation of sediment distribution. The scenarios were first analyzed in terms of suspended sediment dynamics on time scales ranging from one tidal cycle to a period of a fortnight. Then, morphological evolution of the Rance estuary simulated over 3 months by both configurations is discussed to quantify the impact of the plant on bed level change.

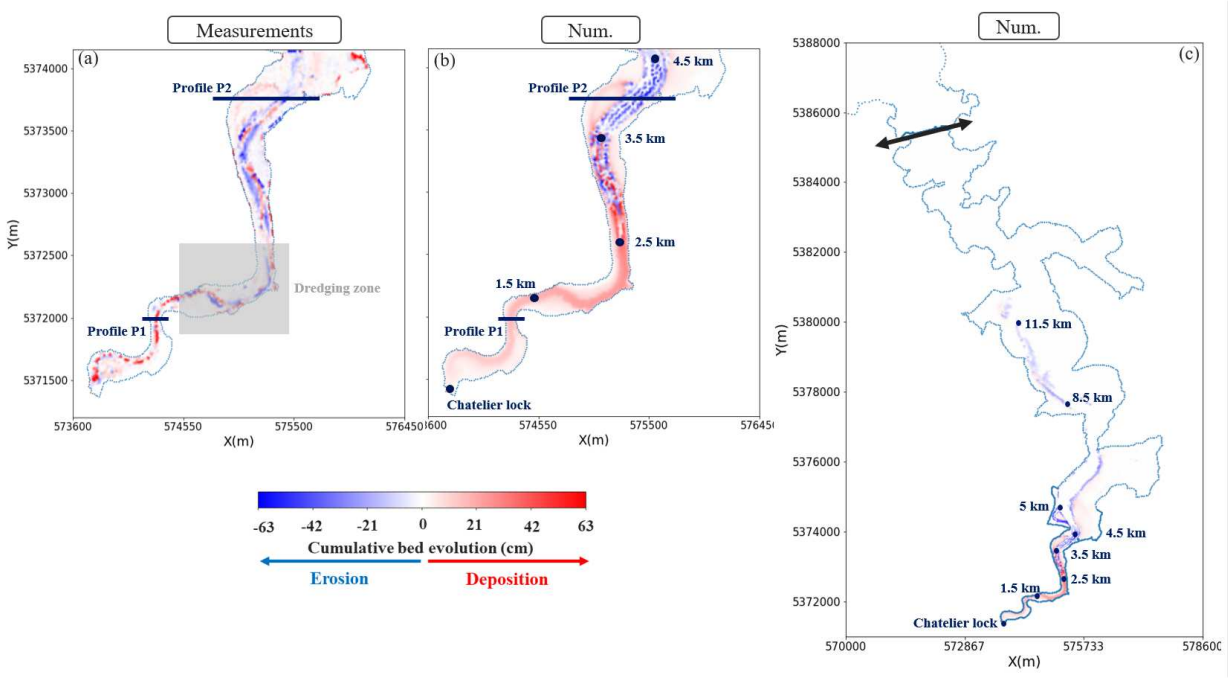

Figure 5.12: (a) Measured and (b,c) numerical cumulative bed evolution over seven fortnights (February-May 2021). (a,b) Maps focus on the lower estuary and (c) map covers the whole estuary. Light-grey box delimit the dredging zone where operations occurred between the 5th and 12th March 2021.

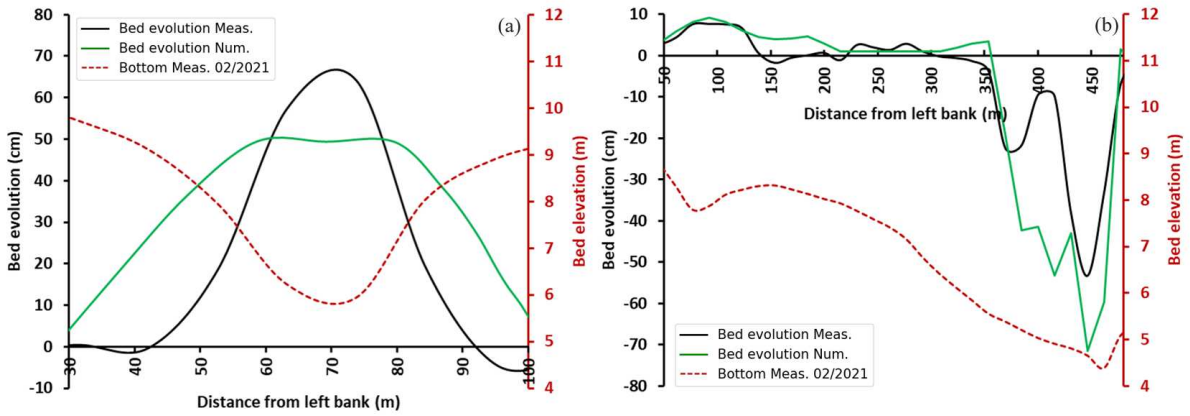

Figure 5.13: Measured and simulated bed evolution over seven fortnights (February-May 2021) at (a) profile P1 and (b) profile P2 (see Figures 5.1 and 5.12 for profiles location). Red-dashed line represents measured bed elevation on February 2021.

5.6.1 Hydro-sedimentary dynamics

Rtimi *et al.* assessed that the plant reduces currents magnitude inside the estuary which would impact the suspended sediment concentration [Rtimi et al., 2021a]. Comparison of depth-averaged tide-averaged SSC between configuration with TPS and without TPS (Figure 5.14) showed that the TPS does not influence the composition of the suspended matter. Indeed, in both configurations high concentrations correspond to suspended cohesive sediment. In addition, With and without TPS, the highest concentrations are noticed in the upper estuary and can reach up to $100 mg/l$. Contrastingly, scenario without TPS showed concentrations between 10 to $35 mg/l$ in the main channels of the middle estuary, while concentrations in the scenario with TPS are below $5 mg/l$. Therefore, the presence of the plant seems to reduce suspended sediment concentrations in the middle estuary's channel.
To further analyze the related physical processes, SSC were plotted against along-channel velocity at four selected locations (T1, T2, S1 and M2, Figure 5.1) over a spring tidal cycle (Figure 5.15). Upstream of the ETM zone (Figure 5.15.a), even though along-channel flood currents are reduced by the TPS, the increase of SSC occurred while the along channel velocity is constant. Consequently, upstream of the ETM zone, SSC are increasing due to sediment advection in both configurations. Then, in the ETM zone (Figure 5.15.b), peak flood SSC are reduced by the presence of the plant ($225 mg/l$ without TPS, $175 mg/l$ with TPS) due to the reduction of currents magnitude ($0.62 m/s$ without TPS, $0.5 m/s$ with TPS). Moreover, downstream of the ETM zone (Figure 5.15.c), SSC could reach higher values ($50 mg/l$ during flood and $20 mg/l$ during ebb) under natural conditions (without TPS) comparing to those observed with the artificial hydrodynamic forcing ($25 mg/l$ during flood and $0 mg/l$ during ebb). Indeed, as flood currents without TPS (likewise for ebb currents) are stronger than those with TPS, local sediments would be more resuspended within the limit of the available stock (*e.g.,* horizontal dashed blue line observed for values of U between 0.3 and $0.6 m/s$). Further downstream (Figure 5.15.d), peak flood (resp. ebb) SSC could reach up to $2 mg/l$ (resp. $1.75 mg/l$) in the absence of the TPS while SSC are below $0.5 mg/l$ in the presence of the TPS. Actually, currents decrease induced by the plant in this area influences local particles resuspension and also their transport. Besides, configurations with and without TPS showed a significant asymmetry between flood and ebb at stations T1, T2 and S1. However, at station M2, suspended concentrations are less asymmetrical between flood and ebb for configuration without TPS than for configuration with TPS. Consequently, analyses of residual components at stations T2 and M2 for scenarios with and without TPS were performed at a fortnight time scale.
In the upper estuary (station T2), the presence of the tidal power station allows this area to be constantly submerged while it emerges in the scenario without TPS (Figure 5.16.a). Figure 5.16.c shows that residual depth-averaged SSC ($< \overline{SSC} >$) in the presence of the plant are lower comparing to the scenario without the plant ($40 mg/l$ vs $70 mg/l$ respectively) for the first spring tides (14-19 days) and then become greater ($35 mg/l$ vs $15 mg/l$ respectively) during the transition to neap tides (20-22 days). Therefore, residual SSC dynamics is strongly modulated by fortnightly time scales for scenario without TPS than for the scenario with TPS. Likewise for residual depth-averaged along-channel currents ($< \overline{U} >$) as illustrated in Figure 5.16.e. In addition, $< \overline{U} >$ is continually negative at station T2 for both scenarios with and without the plant. The corresponding advective sediment flux (F_S) is thus continually negative (into the estuary) for both scenarios (Figure 5.16.g). It means that in the upper estuary the plant does not influence the direction of residual sediment flux. However, in the configuration with TPS, both residual SSC and currents, and thus the advective sediment flux, are maintained almost constant during the whole spring tidal period (14-21 days). This behavior is explained by the need to hold

a sufficient water level difference between the estuary and the sea to produce electricity during both neap and spring tides. This artificial forcing induces thus a negative residual sediment flux between 19.5 and 21.5 days. Therefore, the resulting cumulative sediment flux (Figure 5.16.i) is greater in configuration with the plant (-50 tons/m) than in configuration without the plant (-35 tons/m) over a period of a fortnight.
In the middle estuary, station M2 is constantly submerged for both configurations (Figure 5.16.b). Then, configuration without TPS shows greater residual depth-averaged SSC ($< \overline{SSC} >$), $2mg/l$, comparing to configuration with TPS, which exhibits $0mg/l$ (Figure 5.16.d). Moreover, residual depth-averaged currents ($< \overline{U} >$) are continuously positive (towards the sea) for both scenarios, with a distinct spring-neap variation (Figure 5.16.f). Consequently, F_S is close to zero with the TPS and could reach up to $0.008kg/m/s$ without the TPS (Figure 5.16.h). Indeed, even though residual $< \overline{SSC} >$ is significantly lower in station M2 comparing to station T2, residual $< \overline{U} >$ is much stronger and the water column is much deeper in M2 comparing to T2. Therefore, following Equation 5.17, F_S could reach high values in the middle estuary for the scenario without the TPS. Likewise for the cumulative residual sediment flux (Figure 5.16.j) which is oriented towards the sea (positive) and could reach up to 50 tons/m over a spring-neap tidal period. The presence of the plant reduces thus the sediment transport towards the sea in the middle estuary.

5.6.2 Bed level evolution

In order to complement previous analyses on suspended sediment dynamics, bed level evolution were evaluated for scenarios with and without the tidal power station over a period of 3 months, between February-May 2021 (Figure 5.17). As assessed previously in section 5.5.4, significant bed evolution occurs mainly in the upper estuary in the configuration with the TPS. Contrastingly, for the scenario without the TPS, significant bed evolution would not be limited to the upper estuary but could also occur in the middle estuary (Figure 5.17.b). Indeed, without the TPS, the eastern channel between 8 and $12km$ from the Chatelier lock would be subject to erosion, with rates of the order of $40cm$ over 3 months. Moreover, the same configuration estimates that sediment could be deposited in the region near Saint-Hubert port, with rates of $15cm$ over three months. Further upstream (Figures 5.17.c-d), between 3.5 and $4.5km$ downstream of the Chatelier lock, the eastern channel would be mainly eroded and the western channel would be subject to sedimentation under natural tidal forcing. Besides, the main channel, between 0 and $2.5km$ from the Chatelier lock, would be also subject to sediments deposition. Consequently, the presence of the plant does not modify the natural morphodynamics tendency in the upper estuary. However, for the considered scenarios, sedimentation rates $2.5km$ downstream of the Chatelier lock can reach up to $50cm/3$ months in the configuration with the TPS and only $25cm/3$ months in the configuration without TPS. Therefore, sediments are mainly trapped in the upper estuary under the artificial forcing induced by the plant, while they could be homogeneously distributed further downstream under natural tidal forcing.

5.7 Discussion

This work carried out the calibration and validation of a 3D numerical model of the Rance estuary to improve the understanding of sediment dynamics in response to power generation and also to quantify the impact of the plant on sediment transport and morphodynamics. Accurate sediment transport and morphodynamics simulation was accomplished through calibration of

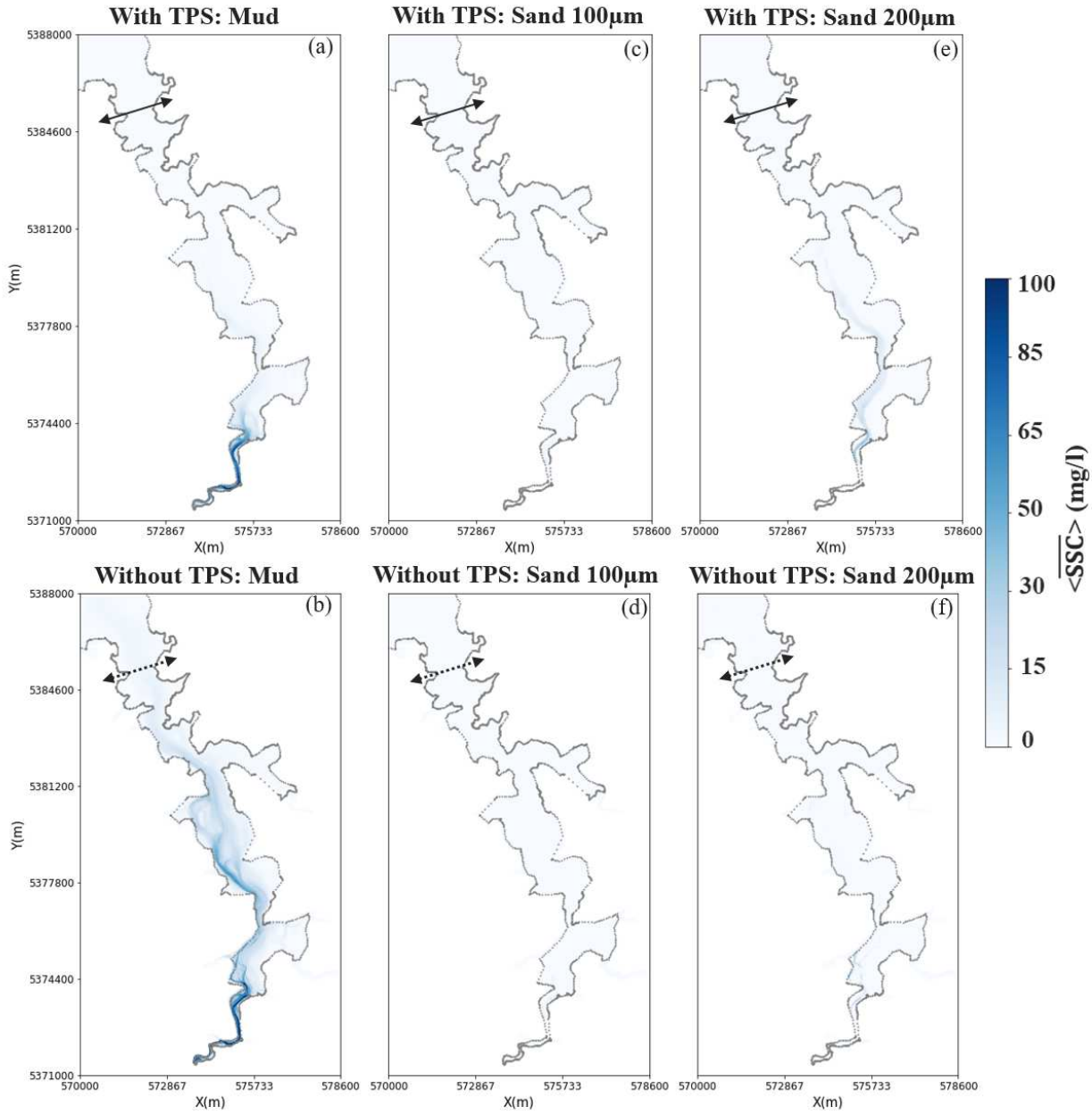

Figure 5.14: Depth-averaged and spring tide-averaged concentration of suspended (a,b) cohesive sediments, (c,d) sand of 100μm and (e,f) sand of 200μm for configurations with TPS and without TPS respectively.

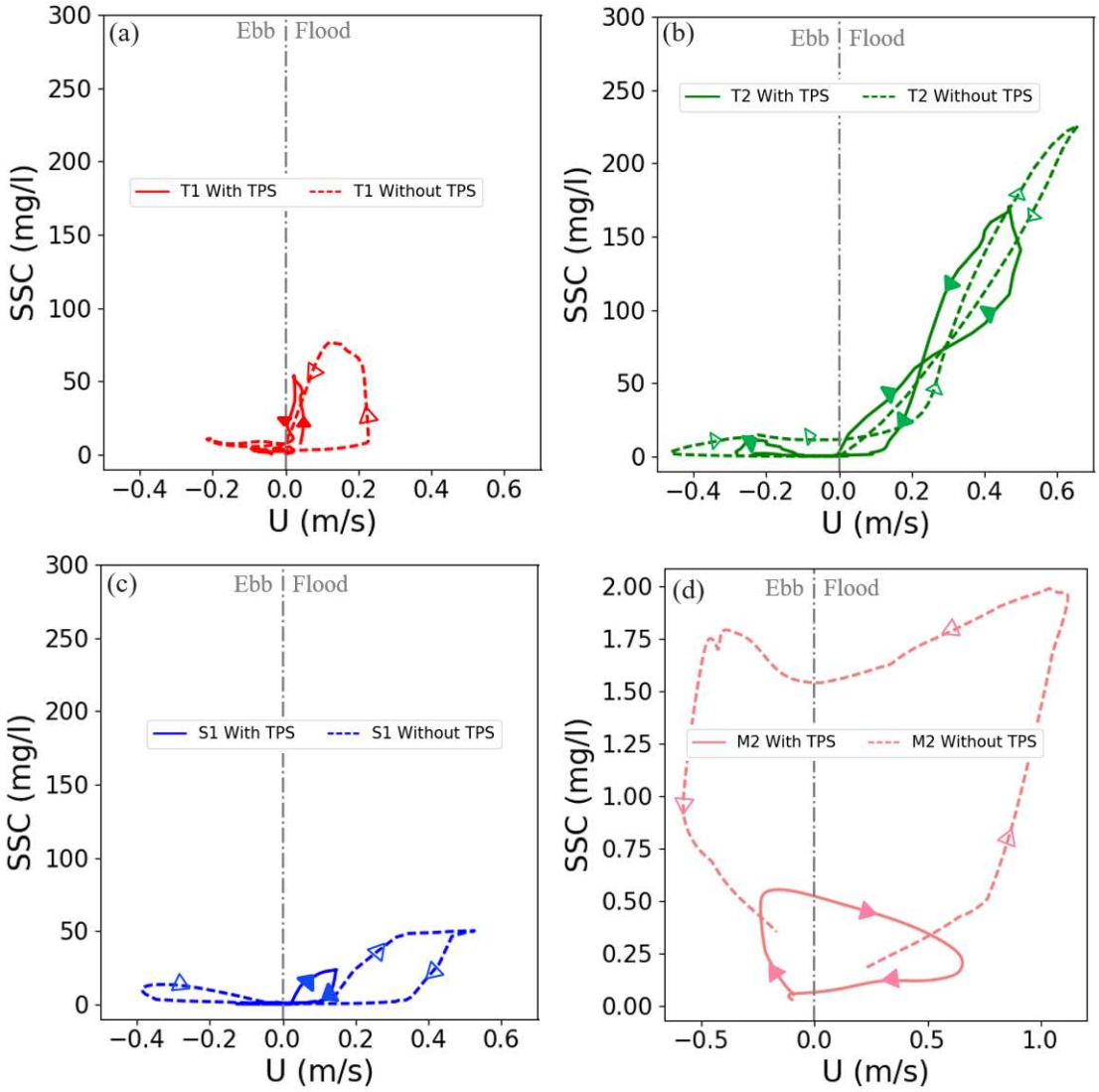

Figure 5.15: Correlation between SSC and along-channel current over a spring tidal cycle for configurations with TPS and without TPS at locations (a) T1, (b) T2, (c) S1 and (d) M2. (see Figure 5.1 for probes locations).

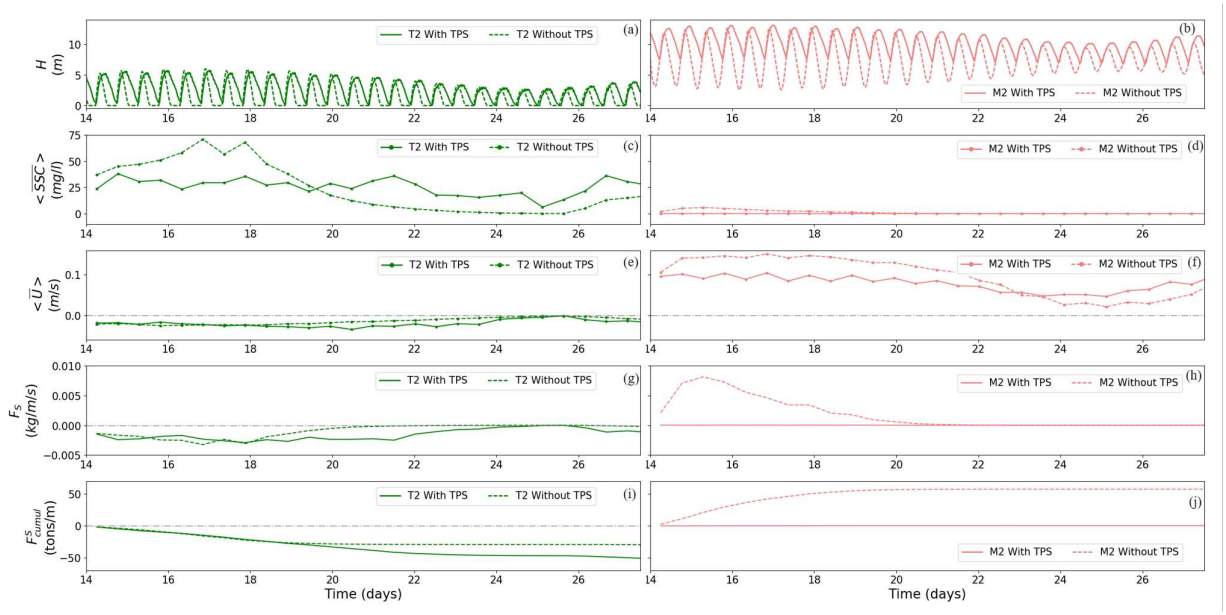

Figure 5.16: Residual components for configurations with TPS and without TPS at positions T2 and S2 respectively: (a,b) water depth, (c,d) depth- and tide-averaged suspended sediments concentration, (e,f) residual depth-averaged along-channel velocity, (g,h) residual sediment flux (Equation 5.17), and (i,j) cumulative net sediment flux (Equation 5.18). See Figure 5.1 for locations T2 and S2.

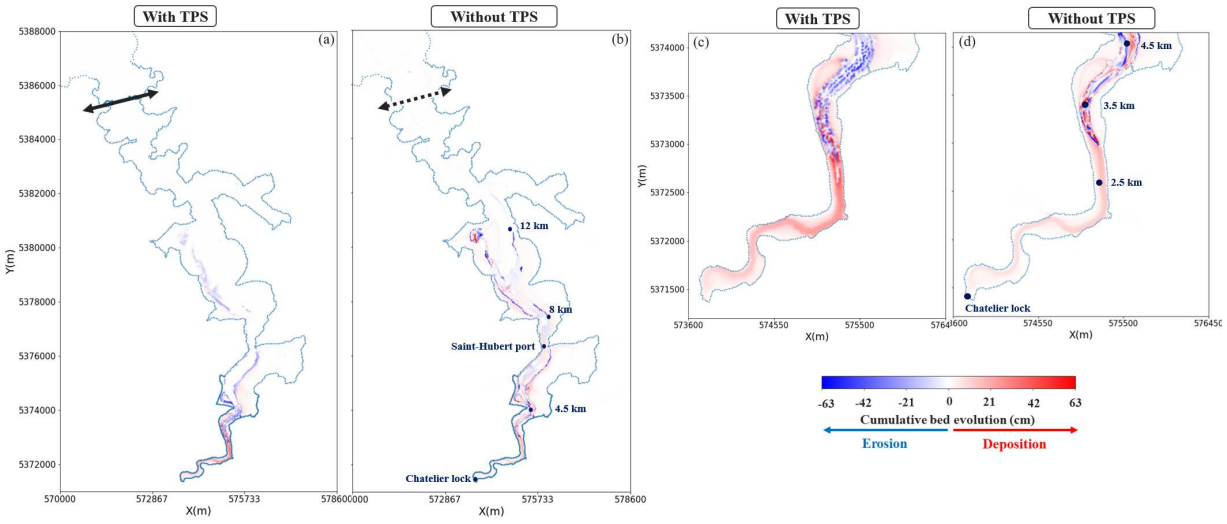

Figure 5.17: Cumulative bed evolution over seven fortnights (February-May 2021) for configurations with and without tidal power plant. (a,b) Maps cover the whole estuary and (c,d) maps focus on the lower estuary.

the numerical model on measured SSC and bed level change respectively over timescales of fortnight to three months. Some discrepancy at peak SSC was noted in station T2 mainly related to high uncertainties due to NTU-SSC calibration. Associated error margins were however satisfactorily comparing to confidence ranges from other macrotidal estuaries [Grasso et al., 2018; Toublanc et al., 2016; Amoudry et al., 2014]. The morphodynamic model presented also satisfactorily agreement with observed bed level changes over fortnightly to 3 months periods. It should be noted that calibration and validation of morphodynamics in such complex estuarine systems are not often fully achieved. For instance, work on Bristol channel [Neill et al., 2009] assessed the impact of tidal stream turbines on large-scale sediment dynamics without a prior validation of the simulated bed level changes on measured dataset. Likewise for work on the Pentland Firth [Fairley et al., 2015] where the morphodynamics model validation relies only on hydrodynamics validation. Similarly, previous study on bed level evolution in the Rance estuary [Thiebot, 2008] were only validated on SSC survey. Consequently, the validation performed in this work enhances the reliability of the numerical model to assess the impact of the tidal power station on sediment dynamics.

Beyond the calibration and validation of the numerical model, this work helped to improve the understanding of sediment dynamics in response to power generation. Indeed, suspended sediment dynamics in the Rance estuary are modulated by the operation modes of turbines and sluice gates. During flood, resupension and sediment transport into the upper estuary occur during the estuary's infilling phase and mainly on spring tides periods (Figures 5.10 and 5.11). Unbalanced with sediment transport during ebb resulting from weak ebb currents and low river discharge, sediments are accumulated in the upper estuary, mainly between 0 and 2.5km and on the western channel between 3.5 and 4.5km downstream of the Chatelier lock (Figures 5.12 and 5.13). This morphodynamics behavior is not fully induced by the tidal power plant since scenario without the plant simulated the same tendency of bed level change in the upper estuary (Figure 5.17). Although sedimentation rates over 3 months in the upper estuary were 2 times lower in scenario without TPS comparing to scenario with TPS, other deposition zones, namely near Saint-Hubert port, might appear in configuration without TPS. Consequently, the plant tends to trap sediments primarily in the upper estuary while the natural tidal forcing could have deposited these particles not only in the upper estuary but further downstream as well. Preliminary insights on this sediment accumulation in the upper estuary were also provided by Rtimi *et al.* [Rtimi et al., 2021a] based on analyses of the plant's impact on tidal asymmetry, tidal prism and flushing time. In order to recover to this sediment trapping issue, occasional dredging operations in specified area are organized, in addition to regular hydraulic flushes from the Chatelier lock. Actually, the sediment should be exported out of the upstream towards the downstream to maintain a sufficient depth for navigation in the up-stream's main channel. Bonnot-Courtois [1993] assessed the efficiency of these hydraulic flushes. However, alternative operation modes of turbines and sluice gates aiming to enhance sediment resuspension during ebb while maintaining electricity generation would be proposed. For instance, sluice gates could be opened simultaneously with the turbines during ebb to increase ebb currents in the upper estuary. The present numerical model would be thus a valuable and efficient tool to test various scenarios to help the estuary's management. Furthermore, It could identify zones where sedimentation rates are the highest in order to optimize organization of costly dredging operations. This sediment accumulation matter is not only limited to ebb-flood generation type of tidal power stations, but was also assessed in the Sihwa Lake where the world's largest tidal power plant (flood generation type) is installed [Kim et al., 2017, 2021].

Numerical results were analysed over fortnightly periods and 3 months periods, mainly because

of the availability of validation dataset and also due to available computational resources. The selected timescales were relevant to understand the main sediment transport processes in this complex estuarine system. However, morphological patterns over these timescales could be modified over longer timescales of years to decades. Another interesting aspects are the impact of waves, wind and storm surges on sediment transport in the Rance estuary. For instance, previous studies on the Rance estuary assessed that sediment present in the basin are mainly originated from the sea [Bonnot-Courtois et al., 2002; Rtimi et al., 2021a], then Thiebot [2008] revealed that marine sediments do not continuously enter the estuary but they rather arrive massively during exceptional events (e.g. storm surges). Theses physical processes were not addressed in the present study.

5.8 Conclusions

The impact of the world's second tidal power station on sediment dynamics and bed evolution in the Rance estuary was evaluated from a calibrated and validated 3D numerical model. Numerical suspended concentrations were first validated on continuous measurements on timescale of a fortnight. Then, simulated bed evolution captured the first order morphodynamics in the Rance estuary on timescales of a fortnight to months. On the scale of a tidal cycle, peak SSC are noticed during flood specifically during the estuary's filling phase where both turbines and sluice gates are open. Contrastingly, sediments could be resuspended locally during ebb, specifically during turbining phase (electricity production stage), but would not be transported further than $3km$ from the uppermost limit. On the scale of a fortnight, residual sediment flux is continuously oriented towards the upper estuary with peak magnitudes reached during spring tides. Consequently, significant sedimentation rates were observed in the main upstream channel ($2.5km$ from the river boundary) and western channel near Mordreuc (3.5-$4.5km$ from the river boundary). This morphodynamic behavior was also produced under natural tidal forcing (without TPS) but with lower sedimentation rates. Moreover, sediment could also be deposited near Saint-Hubert port zone in the scenario without TPS. Therefore, sediments are mainly trapped in the upper estuary under the artificial forcing induced by the plant, while they could be homogeneously distributed further downstream under natural tidal forcing. Finally, the present 3D numerical model would be a promising operational tool to test various scenarios from hydraulic flushes to alternative operation modes of the plant to help the estuary's management.

Acknowledgements

This work was funded by the French National Association of Research and Technology (ANRT) and EDF R&D with the Industrial Conventions for Training through REsearch (CIFRE grant agreement 2018/1653). The authors are grateful to Christine Bertier, Matthieu Le Brun, EDF R&D-MMN team and measurements crew of EDF-DTG and University of Bordeaux for carrying out field measurements used to validate the numerical model. The authors are thankful to members of Rance Energie, EDF CIH and Nicolas Huybrechts (CEREMA) for providing feedback on the numerical model. Authors thank also Luca Parquet for analysing, pre- and post-processing the collected field data.

Notation

S = Salinity (g/l);
T = Temperature (°);
V_s = Speed of sound (m/s);
C, SSC = suspended sediment concentration (g/l);
u, v, w = velocity component along x, y and z directions (m/s);
U = Along-channel velocity (m/s);
$\epsilon_{sh}, \epsilon_{sv}$ = diffusion coefficients in the horizontal and vertical directions (m^2/s);
w_s = Settling velocity (m/s);
H = Water depth (m);
D = Deposition flux ($kg/m^2/s$);
E = Erosion flux ($kg/m^2/s$);
C_{zref} = Near-bed concentration (g/l);
τ_b = Near-bed shear stress (Pa);
$\tau_c d$ = Critical shear stress for mud deposition (Pa);
$\tau_c e$ = Critical shear stress for mud erosion (Pa);
M = Krone-Partheniades erosion law constant ($kg/m^2/s$);
d_{50} = Median diameter (m);
ρ = Water density (kg/m^3);
ρ_s = Sediment density (kg/m^3);
ν = Water kinematic viscosity (m^2/s);
λ = Sediment porosity ($--$);
μ = Correction factor for skin friction ($--$);
θ = Shields parameter ($--$);
θ' = Shear stress due to skin friction ($--$);
θ_{cr} = Critical Shields parameter ($--$);
g = Gravitational constant (m/s^2);
F_{coh} = Fraction of cohesive sediment ($--$);
b = Bed elevation (m);
$B.E.$ = Cumulative bed evolution (m);
F_S = Residual advective sediment flux ($kg/m/s$);
F^S_{cumul} = Cumulative sediment flux ($tons/m$);
RMT = Rate of mass transfer (s^{-1});
$\overline{X}$ = Depth-averaged X ($[X]$);
$< X >$ = Tide-averaged X ($[X]$);

CHAPTER 6

ANALYSIS OF FLOW AND SEDIMENT TRANSPORT PROCESSES IN THE RANCE ESTUARY THROUGH HYPOTHETICAL SCENARIOS

▷ Objectives of this chapter

The main objectives of this chapter are (*i*) to implement an operational numerical tool capable to reproduce the main features of morphodynamics in the Rance estuary over time scales ranging from a neap-spring tidal cycle to a one year period, within reasonable computational times ; (*ii*) to investigate the influence of occasional mechanisms on sediment dynamics such as variable river discharge and marine sediment supply inside the estuary during storm periods ; and (*iii*) to evaluate the efficiency of hydraulic flushes and alternative operation mode of the tidal power station at reducing sediment accumulation in the upper estuary. Therefore, this chapter addressed the following research questions formulated in Chapter 1:

- *How relevant are 2D and 3D numerical models at reproducing the main features of hydro-sedimentary dynamics observed in macrotidal estuaries influenced by the presence of a tidal power station?*
- *Which are the dominant physical mechanisms driving the sediment dynamics in the Rance estuary?*
- *What recommendations can be given to stakeholders for a more efficient estuary management?*

Highlights

- Accurate river discharge considering hydraulic flushes need to be provided to correctly simulate bed evolution over long timescales (in the order of a year).
- A typical storm event would not significantly influence the main long term morphodynamic processes in the Rance estuary.
- Hydraulic flushes with a sufficient flow rate and over sufficient tidal cycles are efficient to decrease sediment accumulation in the upper estuary.
- Alternative operation mode of the TPS based on opening of sluice gates during ebb and adjusting the opening of turbines decreases sediment trapping in the upper estuary.

Abstract

The Rance estuary is a relatively small low-discharge steep-sided *ria*, located along the Brittany coast in northern France, with a maximum spring tidal range of 13.5 m. Taking advantage of this significant tidal regime, the first and currently the second largest operational tidal power station in the world was built at the estuary's mouth, with peak outpout capacity of $240MW$. A depth-averaged two-dimensional (2D) coupled hydrodynamic and morphodynamic numerical model was developed to reproduce the main features of sediment transport and morphodynamics in the Rance estuary over time scales ranging from a neap-spring tidal cycle to a one year period, within reasonable computational times. After calibration and validation of the model for present-day conditions, complementary sediment transport processes were assessed through hypothetical scenarios evolving constant and variable river discharge, marine sediment supply inside the estuary during storm periods and alternative operation mode of the power plant aiming to reduce sediment accumulation in the upper estuary. Comparison between scenarios with a constant and variable river flowrates enhanced the importance of an accurate variable river discharge at the uppermost limit to correctly reproduce bed level evolution in the upper estuary over a time scale of the order of 1 year. Furthermore, a hypothetical hydraulic flush scenario could decrease sediment trapping in the upper estuary by 30-60% over a spring-neap tidal period. The opening of sluice gates during ebb induced also a reduction in sediment accumulation in the upper estuary. Finally, a typical storm would induce a marine sediment supply from the coastal area into the basin. Next, spring tides would be responsible of transporting and depositing sediment particles in the coves along the estuary.
Keywords: Sediment dynamics, estuary management, hydraulic flush, tidal power plant, numerical modeling.

6.1 Introduction

Sediment dynamics in estuarine systems are highly complex due to natural factors, namely river discharge, tides, waves, wind, sediment distribution, and due to anthropogenic disturbance such as the presence of dams and tidal power structures [Dyer, 1997; Wu et al., 2017]. The understanding of these physical processes in estuarine environments relies on analyses of suspended sediment transport and morphodynamics [Dronkers, 2005]. The former can be characterized from the variability of suspended sediment concentration (SSC), examined on timescales from the semidiurnal tidal cycle to seasonal periods [Grasso et al., 2018; Feng et al., 2019]. The later can be analyzed from bed level evolution over timescales ranging from a fortnight to decades [Orseau et al., 2020; Brand et al., 2021].
Proper calibrated and validated numerical models demonstrated their ability to correctly simulate sediment dynamics in various estuarine systems, which made them useful tools to characterize these environments and predict their behaviour under different scenarios. Three distinctive approaches are widely deployed to numerical modelling of sediment transport in estuaries under natural and/or artificial forcing: (i) lateral-averaged vertical two-dimensional models [Sinha et al., 2004; Etemad-Shahidi et al., 2010], (ii) depth-averaged horizontal two-dimensional models [Gourgue et al., 2013; Santoro et al., 2017; Gourgue et al., 2021] and (iii) three-dimensional models [Fairley et al., 2015; Hesse et al., 2019]. Three-dimensional models provide detailed hydrodynamics and sediment transport processes within the water column, namely water circulation, velocity and density vertical gradients, in estuarine configurations which may account for the presence of tidal installations [Amoudry et al., 2014; Robins et al., 2014; Burchard et al., 2018].

However, they could be computationally costly for long term simulations and highly costly for testing diverse scenarios for operational purposes. In shallow and vertically well mixed estuaries, such as the Rance estuary, the depth-averaged horizontal two-dimensional approach demonstrated its ability to correctly simulate hydrodynamics (Chapter 3 and [Angeloudis et al., 2016]) and sediment dynamics [Nnafie et al., 2018; Feng et al., 2019].
Various modeling systems are available for simulating hydrodynamics, sediment transport and bed evolution processes. Relying on finite-element discretization based on an unstructured grid suitable for estuaries with complex geomorphology as the Rance estuary [Bonnot-Courtois et al., 2002], the open source TELEMAC-MASCARET system was selected for this work. Furthermore, its sediment transport and morphodynamic module GAIA has been successfully applied to estuarine environments evolving cohesive sediments [Giardino et al., 2009; Santoro et al., 2017], non-cohesive sediment [Luo et al., 2013] and a mixture of cohesive and non-cohesive sediments [Van, 2012].
The Rance estuary is a small steep-sided *ria* [Evans and Prego, 2003] located on the Brittany coast of northern France, characterised by the presence of a tidal power station (TPS) on its mouth (Figure 6.1.a). With a maximum perigean spring tidal range of 13.5m, the Rance TPS can produce electricity during both ebb and flood, with a peak output capacity of 240MW [Neil et al., 2018]. The power plant supplies 0.12% of the power demand in France, which is equivalent to a medium-size city like Rennes with 360,000 inhabitants [EDF, 2020]. The head of the estuary is located at the Chatelier lock (Figure 6.1.a), where the Rance river drains a small catchment area, with an average freshwater discharge of $7m^3/s$, low water flow rate of $0.5m^3/s$ and a decennial flood of $80m^3/s$ [Bonnot-Courtois et al., 2002].
Using a 2D depth-averaged numerical modelling approach, Thiebot [2008] studied cohesive sediment dynamics in the Rance estuary in response to the artificially distorted tidal forcing under the presence of the plant. However, sediment processes related to the mixture between cohesive and non-cohesive sediment were not addressed and the morphodynamic model could not be validated due to lack of bathymetry data. In addition, the former work considered a continuous solid discharge at the plant while marine sediment enter inside the Rance estuary occasionally during storm periods [LCHF, 1982]. Therefore, to better understand sediment dynamics in this complex system, each physical process needs to be analysed separately. Moreover, Chapter 5 provided detailed analyses on sediment dynamics in the Rance estuary based on a calibrated and validated three-dimensional hydro-sedimentary numerical model. The latter quantified also the impact of the TPS on first-order sedimentary processes based on comparison between scenarios with and without the plant. However, only short term simulations (maximum period of 3 months) were performed due to the costly computational time. In addition, these three-dimensional simulations focused on the primary physical processes, and did not address other occasional physical processes such as variable river discharge, storm-like conditions and alternative scenarios to decrease sediment accumulation in the upper estuary. Bonnot-Courtois [1993] reported qualitative impact of a hydraulic flush at the Chatelier lock (Figure 6.1.a) mainly based on measurements of suspended sediment concentration that could not provide quantitative analyses on the efficiency of these hydraulic flush operations.
The main objective of this work is to implement an operational numerical tool capable to reproduce the main features of morphodynamics in the Rance estuary over time scales ranging from a neap-spring tidal cycle to a one year period, within reasonable computational times. To this goal, a depth-averaged horizontal two-dimensional hydro-morphodynamic model is developed in section 6.2.1 and validated in section 6.3.1. Afterwards, the numerical model is carried out to investigate the influence of occasional mechanisms on sediment dynamics such as variable

river discharge and marine sediment supply inside the estuary during storm periods (sections 6.3.2 and 6.3.3). Furthermore, the efficiency of two scenarios (proposed in Chapter 5) aiming to reduce sediment accumulation in the upper estuary, is examined in sections 6.3.2 and 6.3.4. Finally, section 6.4 discusses the simultaneously the results and efficiency of each recommended alternative.

6.2 Materials and methods

6.2.1 Numerical model

The numerical model deployed in this Chapter is the 2D depth-averaged hydrodynamic model presented in Chapter 3 coupled with the sediment transport and bed evolution module GAIA presented in Chapter 5. Indeed, the benefit of deploying this later is its full compatibility between 2D and 3D hydrodynamic processes [Audouin et al., 2019]. In the TELEMAC-MASCARET system, suspended sediment transport processes are dealt with by the hydrodynamic module, while near-bed processes in the bottom layer are handled by GAIA. Therefore, the suspended sediment transport is accounted by solving the 2D advection-diffusion equation expressed in Equation 6.1.

$$\frac{\partial h\overline{C}}{\partial t} + \frac{\partial (h\overline{u}\overline{C})}{\partial x} + \frac{\partial (h\overline{v}\overline{C})}{\partial y} = \frac{\partial}{\partial x}\left(h\epsilon_{sh}\frac{\partial \overline{C}}{\partial x}\right) + \frac{\partial}{\partial y}\left(h\epsilon_{sh}\frac{\partial \overline{C}}{\partial y}\right) + E - D + S, \tag{6.1}$$

where $h = h(x, y, t)$ is the water depth, $\overline{C} = \overline{C}(x, y, t)$ is the depth-averaged suspended sediment concentration, $(\overline{u}, \overline{v})$ are the depth-averaged components of the velocity along the x and y directions, respectively, ϵ_{sh} is the diffusion coefficients in the horizontal direction, D, E are deposition and erosion fluxes respectively and S includes source and/or sink terms. As near bed-bed processes are managed by GAIA, deposition and erosion fluxes (D, E) are computed following equations previously presented in Chapter 5.

The computational domain covers the sea-side and the estuary-side areas extending from the oceanic open boundary ($10km$ from the tidal power plant) to the upstream limit (Chatelier lock). It is discretized with an unstructured mesh of 199 625 nodes and 389 766 triangular elements, with variable resolution ranging between 200m near the coastline, 50m around the estuary's mouth, 20m inside the estuary and 5m close to power station and within the upper estuary between Mordreuc and Chatelier lock. Bed level in the computational domain was extracted from high-resolution bathymetry dataset from Lidar and field survey records collected in 2018. In this work, the Strickler friction coefficient is used. The Boussinesq approximation is used for the turbulence parameterization, with eddy viscosities values calculated with the $k - \epsilon$ model. The Coriolis force is considered in the model, with the Coriolis parameter equal to $1.0909970 \times 10^{-4}\ s^{-1}$. Two open boundaries are considered :

- the oceanic boundary where water level and depth-averaged velocity components were through 11 tidal constituents (M2, S2, N2, K2, K1, O1, P1, Q1, M4, MS4 and MN4) from the OSU TPXO European Shelf 1/30 regional model [Egbert and Svetlana, 2002] and a constant suspended sediment concentration set equal to $0g/l$ (except for scenario SC 21, see section 6.2.2),
- the river boundary at the Chatelier lock where a constant flow rate is set equal to $7m^3/s$ representing the mean Rance river discharge [Bonnot-Courtois et al., 2002] and a constant

Figure 6.1: (a) Bed level in the Rance estuary with turbidity probes and key sites. (b,c,d) Initial state of fractions of fine sand (200μm), very fine sand (100μm) and mud (20μm) respectively deployed for the 2D hydro-sedimentary simulations.

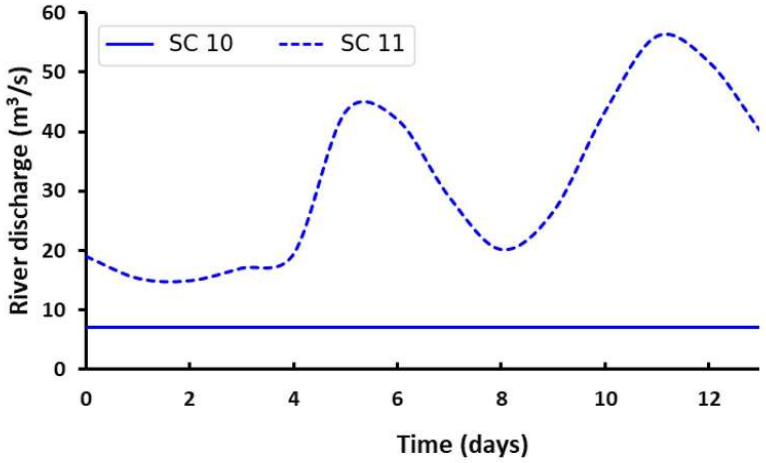

Figure 6.2: River discharge imposed at the uppermost boundary (Chatelier lock) for scenarios SC 10 and SC 11 (Table 6.1).

suspended sediment concentration set equal to $0 g/l$ (except for scenario SC 11, see section 6.2.2).

The initial sediment distribution used in 3D hydro-sedimentary simulations presented in Chapter 5 (Figure 6.1.b-d) served also as the initial state of all the 2D hydro-sedimentary simulations analyzed in the present chapter (except for scenario SC 21, see section 6.2.2).

6.2.2 Scenarios

The Rance estuary is characterized by the complex configuration of its upstream boundary (Chatelier lock, Figure 6.1.a). Indeed, this boundary is composed by a lock and 2 sluice gates that maintain a constant water level in the port located upstream. This boundary is also deployed to perform occasional hydraulic flushes during flood events. The flow rate passing through this boundary is not measured and the nearest hydrometric station is located $33 km$ upstream, which cannot be used as representative of the value at the boundary. Only dates and duration of hydraulic flushes are saved. In order to assess the impact of these operations on morphodynamics in the estuary, two configurations were designed (Table 6.1):

- SC 10, consisting of a hydro-sedimentary simulation with a constant river discharge equal to $7 m^3/s$ (Figure 6.2),
- SC 11, consisting of a hydro-sedimentary simulation with a variable daily-averaged river discharge estimated from measured water levels at the upstream and the downstream of the lock [EPTB, 2021] (Figure 6.2).

The comparison between configurations SC 10 and SC 11 highlights the importance of providing the numerical model an accurate river discharge at its upstream boundary. Furthermore, this comparison evaluates the efficiency of a hydraulic flush operation to minimize sediment trapping in the estuary's upper channel.

Table 6.1: Modeling scenarios

Name	Run	Type
Hydraulic flush	SC 10	Constant river discharge, Figure 6.2
	SC 11	Variable river discharge, Figure 6.2
Storm-like condition	SC 21	Forced SSC = 15mg/l at the TPS
Alternative operation modes	SC 30	Current operation mode of the TPS, Figure 6.3
	SC 31	Modified operation mode of the TPS, Figure 6.3

Marine sediments do not continuously enter the Rance estuary, but could be occasionally introduced during storm periods [LCHF, 1982; Bonnot-Courtois et al., 2002; Thiebot, 2008]. Studies from LCHF [1982] and Bonnot-Courtois et al. [2002] measured SSC values of 15mg/l upstream of the plant during storm periods while SSC values are below 1mg/l. Although the presented numerical model does not consider storm surge and waves processes, imposing a SSC value equal to 15mg/l upstream the power station would represent a storm-like conditions. Therefore, scenario SC 11 (Table 6.1) is proposed to identify sedimentation rates and deposition zones of marine sediments and needed time to reach the estuary's uppermost limit in a storm-like conditions. To this goal, simulation SC 11 consists of two phases: (i) the first stage corresponds to a 2 days storm period with SSC equal to 55mg/l at the oceanic boundary, and (ii) the second stage corresponds to the continuity of the first stage over a neap-spring tidal period with SSC equal to 0mg/l at the oceanic boundary. One non-cohesive sediment class =200µm and one cohesive sediment class =20µm were chosen for this scenario, as they would represent the type of sediment prone to enter the estuary [Bonnot-Courtois et al., 2002]. The chosen value at the ocean boundary (55mg/l = 35mg/l(cohesive sediment) + 20mg/l(non-cohesive sediment)) was calibrated to obtain 15mg/l directly upstream the tidal power station. To analyze marine sediment entry inside the estuary, the whole computational domain is set initially as a rigid bed so that the single sediment source is the contribution of the oceanic boundary.

As assessed in Chapter 5, the reduction of ebb currents induced by the tidal power station promotes increasing sedimentation rates in the upper estuary. An alternative operation mode of the plant was thus proposed, aiming to increase ebb currents during two consecutive tidal cycles without significantly penalizing electricity production. In order to assess the efficiency of this alternative mode, two scenarios were designed (Table 6.1):

- SC 30, consisting of a hydro-sedimentary simulation with current operation modes of the plant (Figure 6.3),
- SC 31, consisting of a hydro-sedimentary simulation with modified operation modes of the TPS consisting on: (i) opening sluice gates during two consecutive ebb stages to increase ebb currents in the estuary (Figure 6.3.a) and (ii) adjusting turbines opening to reduce currents asymmetry flood dominated (Figure 6.3.b).

Table 6.1 summarizes the different hypothetical scenarios presented in this Chapter.

6.3 Results

The numerical model was first validated in terms of suspended sediment concentration (SSC) over a neap-spring tidal period (July 20th - August 3rd 2020). Then, simulated bed evolution was

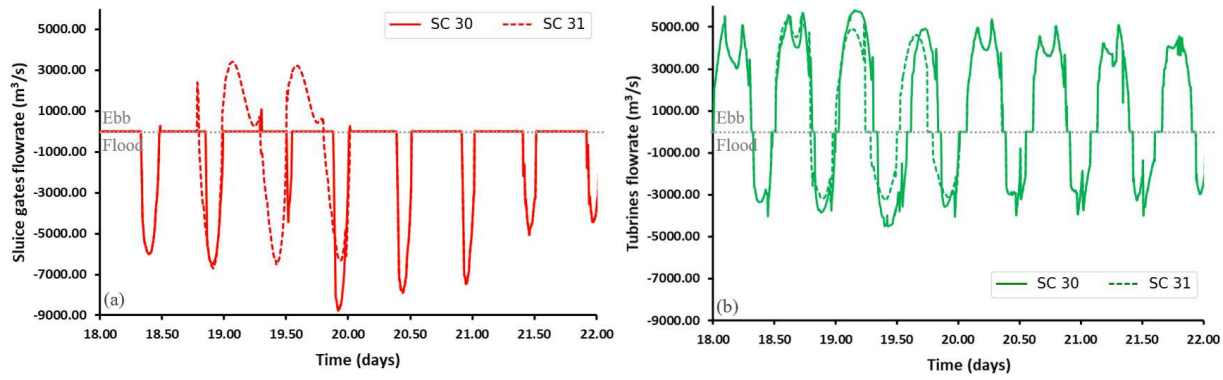

Figure 6.3: Flow rates passing through (a) turbines and (b) sluice gates for scenarios SC 30 and SC 31 (Table 6.1).

validated over a 3 months period and over a 1 year period (section 6.3.1). Afterwards, a hydraulic flush scenario was designed to assess the sensitivity of simulated bed evolution to the river discharge and particularly to the Chatelier lock management (section 6.3.2). A second scenario was designed to simulate a storm-like conditions to describe the entry of sea-sediment in the estuary and their preferable zones of deposition (section 6.3.3). The last scenario considered an alternative operation mode of the tidal power plant to evaluate its efficiency on decreasing sediment trapping in the upper estuary (section 6.3.4).

6.3.1 Validation of 2D numerical model

Sediment transport and morphodynamic variables simulated by the 2D numerical model were validated base on SSC and bed evolution measurements (Chapter 2) and also compared to sedimentary variables computed by the 3D numerical model presented in Chapter 5. The following numerical results were obtained after a spin-up of 28 days and with the calibrated parameters presented in Chapter 5.

Depth-averaged tide-averaged SSC simulated by the 2D numerical model were compared to measured SSC and to tide-averaged sub-surface (80cm below the surface) SSC simulated by the 3D numerical model. The comparison was made at four locations along the estuary (T1, T2, S1 and S2) over a neap-spring tidal cycle in Figure 6.4. The 2D model reproduces correctly magnitude and neap-spring variation of the observed SSC at the four stations. Furthermore, similar SSC patterns captured by the 3D numerical model were also captured by the 2D model. Indeed, at station T1 (Figure 6.4.c), both 2D and 3D models showed higher SSC values that can reach up to $40mg/l$ during spring tides comparing to neap tides where SSC values are below $5mg/l$. Few kilometers downstream, at station T2 close to the ETM zone (Figure 6.4.d), the 2D model seems to underestimate SSC values during neap tides. Indeed, differences between numerical depth-averaged SSC values and those simulated by the 3D model can reach up to $40mg/l$. Further downstream, at stations S1 and S2 (Figures 6.4.e-f), depth-averaged SSC values are consistent with observations and near-surface SSC values computed by the 3D model. As discussed in Chapter 5, S1 and S2 stations are far downstream of the ETM area with SSC values below $20mg/l$. In summary, the calibrated 2D numerical model was reliable enough to reproduce suspended sediment concentrations tendencies along the Rance estuary.

To validate morphodynamic processes simulated by the 2D numerical model, bed level

evolution from the depth-averaged model was compared to bathymetry measurements in the upper estuary and to bed level evolution computed by the 3D morphodynamic model over a period of 3 months between February 1st and May 13th 2021 (Figures 6.5 and 6.6). The 2D numerical model captures correctly the global bed evolution tendencies in the upper estuary (Figure 6.5). Indeed:

- Between 0-2.5km downstream of the Chatelier lock, a general trend to sediment deposition in the main channel was observed from the field measurements (with a thickness of 63cm in 3 months), in the 3D results (with a thickness of 50cm in 3 months) and in the 2D results (with a thickness of 60cm per 3 months). Sedimentation rates computed by the 2D model are more consistent with measured sedimentation rates compared to the 3D model.
- Between 2.5-3.5km downstream of the Chatelier lock, the main channel is subject to erosion while the banks are subject to sediment deposition. This tendency is correctly captured by the 2D model compared to the 3D model.
- Between 3.5-4.5km downstream of the Chatelier lock, an overall tendency to erosion is observed in the eastern channel and a deposition tendency is noticed in the western secondary channel and eastern bank exactly 4.5km downstream of the Chatelier lock. It should be noted that the 2D numerical model provides a more accurate erosion zones in the eastern channel compared to the 3D model.

As explained previously in Chapter 5, numerical mesh need to be very fine in the upper estuary to capture a more accurate sedimentation rate. The mesh resolution in the upper estuary is two times finer in the 2D model than in the 3D model, with a cell length of 5m for the 2D model and 10m for the 3D model. Thus the 2D model provided a more accurate sedimentation rate in this area.
Both 2D and 3D morphodynamic models of the Rance estuary revealed that substantial bed evolution occurred in the upper estuary (Figure 6.6). In a nutshell, the 2D numerical reproduced satisfactorily the main morphodynamic tendencies in the Rance estuary over a 3 months period. The robustness of the 2D model was then tested on a longer time scale of one year. To this goal, bathymetry datasets covering the upper estuary and available on January 13th 2020 and February 1st 2021 were deployed. It should be noted that the horizontal resolution of the available measurements was below 1m while the horizontal resolution of the 2D numerical model is 5m in the upper estuary. Figure 6.7.a shows that the main channel between 0-2.5km from the Chatelier lock is subject to erosion while the main channel 2.5-4.5km downstream of the Chatelier lock is subject to sediment deposition. These trends are in contrast with those observed over 3 months (Figure 6.5.a). Moreover, the 2D numerical model seems to reproduce the same morphodynamic patterns as those simulated over the 3 months period (Figures 6.7.b-c, 6.5.c and 6.6.b). Indeed, hydraulic flushes are often organized at the Chatelier lock, at a maximum frequency of 4 times per month, and a mean duration of 2 hours per flush. Only dates and duration of these hydraulic flushes are saved, without any detail on the corresponding river discharge. A total of 53 hydraulic flushes were scheduled during the computation period between January 13th 2020 and February 1st 2021. Lacking these input data, a constant mean river discharge value, equal to $7m^3/s$, was imposed at the uppermost boundary of the numerical model (Chatelier lock). Therefore, the assumption of a constant river discharge seem to be less relevant to simulate long term morphodynamics in the Rance estuary. To complement these findings, a hydraulic flush scenario was proposed hereafter to examine the influence of such event on bed evolution in the estuary (section 6.3.2).

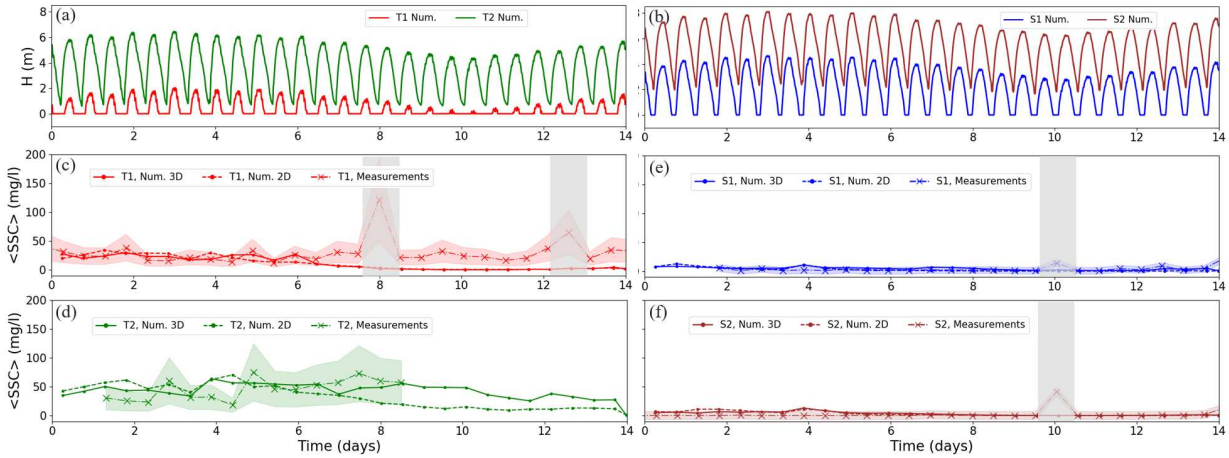

Figure 6.4: Simulated water level at (a) T1, T2 and (b) S1, S2. Measured and simulated tide-averaged suspended mud concentration at (c) T1, (d) T2, (e) S1 and (f) S2. (see locations in Figure 6.1.a). Light colored areas represent measurements uncertainties. Light-grey box delimit periods where the probe is near the bottom, thus the probe measures bed mud concentration rather than suspended mud concentration. Period corresponding to July 20th - August 3rd 2020.

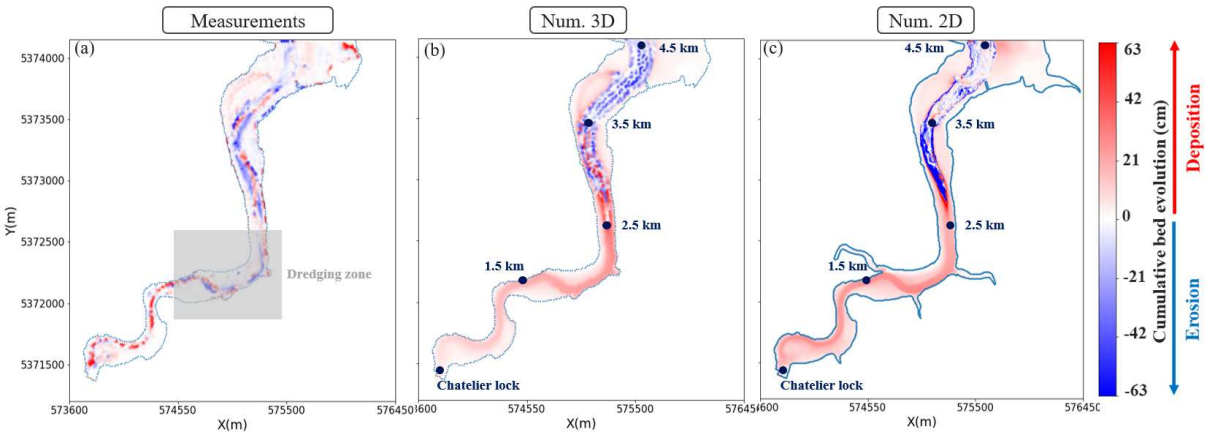

Figure 6.5: (a) Measured, (b) 3D and (c) 2D numerical cumulative bed evolution in the lower estuary over seven fortnights (February-May 2021). Light-grey box delimit the dredging zone where operations occurred between the 5th and 12th March 2021.

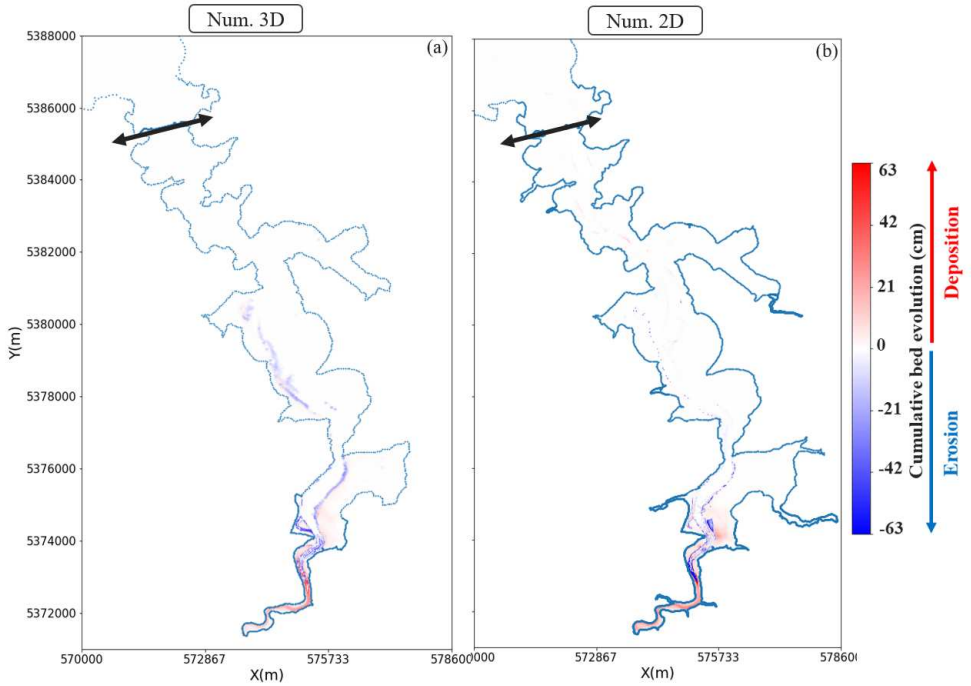

Figure 6.6: (b) 3D and (c) 2D numerical cumulative bed evolution in the Rance estuary over seven fortnights (February-May 2021).

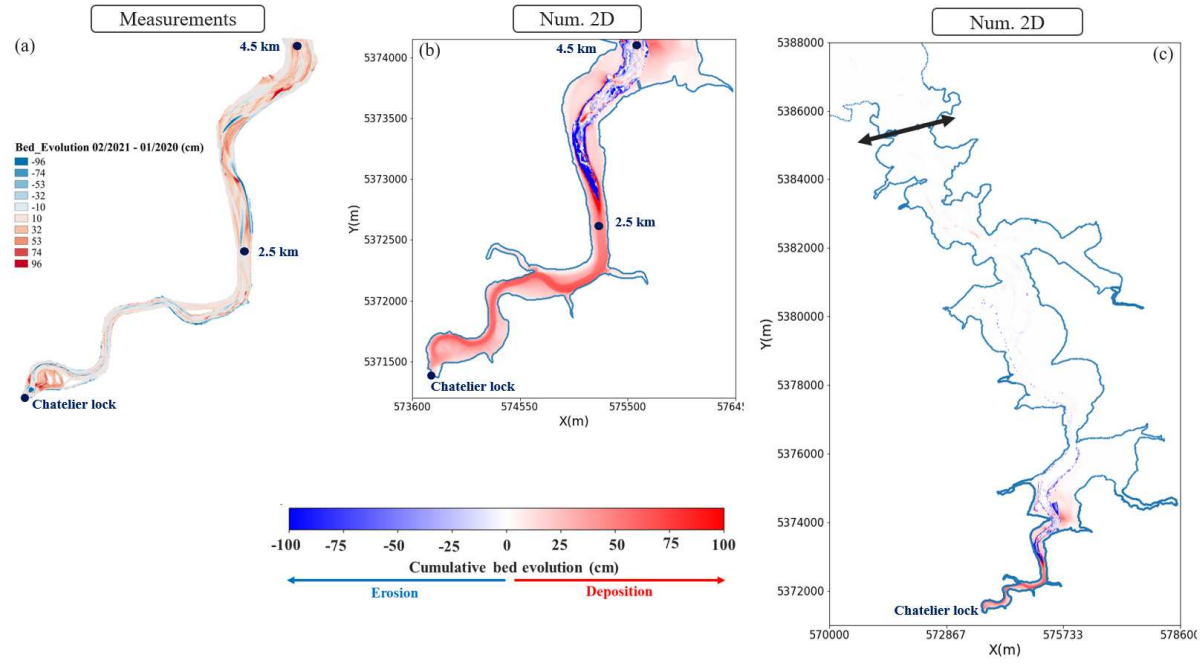

Figure 6.7: (a) Measured and (b,c) 2D numerical cumulative bed evolution over 13 months (January 2020 - February 2021). (a,b) Maps focus on the upper estuary and (c) map covers the whole estuary.

6.3.2 Scenario 1: hydraulic flush

Although the Rance is a hyper-tidal estuary with a significant tidal influence comparing to the river's influence, its upstream limit (Chatelier lock) is characterized by occasional hydraulic flush operations that could influence sediment transport and the estuary's morphodynamics. To evaluate this potential impact, suspended sediment concentrations (SSC) and cumulative bed evolution were compared over a neap-spring tidal cycle between configurations SC 10 and SC 11 (Table 6.1).

Comparison of spring tidal averaged SSC of the three considered sediment classes, namely cohesive sediment, very fine sand of 100µm and fine sand of 200µm, between configurations SC 10 and SC 11 is illustrated in Figures 6.8, 6.9 and 6.10. Figure 6.8 assessed that the suspended matter is primarily composed of cohesive sediment and is concentrated in the upper estuary, mainly upstream Saint-Hubert Port, weather the river discharge is constant or variable. Zooming on this zone (Figures 6.9 and 6.10), the variable river discharge in scenario SC 11 seem to decrease tide-averaged suspended sediment concentrations 3.5km downstream of the Chatelier lock by 30mg/l. Indeed, river discharge in scenario SC 11 is higher than the mean river discharge deployed in scenario SC 10, the corresponding ebb currents are thus stronger in configuration SC 11 comparing to configuration SC 10. Therefore, sediment in the upper estuary's channel could be resuspended during ebb in scenario SC 11 conversely to scenario SC 10 due to insufficient river flowrate.

Comparison of cumulative bed evolution over a neap-spring tidal period between scenarios SC 10 and SC 11 was illustrated in Figures 6.11 and 6.12. Significant influence of the hydraulic flush is noted mainly in the area upstream of Saint-Hubert port. Indeed, high river discharge decreased sedimentation rate in the upper estuary, namely in the main channel 0-2.5km downstream of the Chatelier lock and in the western shoal and secondary channel 4km downstream of the Chatelier lock. Differences between configurations SC 10 and SC 11 in the latter zones vary between 1 to 4cm over the fortnight period. Hydraulic flush could thus reduce sediment trapping in the upper estuary by 30-60%. Furthermore, the hydraulic flush scenario (SC 11) reduced erosion rate noted in the eastern channel, 2.5-4.5km downstream of the Chatelier lock, by $\sim$50%.

In summary, these findings reveals the sensitivity of deposition fluxes in the upper estuary to river discharge. They highlight the importance of providing the numerical model an accurate river discharge to correctly simulate bed level changes on long term periods (discussed in section 6.3.1) and particularly over period of hydraulic flushes. Furthermore, hydraulic flushes appear to be an efficient solution to reduce sediment trapping in the upper estuary.

6.3.3 Scenario 2: sediment entry from the sea

Under storm conditions, the oceanic boundary of the numerical model could influence sediment fluxes in the Rance estuary, particularly suspended particles entering through the plant towards the basin [Bonnot-Courtois et al., 2002]. Therefore, a storm-like conditions scenario, SC 21 in Table 6.1, was designed to examine this impact.

The first phase of scenario SC 21 is a 2-day period of constant SSC equal to 55mg/l at the oceanic boundary, in order to mimic sediment resuspension induced by a storm. Figure 6.13 showed that simulated averaged SSC at turbines and sluice gates over the "storm" period is around 15mg/l. It is consistent with measured SSC in this area under effective storm conditions [LCHF, 1982; Bonnot-Courtois et al., 2002]. Peak flood SSC values are noticed during the estuary's filling stage, specifically during G.O. stage for sluice gates and during F.O. stage for

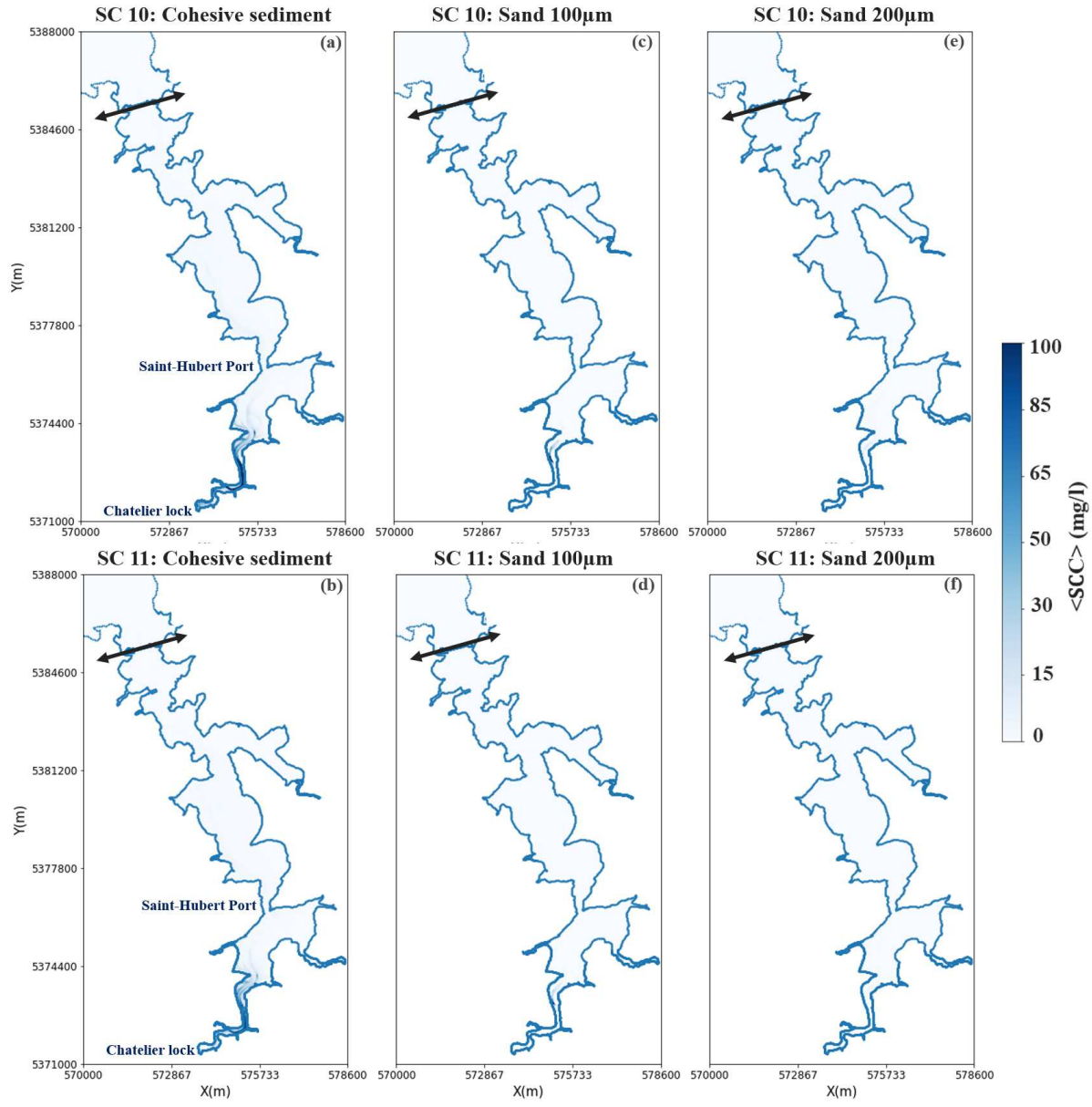

Figure 6.8: Spring tide-averaged concentration of suspended (a,b) cohesive sediments, (c,d) sand of 100μm and (e,f) sand of 200μm for configurations SC 10 and SC 11 respectively (Table 6.1).

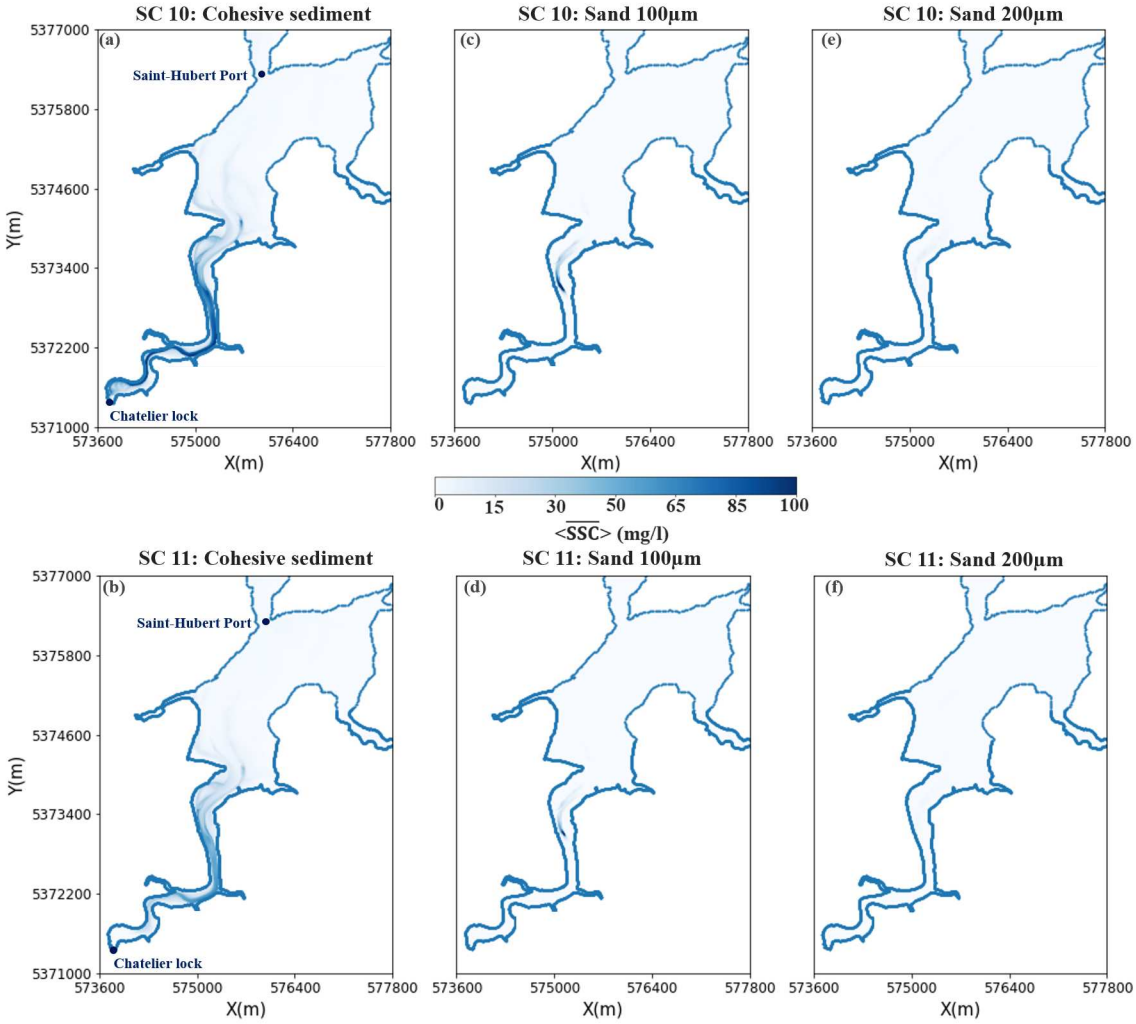

Figure 6.9: Zoom on the upper estuary of spring tide-averaged concentration of suspended (a,b) cohesive sediments, (c,d) sand of 100μm and (e,f) sand of 200μm for configurations SC 10 and SC 11 respectively (Table 6.1).

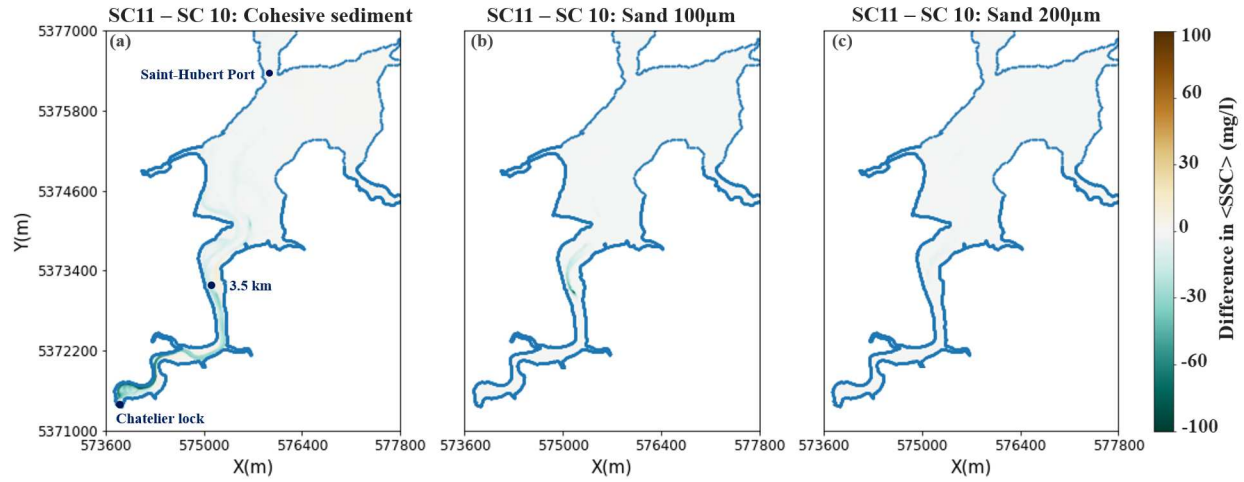

Figure 6.10: Difference between scenarios SC 10 and SC 11 of spring tide-averaged concentration of suspended (a,b) cohesive sediments, (c,d) sand of 100μm and (e,f) sand of 200μm. Positive (negative) values means that sediment are more (less) concentrated in the water column in scenario SC 11 comparing to scenario SC 10. (see Table 6.1 for modeling scenarios).

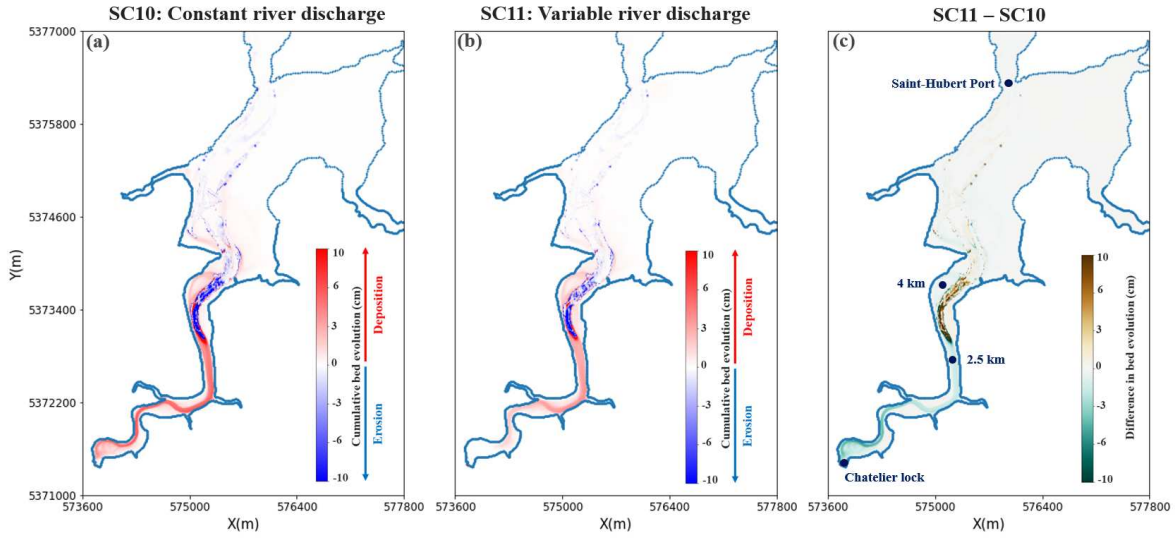

Figure 6.11: Cumulative bed evolution in the upper estuary over a fortnight period for (a) scenario SC 10 and (b) scenario SC 11 (see Table 6.1). (c) Difference in cumulative bed evolution over a spring-neap period between scenario SC 11 and SC 10. Sedimentation rate is increased (decreased) by configuration SC 11 when bed evolution difference is positive (negative). Erosion rate is increased (decreased) by configuration SC 11 when the bed evolution difference is negative (positive).

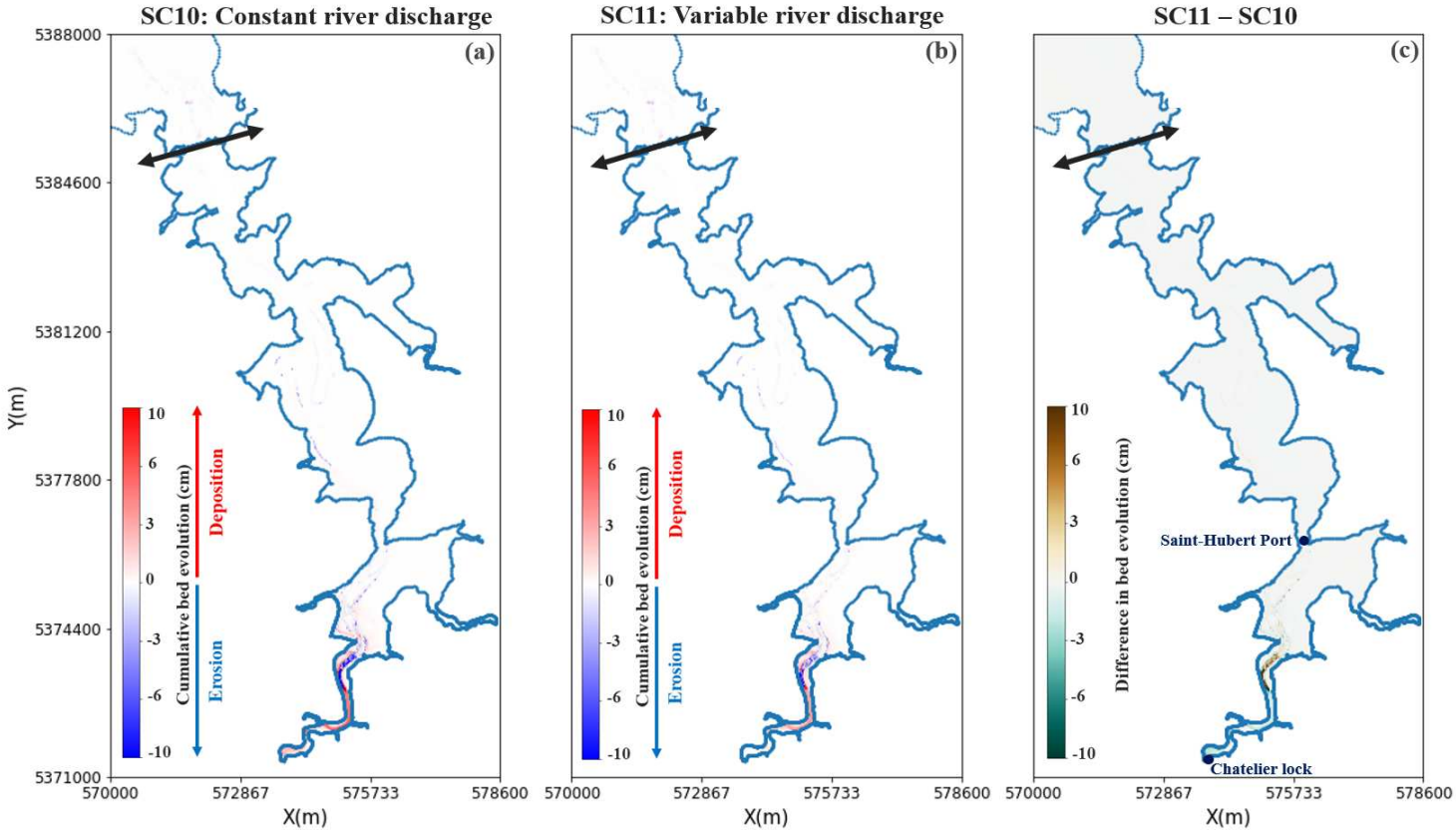

Figure 6.12: Cumulative bed evolution in the whole estuary over a fortnight period for (a) scenario SC 10 and (b) scenario SC 11 (see Table 6.1). (c) Difference in cumulative bed evolution over a spring-neap period between scenario SC 11 and SC 10. Sedimentation rate is increased (decreased) by configuration SC 11 when bed evolution difference is positive (negative). Erosion rate is increased (decreased) by configuration SC 11 when the bed evolution difference is negative (positive).

Table 6.2: Operating modes of sluice gates and turbines.

Structure	Sluice gates		Turbines					
Operating mode	G.O.	G.C.	F.O.	D.O.	I.T.	D.T.	D.P.	T.O.
Definition	Gates Open	Gates Close	Filling On	Draining On	Inverse Turbining	Direct Turbining	Direct Pumping	Turbines Off
Tidal phase	Flood Ebb	Flood Ebb	Flood	Ebb	Flood	Ebb	Flood	Flood Ebb

the turbines (Table 6.2). Conversely, peak ebb SSC values are lower than peak flood SSC and observed only near the turbines during power generation stage (D.T., Table 6.2). Consequently, the mass of suspended particles entering the estuary during flood is larger than the mass of suspended particles leaving the estuary during ebb. This unbalanced sediment transport was previously discussed in chapters 3 and 5. At the end of this first phase, both non-cohesive and cohesive sediment have been deposited inside the basin and could be transported up to Saint-Suliac (Figures 6.14.a and 6.14.b). Sedimentation rates can reach up to $0.4cm$ over 2 days, mainly in the coves upstream and downstream the plant (Figure 6.14.c). Cohesive sediment is preferably deposited on shoals and coves while non-cohesive sediment is removed from the main channel and deposited nearby. In addition, non-cohesive sediment was transported further upstream in the estuary comparing to cohesive sediment.

The second phase of scenario SC 21 is a neap-spring tidal period following the first phase with a SSC value equal to $0mg/l$ at the oceanic boundary. The aim of the second phase is to identify how sediment would be distributed in the Rance estuary after the storm period. Figure 6.15 showed that a neap-spring tidal period was sufficient to transport both cohesive and non-cohesive sediment up to the uppermost boundary limit (Chatelier lock). Indeed, sediment deposited inside the estuary during the first phase were resuspended and transported to the coves further upstream in the estuary. Consequently, deposition zones observed at the end of the first phase (Figure 6.14.c) appeared as erosion zones at the end of the second phase (Figure 6.15.c). A longitudinal and transverse grain-size gradients are noticed in Figures 6.15.a and 6.15.b, with the main channel cleared from fine sediment to the bottom of the coves characterized by muddy sand deposition. This sediment distribution is consistent with the real sediment distribution observed in the Rance estuary, namely near La Richardais, Chateauneuf, Saint-Hubert port, Mordreuc and Chatelier lock [Bonnot-Courtois et al., 2002].

6.3.4 Scenario 3: alternative operation modes of the tidal power plant

To evaluate the efficiency of a proposed alternative operation modes of the plant, suspended sediment concentrations (SSC) and cumulative bed evolution were compared over a neap-spring tidal cycle for configurations SC 30 and SC 31 (Table 6.1).

Two monitoring stations were chosen in the upper estuary, namely T1 and T2 (see Figure 6.1.a for stations location). Figure 6.16 shows that the alternative operation mode of the TPS increases peak flood SSC in both stations T1 and T2 between day 18.75 and 20.25. The maximum difference of $40mg/l$ is noticed in day 19.5 where sluice gates are open in flood for scenario SC 31 and not in SC 30 (Figure 6.3.a). Moreover, high SSC differences are noticed during flood since these stations are not emerged during ebb. Although the operation modes were modified

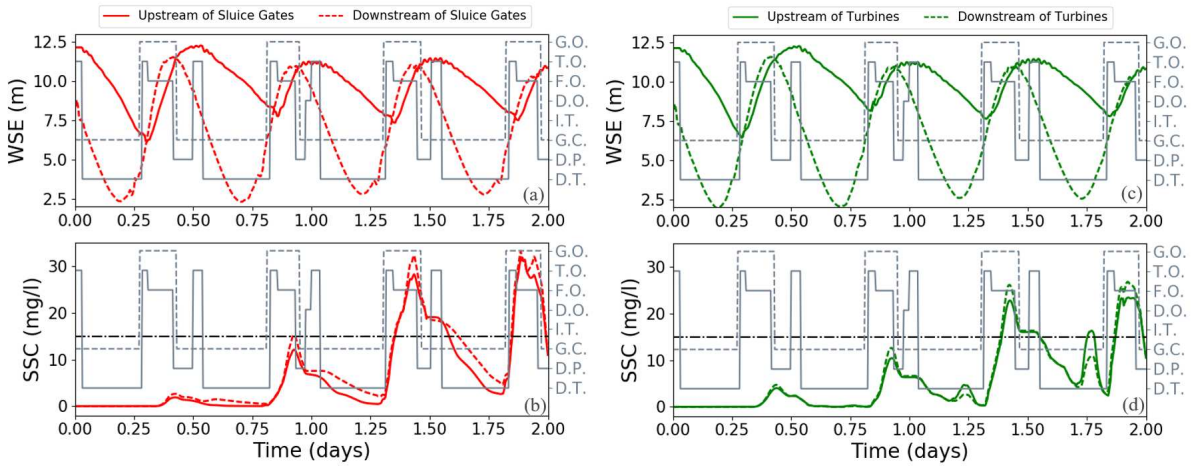

Figure 6.13: Water surface elevation and suspended sediment concentration upstream and downstream of (a,b) sluice gates and (c,d) turbines. Grey filled- and dashed-lines represent turbines and sluice gates operation modes respectively (see Table 6.2). Black line in Figures b and d represent $15 mg/l$.

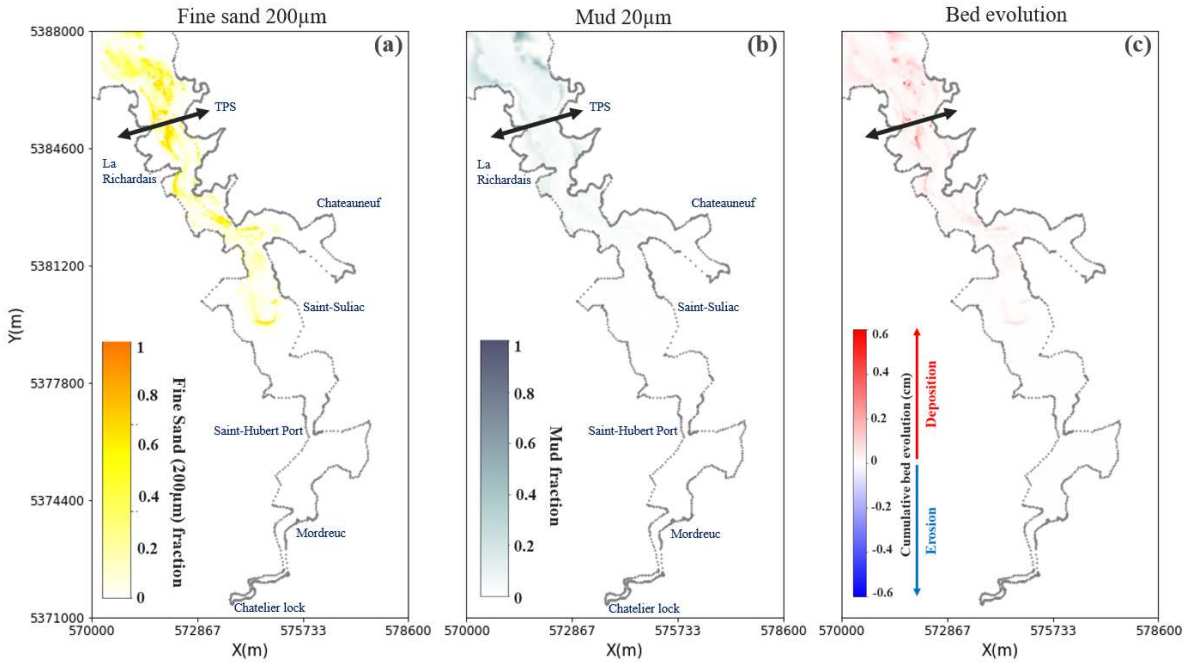

Figure 6.14: Spatial distribution of (a) fine sand of 200 µm, (b) mud of 20 µm and (c) the corresponding bed evolution over 2 days period of storm-like conditions (SC 21, Table 6.1).

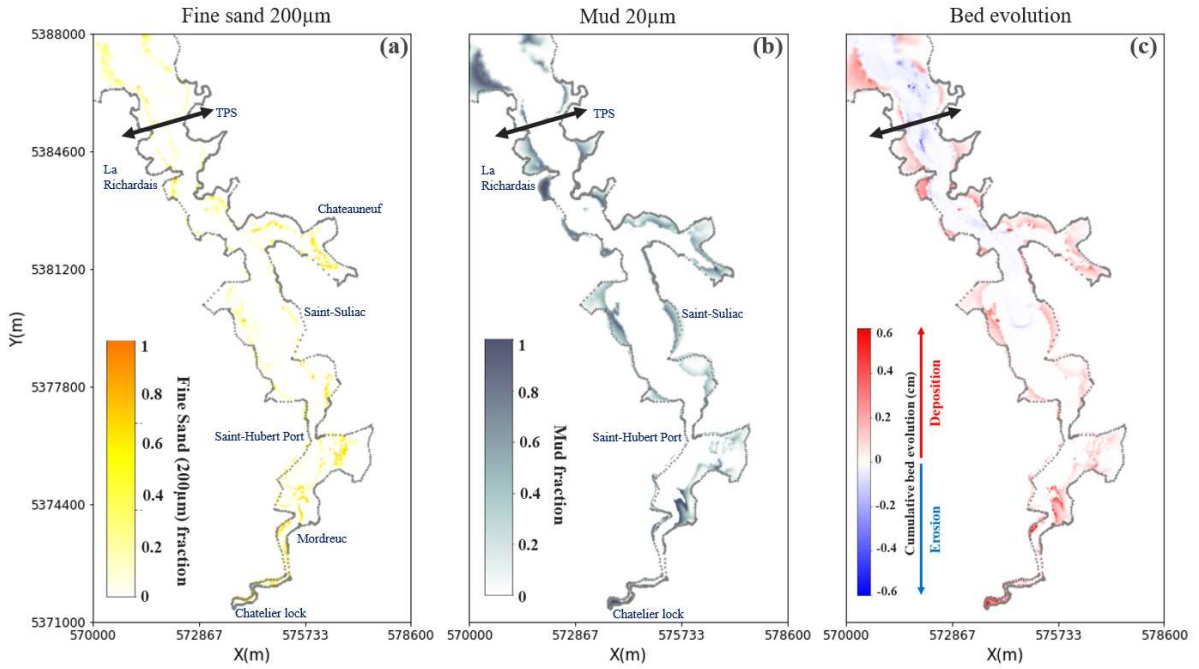

Figure 6.15: Spatial distribution of (a) fine sand of 200 µm, (b) mud of 20 µm and (c) the corresponding bed evolution over spring-neap tides period after the storm (SC 21, Table 6.1).

during 3 consecutive tidal cycles (days 18.75 - 20.25) a lower impact can be noticed during the following two tidal cycles (days 20.25 - 21.25).

Further downstream, stations S2 and M2 were chosen to represent the middle and the lower estuary respectively (see Figure 6.1.a for stations location). The alternative operation mode decreases low water levels by 2m between days 19.25 - 20.00 (Figure 6.17). In addition, the tide is less asymmetric between day 19.25 - 20.00. At station S2, the alternative TPS operation mode generates ebb SSC of 50mg/l thanks to the estuary's draining induced by the sluice gates, while only flood SSC are noticed with the current operation mode of the plant. Furthermore, peak ebb (flood) SSC differences, between SC 31 and SC 30 scenarios, can reach up to 50 mg/l (25mg/l). Further downstream at station M2, SSC values are below 3mg/l. Therefore, no significant differences are noticed. In summary, flood SSC are increased by the alternative operation mode of the plant in the upper and middle estuary, and it generates ebb SSC in the middle estuary.

The alternative operation mode of the TPS does not seem to modify morphodynamic trends (Figures 6.18 and 6.19). Indeed, the important bed level changes occur in the upper estuary for both scenarios SC 30 and SC 31: (i) the main upper channel (0-2.5km downstream of the Chatelier lock) and the secondary western channel (2.5-4.5km downstream of the Chatelier lock) are always subject to sedimentation, and (ii) the eastern channel (2.5-4.5km downstream of the Chatelier lock) is always eroded. Differences between configurations SC 31 and SC 30 in terms of bed evolution assessed that the alternative operation mode of the plant might be effective to decrease sediment trapping in the upper channel by a rate of 0.3cm over a neap-spring period (Figure 6.18.c). Consequently, displaced sediment will be distributed further downstream, namely over the western bank 4km downstream of the Chatelier lock and the zone around Saint-Hubert port (Figures 6.18.c and 6.19.c). Therefore, the modification of the TPS current operation mode during only two tidal cycles could reduce sedimentation rates in the upper

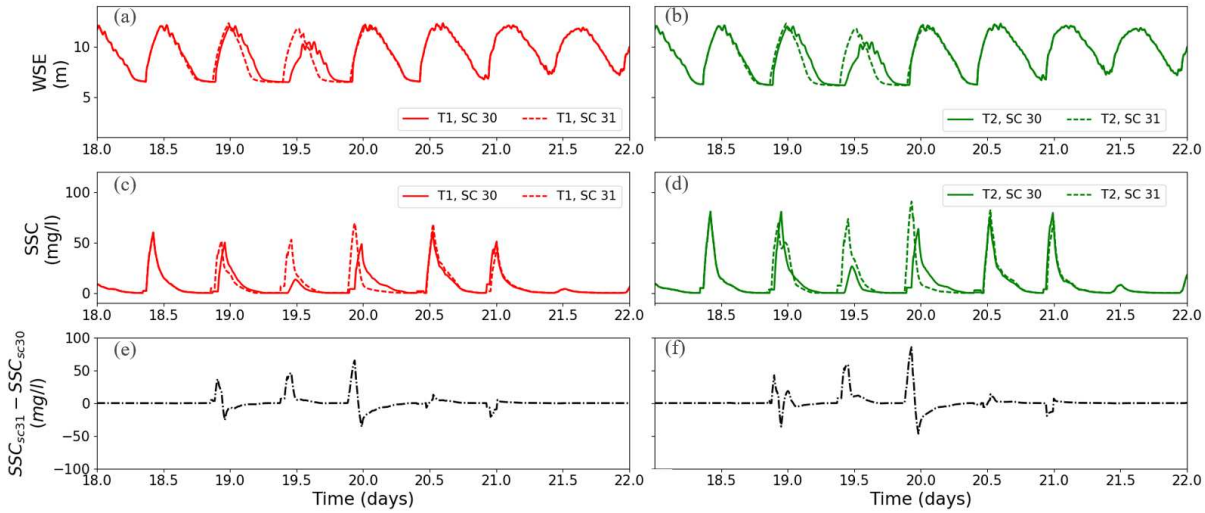

Figure 6.16: Hydro-sedimentary variables for configurations with the current and the alternative operation modes of the TPS (SC 30 and SC 31, Table 6.1) at positions T1 and T2 respectively: (a,b) water surface elevation, (c,d) suspended sediments concentration, (e,f) difference of suspended sediment concentration between scenarios SC 30 and SC 31. See Figure 6.1.a for stations T1 and T2.

channel by 5%.

6.4 Discussion

Despite the intrinsic limitations of 2D depth-averaged models in simulating estuarine environments, sediment transport and morphodynamic results obtained in this chapter satisfactorily reproduced the main features of sediment dynamics in the Rance estuary comparing to field measurements and 3D simulations. Considering its lower computational cost (∼2 times faster than the 3D), this approach is suitable for environmental studies requiring macroscopic overview on morphodynamic trends and on the main sediment transport processes over long-term periods. This approach was also widely deployed and provided correct results in other well-mixed estuarine environments, namely the Scheldt estuary [Gourgue et al., 2013; Nnafie et al., 2018], the Río de la Plata [Santoro et al., 2017] and the Shenzhen River [Feng et al., 2019]. Although, 2D numerical results satisfactorily reproduced bed evolution over a 3 months period in the Rance estuary, sedimentation rates were overestimated over a long-term period of a year. This discrepancy was mainly due to the assumption of a constant river discharge instead of a variable river discharge that considers hydraulic flushes occasionally operated at the river boundary. Comparison between scenarios with constant and variable river flowrates enhanced as well the importance of an accurate variable river discharge at the uppermost limit (Chatelier lock) to correctly reproduce bed level evolution in the upper estuary over long time scales. Furthermore, this comparison highlighted the efficiency of a hydraulic flush to decrease sediment trapping in the upper estuary by 30-60% over a spring-neap tidal period. It should be noted that these reduction rates are related to an exceptional hydraulic flush scenario with a continuous high river flowrate over 4 days and peak flow rate equal to $57 m^3/s$. However, hydraulic flushes often lasted 2 hours during ebb with peak flowrate equal to $42 m^3/s$ [Bonnot-Courtois, 1993].

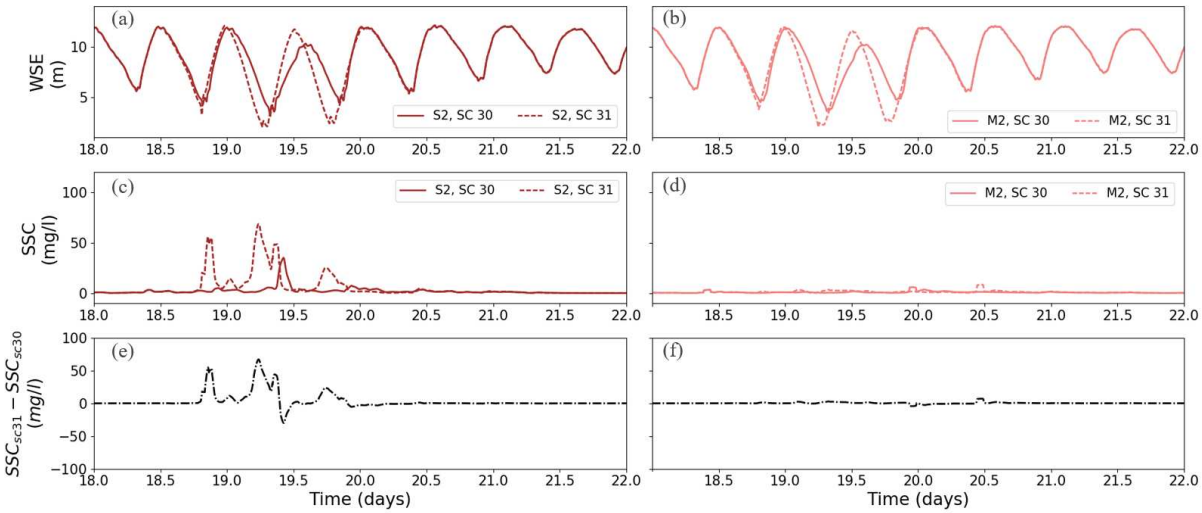

Figure 6.17: Hydro-sedimentary variables for configurations with the current and the alternative operation modes of the TPS (SC 30 and SC 31, Table 6.1) at positions S2 and M2 respectively: (a,b) water surface elevation, (c,d) suspended sediments concentration, (e,f) difference of suspended sediment concentration between scenarios SC 30 and SC 31. See Figure 6.1.a for locations S2 and M2.

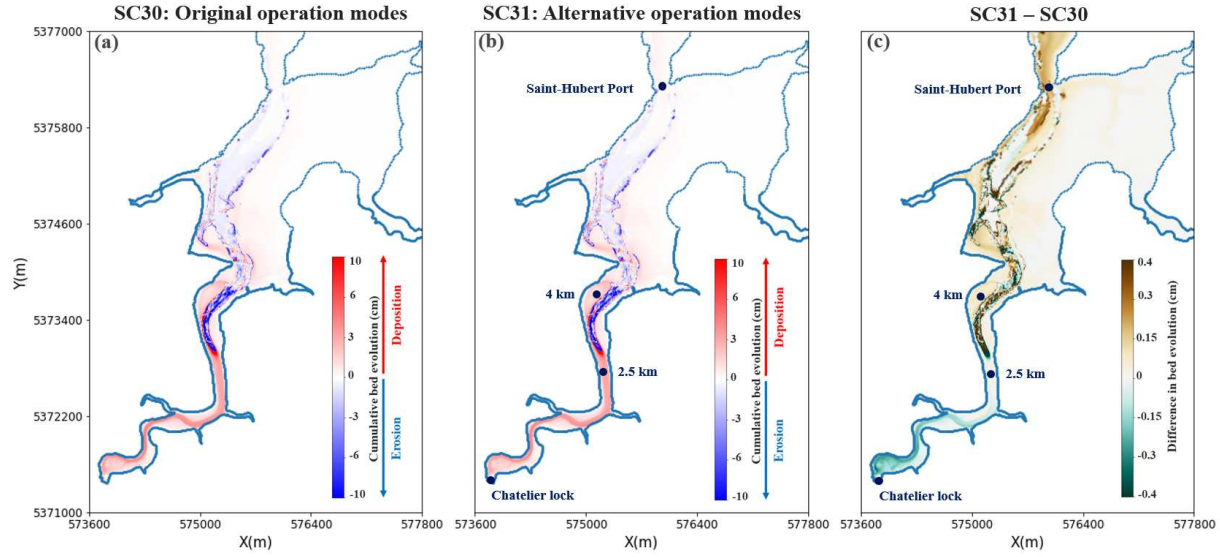

Figure 6.18: Cumulative bed evolution in the upper estuary over a fortnight period for (a) scenario SC 30 and (b) scenario SC 31 (see Table 6.1). (c) Difference in cumulative bed evolution over a spring-neap period between scenario SC 31 and SC 30. Sedimentation rate is increased (decreased) by configuration SC 31 when bed evolution difference is positive (negative). Erosion rate is increased (decreased) by configuration SC 31 when the bed evolution difference is negative (positive).

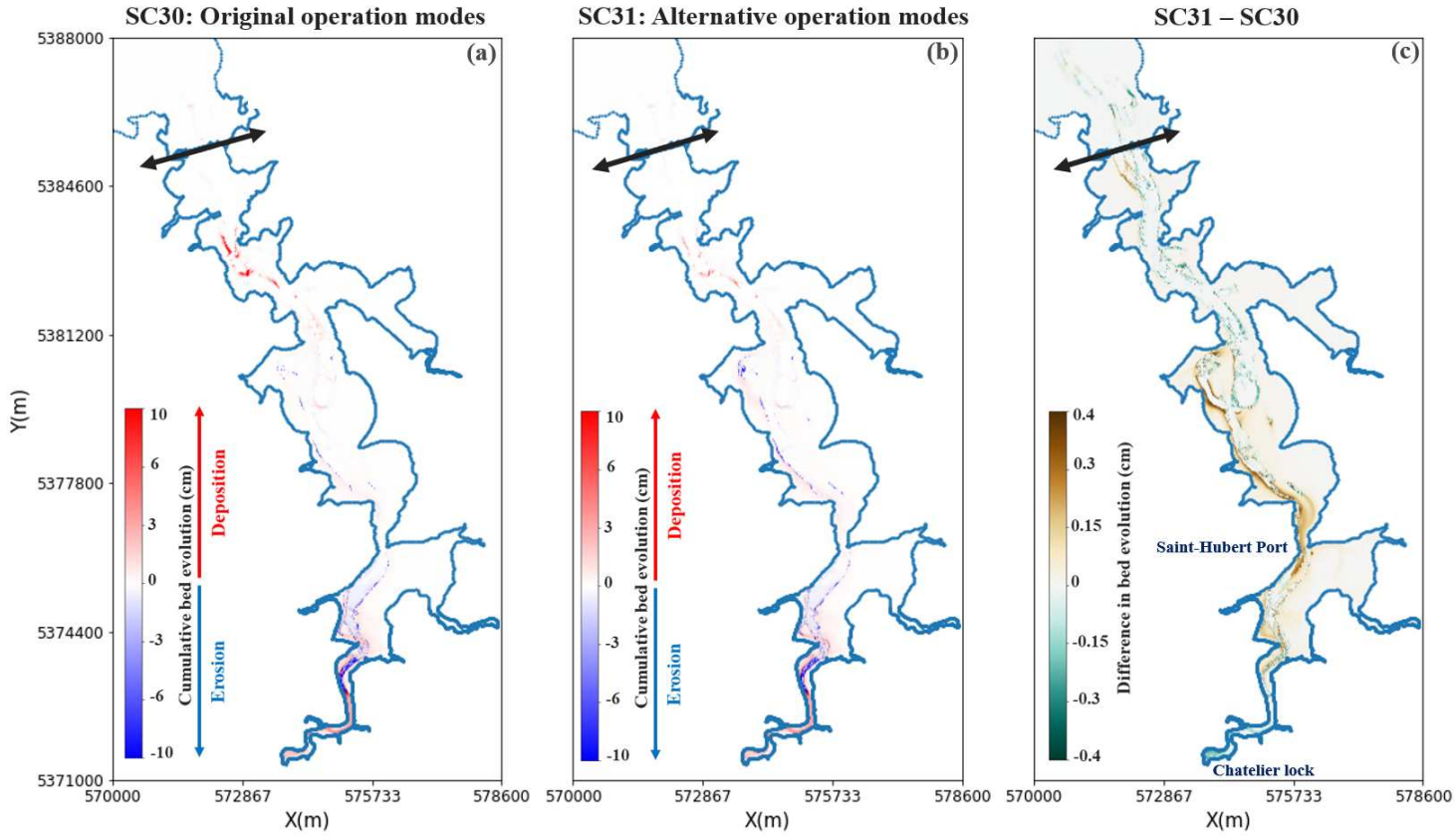

Figure 6.19: Cumulative bed evolution in the whole estuary over a fortnight period for (a) scenario SC 30 and (b) scenario SC 31 (see Table 6.1). (c) Difference in cumulative bed evolution over a spring-neap period between scenario SC 31 and SC 30. Sedimentation rate is increased (decreased) by configuration SC 31 when bed evolution difference is positive (negative). Erosion rate is increased (decreased) by configuration SC 31 when the bed evolution difference is negative (positive).

Bonnot-Courtois [1993] stated that the latter hydraulic flush type does not seem to be very efficient on decreasing sediment trapping in the upper estuary as particles displaced during ebb and transported downstream are resusupended during the next flood and deposited on their preferential trapping zone. Based on these findings, hydraulic flushes may be efficient in decreasing sediment accumulation in the upper estuary if they are performed with a high flowrate over at least 4 consecutive tidal cycles. As these conditions are primarily related to the uncontrolled river's hydrological regime, another recommendation to reduce sediment trapping in the upper estuary was an alternative operation mode of the tidal power station. It consisted of opening sluice gates during ebb and adapt turbines opening to reduce current asymmetry. This alternative scenario revealed its capacity to reduce particles accretion in the upper estuary by 5% over a neap-spring tidal period. It should be noted that the modification of the TPS operation modes was limited to 3 consecutive tidal cycles over a simulation period of 28 tidal cycles. Assuming an equivalent reduction factor over the other spring tides, the efficiency of this alternative operation mode of the plant would be increased. Based on these findings, it appears that alternative operation mode of the plant has the advantage of being under human-control but with a relatively interesting efficiency, while hydraulic flushes would be of higher efficiency but depend strongly on the uncontrolled but predictable river's hydrological regime. Furthermore, the combination of these two recommendations would be of interest to evaluate their efficiency to reduce sedimentation in the upper estuary.
In addition to the river boundary, the oceanic open boundary can also influence sediment dynamics inside the estuary, specifically during storm periods. A typical storm would induce strong resuspension and SSC of $15 mg/l$ during 2 days nearby the upstream of the plant [LCHF, 1982]. The supplied marine sediment would enter the basin during storm period and a fortnight period would be sufficient to transport and deposit them in the coves along the estuary. Furthermore, sedimentation rate can reach up to $0.5 cm$ over a period of a fortnight in the upper estuary, while sedimentation rate in the same zone with the real sediment distribution is approximately 10 times higher. Consequently, the assumption of not considering storm-like conditions was relevant to assess the first order morphodynamics in the Rance estuary. As several processes would impact sediment dynamics in this complex estuarine system, it was mandatory to evaluate first the influence of each physical process individually conversely to studies from [Thiebot, 2008]. However, complementary scenarios, namely (i) a storm-like condition scenario in a configuration without the plant, (ii) a storm-like condition scenario with the real distribution of sediment inside the estuary and (iii) a combination between a hydraulic flush and a storm-like condition scenario, would be interesting to be examined in future work.

6.5 Conclusions

Complementary sediment dynamics processes were assessed from hypothetical scenarios in this complex estuarine environments by its geomorphology, sediment distribution, the presence of a power plant at its mouth and a lock at its uppermost limit (Chatelier lock). A depth-averaged two-dimensional (2D) coupled hydrodynamic and morphodynamic numerical model was calibrated and validated to simulate the present-day main features of sediment transport and morphodynamics in the Rance estuary over fortnightly time scales to monthly time scales. Although provided satisfactory bed evolution results over a 3 months period, the 2D numerical model need to be re-calibrated through the river discharge in order to accurately capture sedimentation rates over a long-term period (in the order of a year). Conversely, a typical storm event would not significantly influence the main long term morphodynamic processes in the

Rance estuary.
Hydraulic flushes revealed their efficiency in decreasing sediment accumulation in the upper estuary if they are performed with a high flowrate, in the order of $50 m^3/s$, over at least 4 consecutive tidal cycles. Under these conditions, sediment trapping could be reduced by the hydraulic flush in the upper estuary by 30-60% over a neap-spring tidal period. Furthermore, the opening of sluice gates during ebb and adapting turbines opening to reduce current asymmetry during spring tides seem to be also a promising alternative to the plant operation mode to reduce particles accretion in the upper estuary. Finally, the present 2D numerical model would be a suitable operational tool to evaluate other scenarios to help the estuary's management.

Acknowledgements

This work was funded by the French National Association of Research and Technology (ANRT) and EDF R&D with the Industrial Conventions for Training through REsearch (CIFRE grant agreement 2018/1653). The authors are grateful to the members of the Conseil Scientifique De La Rance, EPTB, Rance Energie and EDF CIH for providing the Rance river discharge data and feedback on the alternative operation mode of the plant.

CHAPTER 7

CONCLUSIONS AND OUTLOOK

7.1 Conclusions

This section is devoted to answering the four research questions posed in Chapter 1 and to provide the conclusions of this thesis's work.

Q1. *How relevant are 2D and 3D numerical models at reproducing the main features of hydro-sedimentary dynamics observed in macrotidal estuaries influenced by the presence of a tidal power station (TPS) ?*

A two-dimensional (2D) depth-averaged hydrodynamic model of the Rance estuary influenced by the presence of a tidal power station was developed and successfully validated against water level observations and depth-averaged velocity field measurements at many stations throughout the estuary. In particular, flow patterns and tidal asymmetry for diverse scenarios involving past and present bed elevations, the presence/absence of the dam and the existence of a lock at the estuary's upper limit were studied. Nevertheless, the understanding of flow structure within the water column, and the effect of the operation modes of the sluice gates and turbines of the TPS, did not account for three-dimensional (3D) processes. To this goal, a 3D Reynolds-Averaged Navier-Stokes hydrodynamics model accounting for salinity was developed. Numerical results showed that the model correctly reproduces the horizontal and vertical distribution and temporal evolution of ebb and flood currents along the estuary. Moreover, salinity patterns are also satisfactorily captured by the model. These results highlight the added-value (addressed in **Q2**) of 3D hydrodynamic numerical modeling of the Rance estuarine system with respect to the 2D depth-averaged model, namely, the water circulation, salinity distribution and velocity gradients within the water body. Sediment transport and morphodynamic processes are better simulated when these 3D hydrodynamic features are taken into account.
A 3D hydro-morphodynamic model was calibrated and validated in terms of sediment transport and bed evolution on the basis of measurements captured from field survey campaigns and probes installed in the Rance estuary. Numerical results were analysed over fortnightly periods and 3-month periods, mainly because of the availability of validation dataset and also due to available computational resources. The selected timescales were relevant to understand the main sediment transport processes in this complex estuarine system and to quantify the impact of the TPS on sediment dynamics (addressed in **Q2** and **Q3**). However, only short term simulations (maximum period of 3 months) were performed due to the costly computational time. In addition, these three-dimensional simulations focused on the primary physical processes, and did not address other occasional physical processes such as variable river discharge, storm-like conditions and alternative scenarios to decrease sediment accumulation in the upper estuary. To this goal, a depth-averaged 2D coupled hydrodynamic and morphodynamic numerical model was calibrated and validated to simulate the present-day main features of sediment transport and morphodynamics over fortnightly time scales to monthly time scales. Although it provided satisfactory bed evolution results over a 3 months period, the 2D numerical model needs to be re-calibrated through the river discharge in order to accurately capture sedimentation rates over a long-term period (in the order of a year).

Q2. *How hydrodynamics, sediment transport and morphodynamics processes are influenced by the presence of the world's second-largest tidal power station?*

Numerical results indicated that, in the absence of the TPS, bathymetry changes do not have any significant impact on hydrodynamics. However, the presence of the dam substantially modifies tidal patterns. The main consequences of the presence of the dam at the estuary mouth

are: (i) a major decrease in tidal range and tidal prism along with the amplification of the estuary's low-water level switches a large part of intertidal zones, which become permanently submerged; (ii) a limitation of the high-water level inside the estuary which protects the basin against marine flooding; (iii) there is an overall decrease in tidal currents in the estuary, except upstream of the sluice gates and downstream of the turbines; (iv) flood currents and ebb currents are locally amplified upstream of the sluice gates and downstream of the turbines respectively. Furthermore, the morphology of the estuary significantly influences currents, with strongest ebb velocity observed in the narrowing at Saint-Hubert-Port. In addition, Saint-Suliac zone is characterized by the heterogeneity in the distribution of the along-channel and cross-channel components along the transect. Moreover, currents do not seem to considerably vary along the water column except at Saint-Hubert-Port and Saint-Suliac during flood. After over 50 years of service, the Rance hydro-electric power station induces modification in the natural hydraulic regime which led to a different distribution of salinity compared to that before the dam's construction. Dynamics of freshwater-saltwater interface is sensitive to seasonal river discharge variation, hydraulic flushes occurred at the Chatelier Lock and plants operating cycles. The 3D hydro-sedimentary model revealed that at the scale of a tidal cycle, (i) peak SSC are noticed during flood, specifically during the estuary's infilling phase where both turbines and sluice gates are open; (ii) sediments could be resuspended locally during ebb, specifically during turbining phase (electricity production stage), but would not be transported further than $3km$ from the uppermost limit. At the scale of a fortnight, residual sediment flux is continuously oriented towards the upper estuary with peak magnitudes reached during spring tides. Consequently, significant sedimentation rates were observed in the main upstream channel and western channel near Mordreuc. This morphodynamic behavior was also captured under natural tidal forcing (without TPS), but at lower sedimentation rates. Therefore, sediments are mainly trapped in the upper estuary under the artificial forcing induced by the plant, while they could be homogeneously distributed further downstream under natural tidal forcing.

Q3. *Which are the dominant physical mechanisms driving the sediment dynamics in the Rance estuary?*

This study revealed that as the tide passes through the TPS and propagates along the estuary, it becomes more distorted and more asymmetric. This effect has both natural and artificial origins, due to the estuary's morphology and to hydrodynamic forcing by the plant. For both the natural condition and the artificially-induced hydrodynamic forcing due to the presence of the plant, numerical results showed that the Rance estuary mainly exhibits flood-dominant behavior, with a longer duration of falling than rising water and stronger peak flood currents than ebb currents. Consequently, sediment transport tends to be in the landward direction: *i.e.*, the plant does not impact the source of sediment present inside the basin. Conversely, the presence of the plant has a profound impact on hydrodynamics, which in turn drives sediment dynamics in the estuary. This aspect is addressed in **Q2**.
2D numerical results revealed that river discharge variation at the Chatelier lock must be considered in order to accurately reproduce sedimentation rates over long-term timescales (in the order of a year). Conversely, a typical storm event would not significantly influence the main long-term morphodynamic processes in the Rance estuary.

Q4. *What recommendations can be given to stakeholders for a more efficient estuary management?*

Hydraulic flushes revealed their efficiency in decreasing sediment accumulation in the upper estuary if they are performed at a high flowrate, in the order of $50m^3/s$, over at least 4

consecutive tidal cycles. Under these conditions, sediment trapping could be reduced by the hydraulic flush in the upper estuary by 30-60% over a neap-spring tidal period. Furthermore, the opening of sluice gates during ebb and adapting turbines opening to reduce current asymmetry during spring tides seem to be also a promising alternative to the plant operation mode to reduce particles accretion in the upper estuary.

This PhD thesis allowed to better understand hydro-sedimentary dynamics in the Rance estuary. Furthermore, this work quantified the impact of the plant on hydrodynamics, sediment transport and morphodynamics in this highly engineered system, characterized by the presence of a tidal power plant on its mouth and a lock on its upstream limit. In addition, the developed numerical models showed to be invaluable and complementary tools to define a sustainable management plan that conciliate electricity production and environmental impacts. The 2D numerical model showed to be a reliable operational tool to evaluate various scenarios by keeping a good ratio between model accuracy versus CPU time. The 3D numerical model would be more suitable for detailed analyses and scientific investigations of flow and sediment transport processes at shorter space and time scales. For an equivalent model setup and parameterization of the Rance estuary, 2D hydro-sedimentary simulations are roughly 2 times faster than 3D simulations.
Research outcomes and recommendations from this thesis can be extrapolated to existing and future projects involving estuarine systems presenting anthropogenic structures such as dams and tidal power plants, namely Sihwa lake, Bristol channel, Pentland Firth and others.

7.2 Outlook

Suggestions for future research work and thesis's outcomes exploitation are provided thereafter. Numerical results assessed the capabilities of the 2D and 3D models at reproducing the main features and sediment dynamics in the Rance estuary under hypothetical scenarios. Consequently, the hydro-sedimentary behaviour of this complex estuarine system would be investigated for supplementary alternative operation modes, by following the modelling strategies and recommendations proposed in this work.
As pointed-out in Chapter 6, river discharge values at Chatelier lock are relevant for an accurate representation of sediment transport processes in the upper estuary. It is therefore suggested a continuous monitoring of the Rance river's discharge at the estuary's uppermost limit.
To further validate the models, continuous monitoring of suspended sediment concentration downstream and upstream of the tidal power station is essential to quantify marine sediments exchanges between the basin and the coastal zone. It is also worthwhile to correlate this information with marine environmental conditions such as wind, waves and storm surges, particularly during extreme events.
A smaller, more refined model of the upper estuary would allow to perform further investigations with the sediment transport and bed evolution model that incorporates multi-layers and consolidation processes. Ideally, this task must be supported by field measurements at selected locations.
The effect of sea level rise, estimated to be approximately equal to 10 cm between 1957 and 2019, could also be evaluated to have a more consistent overview of the long term evolution of this particular estuarine system.
Finally, the developed hydro-sedimentary models would be coupled to water quality and/or ecological models to perform quantitative analyses of the impact of TPS operation modes on the

environment and habitat.

Scientific publications

Journal papers

- Rtimi, R., Sottolichio, A., and Tassi, P. (2022). The Rance tidal power station: toward a better understanding of sediment dynamics in response to power generation. *Submitted to Renewable Energy Journal.*

- Rtimi, R., Sottolichio, A., and Tassi, P. (2021). Hydrodynamics of a hyper-tidal estuary influenced by the world's second largest tidal power station (Rance estuary, France). *Estuarine, Coastal and Shelf Science*, doi:10.1016/j.ecss.2020.107143.

- Rtimi, R., Sottolichio, A., Tassi, P., Bertier, C., Le Brun, M., Vandenhove, M., and Parquet, L. (2021). Three-dimensional hydrodynamic model of the Rance estuary (France) influenced by the world's second largest tidal power plant. *La Houille Blanche - Hydroscience Journal*, doi:10.1080/27678490.2021.2016025.

- Rtimi, R., Sottolichio, A., and Tassi, P. (2020). Tidal patterns and sediment dynamics in a hypertidal estuary influenced by a Tidal Power Station. *Journal of Coastal Research*, 95 (SP1), doi:10.2112/SI95-293.1.

International conferences

- Rtimi, R., Sottolichio, A., Tassi, P., Bertier, C., Le Brun, M., Vandenhove, M., and Parquet, L. (2021). Three-dimensional hydrodynamic model of the Rance estuary (France) influenced by the world's second largest tidal power plant. *6th SimHydro 2021, June 16th-18th 2021, Sophia Antipolis-Nice (France).* (Oral presentation).

- Rtimi, R., Sottolichio, A. and Tassi, P. (2021). Tidal patterns and sediment dynamics in a hypertidal estuary influenced by a tidal power station. *International Coastal Symposium, May 3rd-5th 2021, Online.* (Oral presentation).

- Rtimi, R., Sottolichio, A. and Tassi, P. (2020). The Rance tidal power station: a preliminary study of its impact on tidal patterns and sediments dynamics in the Rance estuary (France) from 1957 to 2018. *European Geo-sciences Union General Assembly, May 4th-8th 2020, Online.* (Oral presentation).

- Rtimi, R., Sottolichio, A. and Tassi, P. (2019). A preliminary study of tide propagation and sediment dynamics in a macro tidal estuary influenced by the presence of a tidal power station. *26th TELEMAC-MASCARET User Conference, October 15th-17th 2019, Toulouse (France).* (Oral presentation).

- Rtimi, R., Sottolichio, A. and Tassi, P. (2021). Sediments dynamics in a closed macrotidal estuary (Rance estuary, France): from mud to a mixture of mud-sand-gravel. *INTERCOH, September 13th-17th 2021, Online.* (Poster).

- Rtimi, R., Sottolichio, A. and Tassi, P. (2019). Analysis of tides and sediment dynamics in a macrotidal estuary influenced by the presence of a tidal power station. *11^{th} Symposium on River, Coastal and Estuarine Morphodynamics, November 16^{th}-21^{st} 2019, Auckland (New Zealand).* (Poster).

References

Achilleos, G. (2011). The inverse distance weighted interpolation method and error propagation mechanism – creating a DEM from an analogue topographical map. *Journal of Spatial Science*, 56(2):283–304. 52

Amoudry, L. O., Ramirez-Mendoza, R., Souza, A. J., and M., B. J. (2014). Modelling-based assessment of suspended sediment dynamics in a hypertidal estuarine channel. *Ocean Dynamics*, 64(5):707–722. 80, 92, 98, 109, 126, 131

Angeloudis, A., Falconer, R., Bray, S., and Ahmadian, R. (2016). Representation and operation of tidal energy impoundments in a coastal hydrodynamic model. *Renewable Energy*, 99:1103–1115. 52, 132

Angeloudis, A. and Falconer, R. A. (2017). Sensitivity of tidal lagoon and barrage hydrodynamic impacts and energy outputs to operational characteristics. *Renewable Energy*, 114:337 – 351. 3, 6, 51, 79

Aubrey, D. and Speer, P. (1985). A study of non-linear tidal propagation in shallow inlet/estuarine systems Part I: Observations. *Estuarine, Coastal and Shelf Science*, 21:185–205. 4, 47, 48, 74

Audouin, Y., Benson, T., Delinares, M., Fontaine, J., G. B., Huybrechts, N., Kopmann, R., Leroy, A., Pavan, S., Pham, C., Taccone, F., Tassi, P., and Walther, R. (2019). Introducing GAIA, the brand new sediment transport module of the TELEMAC-MASCARET system. *Proceedings of the TELEMAC-MASCARET User Conference*. 103, 133

Bagnold, R. (1966). An approach to the sediment transport problem from general physics. *US Geological Survey*, 442-1:37. 103, 190

Barton, A. (2019). Bluekenue enhancements from 2014 to 2019. In *Proceedings of the 26th TELEMAC-MASCARET User Conference*, pages 1–9. 52, 106

Bauer, H. A. (1993). A world map of tides. *Geographical Review*, 23:259–270. 72

Bellman, R. (1954). The theory of dynamic programming. *Bulletin of the American Mathematical Society*, 60:503–515. 52

Bertier, C. (2020a). Estuaire de la Rance : Essais de laboratoire pour la détermination du rapport NTU-MES des mesures d'octobre 2020. Technical report, Électricité de France (EDF). 26, 102

Bertier, C. (2020b). Field campaign reports of continuous measurement in the Rance estuary (2020-12). Technical report, Électricité de France (EDF). xi, 19, 20, 21, 99, 102

Bi, Q. and Toorman, E. (2015). Mixed-sediment transport modelling in Scheldt estuary with a physics-based bottom friction law. *Ocean Dynamics*, 65(4):555–587. 51

Bizien, H. and Soenen, A. (2012). Mesures de courants aux abords de la centrale marémotrice de la rance. 52, 55

Bolle, A., Bing Wang, Z., Amos, C., and De Ronde, J. (2010). The influence of changes in tidal asymmetry on residual sediment transport in the western Scheldt. *Continental Shelf Research*, 30:871–882. 4, 48

Bonnot-Courtois, C. (1993). Analyse comparée des effets de dragage et de chasse hydraulique sur l'envasement à l'amont du bassin maritime de la Rance. *La Houille Blanche*, 8:539–550. 11, 98, 126, 132, 149, 152

Bonnot-Courtois, C., Caline, B., L'Homer, A., and Le Vot, M. (2002). *Mont-Saint-Michel Bay and the Rance estuary*. Bull. Centre Rech. Elf Explor. xiv, 9, 11, 49, 50, 74, 80, 90, 91, 92, 93, 98, 99, 101, 109, 127, 132, 133, 136, 141, 146

Bonnot-Courtois, C. and Lafond, L. (1991). Caractérisation et comportement des vases dans l'estuaire de la Rance. Technical report, EDF de Geomorphologie EPHE. 9

Bonnot-Courtois, C. and Le Vot, M. (1993). Dynamique sédimentaire estuarienne dans le bassin maritime de la Rance. *Congrès français de Sédimentologie. Lille, 17-20 nov*, 19:53–54. 11, 98, 113

Bourgoin, A., Guillou, S. S., Thiébot, J., and Ata, R. (2019). *Turbulence characterization at a tidal energy site using large-eddy simulations: case of the Alderney Race*. InTech. 7

Brand, M., Guo, L., Stein, E. D., and Sanders, B. F. (2021). Multi-decadal simulation of estuarine sedimentation under sea level rise with a response-surface surrogate model. *Advances in Water Resources*, 150:103–876. 97, 131

Brenon, I. and Le Hir, P. (1999). Modelling the turbidity maximum in the Seine estuary (France): Identification of formation processes. *Estuarine, Coastal and Shelf Science*, 49:525–544. 7

Brossault, J., Rangeard, D., and Mélinge, Y. (2013). Suivi de la sédimentation dans les vasières de la Rance. Technical report, EDF de Geomorphologie EPHE. 9

Brown, J. and Davies, A. (2010). Flood/ebb tidal asymmetry in a shallow sandy estuary and the impact on net sand transport. *Geomorphology*, 114(3):431–439. 51

Burchard, H., Schuttelaars, H. M., and Ralston, D. K. (2018). Sediment trapping in estuaries. *Annual Review of Marine Science*, 10:71–95. xi, 5, 6, 80, 92, 97, 98, 131

Cameron, W. and Pritchard, D. (1963). *Estuaries*, volume 2. Hill MN (ed) The Sea, John Wiley Sons, New York. 2

Caude, G., Clément, P., Pillet, D., and Vindimian, E. (2017). *Gestion sédimentaire de l'estuaire de la Rance*. (in French). 12, 58, 72

Charlier, R. (2007). Forty candles for the Rance river TPP tides provide renewable and sustainable power generation. *Renewable and Sustainable Energy Reviews*, 11:2032–2057. 2, 8, 50, 79

Chavarrias, V., Stecca, G., and Blom, A. (2018). Ill-posedness in modeling mixed sediment river morphodynamics. *Advances in Water Resources*, 114:219 – 235. 8

Chevé, J. and Le Noc, S. (2018). VibRance : Evaluation des impacts bacteriologiques dans l'estuaire de la Rance. 11, 49

Cochet, C. and Lambert, M. (2017). The Rance tidal power plant model. In *Proceedings of the 24th TELEMAC-MASCARET User Conference*, pages 191–196. 52

Coppens, A. B. (1980). Simple equations for the speed of sound in neptunian waters. *J. Acoust. Soc. Am.*, 69:862–863. 103

Cornett, A., Cousineau, J., and Nistor, I. (2013). Assessment of hydrodynamic impacts from tidal power lagoons in the bay of Fundy. *International Journal of Marine Energy*, 1:33–54. 3, 7, 47, 49, 51, 52, 74, 97

Cornett, A., Durand, N., and Serrer, M. (2010). 3-D modelling and assessment of tidal current resources in the bay of Fundy, Canada. *Proc. 3rd Int. Conf. on Ocean Energy*. 7, 49

Davis, R. and Fitzgerald, D. (2004). *Beaches and Coasts*. Blackwell Science, Malden, MA. 53

De Brauwere, A., De Brye, B., Blaise, S., and Deleersnijder, E. (2011). Residence time, exposure time and connectivity in the Scheldt estuary. *Journal of Marine Systems*, 84:85–95. 54

Deloffre, J., Lafite, R., Lesueur, P., Lesourd, S., Verney, R., and Guézennec, L. (2005). Sedimentary processes on an intertidal mudflat in the upper macrotidal Seine estuary, France. *Estuarine, Coastal and Shelf Science*, 64(4):710–720. 7

Dronkers, J. (2005). *Dynamics of coastal systems*, volume 25. World Scientific. 4, 48, 74, 97, 131

Dubien, I. and Waeraas De Saint Martin, G. (1994). Le phénomene NIMBY: le cas de l'usine marémotrice de la Rance. Technical report, EDF. 9

Duclercq, M. (2020). La Rance: Impact du nouveau mode dechargeur sur l'intumescence dans l'estuaire en cas de declenchement. 58

Dutta, S., Wang, D., Tassi, P., and Garcia, M. H. (2017). Three-dimensional numerical modeling of the Bulle effect: the nonlinear distribution of near-bed sediment at fluvial diversions. *Earth Surf. Process. Landforms*, 42:2322–2337. 83

Dyer, K. (1997). *Estuaries: A Physical Introduction*, volume 140. John Wiley and Sons/Wiley & Sons: Chichester. 2, 131

EDF (2018). Rapport de fin d'intervention de la campagne 2018. 50

EDF (2020). L'usine marémotrice de la Rance. 8, 48, 98, 132

Egbert, G. and Svetlana, Y. (2002). Efficient inverse modeling of barotropic ocean tides. *Journal of Atmospheric and Oceanic Technology*, 19.2:183–204. 52, 107, 133

Elliott, M. and McLusky, D. (2002). The need for definitions in understanding estuaries. *Estuarine, Coastal and Shelf Science*, 55(6):815–827. 2

EPTB (2021). Débit simulé SIMFEN 2019-2020. Technical report, Etablissement Public Territorial de Bassin. 135

Etemad-Shahidi, A., Shahkolahi, A., and Liu, W. (2010). Modeling of hydrodynamics and cohesive sediment processes in an estuarine system: Study case in Danshui river. *Environmental Modeling & Assessment*, 15:261–271. 131

Evans, G. and Prego, R. (2003). Rias, estuaries and incised valleys. *Marine geology*, 196:171–175. 8, 48, 80, 98, 132

Fairley, I., Masters, I., and Karunarathna, H. (2015). The cumulative impact of tidal stream turbine arrays on sediment transport in the Pentland Firth. *Renewable Energy*, 80:755–769. 97, 98, 126, 131

Falconer, R. and Chen, Y. (1991). An improved representation of flooding and drying and wind stress effects in a 2D tidal numerical model. *Institution of Civil Engineers*, 2:659–672. 74

Feng, Z., Tan, G., Xia, J., Shu, C., Chen, P., and Yi, R. (2019). Two-dimensional numerical simulation of sediment transport using improved critical shear stress methods. *International Journal of Sediment Research*, 35:15–26. 131, 132, 149

Fettweis, M., Riethmüller, R., Verney, R., Becker, M., Backers, J., Baeye, M., Chapalain, M., Claeys, S., Claus, J., Cox, T., Deloffre, J., Depreiter, D., Druine, F., Flöser, G., Grünler, S., Jourdin, F., Lafite, R., Nauw, J., Nechad, B., Röttgers, R., Sottolichio, A., Van Engeland, T., Vanhaverbeke, W., and Vereecken, H. (2019). Uncertainties associated with in situ high-frequency long-term observations of suspended particulate matter concentration using optical and acoustic sensors. *Progress in Oceanography*, 195:12. 28

Figueroa, S. M., hong Lee, G., and Shin, H.-J. (2020). Effects of an estuarine dam on sediment flux mechanisms in a shallow, macrotidal estuary. *Estuarine, Coastal and Shelf Science*, 238:106718. 6

Fossati, M. and Piedra-Cueva, I. (2008). Numerical modelling of residual flow and salinity in the río de la plata. *Applied Mathematical Modelling*, 32:1066–1086. 6

Fossati, M. and Piedra-Cueva, I. (2013). A 3d hydrodynamic numerical model of the Río de la Plata and Montevideo's coastal zone. *Applied Mathematical Modelling*, 37:1310–1332. 6

Fossati, M. Santoro, P., Urrestarazu, S., and Piedra-Cueva, I. (2011). Numerical study of the effect of a power plant cooling water discharge in the Montevideo bay. *Applied Mathematical Modelling*, 9:1–23. 6

Friedrichs, C. and Aubrey, D. (1988). Non-linear tidal distortion in shallow well-mixed estuaries: a synthesis. *Estuarine, Coastal and Shelf Science*, 27:521–454. 4, 47, 48, 49, 55, 72, 74, 92, 98

García-Oliva, M., Djordjević, S., and Tabor, G. R. (2017). The impacts of tidal turbines on water levels in a shallow estuary. *International Journal of Marine Energy*, 19:177 – 197. 51

Geyer, W. and MacCready, P. (2014). The estuarine circulation. *The Annual Review of Fluid Mechanics*, 46:175–197. xvii, 2, 184, 185

Geyer, W., Woodruff, J., and Traykovski, P. (2001). Sediment transport and trapping in the Hudson River estuary. *Estuaries*, 24:670–679. 97, 108

Giardino, A., Ibrahim, I., Adam, S., Toorman, E., and Monbaliu, J. (2009). Hydrodynamics and cohesive sediment transport in the Ijzer estuary, Belgium: Case study. *Journal of Waterway, Port, Coastal, and Ocean Engineering*, 135:176–184. 132

Google Earth (2020). La Rance. xi, 9

Gourgue, O., Baeyens, W., Chen, M., De Brauwere, A., De Brye, B., Deleersnijder, E., Elskens, M., and Legat, V. (2013). A depth-averaged two-dimensional sediment transport model for environmental studies in the Scheldt estuary and tidal river network. *Journal of Marine Systems*, 128:27–39. 131, 149

Gourgue, O., van Belzen, J., Schwarz, C., Vandenbruwaene, W., Vanlede, J., Belliard, J.-P., Fagherazzi, S., Bouma, T. J., van de Koppel, J., and Temmerman, S. (2021). Biogeomorphic modeling to assess resilience of tidal marsh restoration to sea level rise and sediment supply. *Earth Surface Dynamics Discussions*, 2021:1–38. 131

Grabemann, I. (1989). Transport processes of suspended matter derived from time series in a tidal estuary. *Journal of Geophysical Research*, 94:373–14379. 97

Grasso, F. and Le Hir, P. (2019). Influence of morphological changes on suspended sediment dynamics in a macrotidal estuary: diachronic analysis in the Seine estuary (France) from 1960 to 2010. *Ocean Dynamics*, 69:83–100. 97

Grasso, F., Verney, R., Le Hir, P., Thouvenin, B., Schulz, E., Kervella, Y., Khojasteh Pour Fard, I., Lemoine, J.-P., Dumas, F., and Garnier, V. (2018). Suspended sediment dynamics in the macrotidal Seine estuary (France): 1. Numerical modeling of turbidity maximum dynamics. *Journal of Geophysical Research: Oceans*, 123:558–577. 5, 7, 97, 109, 126, 131

Guesmia, M. (2001). Régime hydrodynamique et sédimentaire de l'estuaire de la Rance. 9, 49

Guesmia, M., Cheviet, C., and Macur, O. (2001). Modélisation hydrosédimentaire de l'estuaire de la Rance – modélisation courantologique bidimensionnelle. 9, 11, 49

Guillou, S., Thiebot, J., Chauchat, J., Verjus, R., Besq, A., Nguyen, D. H., and Keang, S. (2011). The Filling Dynamics of an Estuary: From the Process to the Modelling. In *Sediment Transport in Aquatic Environments*, pages 125–146. intech. 4, 11

Guo, L., Brand, M., Sanders, B. F., Foufoula-Georgiou, E., and Stein, E. D. (2018). Tidal asymmetry and residual sediment transport in a short tidal basin under sea level rise. *Advances in Water Resources*, 121:1–8. 4, 47

Hendry, C. (2017). The role of tidal lagoons. Technical report, Final Report. 2

Hesse, R., Zorndt, A., and Fröhle, P. (2019). Modelling dynamics of the estuarine turbidity maximum and local net deposition. *Ocean Dynamics*, 69:489–507. 80, 92, 98, 131

Hoitink, A. J. F., Hoekstra, P., and van Maren, D. S. (2003). Flow asymmetry associated with astronomical tides: Implications for the residual transport of sediment. *Journal of Geophysical Research: Oceans*, 108(C10). 4, 48

Hydrelect (2012). La turbine Kaplan. *hydrelect.info*. 8, 50

Jalón-Rojas, I., Schmidt, S., and Sottolichio, A. (2015). Turbidity in the fluvial gironde estuary (southwest france) based on 10-year continuous monitoring: sensitivity to hydrological conditions. *Hydrology and Earth System Sciences*, 19(6):2805–2819. 7

Jalón-Rojas, I., Dijkstra, Y. M., Schuttelaars, H. M., Brouwer, R. L., Schmidt, S., and Sottolichio, A. (2021). Multidecadal evolution of the turbidity maximum zone in a macrotidal river under climate and anthropogenic pressures. *Journal of Geophysical Research: Oceans*, 126(5):e2020JC016273. e2020JC016273 2020JC016273. 7

Jestin, H., Bassoullet, P., Le Hir, P., L'Yavanc, J., and Degres, Y. (1998). Development of ALTUS, a high frequency acoustic submersible recording altimeter to accurately monitor bed elevation and quantify deposition or erosion of sediments. In *IEEE Oceanic Engineering Society. OCEANS'98. Conference Proceedings (Cat. No.98CH36259)*, volume 1, pages 189–194 vol.1. 21, 102

Jigorel, A. and Ledrappier, M. (2003). Sedimentary and biological impacts of the management of sediments in the marine basin of the Rance. Technical report, INSA de Rennes. 9

Kervella, S., Sottolichio, A., Maneux, E., Berier, C., and Libaud, J. (2012). Dynamique sédimentaire des vasières intertidales de l'estuaire de la loire. In *XIIth Journées Nationales Génie Côtier – Génie Civil Proceedings*. 7

Kim, J., Ha, H., and Woo, S.-B. (2017). Dynamics of sediment disturbance by periodic artificial discharges from the world's largest tidal power plant. *Estuarine, Coastal and Shelf Science*, 190:69–79. 79, 126

Kim, J., Ha, H., Woo, S.-B., Kim, M.-S., and Kwon, H.-K. (2021). Unbalanced sediment transport by tidal power generation in Lake Sihwa. *Renewable Energy*, 172:1133–1144. 3, 6, 98, 108, 117, 126

Kirby, R. and Retière, C. (2009). Comparing environmental effects of Rance and Severn barrages. *Proceedings of the Institution of Civil Engineers - Maritime Engineering*, 162(1):11–26. 3, 5, 9, 47, 49, 74, 80, 97

Knudsen, M. (1900). Ein hydrographischer lehrsatz. *Hydrogr. Marit. Meteorol.*, 28:316–20. 5

Lan, A. (2012). *Numerical modelling of sand-mud mixtures settling and transport processes: application to morphodynamic of the Gironde estuary (France)*. PhD thesis, université Paris-Est, Paris, France, 2012. 190

Lane, S. N. (1998). Hydraulic modelling in hydrology and geomorphology: a review of high resolution approaches. *Hydrological Processes*, 12(8):1131–1150. 51

LCHF (1982). Étude sédimentologique de l'estuaire de la Rance. Technical report, Institution interdépartementale pour l'aménagement de la Rance propre. 9, 11, 74, 132, 136, 141, 152

Le Hir, P., Cayocca, F., and Waeles, B. (2011). Dynamics of sand and mud mixtures: A multiprocess-based modelling strategy. *Continental Shelf Research*, 31:135–149. 105, 106

Libaux, A. and Drouot, J. (2020). Remplacement de la conduite de la Rance - Présentation du package RANG 3-AGRA Version 0.7.0. 52

Luo, J., Li, M., Sun, Z., and OĆonnor, B. (2013). Numerical modelling of hydrodynamics and sand transport in the tide-dominated coastal-to-estuarine region. *Marine Geology*, 342:14–27. 132

MacCready, P. and Geyer, W. (2004). Advances in estuarine physics. *Annu. Rev. Marine. Sci.*, 2:35–58. 5

Mandal, S., Sil, S., Gangopadhyay, A., Jena, B., and Venkatesan, R. (2020). On the nature of tidal asymmetry in the gulf of Khambhat, Arabian sea using HF radar surface currents. *Estuarine, Coastal and Shelf Science*, 232:106–481. 4, 48

Manning, A. (2004). The observed effects of turbulence on estuarine flocculation. *Journal of Coastal Research*, 41:90–104. 5

Manning, A., Baugh, J., Soulsby, R., Spearman, J., and Whitehouse, R. (2011). *Sediment Flocculation and the Application to Settling Flux Modelling, Sediment Transport*. InTech. 5

Marsooli, R., Orton, P., Fitzpatrick, J., and Smith, H. (2018). Residence time of a highly urbanized estuary: Jamaica bay, New York. *Journal of Marine Science and Engineering*, 6:44. 54

McLachlan, R., Ogston, A., Asp, N., Fricke, A., Nittrouer, C., and Gomes, V. (2020). Impacts of tidal-channel connectivity on transport asymmetry and sediment exchange with mangrove forests. *Estuarine, Coastal and Shelf Science*, 233. 4, 48, 74

Mehta, A. (2014). *An introduction to hydraulics of fine sediment transport*. Advanced series on ocean engineering. World Scientific, New Jersey. xi, 5, 6

Mehta, A. and McAnally, W. (2008). *Fine Grained Sediment Transport*. Sedimentation Engineering. American Society of Civil Engineers. 5

Monsen, N., Cloern, J., Lucas, L., and Monismith, S. (2002). A comment on the use of flushing time, residence time, and age as transport time scales. *Limnol. Oceanogr.,*, 47:1545–1553. 54

Motte, E. (2017). *Iconographie et Géomorphologie : l'usage de représentations artistiques des rivages comme outil de connaissance de l'évolution du littoral*. PhD thesis, Université Bretagne Loire. 11

Neil, S., Angeloudis, A., Robins, P., Walkington, I., Ward, S., Masters, I., Lewis, M., Piano, M., Avdis, A., Piggot, M., Aggidis, G., Evans, P., Adcock, T., Ẑidonus, A., Ahmadian, R., and Falconer, R. (2018). Tidal range energy resource and optimization - Past perspectives and future challenges. *Renewable Energy*, 127:763–778. 3, 51, 72, 97, 98, 132

Neill, S. P., Litt, E. J., Couch, S. J., and Davies, A. G. (2009). The impact of tidal stream turbines on large-scale sediment dynamics. *Renewable Energy*, 34:2803–2812. 126

Ng, K., Lam, W., and Ng, K. (2013). 10 years of research progress in horizontal-axis marine current tubines. *Energies*, 6:526–1497. 97

Nguyen, V. T., Guillou, S. S., Thiébot, J., and Santa Cruz, A. (2016). Modelling turbulence with an actuator disk representing a tidal turbine. *Renewable Energy*, 97:625–635. 7

Nidzieko, N. and Ralston, K. (2012). Tidal asymmetry and velocity skew over tidal flats and shallow channels within a macrotidal river delta. *Journal of Geophysical Research*, 117. 4, 47, 48, 49, 54, 55, 69, 72, 74, 98

Nnafie, A., Van Oyen, T., De Maerschalck, B., van der Vegt, M., and van der Wegen, M. (2018). Estuarine channel evolution in response to closure of secondary basins: An observational and morphodynamic modeling study of the Western Scheldt Estuary. *Journal of Geophysical Research: Earth Surface*, 123:167–186. 132, 149

O'Rourke, F., Boyle, F., and Reynolds, A. (2010). Tidal energy update 2009. *Appl. Energy*, 87:398–409. 97

Orseau, S., Huybrechts, N., Tassi, P., Kaidi, S., and Klein, F. (2021). Navtel: Open-source decision support tool for ship routing and underkeel clearance management in estuarine channels. *Journal of Waterway, Port, Coastal, and Ocean Engineering*, 147(2):04020053. 3

Orseau, S., Huybrechts, N., Tassi, P., Pham Van Bang, D., and Klein, F. (2020). Two-dimensional modeling of fine sediment transport with mixed sediment and consolidation: Application to the Gironde estuary, france. *International Journal of Sediment Research*. 51, 131

Parquet, L. (2021). Hydro-sedimentary behavior of the Rance estuary (France) influenced by a tidal power plant : an experimental approach based on field measurement. Technical report, Électricité de France (EDF). 16, 35, 102, 103

Passy, P., Le Gendre, R., Garnier, J., Cugier, P., Callens, J., Paris, F., Billen, G., Riou, P., and Romero, P. (2016). Eutrophication modelling chain for improved management strategies to prevent algal blooms in the Bay of Seine. *Marine Ecology Progress Series*, 543:107–125. 5

Pawlowicz, R., Beardsley, B., and Lentz, S. (2002). Classical tidal harmonic analysis including error estimates in MATLAB using T-TIDE. *Computers and Geosciences*, 28:929–937. xix, 55, 59, 72, 73

Pelc, R. and Fujita, R. (2002). Renewable energy from the ocean. *Marine Policy*, 26:471–479. 8, 48, 80, 97

Perillo, G. (1995). *Geomorphology and Sedimentology of Estuaries*. Developments in sedimentology. Elsevier. 2

Robins, P., Lewis, M., and Neill, S. (2014). Impact of tidal-stream arrays in relation to the natural variability of sedimentary processes. *Renewable Energy*, 72:311–321. 98, 131

Ross, L., Sottolichio, A., Maury, T., Lesourd, S., and Gardel, A. (2019). Intratidal and subtidal circulation in a tropical estuary during wet season: The Maroni, French Guiana. *Journal of Marine Science and Engineering*, 7(12):433. 22

Ross, L., Valle-Levinson, A., Sottolichio, A., and Huybrechts, N. (2017). Lateral variability of subtidal flow at the mid-reaches of a macrotidal estuary. *Journal of Geophysical Research: Oceans*, 122(9):7651–7673. 6

Rtimi, R., Sottolichio, A., and Tassi, P. (2021a). Hydrodynamics of a hyper-tidal estuary influenced by the world's second largest tidal power station (Rance estuary, France). *Estuarine, Coastal and Shelf Science*, 250:107143. 79, 80, 82, 83, 85, 91, 98, 107, 108, 109, 113, 115, 117, 121, 126, 127

Rtimi, R., Sottolichio, A., Tassi, P., Bertier, C., Le Brun, M., Vandenhove, M., and Parquet, L. (2021b). Three-dimensional hydrodynamic model of the Rance estuary (France) influenced by the world's second largest tidal power plant. *La Houille Blanche - Hydroscience Journal*, XX:XX. 98, 103, 107, 108, 117

Sanford, L., Boicourt, W., and Rives, S. (1992). Model for estimating tidal flushing of small embayments. *Journal of Waterway, Port, Coastal, and Ocean Engineering*, 118:635–65. 54

Santoro, P., Fossati, M., and Piedra-Cueva, I. (2013). Study of the meteorological tide in the Río de la Plata. *Continental Shelf Research*, 60:51–63. 51

Santoro, P., Fossati, M., Tassi, P., Huybrechts, N., Pham Van Bang, D., and Piedra-Cueva, J. (2017). A coupled wave–current–sediment transport model for an estuarine system: Application to the Río De La Plata and Montevideo Bay. *Applied Mathematical Modelling*, 52:107–130. 7, 131, 132, 149

SHOM (2015). Dalles bathymétriques fra-14581 et fra-14582. 50

SHOM (2020). Permanent Service for Mean Sea Level. 75

Sinha, P., Guliani, P., Jena, G., Rao, A., Dube, S., Chatterjee, A. K., and Murty, T. (2004). A breadth averaged numerical model for suspended sediment transport in Hooghly Estuary, East coast of India. *Natural Hazards*, 32:239–255. 131

Sottolichio, A., Castaing, P., Etcheber, H., Maneux, E., Schmeltz, M., and Schmidt, S. (2011). Observations of suspended sediment dynamics in a highly turbid macrotidal estuary, derived from continuous monitoring. *Journal of Coastal Research*, 64:1579–1583. 5, 7, 97

Sottolichio, A., Le Hir, P., and Castaing, P. (2000). Modeling mechanisms for the stability of the turbidity maximum in the Gironde estuary, France. *Coastal and Estuarine Fine Sediment Processes*, 3:373–386. 92

Speer, P. and Aubrey, D. (1985). A study of non-linear tidal propagation in shallow inlet/estuarine systems Part II: Theory. *Estuarine, Coastal and Shelf Science*, 21:207–224. 4, 47, 48, 74

Stark, J., Meire, P., and Temmerman, S. (2017a). Changing tidal hydrodynamics during different stages of eco- geomorphological development of a tidal marsh: a numerical modeling study. *Estuarine, Coastal and Shelf Science*, 188:56–68. 4, 47

Stark, J., Smolders, S., Meire, P., and Temmerman, S. (2017b). Impact of intertidal area characteristics on estuarine tidal hydrodynamics: A modelling study for the Scheldt estuary. *Estuarine, Coastal and Shelf Science*, 198:138–155. 4, 47

Sumich, J. (1996). *An Introduction to the Biology of Marine Life*. Dubuque, New York, 6^{th}*edition*.4, 47

Telemac-Mascaret Modelling System (2018). *TELEMAC-2D User's Manual*. 52

The Open University (1999). *Waves, Tides and Shallow Water Processes*. Butterworth-Heinemann, Oxford. xi, 2, 3

Thiebot, J. (2008). *Numerical modelling of the processes which govern the formation and the degradation of muddy massifs -Application to the Rance estuary and to the Sèvre Niortaise river banks*. PhD thesis, Sciences of the Universe, AgroParisTech. 9, 11, 49, 74, 98, 106, 109, 113, 126, 127, 132, 136, 152, 190

Thurman, H. (1994). *Introductory Oceanography*. NY: Macmillan, New York, 7^{th}*edition*.4, 47

Tidal Lagoon Power (2020). Press release 22nd june 2020. xi, 4

Tide Mill (2018). 1700s tide mill. xi, 4

Toublanc, F. (2013). *Hydrodynamique et dynamique des sédiments fins dans l'estuaire de la Charente*. PhD thesis, Université de la Rochelle. 7

Toublanc, F., Brenon, I., and Coulombier, T. (2016). Formation and structure of the turbidity maximum in the macrotidal Charente estuary (France): Influence of fluvial and tidal forcing. *Estuarine, Coastal and Shelf Science*, 169:1–14. 5, 97, 109, 126

Trubert, B. and Ichstchenko, S. (2016). Estuaire de la Rance de l'écluse du Chatelier à la mer. 50

Uncles, R. J., Elliott, R., and Weston, S. A. (1985). Observed fluxes of water, salt and suspended sediment in a partly mixed estuary. *Estuarine Coastal and Shelf Science*, 20(2):147–167. 7

Valle Levinson, A. (2010). *Contemporary Issues in Estuarine Physics*. Cambridge University Press. 2

Valle-Levinson, A. and Guo, X. (2009). Asymmetries in tidal flow over a Seto Inland Sea scour pit. *Journal of Marine Research*, 67:619–635. 117

Van, L. A. (2012). *Numerical modelling of sand-mud mixtures settling and transport processes: application to morphodynamic of the Gironde estuary (France)*. PhD thesis, Université Paris-Est. 51, 132

Van Leussen, W. (1994). *Estuarine macroflocs and their role in fine-grained sediment transport*. PhD thesis, University of Utrecht, The Netherlands. 5

Van Rijn, L. (1984). Sediment transport, Part II: Suspended load transport. *Journal of Hydraulic Engineering*, 110:1613–1641. 74

Van Rijn, L. (2006). *Principles of Sediment Transport in Rivers, Estuaries and Coastal Seas: Supplement (update) 2006*. Number ptie. 2. Aqua Publications. 4

Vandenhove, M. (2021). Analyse de la circulation et de la dynamique sédimentaire dans un estuaire barée par une usine. Technical report, EPOC, Bordeaux Universty. 16, 35

Vellinga, N., Hoitink, A., van der Vegt, M., Zhang, W., and Hoekstra, P. (2014). Human impacts on tides overwhelm the effect of sea level rise on extreme water levels in the Rhine–Meuse delta. *Coastal Engineering*, 90:40 – 50. 4, 48

Verney, R., Brun-Cottan, J., Lafite, R., Deloffre, J., and Taylor, J. (2006). Tidally-induced shear stress variability above intertidal mudflats in the macrotidal seine estuary. *Estuaries and Coasts*, 29:1559–2731. 7

Villaret, C., Van, L. A., Huybrechts, N., Pham Van Bang, D., and Boucher, O. (2010). Consolidation effects on morphodynamics modelling:application to the gironde estuary. *La Houille Blanche*, 96(6):15–24. 190

Vreugdenhil, C. B. (2013). *Numerical methods for shallow-water flow*, volume 13. Springer Science & Business Media. 51

Walther, R., Schaguene, J., Hamm, L., and David, E. (2012). Coupled 3d modeling of turbidity maximum dynamics in the loire estuary, france. *Coastal Engineering Proceedings*, 1(33):sediment.22. 7

Wang, Z., Jeuken, C., and De Vriend, H. (1999). Tidal asymmetry and residual sediment transport in estuaries. *Delft Hydraulics report Z2749*. 47

Whitfield, A. and Elliott, M. (2011). 1.07 - ecosystem and biotic classifications of estuaries and coasts. In Wolanski, E. and McLusky, D., editors, *Treatise on Estuarine and Coastal Science*, pages 99–124. Academic Press, Waltham. 2, 8

Wikipédia (2019). Normalized Root Mean Square Error. 108

Winterwerp, J. (2002). On the flocculation and settling velocity of estuarine mud. *Continental Shelf Research*, 22:1339–1360. 5

Winterwerp, J. (2011). Fine sediment transport by tidal asymmetry in the high-concentrated Ems River: indications for a regime shift in response to channel deepening. *Ocean Dynamics*, 61:203–215. 7

Wu, W. (2008). *Computational River Dynamics*. NetLibrary, Inc. CRC Press. 7

Wu, Y., xu, C., Ke, Y., Chen, K., and Xu, H. (2017). Multi-criteria decision-making on assessment of proposed tidal barrage schemes in terms of environmental impacts. *Marine Pollution Bulletin*, 125:271–281. 97, 131

Xia, J., Falconer, R., and Lin, B. (2010). Impact of different tidal renewable energy projects on the hydrodynamics processes in the Severn estuary, UK. *Ocean Modelling*, 32:86–104. 3, 6, 47, 49, 52, 72, 74, 97

Xie, D., Gao, S., Wang, Z. B., Pan, C., Wu, X., and Wang, Q. (2017). Morphodynamic modeling of a large inside sandbar and its dextral morphology in a convergent estuary: Qiantang estuary, China. *Journal of Geophysical Research: Earth Surface*, 122(8):1553–1572. 51

Young, H., Kyeong, O., and Byung, H. (2010). Lake Sihwa tidal power plant project. *Ocean Engineering*, 37:454–463. 6, 8, 49, 50, 72, 74

Zhang, W., Cao, Y., Zhu, Y., Zheng, J., Ji, X., Xu, Y., Wu, Y., and Hoitink, A. (2018). Unravelling the causes of tidal asymmetry in deltas. *Journal of Hydrology*, 564:588 – 604. 4, 47

Zhou, Z., Coco, G., Townend, I., Olabarrieta, O., van der Wegen, M., Gong, Z., D'Alpaos, A., Gao, S., Jaffe, B., Gelfenbaum, G., He, Q., Wang, Y., Lanzoni, S., Wang, Z., Winterwerp, H., and Zhang, C. (2017). Is "morphodynamic equilibrium" an oxymoron? *Earth-Science Reviews*, 165:257–267. 3

Zyserman, J. and Fredsoe, J. (1994). Data analysis of bed concentration of suspended sediment. *Journal of Hydraulic Engineering*, 120:1021–1042. 104

Énergie marémotrice (2018). Connaissance des Énergies. 3

Appendices

APPENDIX A

COMPLEMENTARY INSIGHTS ON FIELD MEASUREMENTS

A.1 Data preparation

A.1.1 Salinity

Raw data from SAMBAT probes at stations S2 and S3 are presented in Figures A.1 and A.2 respectively. Raw data from STPS probes at stations P1 and A3 are presented in Figures A.3 and A.4 respectively.

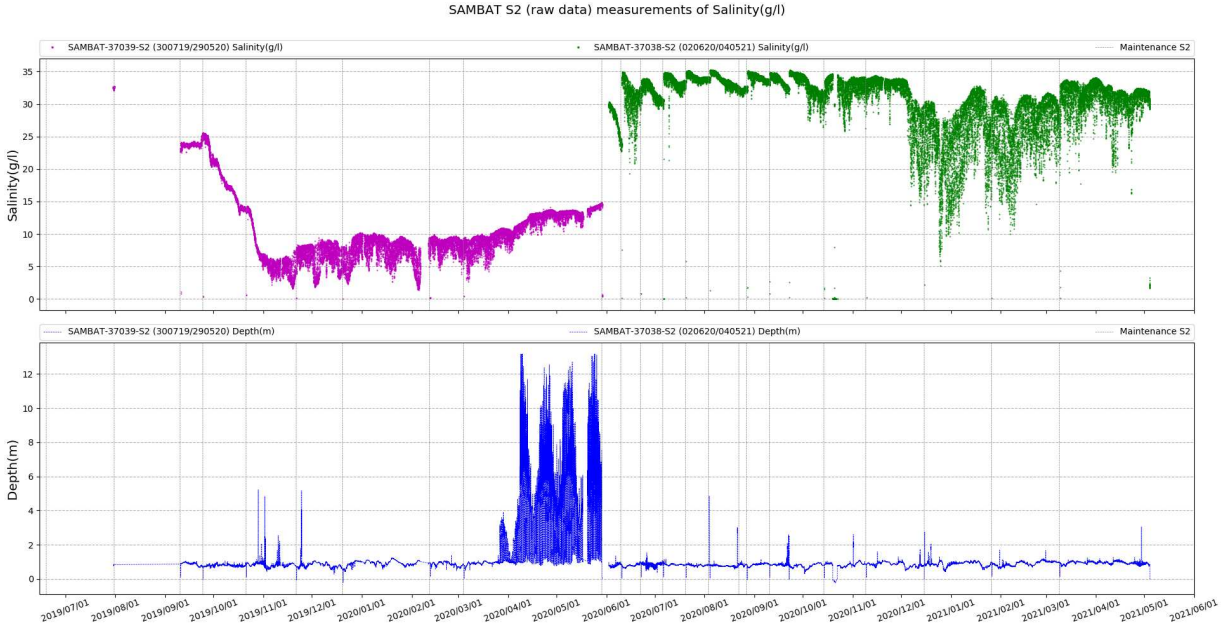

(a) On subplot 1: *Salinity* (g/l) measurements from `SAMBAT` probes at location S2. **(b)** On subplot 2: *Depth* (m) measurements from `SAMBAT` probes at location S2.

Figure A.1: `SAMBAT` S2 Raw data.

A.1.2 Bed evolution

Raw data from Altus probes at stations A2 and A3 are presented in Figures A.5 and A.6 respectively.

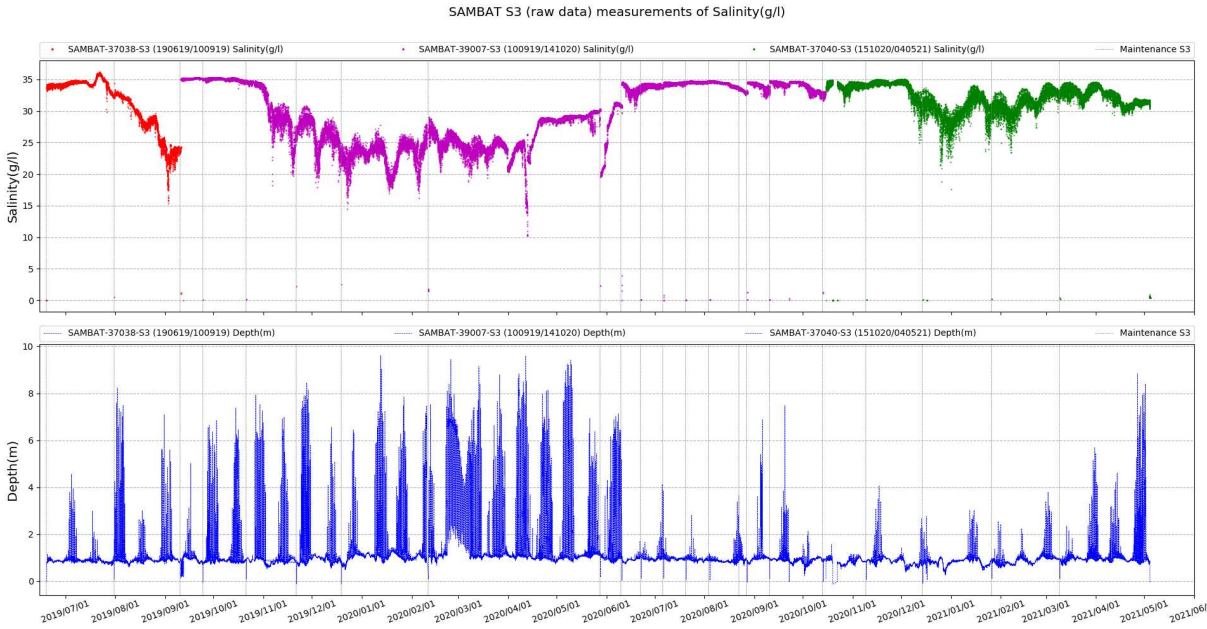

(a) On subplot 1: *Salinity* (g/l) measurements from SAMBAT probes at location S3. **(b)** On subplot 2: *Depth* (m) measurements from SAMBAT probes at location S2.

Figure A.2: SAMBAT S3 Raw data.

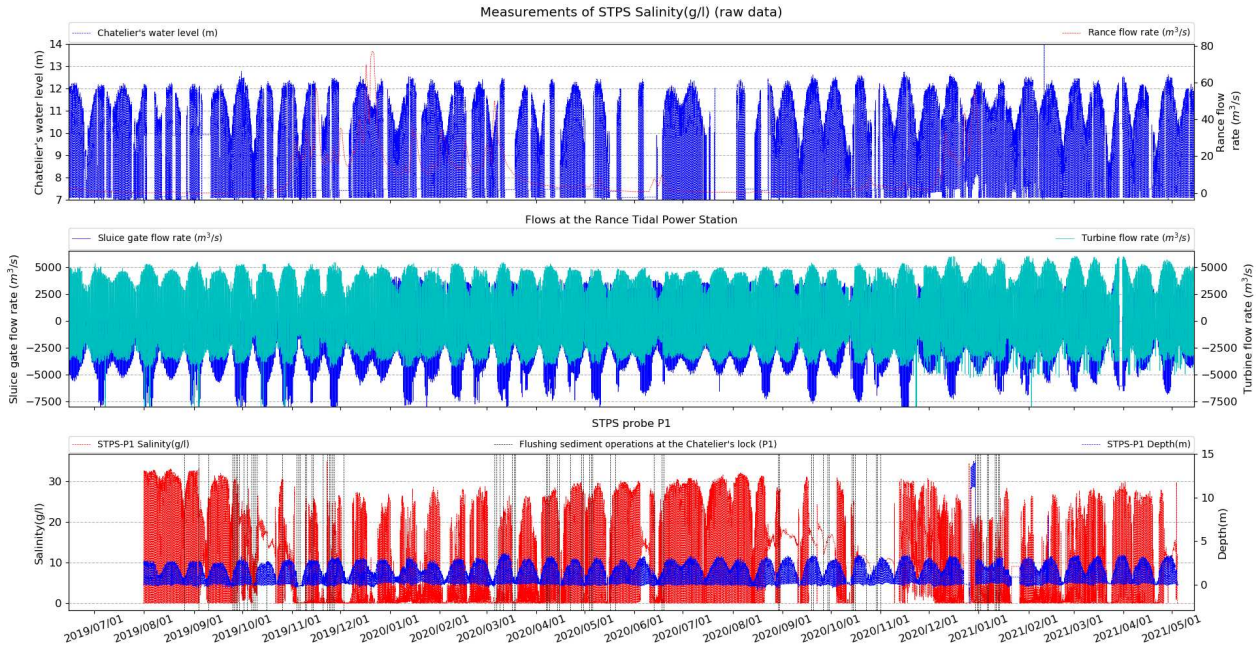

(a) On the primary axis of subplot 1: Water *Depth(m)* at Châtelier. On the secondary axis of subplot 1: *Simulated Rance flow rate* (m^3/s). **(b)** On the primary axis of subplot 2: *Sluice gate flow rate* (m^3/s) *of the Rance TPP*. On the secondary axis of subplot 2: *Turbine flow rate* (m^3/s) *of the Rance TPP*. **(c)** On the primary axis of subplot 3: *Salinity* (g/l) measurements from STPS probe at location P1. On the secondary axis of subplot 3: *Depth* (m) measurements from STPS probe at location P1.

Figure A.3: STPS P1 raw data.

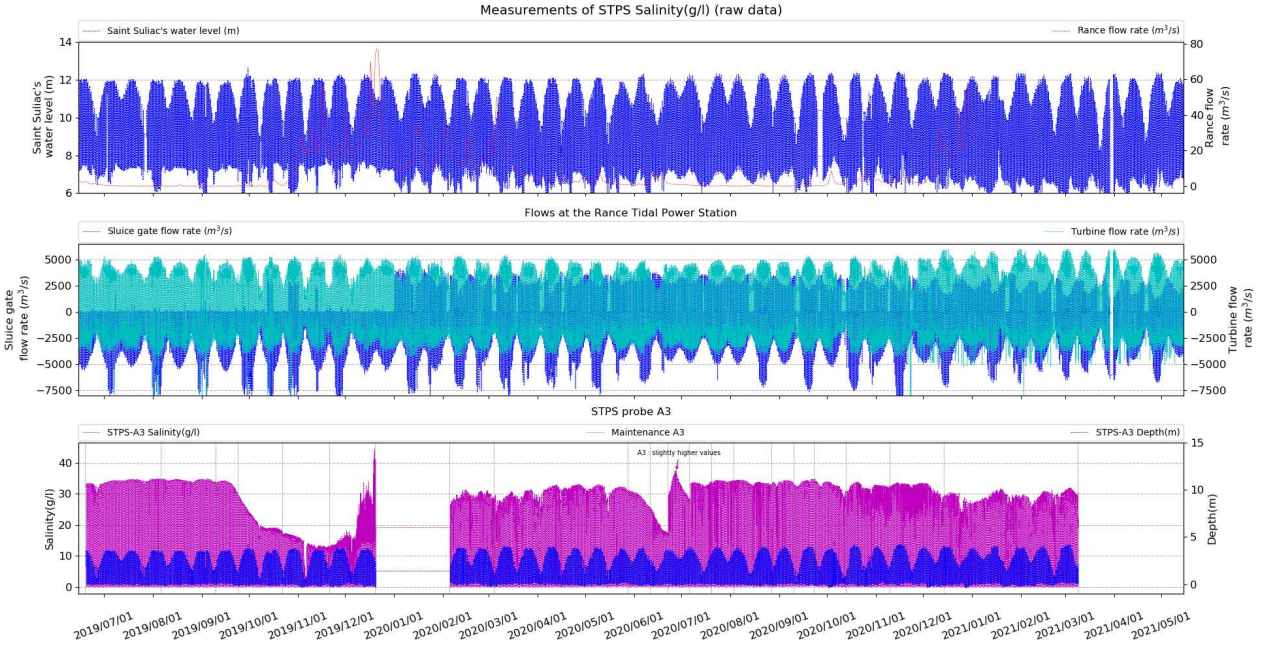

(a) On the primary axis of subplot 1: Water *Depth(m)* at Saint-Suliac. On the secondary axis of subplot 1: *Simulated Rance flow rate* (m^3/s). **(b)** On the primary axis of subplot 2: *Sluice gate flow rate* (m^3/s) *of the Rance TPP*. On the secondary axis of subplot 2: *Turbine flow rate* (m^3/s) *of the Rance TPP*. **(c)** On the primary axis of subplot 3: Salinity (g/l) measurements from STPS probe at location A3. On the secondary axis of subplot 3: *Depth* (m) measurements from STPS probe at location A3.

Figure A.4: STPS A3 raw data.

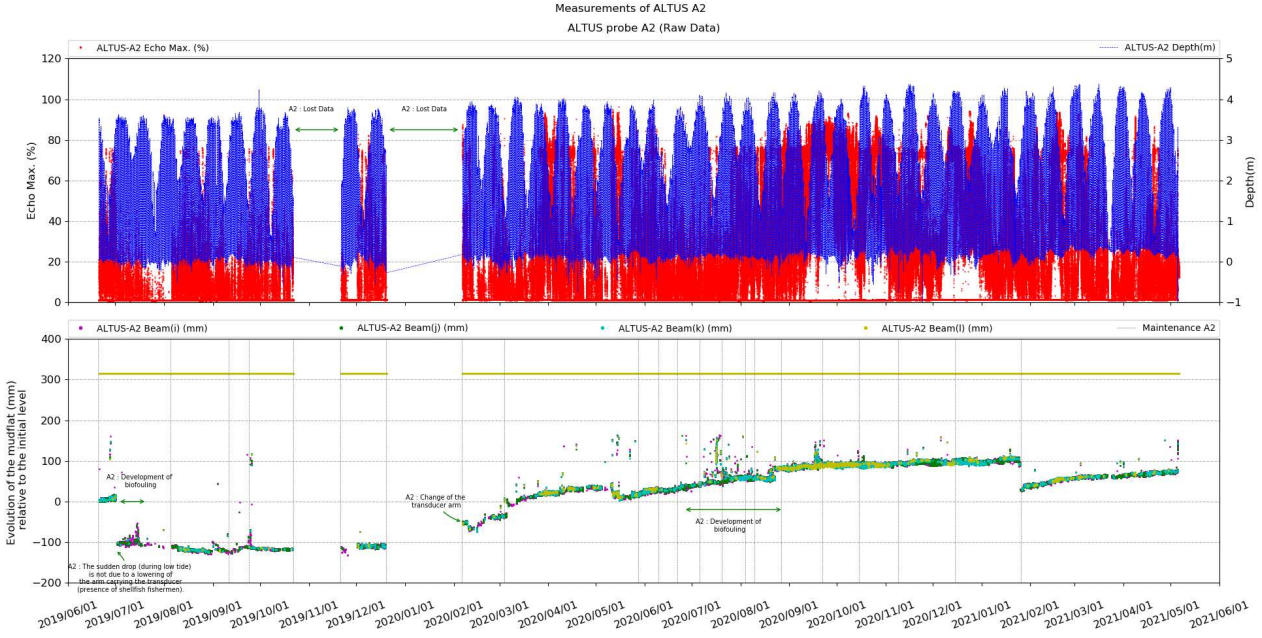

(a) On the primary axis of subplot 1: *Echo. Max (%)* return signal. On secondary axis of subplot 2: *Water Depth(m)*. **(b)** On the primary axis of subplot 2: Mudflat evolution of the 4 beams.

Figure A.5: ALTUS A2 Raw Data.

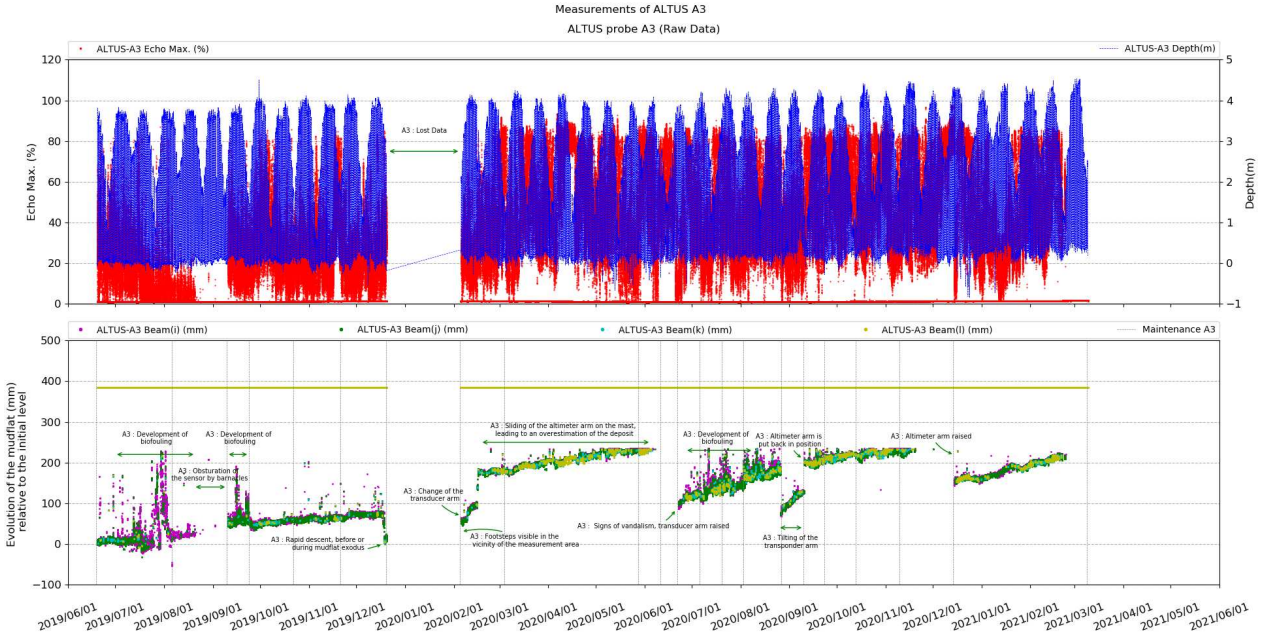

(a) On the primary axis of subplot 1: *Echo. Max (%)* return signal. On secondary axis of subplot 2: *Water Depth(m)*. **(b)** On the primary axis of subplot 2: Mudflat evolution of the 4 beams.

Figure A.6: ALTUS A3 Raw data.

APPENDIX B

COMPLEMENTARY ANALYSES OF HYDRODYNAMICS IN THE RANCE ESTUARY

B.1 The Rance estuarine classification

Geyer and MacCready [2014] estuarine classification is based on freshwater Froude number Fr_f and mixing parameter M defined in Eqs. B.1 & B.2 respectively [Geyer and MacCready, 2014].

$$Fr_f = \frac{U_R}{\sqrt{\lambda g s_{ocean} h}} \tag{B.1}$$

$$M^2 = \frac{C_D U_T^2}{\omega N_0 h^2} \tag{B.2}$$

Where $U_R = Q_{river} / \sum$ is the cross-sectional averaged river discharge velocity, Q_{river} is the river discharge, $\sum$ is the channel cross-sectional area, $\lambda = 7.7 \times 10^4$ is the haline contraction coefficient, g is the acceleration due to gravity, s_{ocean} is the ocean salinity, h is the mean channel depth, C_D is the drag coefficient, U_T is the amplitude of the depth-averaged tidal velocity, ω is the tidal frequency, and $N_0 = \sqrt{\frac{\lambda g s_{ocean}}{h}}$ is the buoyancy frequency for maximum bottom-to-top salinity variation in an estuary. Fr_f is the net velocity of the river flow scaled by the maximum possible frontal propagation speed. M is the ratio of tidal timescale to the mixing timescale [Geyer and MacCready, 2014]. These parameters were estimated from ADCP data set (June 2012) located at the estuary's mouth (Figure 5.1) representing a spring tide and low river discharge scenario. They were complemented by values from numerical simulation (September 2019) for a neap tide and high river discharge scenario. Thus, the Rance estuary is represented by a gray rectangle in the $Fr_f - M$ parametric plot (Figure B.1), indicating approximate influence of spring-neap tidal variation and river flow variation [Geyer and MacCready, 2014]. Based on the estimated Fr_f and M, the Rance estuary is classified mainly as a well-mixed estuary with a slight seasonal variation to a strain-induced periodically stratified (SIPS) estuary.

B.2 Complementary comparisons between the three modeled scenarios

To complement analyses performed in Sections 3.4.3.2 and 3.4.3.3 for the three modeled scenarios, plots of current differences and velocity skew ratios are shown in Figures B.2 & B.3. Scenario C2, corresponding to the bathymetry of 2018 without the tidal power station (see Table 3.5), is set as reference. Figures B.2.a;c show that sediment deposition zones observed near Mordreuc (see Figure 3.2.c) could significantly impact the velocity magnitude in the main channel, where currents are reduced by $\sim 0.25 m/s$. Figures B.2.b;d show that the presence of the dam reduces the current velocities in the estuary main channel by $\sim 0.5 m/s$. However, it amplifies flood (ebb) currents directly upstream of sluice gates (downstream of turbines) by $\sim 1 m/s$.
Velocity skewness ratio depicted in Figure B.3.a shows that estuarine morphological changes between 1957 and 2018 near Mordreuc might have switched the ebb-dominance seen in 1957 to flood-dominance in 2018, although this finding may present inaccuracies due to measurement uncertainty in the older maps. Figure B.3.b shows that the tidal power station decreases flood-dominance by a factor of ~ 0.9 along the estuary main channel. Moreover, velocity skewness changes are visible in the area surrounding the dam, where the ebb dominance (flood dominance) upstream of the sluice gate (downstream of the turbines) switches to flood dominance (ebb dominance) due to the presence of the TPS.

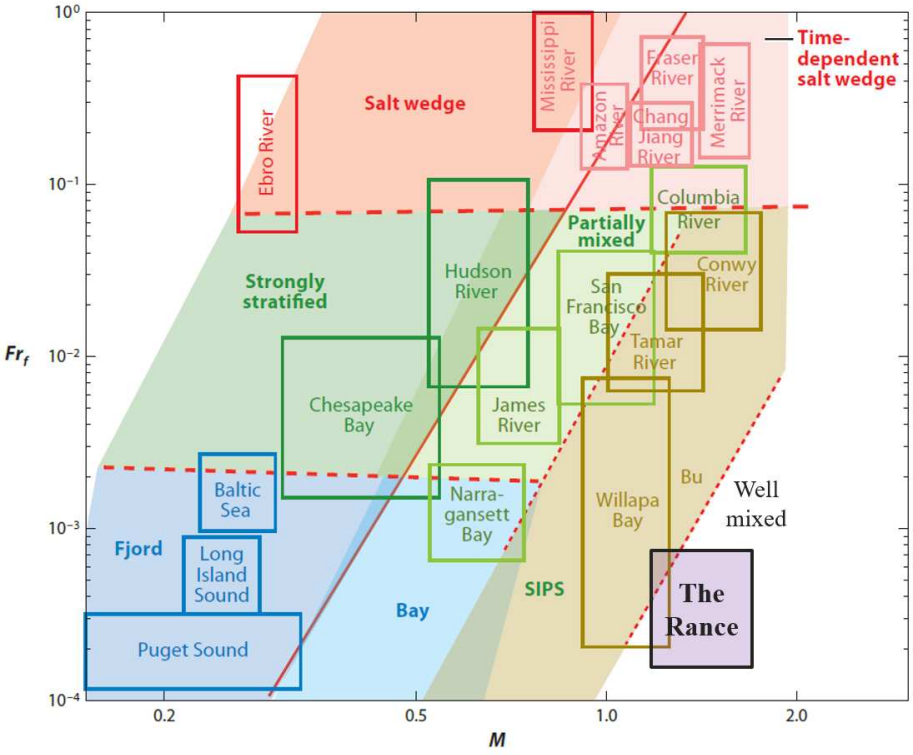

Figure B.1: Classification of the Rance estuary based on freshwater Froude number and mixing parameter. Adapted from Geyer and MacCready [2014].

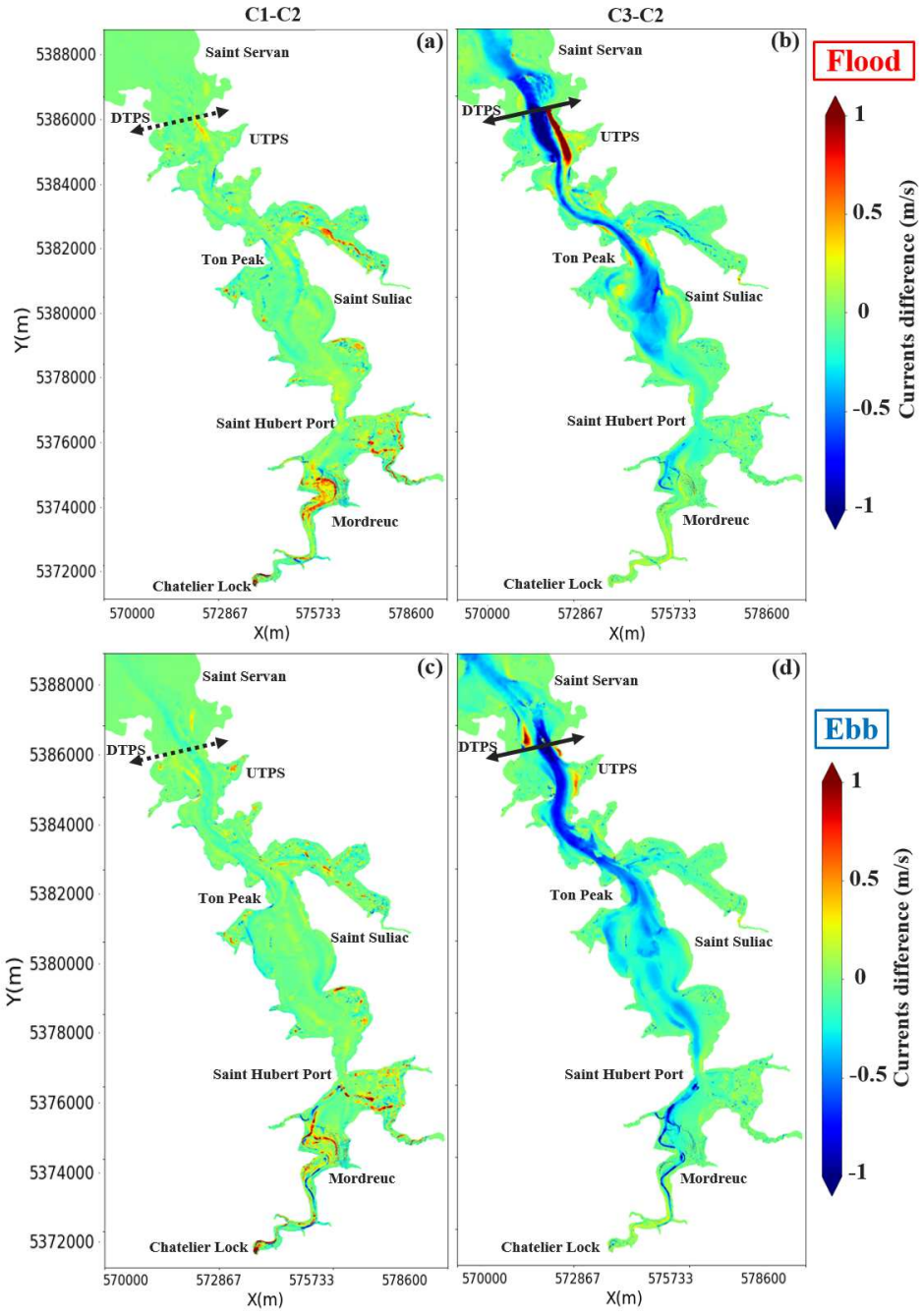

Figure B.2: Spatial distribution of (a;b) maximum flood current differences and (c;d) maximum ebb current differences between the three modeled scenarios. The reference scenario is C2 (see Table 3.5). Positive (negative) current differences mean flow acceleration (deceleration).

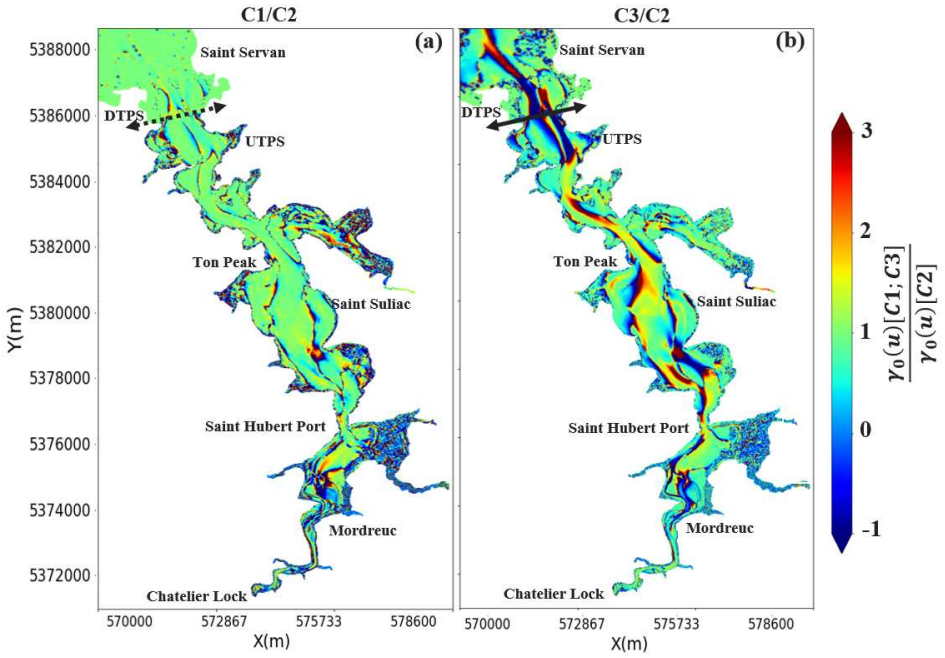

Figure B.3: Spatial distribution of velocity skewness ratio between (a) C1 and C2 scenarios and (b) C3 and C2 scenarios. The reference scenario is C2 (see Table 3.5). If velocity skewness ratio is negative, both C1 and C3 scenarios switch the flood (ebb) dominance to ebb (flood) dominance. The flood dominance is amplified (decreased) for both C1 and C3 scenarios when the velocity skewness ratio is larger than one (between zero and one). The ebb dominance is amplified (decreased) for both C1 and C3 scenarios when the velocity skewness ratio is between zero and one (larger than one).

APPENDIX C

COMPLEMENTARY INSIGHTS ON SEDIMENT DYNAMICS IN THE RANCE ESTUARY

C.1 Type of sediment transport in the Rance estuary

Based on the superficial sediment distribution in the estuary (Figure 5.2), the dominant classes of non-cohesive sediment present in the Rance estuary are :(i) very fine sand of a mean diameter $d_{50} = 100\mu m$, (ii) fine sand of a mean diameter $d_{50} = 200\mu m$ and (iii) gravel of a mean diameter of $d_{50} = 3000\mu m$. In order to characterise the type of sediment transport of these classes in the Rance estuary, the spatial distribution of Bagnold criterion [Bagnold, 1966] was depicted in Figure C.1. Based on friction velocity u_* and particles settling velocity w_s, Bagnold [1966] assessed that if $u_* > 0.8w_s$, non-cohesive particles are transported by suspension, otherwise they are either transported by bedload or are standing still. Figure C.1 showed that non-cohesive sediment in the Rance estuary present in the main channels are transported by suspension, while particles in the coves are either immobilized or transported by bedload. Since non-cohesive classes considered in the numerical model are primarily present in areas where suspension is dominant, suspension is the single mode of sediment transport considered in this work.

C.2 Multi-layer morphodynamic model of the Rance estuary

In order to evaluate bed evolution sensibility to consolidation processes, two configurations were compared: (i) case C1 representing the calibrated single-layer model validated in section 5.4, and (ii) case C2 representing a multi-layer model described here after (Figure C.2).
For the current version of GAIA, consolidation processes are based on the semi-empirical formulation originally developed by Villaret et al. [2010], which uses the iso-pycnal and first-order kinetics formulations. Consolidation of mud deposits is modeled using a layer discretization, where the first layer corresponds to the freshest deposit, while the lower layer is the most consolidated layer. Sediment deposition from the water column is added directly to the first layer. A flux of consolidation is computed for each layer and for each class of cohesive sediment separately. The values of the computed fluxes depend on the availability of each class in the layer considered [Lan, 2012].
Following Thiebot [2008], the multi-layer model set up in this work (C2) divided the Rance estuary's bed into a total of 10 layers :

- 9 layers with an initial thickness of $0.1m$ and fixed mud concentration $C(i)$ ranging from $200g/l$ to $1000g/l$ (Figure C.2.b),
- an active layer initialized with concentration of the first layer $=200g/l$ (Figure C.2.b).

Each layer is characterised by a critical shear stress for mud erosion $\tau_{ce}(i)$ computed from Equation C.1, proposed by Thiebot [2008].

$$\tau_{ce}(i) = \begin{cases} 2.238 \times 10^{-6} C^{1.953}(i) & \text{if } C(i) < 367\text{g/l} \\ 4.11 \times 10^{-10} C^{3.41}(i) & \text{otherwise} \end{cases} \tag{C.1}$$

Consolidation flux is computed for each layer and transferred to the layer underneath (orange arrows in Figure C.2.b) following Equation C.2 .

$$\frac{dM(i)}{dt} = RMT(i) \times M(i) \tag{C.2}$$

Where $M(i)$ and $RMT(i)$ are mud mass and rate of mass transfer at layer i. Lacking measurements to evaluate RMT values, these parameters were calibrated from the bed evolution

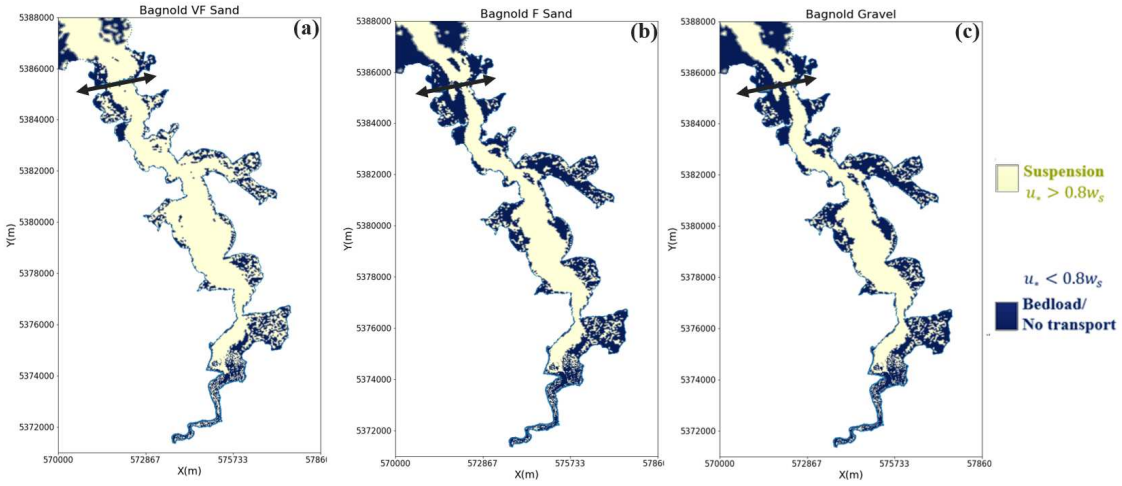

Figure C.1: Spatial distribution of Bagnold criterion $u_*/0.8w_s$ for (a) very fine sand of a mean diameter $d_{50} = 100\mu m$, (b) fine sand of a mean diameter $d_{50} = 200\mu m$ and (c) gravel of a mean diameter of $d_{50} = 3000\mu m$.

Table C.1: Rate of mass transfer RMT values for the multi-layer model (C2).

Layer	1	2	3	4	5	6	7	8	9
$RMT(s^{-1})$	10^{-4}	10^{-4}	10^{-5}	10^{-5}	10^{-5}	10^{-6}	10^{-6}	10^{-6}	0

measurements. The retained values are given in Table C.1.

The initial sediment distribution from the single-layer model was duplicated along the 10 layers considered to create a first initial sediment distribution for the multi-layer model. Then, a spin-up of a neap-spring tidal cycle was necessary to stabilize the numerical model. Morphodynamic model parameters are set as for the single-layer model (Table 5.1) except for the critical shear stress of mud erosion $\tau_{ce}(i)$ (computed by Equation C.1) and mud concentrations at each layer (Figure C.2.b).

Measured and simulated tide-averaged bed evolution from the multi-layer model (C2) are compared at locations A1, A2 and A3 in Figure C.3. The measured bed evolution at location A3 is reasonably well reproduced by the multi-layer model in terms of magnitude over the neap-spring tidal scale. Furthermore, the small scale dynamic effect, namely the bottom decreasing of ~ 2 cm observed at A3 during the neap tide between days 21.5 and 22.5 in Figure C.3.b, is well captured by the multi-layer model. Over the fortnightly period, a general tendency to sedimentation is noticed at the three locations, with increasing rates from probe A1, A2 to A3. This morphodynamic pattern over neap-spring tidal period is also captured by the single-layer model (C1) with similar rates (Figure C.4). For locations A1 and A3, the simulated bed evolution over the 14 days period are equivalent between the single- and the multi-layer models (differences of $1mm$). Nevertheless, configuration C1 seem to underestimate sedimentation rates, by $\sim 0.6cm$ at location A2 comparing to configuration C2. Furthermore, this difference is also noticed over spring tides (between days 14 and 19) at A1, A2 and A3 (Figure C.4). Indeed, mud is easily eroded from the superficial layer in the multi-layer model comparing to the single-layer model due to the mud concentrations considered in each configuration (Figure C.2). Therefore, particles eroded elsewhere are deposited for instance at locations A1, A2 and A3 with higher

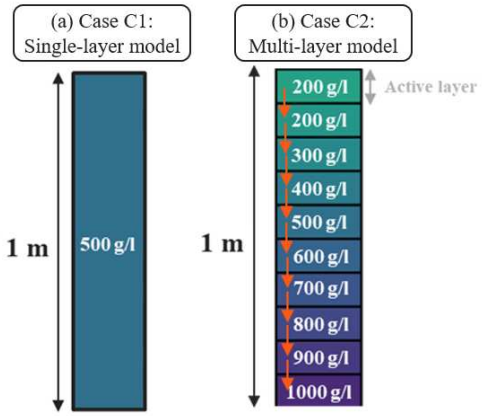

Figure C.2: Bed composition with mud concentrations for configuration (a) C1 with a single-layer model and (b) C2 with a multi-layer model.

rates and can be consolidated or eroded afterwards. In summary, both single- and multi-layer models provide correct bed evolution results over a neap-spring tidal period, with the advantage to multi-layer model to capture small scale bed dynamics, namely over neap tides. Thanks to its reasonable CPU time ($\sim$ 1.5 faster than the multi-layer model) and its reliable results over periods of interest (longer than 14 days), the single-layer morphodynamic model was deployed to investigate sediment dynamics in the Rance estuary.

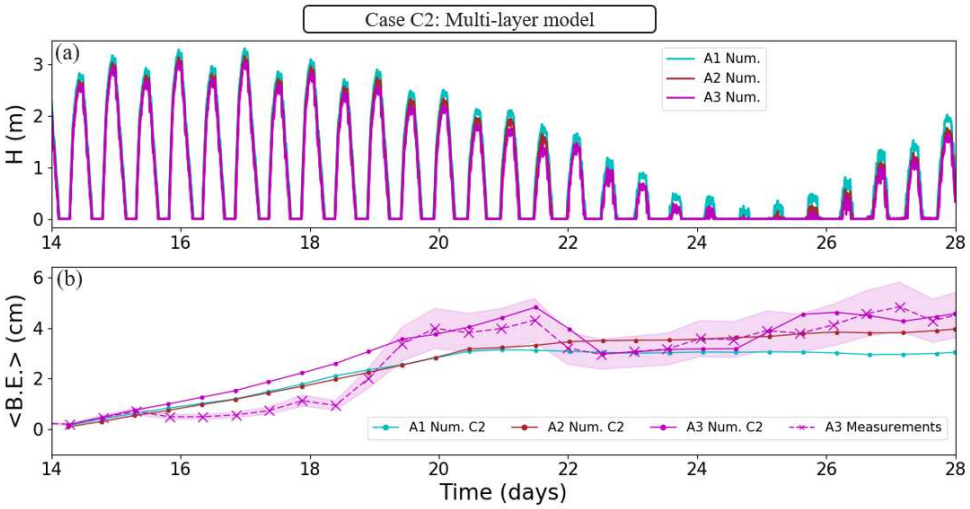

Figure C.3: (a) Simulated water levels at A1, A2 and A3. (b) Measured and simulated tide-averaged bed evolution for configuration C2 with a multi-layers model at A1, A2 and A3 locations. Light colored areas represent measurements uncertainties. (see stations location in Figure 5.1)

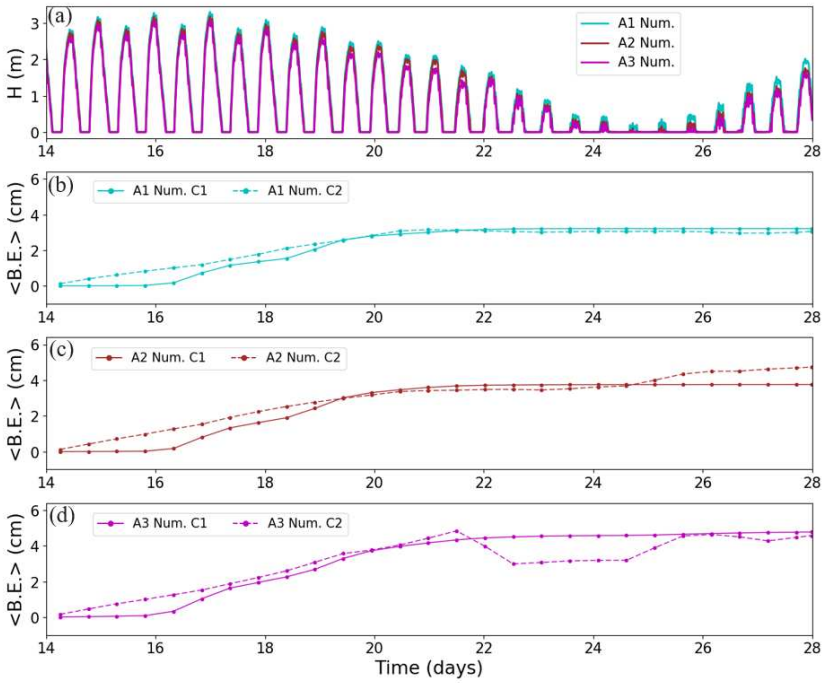

Figure C.4: (a) Simulated water levels at A1, A2 and A3. Simulated tide-averaged bed evolution for configurations with a single-layer model (C1) and multi-layers model (C2) at (b) A1, (c) A2 and (d) A3 locations. (see stations location in Figure 5.1)